Dissertation

submitted to the

Combined Faculty of Mathematics, Engineering and Natural Sciences

of

Heidelberg University, Germany

for the degree of

Doctor of Natural Sciences

Put forward by

Stefan Dickopf

born in Bad Kreuznach

Oral examination: 19.06.2024

High-precision Penning-trap measurements of the magnetic moments and hyperfine splitting in hydrogen-like beryllium-9

Referees:

Prof. Dr. Klaus Blaum

Prof. Dr. Selim Jochim

Abstract

During this work, microwave spectroscopy of the Zeeman and hyperfine structure of $^{9}Be^{3+}$ was performed to measure its magnetic moments and zero-field splitting. To this end, the experimental Penning-trap setup, previously used for spectroscopy on $^{3}He^{+}$, was upgraded, and the measurement techniques were improved. Most significantly, the implementation of phase-sensitive methods served a twofold improvement. Firstly, the statistical measurement uncertainty was reduced by a factor of 20. Secondly, they enabled the development of robust methods to characterize the fields and motion inside the trap, resulting in relative systematic uncertainties due to field imperfections well below 10^{-11}. By measurement of nuclear-spin transitions in $^{9}Be^{3+}$, its nuclear magnetic moment and zero-field splitting were determined with relative uncertainties of 0.6×10^{-9} and 4×10^{-12}, respectively. Compared to previous determinations, the uncertainty of the nuclear magnetic moment of ^{9}Be was improved by a factor 30 with only the magnetic moment of the proton being more precise. Further, a comparison with established measurements on $^{9}Be^{+}$ enabled a crucial test of diamagnetic shielding parameters essential for transferring nuclear magnetic moments across different charge states. Additionally, electron-spin transitions were measured using the phase-sensitive measurement technique. The resonance centers could be determined with relative statistical uncertainties of 2×10^{-11} improving on state-of-the-art bound-electron g-factor measurements. These measurements pave the way towards a determination of the electron mass in atomic mass units with relative uncertainties below 10^{-11}.

Zusammenfassung

In der vorliegenden Arbeit wurde Mikrowellenspektroskopie an der Zeeman und Hyperfeinstruktur von $^{9}Be^{3+}$ durchgeführt, um dessen magnetischen Momente und Nullfeldaufspaltung zu messen. Dafür wurden der experimentelle Penningfallenaufbau, welcher zuvor für Spektroskopie an $^{3}He^{+}$ benutzt wurde, überarbeitet und die Messmethoden verbessert. Am bedeutendsten war dabei die Implementierung von phasensensitiven Methoden, die eine Verbesserung in zwei Aspekten ermöglichte. Zum einen konnte damit die statistische Messunsicherheit um einen Faktor 20 reduziert werden. Zum anderen ermöglichte sie die Entwicklung von robusten Methoden zur Charakterisierung der Felder und Bewegung in der Falle, womit relative systematische Unsicherheiten durch Feldfehler kleiner als 10^{-11} erreicht werden konnten. Durch die Messung von Kernspinübergängen in $^{9}Be^{3+}$ wurden das Kernmoment und die Nullfeldaufspaltung mit relativen Unsicherheiten von 0.6×10^{-9} beziehungsweise 4×10^{-12} bestimmt. Verglichen mit vorherigen Messungens wurde die Unsicherheit des Kernmoments von ^{9}Be um einen Faktor 30 verbessert, wobei nun nur das Kernmoment des Protons genauer bekannt ist. Desweiteren hat der Vergleich mit fundierten Messsungen an $^{9}Be^{+}$ einen wichtigen Test von diamagnetischen Abschirmkonstanten ermöglicht. Dieser ist essentiell um Kernmomente zwischen verschiedenen Ladungszuständen zu übertragen. Desweiteren wurden mithilfe der phasensensitiven Methoden Elektronspinübergängen gemessen. Die Zentren der Resonanzen konnten mit relativen statistischen Unsicherheit von 2×10^{-11} bestimmt werden, was einer Verbesserung von state of the art Messungen des Elektron g-Faktors im gebundenen Zustand gleich kommt. Diese Messungen schaffen die Vorrausetzung für eine Bestimmung der Masse des Elektrons in atomaren Masseneinheiten mit einer relativen Unsicherheit niedriger als 10^{-11}.

Table of contents

Chapter 1.

Introduction

Though the Standard Model of particle physics has proven to successfully explain many observable phenomena in physics, it is known to be incomplete [1]. More thorough tests and searches for physics beyond the Standard Model are thus being carried out by various means, including astronomical observations [2], large-scale experiments with particle accelerators [3], and precision atomic physics measurements in laboratory experiments [4]. Within the latter, theoretical predictions of the Standard Model or proposed theory models are benchmarked against the precise measurement of fundamental particle properties.

In single-ion Penning-trap experiments, properties such as ion masses and magnetic moments can be measured with the highest achievable precision, allowing various fundamental physics tests, see e.g. refs. [5–11]. Within this work, microwave spectroscopy on the Zeeman and hyperfine structure in hydrogen-like beryllium-9 ($^9Be^{3+}$) was conducted in a Penning-trap experiment previously used to perform spectroscopy on $^3He^+$. Besides determining the magnetic moments and hyperfine splitting with high precision, this enabled testing several state-of-the-art theoretical calculations.

In the following chapter, the three main motivations are outlined and the structure of the thesis is presented.

The electron magnetic moment

The significance of the spin of the electron, and with it its intrinsic magnetic moment, to modern physics cannot be overstated. Beginning with its discovery [12] and the initial theoretical predictions by relativistic quantum mechanics [13], measurements of the electron magnetic moment now serve as a high-precision probe of quantum electrodynamics (QED). The gyromagnetic ratio, short g-factor, is the dimensionless proportionality of the magnetic moment to the magneton and can be calculated for both the free electron and for electrons bound to nuclei.

For the free electron, its value $g_s - 2 = 2\alpha/\pi + \ldots$ slightly deviates from 2 due to QED corrections evaluated in a series expansion $\sum_n a_n \alpha^n$ of the fine-structure constant α [14]. Presently, using an independent value of α, the QED calculations of the g-factor reach relative uncer-

tainties better than one part-per-trillion (ppt), limited by the uncertainty of the fine-structure constant. This precision is matched by the experimental Penning-trap measurements, ref. [15], and used to rigorously test QED. In turn, by using the QED theory as input, the measurement can provide a competitive value for the fine-structure constant [15].

In ions, the electron is bound to a nucleus of charge Z which alters the g-factor of the free electron - thus termed bound-electron g-factor. Specifically, in hydrogen-like ions in the $1s$ orbital, a first-order fractional change of the free electron g-factor by $-(\alpha Z)^2/3$ occurs due to special relativity [16]. Besides the QED corrections of the free electron g-factor, bound-state QED corrections, which scale in powers of $(Z\alpha)$, must be included in the calculations. Stringent tests of bound-state g-factors of hydrogen-like ions have been performed in Penning traps with e.g. $^{28}Si^{13+}$ [17], and more recently with $^{20,22}Ne^{9+}$ [18, 19] and $^{118}Sn^{49+}$ [5]. For bound-electron g-factor measurements in Penning traps, the measured ratio of the electron's spin-precession frequency to the ion's cyclotron frequency depends on the product of the g-factor and the ion-to-electron mass ratio. Thus, the QED tests depend in equal measure on accurate values of the ion masses, determined typically by (the combination of) mass ratios measured in other Penning-trap experiments, and the electron mass in atomic mass units. For low-Z hydrogen-like ions, the precision of the theoretical g-factors allows inverting the measured frequency ratio for the ion-to-electron mass ratio [20]. Given an independent and similarly precise measurement of the ion mass in atomic mass units, the electron mass can be determined. Thus, the accuracy of the atomic mass of the electron, as provided in the CODATA evaluations of 1998 and 2018, has steadily improved by nearly two orders of magnitude, largely due to several Penning-trap bound-electron g-factor measurements [21, 22].

The last improvement of the electron mass with a Penning-trap measurement to a relative precision of 30 ppt was limited by the statistical measurement uncertainty and a systematic effect called the image charge shift [23]. While solutions exist to improve on the latter [24, 25], the statistical uncertainties of bound-electron g-factor measurements have not improved since [5, 18, 26]. Within this work, it is demonstrated that this limit can be surpassed, paving the way toward a measurement of the electron mass in atomic mass units with a relative uncertainty below 10 ppt.

Nuclear magnetic moments and diamagnetic shielding

While the g-factor of the electron can be calculated from QED and α to one ppt [15], state-of-the-art quantum chromodynamics (QCD) calculations of magnetic moments of even the simplest nuclei, the proton and neutron, only reach about three significant digits [27]. Achieving the latter uncertainties in measurements typically poses no significant challenges, rendering stringency tests of QCD with magnetic moments experimentally uninteresting. However, a more fundamental test of charge-parity-time symmetry in the baryonic section is conducted via the comparison of the magnetic moments of the proton and antiproton [6, 28].

In the context of this thesis, two additional and important applications for precise values of nuclear magnetic moments will be discussed.

The first concerns QED tests via the (magnetic dipole) hyperfine splitting (HFS), see also the next section. As the HFS arises due to the interaction of the nuclear magnetic moment

with the magnetic moment of the orbiting electrons, its value directly depends on the nuclear g-factor [29]. Again, as noted above, calculations of nuclear magnetic moments from theory models are not precise enough, and rather experimental values have to be used.

Another application is their use in absolute magnetometry with nuclear magnetic resonance (NMR). Specifically, ^{3}He is an ideal candidate due to its simple atomic structure, large magnetic moment, and ability to hyperpolarize it using optical pumping techniques [30]. Being used at the muon $g-2$ experiment, hyperpolarized ^{3}He NMR cells already find application in precision physics [31]. In an effort to determine the magnetic moment of ^{3}He independently of NMR references, its measurement via the Zeeman and hyperfine structure of hydrogen-like ^{3}He$^+$ was recently performed at this experiment, additionally achieving a tenfold improvement of its relative uncertainty to 0.7 parts-per-billion [11].

However, the experiment probed the magnetic moment in the hydrogen-like ion, and theoretical calculations are required to transfer it to the value of the atom. This is because the presence of the orbiting electron(s) induces a shift of the magnetic field at the nucleus, different for the hydrogen-like ion and the atom, known as diamagnetic shielding [32]. More broadly, these shielding effects manifest in any bound state of the nucleus, including atoms, molecular gases, and solids, and typically adjust the nuclear magnetic moment from 10^{-5} to a few percent [33]. Since most measurements with nuclear magnetic moments are conducted in some form of bound state, except e.g. those of the proton and antiproton performed in Penning traps[1], the calculation of shielding parameters holds significant importance. In the past, tabulations of bare-nuclear magnetic moments revealed significant discrepancies among several values, largely attributed to underestimated or omitted uncertainties of the diamagnetic shielding parameters [33, 34]. Moreover, underestimated uncertainties of shielding calculations directly resulted in major disparities within HFS tests, such as ^{165}Ho^{66+} [35], ^{207}Pb^{81+} [36], and the recent 7-σ deviation in the specific difference of ^{209}Bi$^{82+,80+}$ [37, 38].

For ^{3}He, such issues are remedied by using advanced calculations employing non-relativistic QED (NRQED) methods to evaluate the diamagnetic shielding. Within the NRQED calculations, uncertainties are explicitly evaluated and amount to only a fraction of the experimental uncertainty for both the shielding of the hydrogen-like ion and two-electron atom [39]. Though recently, adjustments to the NRQED shielding of ^{3}He on par with the experimental value of the nuclear magnetic moment of ^{3}He$^+$ have been performed [40]. This further motivates an experimental verification of these calculations at the parts-per-billion precision level using other systems, which is a goal pursued with the measurements performed in this work.

The hyperfine splitting and nuclear structure

In this work, specifically, the HFS in s-states caused by the interaction of the spin-magnetic moments of the nucleus with the valence shell electron is investigated.

Since the potential of the magnetic dipole-dipole interaction scales with the inverse cube of the separation of the dipoles [29], it is strongly influenced by the structure of the nucleus due to the non-vanishing wave function of the electron inside the nucleus. This leads to a nuclear

[1] Here, they are bound in the trap potentials, which is, however, a much weaker binding compared to the previously mentioned ones.

structure dependence of the HFS which scales as r_Z/a_0 [41], where a_0 is the Bohr radius and r_Z is the so-called Zemach radius. The latter is related to both electric and magnetic form factors of the nucleus and in a simple approximation slightly larger than the root-mean-square charge radius r_0, $r_Z \approx 1.3\,r_0$ [42]. In comparison, the corrections to binding energies [43] or electron g-factors [44] from the Coulomb interaction have the weaker dependency $(r_0/a_0)^2$. For example, in hydrogen, the relative nuclear structure contribution to the 1s HFS is 3×10^{-5} [45], while the contributions to optical transitions are in the range of 10^{-10} [46]. Paired with the limitations of nuclear structure theory to predict r_Z, this strong dependence makes precise theoretical predictions of hyperfine splittings very challenging. However, tests of the HFS are very intriguing because the scaling of the interaction also increases the sensitivity of the HFS to the stronger fields near the nucleus. Consequently, the bound-state QED contributions of the HFS are larger than e.g. for the g-factor in the same system [47]. For example in the $^3He^+$ ion, the fractional bound-state contribution to the 1s HFS is of the order of 100×10^{-6} while for its electron g-factor it is only $\sim 40\times10^{-9}$ [11].

To circumvent the nuclear structure limitations, comparisons between different hyperfine intervals in the same atom or ion, with one serving as a reference to the nuclear structure contributions, can be performed [37, 45]. Since the theoretical calculations, apart from the nuclear structure, can be performed most accurately in single-electron, hydrogen-like atoms, measurements of their ground-state 1s HFS serve as an ideal reference [45]. For low Z, such measurements exist only for the hydrogen-isotopes, refs. [48–50], and $^3He^+$ [11, 51] and QED has been tested by comparison to measurements of the 2s HFS in the hydrogen-like systems [45]. In contrast, for high Z, several measurements exist but the HFS tests are limited by the precision of the magnetic moment [38, 47]. Additionally, as pointed out in the previous paragraph, quite a number of these tests have significant discrepancies due to underestimated uncertainties of the nuclear magnetic moment.

Recently, tests of the 2s HFS by comparison of helium-like and atomic (lithium-like) charge states in ^{6,7}Li have been investigated [52–55]. Additional to ^{6,7}Li, the 2s HFS of the lithium-like $^9Be^+$ ion has been measured with very high precision in a Penning trap [56]. While a hyperfine structure measurement in the helium-like $^9Be^{2+}$ as well, ref. [57], its large uncertainty does not allow for a precise test and new measurements are planned by the same group that performed the $^{6,7}Li^+$ spectroscopy [58]. Meanwhile, the comparison between helium-like and lithium-like systems, due to the increased complexity, mainly serves to benchmark the calculations of the lithium-like system and the more advanced calculations of the two-electron systems have only been tested using ^{3}He [54, 59].

With the measurement of the 1s HFS of $^9Be^{3+}$ in this work, an additional high-precision reference for the hyperfine interaction is introduced. It is directly compared to $^9Be^+$ to test the QED calculation of the lithium-like 2s HFS. Further, it serves as the ideal reference for future tests of the helium-like HFS of $^9Be^{2+}$ or other HFS intervals.

Structure of this thesis

I will start with Chapter 2 which focuses on the physics of the Penning trap. The primary objective of this chapter is to introduce the means for the high-precision measurement of the free cyclotron frequency, which includes a discussion of the trap geometry, systematic shifts, and detection techniques.

Moving on, I will discuss the specifics of the spectroscopy of the Zeeman and hyperfine splitting in Chapter 3. Here, calculations of the energy levels, transition probabilities, the relativistic shift of the transition frequencies, and the employed Penning-trap detection will be outlined.

In Chapter 4 and Chapter 5, I will give an overview of the experimental apparatus, and a detailed account of the implementation of the Penning trap methods. Additionally, using new methods developed in this thesis, I will perform a precise characterization of the trapping fields and the ion motion.

The spectroscopy of Zeeman and hyperfine transitions of $^{9}Be^{3+}$ is split into two chapters. In Chapter 6, I will present the measurement of transitions sensitive to the properties of the nucleus. As a major result, a comparison to $^{9}Be^{+}$ enables the first high-precision test of multi-electron diamagnetic shielding parameters. In Chapter 7, I will present bound-electron g-factor measurements with statistical uncertainties surpassing the current state-of-the-art. These pave the way toward measurements at the 10 ppt level, allowing, among others, for an improvement of the atomic mass of the electron by at least a factor of 3.

Lastly, in Chapter 8, I will give an outlook on ongoing efforts at our experiment, including a new Penning-trap design for sympathetic laser cooling, and conclude with a summary of this thesis.

Chapter 2.

The Penning trap

A Penning trap provides spatial confinement of particles through a strong magnetic field and an electrostatic field [60]. The static fields of the trap can be tuned to make the particles's motion harmonic to a very high degree, providing a well-understood environment for high-precision spectroscopy. It allows the precise measurement of the magnetic field that a single particle experiences and the non-destructive detection of spin states. Therefore, it is an ideal tool to perform measurements of the particle's magnetic properties via the Zeeman and hyperfine splitting.

In this chapter, I will introduce the basic concepts of a Penning trap as a tool for precision spectroscopy. This includes a description of the ideal motion, typical deviations from it, the trap geometry, and the employed detection techniques. I also give a probabilistic description of the motion of ions coupled to a heat bath in Section A.

2.1. Basic particle motion

A charged particle of mass m and charge q inside a homogeneous magnetic field B_0 is forced on a helical motion around the field lines with angular frequency

$$\omega_c = \frac{q}{m} B_0. \tag{2.1}$$

This frequency is called the free cyclotron frequency. Given the charge and mass of a particle, its determination constitutes a measurement of the magnetic field at the ion's position. As the magnetic field directly determines the transition frequencies in the Zeeman and hyperfine splitting, outlining the means for its high-precision measurement will be one of the main goals of this chapter.

Containing the particle in the direction of the field lines, which define the z-axis, can be achieved with a quadratic electric potential Φ. As this potential needs to fulfill the Laplace equation $\nabla^2\Phi = 0$, it also requires radial components. The choice of a quadrupolar electrostatic field

$$\Phi(\vec{r}) = C_2 \left(z^2 - (x^2 + y^2)/2\right), \tag{2.2}$$

with $\vec{r} = (x, y, z)$ being the coordinate vector and C_2 a tunable free parameter, forces the particle on a harmonic oscillation on the z-axis with eigenfrequency

$$\omega_z = \sqrt{2\frac{q}{m}C_2}. \tag{2.3}$$

For positively charged particles this requires $C_2 > 0$. The radial components act on the particle with an outward force in the xy-plane and split the free cyclotron motion into two eigenmotions with frequencies

$$\omega_\pm = \frac{1}{2}\left(\omega_c \pm \sqrt{\omega_c^2 - 2\omega_z^2}\right) \tag{2.4}$$

called modified cyclotron and magnetron motion respectively. The condition $\omega_c^2 > 2\omega_z^2$ is a stability criterion for the particle's radial orbit. Additionally, to determine the magnetic field B_0 via ω_c, the measurement of at least two of the three eigenfrequencies is needed. Typically, either the sideband relation

$$\omega_c = \omega_+ + \omega_- \tag{2.5}$$

or the quadratic addition of frequencies

$$\omega_c^2 = \omega_+^2 + \omega_z^2 + \omega_-^2 \tag{2.6}$$

is used. The latter is known as the Brown-Gabrielse invariance theorem and is also valid for slight electric field misalignment and ellipticity [61].

Now that all motional frequencies are defined, it is helpful to mention some typical values. In this experiment, which uses light ions, 10 MHz $< \frac{\omega_c}{2\pi} <$ 80 MHz, 300 kHz $< \frac{\omega_z}{2\pi} <$ 800 kHz, 3 kHz $< \frac{\omega_-}{2\pi} <$ 20 kHz and $\omega_+ = \omega_c - \omega_-$. This reflects the typical hierarchy of frequencies in a Penning trap

$$\omega_c > \omega_+ \gg \omega_z \gg \omega_-. \tag{2.7}$$

Instead of the angular velocities ω_i in units of radians, the frequencies ν_i in units of Hz may also be used throughout this thesis.

In the following, a more detailed description of the equations of motions (eom) in phase space and their integration with respect to time t is given. To this end, the eom are solved in the form $\frac{\mathrm{d}}{\mathrm{d}t}\vec{a} = A\vec{a}$, which requires computing the eigenvalues and eigenvectors of the matrix A. This allows writing the solution as a superposition of eigenmotions. The components of the phase space vector $\vec{a}$ are the coordinates and the respective velocities. The velocities are termed $v_i = \dot{r}_i$ for the respective coordinate r_i. Additionally, the velocities are scaled by a suitable frequency to transform them into coordinate units.

The eom decouple for the z-coordinate and the xy-plane, so they can be handled separately. For the z-coordinate this gives

$$\frac{\mathrm{d}}{\mathrm{d}t}\begin{pmatrix} z \\ \tilde{z} \end{pmatrix} = \begin{pmatrix} 0 & \omega_z \\ -\omega_z & 0 \end{pmatrix}\begin{pmatrix} z \\ \tilde{z} \end{pmatrix}, \tag{2.8}$$

where $\tilde{z} = v_z/\omega_z$. The eigenvalues are just $\{i\omega_z, -i\omega_z\}$ and the general solution is simply a harmonic oscillation of both the coordinate and the velocity with a 90° phase shift between

them

$$\begin{pmatrix} z(t) \\ \tilde{z}(t) \end{pmatrix} = \rho_z \begin{pmatrix} \cos(\omega_z t + \varphi_z) \\ \sin(\omega_z t + \varphi_z) \end{pmatrix}, \tag{2.9}$$

where ρ_z is the amplitude and φ_z is the phase of the axial oscillation. Similarly, this can be expressed given a valid point in phase space $(z_0, \tilde{z}_0)$. The future evolution of the oscillation is given by the evolution matrix

$$\begin{pmatrix} z(t) \\ \tilde{z}(t) \end{pmatrix} = \begin{pmatrix} \cos(\omega_z t) & \sin(\omega_z t) \\ -\sin(\omega_z t) & \cos(\omega_z t) \end{pmatrix} \begin{pmatrix} z_0 \\ \tilde{z}_0 \end{pmatrix} \equiv E_z \begin{pmatrix} z_0 \\ \tilde{z}_0 \end{pmatrix}. \tag{2.10}$$

In the radial plane, the Lorentz force $\vec{F} = q\vec{v}\times\vec{B}$ couples the x and y motion. Using the substitution $u = x + iy$ and scaling $\tilde{u} = v_u\sqrt{2}/\omega_z = v_u/\sqrt{\omega_+\omega_-}$ the eom are

$$\frac{\mathrm{d}}{\mathrm{d}t}\begin{pmatrix} u \\ \tilde{u} \end{pmatrix} = \begin{pmatrix} 0 & \sqrt{\omega_+\omega_-} \\ \sqrt{\omega_+\omega_-} & -i(\omega_+ + \omega_-) \end{pmatrix} \begin{pmatrix} u \\ \tilde{u} \end{pmatrix}. \tag{2.11}$$

The eigenvalues of the matrix are $\{-i\omega_+, -i\omega_-\}$ and the general solution is a superposition of the eigenvector solutions

$$\begin{pmatrix} u(t) \\ \tilde{u}(t) \end{pmatrix} = \begin{pmatrix} 1 & 1 \\ -i\sqrt{\frac{\omega_+}{\omega_-}} & -i\sqrt{\frac{\omega_-}{\omega_+}} \end{pmatrix} \begin{pmatrix} \rho_+ e^{-i\omega_+ t + i\varphi_+} \\ \rho_- e^{-i\omega_- t + i\varphi_-} \end{pmatrix} \tag{2.12}$$

where $\rho_\pm$ and $\varphi_\pm$ are the amplitudes and phases, respectively. Here, the representation given a valid phase space point $(u_0, \tilde{u}_0)$ is

$$\begin{pmatrix} u(t) \\ \tilde{u}(t) \end{pmatrix} = \frac{1}{\omega_+ - \omega_-} \begin{pmatrix} \omega_+ e^{-i\omega_- t} - \omega_- e^{-i\omega_+ t} & i\sqrt{\omega_+\omega_-}\left(e^{-i\omega_+ t} - e^{-i\omega_- t}\right) \\ i\sqrt{\omega_+\omega_-}\left(e^{-i\omega_+ t} - e^{-i\omega_- t}\right) & \omega_+ e^{-i\omega_+ t} - \omega_- e^{-i\omega_- t} \end{pmatrix} \begin{pmatrix} u_0 \\ \tilde{u}_0 \end{pmatrix} \equiv E_u \begin{pmatrix} u_0 \\ \tilde{u}_0 \end{pmatrix}. \tag{2.13}$$

It is more concise to express the motion through x and y components $x(0) = x_0^+ + x_0^-$, $y(0) = y_0^+ + y_0^-$ of the modified cyclotron and magnetron motion, respectively. This gives the solution in the xy-plane in a very similar fashion as for the axial motion:

$$\begin{aligned} \begin{pmatrix} x(t) \\ y(t) \end{pmatrix} &= \begin{pmatrix} \cos(\omega_+ t) & \sin(\omega_+ t) \\ -\sin(\omega_+ t) & \cos(\omega_+ t) \end{pmatrix} \begin{pmatrix} x_0^+ \\ y_0^+ \end{pmatrix} + \begin{pmatrix} \cos(\omega_- t) & \sin(\omega_- t) \\ -\sin(\omega_- t) & \cos(\omega_- t) \end{pmatrix} \begin{pmatrix} x_0^- \\ y_0^- \end{pmatrix} \\ &\equiv E_+ \begin{pmatrix} x_0^+ \\ y_0^+ \end{pmatrix} + E_- \begin{pmatrix} x_0^- \\ y_0^- \end{pmatrix}. \end{aligned} \tag{2.14}$$

In summary, the full solution of the motion is a superposition of three undamped harmonic motions, see Figure 2.1. While that is clear from the eom in the axial motion, the radial motion also decouples into two harmonic motions, allowing for all three modes to be treated as independent harmonic oscillator modes.

The (non-relativistic) energy of the particle inside the electromagnetic field is $E = \frac{1}{2}m\sum_i v_i^2 + q\Phi$. This result can be calculated starting from the Lagrange function $L = \frac{1}{2}m\sum_i v_i^2 + q\sum_i A_i v_i - q\Phi$, where $\vec{A}$ is the vector potential of the static field. As the Lagrange function is not explicitly time dependent, the energy is $E = \sum_i v_i \frac{\partial L}{\partial v_i} - L$. Inserting the general solutions Eq. (2.9) and

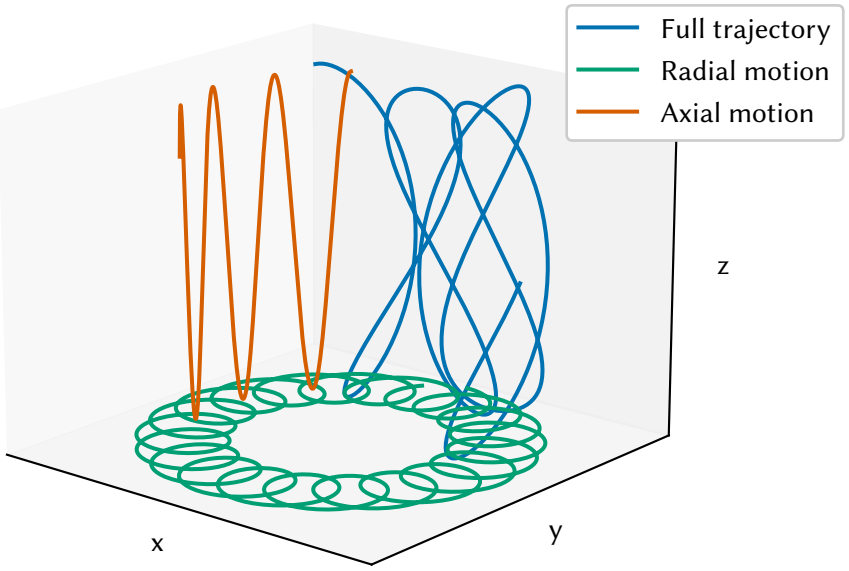

Figure 2.1: Particle motion inside a Penning trap. The blue, orange and green curve show the superposition of all three eigenmotion, the motion in the plane and the axial oscillation, respectively.

Eq. (2.12), defines the individual energies of the eigenmotions in dependence on their respective amplitudes

$$\begin{aligned} E &= \frac{1}{2}m\left[(\omega_+^2 - \omega_z^2/2)\rho_+^2 + (\omega_-^2 - \omega_z^2/2)\rho_-^2 + \omega_z^2\rho_z^2\right] \\ &\equiv E_+ + E_- + E_z \approx \frac{1}{2}m\omega_+^2\rho_+^2 - \frac{1}{4}m\omega_z^2\rho_-^2 + \frac{1}{2}m\omega_z^2\rho_z^2, \end{aligned} \tag{2.15}$$

where the last approximation holds for the typical frequency hierarchy Eq. (2.7).

2.2. Cylindrical Penning traps

The large magnetic field of the Penning trap is commonly generated by superconducting magnet coils far away from the ion's position. When talking about the physical trap itself, what is typically meant is the set of electrodes that generate the electrostatic field, which are in comparison to the coils much smaller and very close to the charged particle. To create the best approximation of an ideal quadrupolar electrostatic field, two major Penning-trap designs exist. The classical Penning trap uses hyperbolically shaped electrodes whose surfaces match the equipotential surfaces of a quadrupolar field [62]. This design has been and is still used in several successful experiments [15, 63]. The open-endcap cylindrical Penning trap, see Figure 2.2, has the advantage of a much simpler geometry and intrinsic axial access of the trapping region [64].

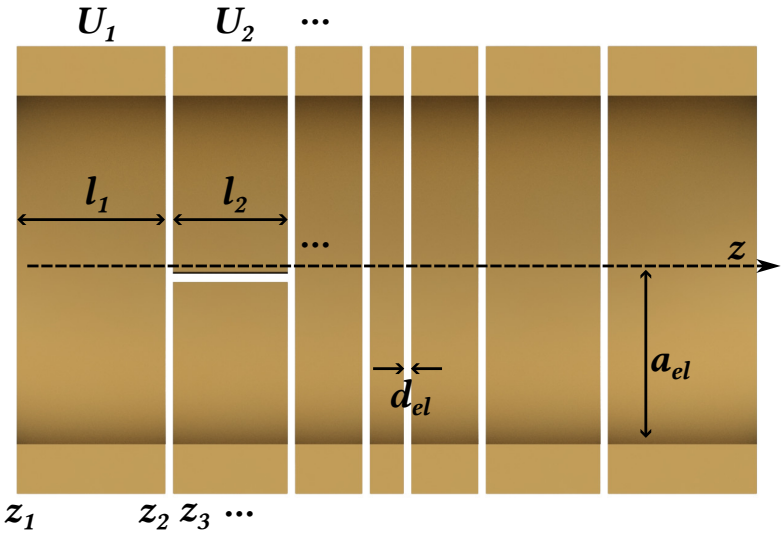

Figure 2.2: Cyclindrical Penning trap. This schematic resembles the precision trap of this experiment. The trap consists of electrodes with individual lengths l_i and applied voltages U_i and common spacing d_{el} and radius a_{el}. The coordinates z_i represent the extent of each electrode on the z-axis.

As this experiment uses a stack of cylindrical electrodes, consisting of four traps and adjacent transport electrodes, an overview of this configuration is now given. On the axis of symmetry, a general electrostatic potential may be written as

$$\Phi(z) = \sum_k C_k(z_0) z^k, \tag{2.16}$$

where C_k are the expansion coefficients around a position z_0. Given the axial symmetry of the potential, the radial dependencies have a fixed relation to the axial dependencies, see e.g. ref. [65]. The design goals for a Penning trap for precision measurements are a C_2 value that gives a reasonable ω_z, compare Eq. (2.3), and small higher order anharmonic terms that lead only to negligible or correctable systematic shifts, see the next Section.

The potential for a stack of p cylindrical electrodes, with a geometry as shown in Figure 2.2 and assuming a vanishing potential at the boundaries of the trap, can be calculated analytically. Here, only the result is quoted, for a full derivation see e.g. refs. [64, 66]. Setting the voltage at the outer electrodes to zero, $U_1 = U_p = 0$, to ensure the vanishing potential at the trap boundaries, gives

$$\Phi(z) = \sum_{n=1}^{\infty} \frac{2}{I_0(k_n a_{el})} \frac{\sin(k_n z)}{k_n^2 L d_{el}} \sum_{i=2}^{p} (U_i - U_{i-1})(\sin(k_n z_{2i-1}) - \sin(k_n z_{2i-2})), \tag{2.17}$$

where $k_n = n\pi/L$, with $L = z_{2p} - z_1$ being the trap's total length and I_0 is the modified Bessel function of zeroth order. For actual computations, the sum has to be truncated at a sufficiently large order $n = n_0$, where typically $n_0 \approx 1000$ to ensure convergence. Given a trap geometry

defined by the parameters, $\{a_{el}, d_{el}, z_i\}$ it is convenient to write the potential as a linear equation in the applied voltages $\vec{U} = (U_2, \ldots, U_{p-1})^T$

$$\Phi(z) = \vec{g}_0^T(z) W \vec{U}, \tag{2.18}$$

where the $n_0 \times (p-2)$ matrix W depends only on the geometry

$$W_{ni} = \frac{1}{I_0(k_n a_{el})} \frac{1}{k_n^2 d_{el}} (\sin(k_n z_{2i-1}) - \sin(k_n z_{2i-2}) - \sin(k_n z_{2i+1}) + \sin(k_n z_{2i})) \tag{2.19}$$

and $(g_0)_n(z) = 2/L \sin(k_n z)$ only on the position and total length L. As the position z occurs only in $(g_0)_n(z)$, the expansion coefficients $C_k(z_0)$ can be easily expressed as

$$C_k(z_0) = \frac{1}{k!} \vec{g}_k^T(z_0) W \vec{U}, \tag{2.20}$$

where

$$(g_k)_n(z_0) = \frac{2k_n^k}{L} \sin\Big(\frac{\pi}{2}k + k_n z_0\Big). \tag{2.21}$$

The most commonly used cylindrical Penning trap uses 5 electrodes. This configuration has grounded endcaps of length $l_1 = l_5 = l_{ec}$, correction electrodes of length $l_2 = l_4 = l_{ce}$ and a central ring electrode with length $l_3 = l_r$. Voltages are applied symmetrically $\vec{U} = U_0\ (\mathrm{TR}, 1, \mathrm{TR})^T$. Because of the mirror symmetry around $z_0 = z_1 + L/2$ the odd order coefficients $C_1 = C_3 = \ldots = 0$. The tuning ratio TR is chosen such that the first anharmonicity $C_4(z_0) = 0$, which consequently requires

$$\begin{aligned} &\vec{g}_4(z_0)^T W \vec{U} = 0 \\ \Rightarrow\ &2(\vec{g}_4(z_0)^T W)_2 \mathrm{TR} + (\vec{g}_4(z_0)^T W)_3 = 0 \\ \Rightarrow\ &\mathrm{TR} = -\frac{1}{2} \frac{(\vec{g}_4(z_0)^T W)_3}{(\vec{g}_4(z_0)^T W)_2}. \end{aligned} \tag{2.22}$$

By further utilizing the freedom of choosing the lengths l_{ce} and l_r, the 5-pole Penning trap can be optimized such that $C_4 = C_6 = 0$ and C_2 can be made first order independent of the tuning ratio $\frac{\partial C_2}{\partial \mathrm{TR}} = 0$ around the above calculated optimal TR. These two conditions make the trap a so called compensated and orthogonal Penning trap, respectively [64]. In practice, the electrodes have slight deviations from their ideal, optimized lengths, which always leads to a slight breaking of the compensation, i.e. C_6 is not zero at the tuning ratio where $C_4 = 0$. Mirror symmetry-breaking deviations lead to odd-order C_k terms. These can be corrected in first order by applying asymmetric voltages on the correction electrodes.

The experiment's 7-pole precision trap, see Figure 2.2, with applied voltages

$$\vec{U} = U_0\ (\mathrm{TR}_C \mathrm{TR}_2, \mathrm{TR}_C \mathrm{TR}_1, 1, \mathrm{TR}_C \mathrm{TR}_1, \mathrm{TR}_C \mathrm{TR}_2)^T \tag{2.23}$$

is optimized with the conditions $C_4 = C_6 = C_8 = C_{10} = 0$ and the combined orthogonality $\frac{\partial C_2}{\partial \mathrm{TR}_C} = 0$, compare ref. [66] and the upcoming thesis of Marius Müller. Due to the additional set of correction electrodes, this configuration allows to have $C_4 = C_6 = 0$ at a set of $\{\mathrm{TR}_1, \mathrm{TR}_2\}$, even with deviations of the electrode lengths.

2.3. Systematic shifts from field imperfections

Deviations from the ideal trapping fields, if not sufficiently suppressed or corrected for, alter the observed motional frequencies and lead to incorrectly determined free cyclotron frequencies Eq. (2.1). Both anharmonicities of the electrostatic field, given by the terms $C_{k>2}$ introduced in Eq. (2.16) and inhomogeneities added to the homogeneous B_0

$$B = B_0 + \sum_{k>0} B_k z^k \tag{2.24}$$

contribute. In ref. [65], all shifts due to even-order imperfections of the fields are calculated via classical first-order perturbation theory. The odd-order imperfections only start to contribute in second-order, as their first-order effect averages to zero over a full orbit of the particle's motion. To gauge the contribution of the imperfections, they must be compared to the perfect field together with the amplitudes of the eigenmotions ρ_i, i.e. $\rho_i^{k-2} C_k/C_2$, $\rho_i^k B_k/B_0$ for even k and $\rho_i^{2k-4} C_k^2/C_2$, $\rho_i^{2k} B_k^2/B_0$ for odd k. In this experiment, the amplitudes and higher-order imperfections are sufficiently small to justify only the treatment of shifts quadratic in the amplitudes.

In this and the following section, all shifts should be considered approximate, as they typically include some (justified) simplifications or are evaluated through perturbation theory. Shifts are expressed with the sign convention $\omega \rightarrow \omega + \delta\omega$, which typically means that the measured quantity needs to be corrected by subtracting $\delta\omega$.

2.3.1. Electrostatic imperfections

The most important electrostatic field imperfection is due to the quartic potential term C_4. The corresponding frequency shifts to the eigenmotions are [65]

$$\begin{aligned} \frac{\delta\omega_z}{\omega_z} &= \frac{3C_4}{4C_2}\left(\rho_z^2 - 2\rho_+^2 - 2\rho_-^2\right), \\ \frac{\delta\omega_\pm}{\omega_\pm} &= \mp\frac{\omega_\mp}{\omega_+ - \omega_-}\frac{3C_4}{2C_2}\left(2\rho_z^2 - \rho_\pm^2 - 2\rho_\mp^2\right). \end{aligned} \tag{2.25}$$

The first odd-order term C_1 adds a constant force term in the axial equations of motion Eq. (2.8)

$$\begin{aligned} \frac{\mathrm{d}}{\mathrm{d}t}\begin{pmatrix} z \\ \tilde{z} \end{pmatrix} &= \begin{pmatrix} 0 & \omega_z \\ -\omega_z & 0 \end{pmatrix}\begin{pmatrix} z \\ \tilde{z} \end{pmatrix} - \begin{pmatrix} 0 \\ \frac{q}{m}\frac{C_1}{\omega_z} \end{pmatrix} \\ &= \begin{pmatrix} 0 & \omega_z \\ -\omega_z & 0 \end{pmatrix}\begin{pmatrix} z + \frac{C_1}{2C_2} \\ \tilde{z} \end{pmatrix}. \end{aligned} \tag{2.26}$$

It is clear that this is easily solved by substituting $z \rightarrow z - \frac{C_1}{2C_2}$, which does not change $\tilde{z}$. A C_1 thus only leads to a constant offset of the equilibrium position of the axial oscillation

$$\Delta z = -\frac{C_1}{2C_2} \tag{2.27}$$

and no frequency shift occurs.

In the case of C_3, the potential term also includes radial dependencies and the potential is modified to

$$\Phi = C_2\left(z^2 - (x^2+y^2)/2\right) + C_3\left(z^3 - 3z(x^2+y^2)/2\right). \tag{2.28}$$

The force components for the radial eigenmotions are proportional to zx and zy which would only lead to frequency shifts for resonant interaction between the axial and radial modes. As all frequencies are separated quite well this is not the case and the effects of these terms average to zero. For the axial motion, it can be shown that a shift of the equilibrium position occurs, but depending on the mode amplitudes [19]

$$\Delta z = \frac{3C_3}{4C_2}\left(-\rho_z^2 + \rho_+^2 + \rho_-^2\right). \tag{2.29}$$

Considering the radial mode amplitudes this can be argued by fixing the x^2+y^2 term in Eq. (2.28) to the respective amplitude and treating it as an effective C_1 term. Performing a series expansion of Eq. (2.28) around the shifted equilibrium positions for the respective amplitudes the frequency shift gives

$$\frac{\delta\omega_z}{\omega_z} = \frac{C_3^2}{16C_2^2}\left(-15\rho_z^2 + 18(\rho_+^2 + \rho_-^2)\right). \tag{2.30}$$

2.3.2. Magnetostatic imperfections

While the electrostatic shifts can always be treated as actual changes to the free cyclotron frequency, for the magnetostatic shifts some intricacies, especially for the Zeeman splitting and hyperfine structure measurements, need to be considered.

The charged particle moving on circular orbits in the radial plane has magnetic moments in the z-direction associated with the two eigenmotions. Given the angular momentum $\vec{L} = \vec{r}\times\vec{v}$ the mean magnetic moments of the individual eigenmotions can be derived from the solutions Eq. (2.9) and Eq. (2.12)

$$\mu_{z,\pm} = -\frac{q}{2}L_{z,\pm} = -\frac{q}{2}\omega_\pm\rho_\pm^2. \tag{2.31}$$

Note that the x and y components of the magnetic moment average to zero [67]. In inhomogeneus magnetic fields, particles with magnetic moments μ_z are subject to the axial force

$$F_z = \mu_z\frac{\partial B_z}{\partial z}, \tag{2.32}$$

which can shift ω_z. Shifts of the radial eigenmotions can occur due to actual mean shifts of the magnetic field at the finite orbit of the particle. In the case of the latter shifts, the measured cyclotron frequency still reflects the magnetic field at the ion's position, while the shifts due to magnetic moments on ω_z and their inclusion with the invariance theorem Eq. (2.6) may not.

A quadratic inhomogeneity B_2 adds the following vector term to the homogeneous field [67]

$$\vec{B} = B_2\begin{pmatrix} -xz \\ -yz \\ z^2 - \frac{1}{2}(x^2+y^2)\end{pmatrix}. \tag{2.33}$$

Here the force $F_z = 2B_2\mu_z z$ is of particular importance as it alters ω_z proportional to the magnetic moment

$$\delta\omega_z = \sqrt{\omega_z^2 - \frac{2B_2\mu_z}{m}} - \omega_z \approx -\frac{B_2\mu_z}{m\omega_z}. \tag{2.34}$$

This particular shift is used together with a strong B_2 in the analysis trap to detect spin states via their respective magnetic moments. The full first-order shifts calculated in ref. [65] are

$$\begin{aligned}\frac{\delta\omega_z}{\omega_z} &= \frac{B_2}{2B_0}\frac{\omega_+ + \omega_-}{\omega_z^2}\left(\omega_-\rho_-^2 + \omega_+\rho_+^2\right),\\ \frac{\delta\omega_\pm}{\omega_\pm} &= \pm\frac{B_2}{2B_0}\frac{\omega_+ + \omega_-}{\omega_+ - \omega_-}\left(\rho_z^2 - \rho_\pm^2 - \left(\frac{\omega_\mp}{\omega_\pm} + 1\right)\rho_\mp^2\right).\end{aligned} \tag{2.35}$$

It can be checked, that Eq. (2.34) with μ_z from Eq. (2.33) reproduces the axial frequency shift above.

The first asymmetric term B_1 produces a constant force $F_z = \mu_{z,\pm}B_1$, which, similar to the discussion of C_1 and C_3, shifts the center of the axial oscillation by

$$\Delta z = -\frac{B_1}{2B_0}\frac{\omega_c}{\omega_z^2}(\omega_+\rho_+^2 + \omega_-\rho_-^2). \tag{2.36}$$

At this position, the magnetic field has changed by $B_1\Delta z$ which leads to the frequency shifts

$$\frac{\delta\omega_\pm}{\omega_\pm} = \mp\frac{B_1^2}{B_0^2}\frac{\omega_c}{2\omega_z^2}(\omega_+\rho_+^2 + \omega_-\rho_-^2). \tag{2.37}$$

Even though this shift happens due to the magnetic moments, it is directly due to second order effect of the shifted magnetic field at the new equilibrium position. Therefore, the shifted cyclotron frequency still reflects the B-field scanned by the particle.

2.3.3. Combined effects

Combined effects of the magnetic and electrostatic fields are second order in nature. The first shift is the combination of C_1 and B_1. Here, the shift of the zero position through C_1 gives a magnetic field change $\delta B = -\frac{B_1C_1}{2C_2}$. If different voltages need to be applied to the trap the fraction $\frac{C_1}{C_2}$ may change and the shift needs to be considered. This may be the case for ion mass comparisons in a Penning trap, as there different voltages may be necessary to bring the ion's axial frequency into resonance with the detection system. Here, this shift is not relevant.

One order higher, the C_3 combination with B_1 has to be treated carefully. In the case of the axial oscillation, the shift of the zero position through the magnetic moments and B_1 gives a change of C_2 through the series expansion of Eq. (2.28), resulting in [19]

$$\frac{\delta\omega_z}{\omega_z} = -\frac{3C_3B_1}{4C_2B_0}\frac{\omega_c}{\omega_z^2}(\omega_+\rho_+^2 + \omega_-\rho_-^2). \tag{2.38}$$

Similarly, the shift of the axial zero position through C_3, Eq. (2.29) leads to a change of the magnetic field, which changes the radial eigenfrequencies by

$$\frac{\delta\omega_\pm}{\omega_\pm} = \pm\frac{3C_3B_1}{4C_2B_0}(-\rho_z^2 + \rho_+^2 + \rho_-^2). \tag{2.39}$$

The latter shifts ω_c due to a mean change of the magnetic field at the ion's position, while the former does not.

The other shift at that order, $C_1 B_3$, can be ignored, as positional shifts due to the magnetic moments lead only to constant offsets of C_0 and shifts on the radial mode again occur only via changing the voltages.

2.4. Other systematic shifts

2.4.1. Relativistic shift

It is possible to calculate first-order corrections to the eigenfrequencies due to special relativity [67]. As these scale with the velocity of the modes, the most important contribution is typically due to the velocity $\omega_+\rho_+$ of the modified cyclotron motion. Here, only the shift in the modified cyclotron frequency

$$\frac{\delta\omega_+}{\omega_+} = -\frac{\omega_+}{\omega_+ - \omega_-}\frac{\omega_+^2\rho_+^2}{2c^2} \approx -\frac{\omega_+^2\rho_+^2}{2c^2}, \tag{2.40}$$

where c is the speed of light, is relevant. The shift can be understood as a relativistic mass increase that reduces ω_c by division with the Lorentz factor

$$\gamma = \frac{1}{\sqrt{1-\frac{\omega_+^2\rho_+^2}{c^2}}} \approx 1 + \frac{1}{2}\frac{\omega_+^2\rho_+^2}{c^2}. \tag{2.41}$$

The influence of relativistic shifts will be discussed in more detail for the transition frequencies of the hyperfine and Zeeman splitting.

2.4.2. Image charge shift

The Coulomb field of the charged particle induces image charges on the trap surfaces which have a backaction on it. An analytical solution of this shift can be found for the approximation of the trap as an infinitely long cylinder [67, 68]. For the radial modes, it is

$$\delta\omega_\pm = \mp\frac{q}{4\pi\epsilon_0 a_{el}^3 B_0}, \tag{2.42}$$

where ϵ_0 is the vacuum permittivity. The shift of $\omega_\pm$ cancels for the sideband relation $\omega_c = \omega_+ + \omega_-$, but not for the invariance theorem. Here the shift is mostly identical to the shift of ω_+

$$\frac{\delta\omega_c}{\omega_c} = -\frac{m}{4\pi\epsilon_0 a_{el}^3 B_0^2}. \tag{2.43}$$

The invariance theorem typically has several advantages over the sideband relation that are hard to give up on, but the image charge shift is often the largest systematic shift and has to be correctly compensated. The measurements, done by comparing ω_c obtained by the sideband and invariance theorem, and simulations in ref. [69] have found that for typical Penning traps the approximate formula holds to better than 5 %. For measurements with large mass ions, the current approach is to rather use bigger traps to reduce the image charge shift by utilizing the strong dependence on a_{el} [66].

2.5. Image current detection and thermalization

The detection of the motional frequencies of a single particle with often only a few elementary charges is a challenging task. In Penning-trap experiments that investigate stable particles with sufficient trapping lifetimes, the non-destructive detection via induced image currents is possible. In the case of the axial motion, the particle's charge induces a charge on the trap's electrodes that depends on its relative position to it. For small amplitudes, this can be treated as a charge moving between a parallel plate capacitor with plate separation d_{eff}. The induced current I_1 is proportional to the velocity of the particle

$$I_1 = \frac{q}{d_{\text{eff}}} v_z. \tag{2.44}$$

The equivalent length d_{eff} can be calculated or simulated for a Penning trap, see ref. [70] and typically has a value similar to the geometrical lengths of the electrodes. For a small, millimeter-sized, trap that has $d_{\text{eff}} = 10$ mm and the typical frequencies and amplitudes, the currents are a few femtoamperes per elementary charge.

To sufficiently amplify these tiny currents over the background noise, the voltage drop over a tuned parallel RLC circuit, called resonator, is measured. At its resonant frequency $\omega_R = 1/\sqrt{LC}$, where L and C are its inductance and capacitance, respectively, the impedance $Z(\omega = \omega_R)$ equals the large effective parallel resistance R. By tuning the axial frequency ω_z to the resonator's frequency this leads to a voltage drop $U = RI_1$ that is further increased by a transistor amplifier. The voltage drop U_1 in turn leads to a damping force on the particle through the electric field generated by the trap's offset voltage

$$F_1 = \frac{q^2 R}{d_{\text{eff}}^2} v_z \equiv m\gamma_z v_z, \tag{2.45}$$

where γ_z is a damping rate. This effectively leads to cooling of the particle's axial motion. Figure 2.3 shows a sketch of the electrical circuit for the detection of the axial motion.

A more complete description needs to include the full dynamics of the RLC circuit and its thermal Johnson-Nyquist noise I_{th}. By employing Kirchhoff's law on the circuit shown in Figure 2.3 and using the voltage-current relations for the resistance, inductance and capacitance, respectively, the relations of the currents are

$$\begin{gathered} I_1 + I_2 + I_3 + I_4 = 0 \\ I_1 = \frac{q}{d_{\text{eff}}} v_z,\ I_2 = \frac{\mathrm{d}}{\mathrm{d}t} q_R - I_{th},\ I_3 = \frac{R}{L} q_R,\ I_4 = RC \frac{\mathrm{d}}{\mathrm{d}t} I_R, \end{gathered} \tag{2.46}$$

with $I_R = U/R$ the current over the resistor and $q_R = \frac{1}{R}\int \mathrm{d}t U$ the integrated charge. The combined eom of the axial motion and the resonator can be summarized as

$$\frac{\mathrm{d}}{\mathrm{d}t}\begin{pmatrix} z \\ \tilde{z} \\ \zeta \\ \tilde{\zeta} \end{pmatrix} = \begin{pmatrix} 0 & \omega_z & 0 & 0 \\ -\omega_z & 0 & 0 & \frac{e\omega_R}{q\omega_z}\gamma_z \\ 0 & 0 & 0 & \omega_R \\ 0 & -\frac{q\omega_z}{e\omega_R}\Gamma_R & -\omega_R & -\Gamma_R \end{pmatrix} \begin{pmatrix} z \\ \tilde{z} \\ \zeta \\ \tilde{\zeta} \end{pmatrix} + \begin{pmatrix} 0 \\ 0 \\ 0 \\ \Gamma_R \tilde{\zeta}_{th}(t) \end{pmatrix}, \tag{2.47}$$

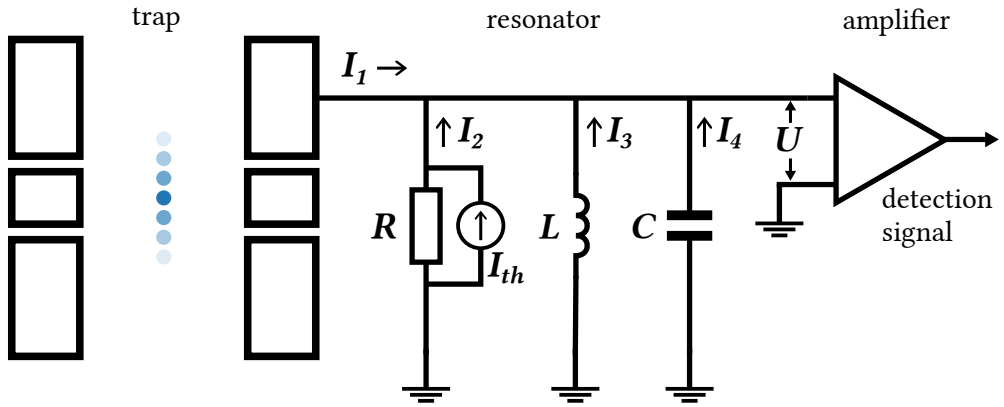

Figure 2.3: Sketch of the image current detection. In blue, the charged particle's axial motion is indicated. The induced current I_1 is routed with wires to the cryogenic tank circuit which is connected to a small signal amplifier.

with the definition of the resonator coordinates $\zeta = \frac{d_{\text{eff}}}{e} q_R$ and $\tilde{\zeta} = \frac{d_{\text{eff}}}{e\omega_R} I_R$. The oscillation of the resonator's coordinates is damped via the resistance with the decay constant $\Gamma_R = \frac{1}{RC}$ and driven by the noise term $\tilde{\zeta}_{th} = \frac{d_{\text{eff}}}{e\omega_R} I_{th}$. The coupling of the particle's axial motion to the thermally driven resonator in turn leads to thermalization of this mode. This is illustratively clear, as the resonator constitutes a heat bath at temperature T to which the particle is coupled via the connected electrode. At thermal equilibrium, the particle's mean amplitude $\rho_{z,th}$ is related to the temperature of the axial detection system T_z via

$$\frac{1}{2} m\omega_z^2 \rho_{z,th}^2 = k_B T_z \equiv E_{z,th}, \tag{2.48}$$

where k_B is the Boltzmann constant and $E_{z,th}$ is the thermal axial energy, compare Eq. (2.15). For a derivation of this, see Section A.4.2. It is also critical to note that, due to the coupling, the free axial motion is not an eigenmotion of the full system, which may lead to a frequency shift. A more complete discussion and a probabilistic solution of the thermal motion and its implications can be found in Section A.

The detection signal $U(t)$ of a particle tuned close to resonance $\omega_z \approx \omega_R$ and at an amplitude larger than the thermal amplitude resembles a noisy sine wave and allows inferring the axial frequency. At the lower, thermal, axial amplitudes, which are preferable due to lower systematic shifts, it does not easily yield any information on the particle's motion. By converting $U(t)$ to a power spectrum in the frequency domain, a thermal detection of the ion's axial frequency is possible. To perform the transformation of Eq. (2.47) to Fourier space[1] with frequency coordinate ω, the dimension of the linear equation can directly be reduced to 2×2 by substituting $\tilde{z}(\omega) = \frac{i\omega}{\omega_z} z(\omega)$ and $\tilde{\zeta}(\omega) = \frac{i\omega}{\omega_R} \zeta(\omega)$

$$\begin{pmatrix} \omega_z^2 - \omega^2 & -i\frac{e}{q}\gamma_z\omega \\ i\frac{q}{e}\Gamma_R\omega & \omega_R^2 - \omega^2 + i\Gamma_R\omega \end{pmatrix} \begin{pmatrix} z(\omega) \\ \zeta(\omega) \end{pmatrix} = \begin{pmatrix} 0 \\ \Gamma_R\omega_R\tilde{\zeta}_{th}(\omega) \end{pmatrix}. \tag{2.49}$$

[1]Due to the damping of all modes, any terms from non-thermal initial amplitudes in the Fourier transform go to zero in the integral over infinite time.

The detection signal is $U = I_R/R$, and solving the above system for the resonator coordinate to extract the frequency domain solution is straight forward

$$U(\omega) = U_{th}(\omega)\frac{1}{1 + i\left(\frac{\omega_R^2-\omega^2}{\omega\Gamma_R} - \frac{\omega\gamma_z}{\omega_z^2-\omega^2}\right)}, \tag{2.50}$$

where $U_{th} = I_{th}/R$. In order to remove the complex parts of the detection signal, the square of the norm is used

$$|U(\omega)|^2 = |U_{th}(\omega)|^2\frac{1}{1 + \left(\frac{\omega_R^2-\omega^2}{\omega\Gamma_R} - \frac{\omega\gamma_z}{\omega_z^2-\omega^2}\right)^2}. \tag{2.51}$$

The thermal Johnson-Nyquist noise [71]

$$U_{th} = \sqrt{4k_B T_z R\frac{\Delta\omega}{2\pi}} \tag{2.52}$$

is simply flat in frequency space and experimentally depends on the detection bandwidth $\Delta\omega$. Without an ion, the signal is just the thermal noise of the RLC circuit and described by setting $\gamma_z = 0$ in Eq. (2.51):

$$|U(\omega)|^2 = |U_{th}(\omega)|^2\frac{1}{1 + \left(\frac{\omega_R^2-\omega^2}{\omega\Gamma_R}\right)^2}. \tag{2.53}$$

Figure 2.4 shows the expected detection signal for typical experimental parameters. At $\omega \approx$

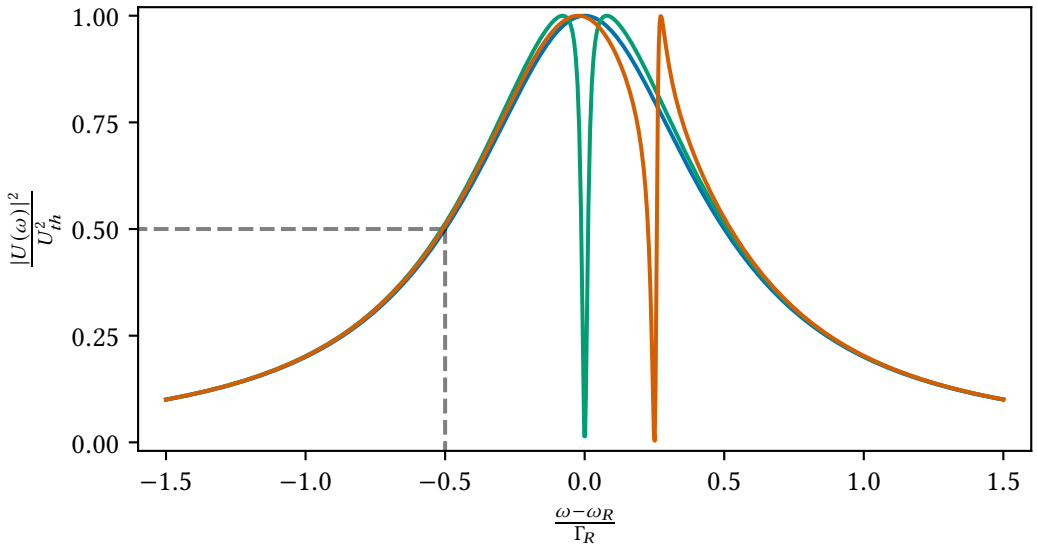

Figure 2.4: Detection signal in the frequency domain. In blue, the detection signal without a particle is shown. In green, the axial frequency is tuned to resonance $\omega_z = \omega_R$. In orange, the axial frequency is detuned by $\omega_z = \omega_R + \Gamma_R/4$.

$\omega_R \pm \Gamma_R/2$ the resonator signal reaches half its amplitude, which defines the 3 dB width of the

resonator. With a particle, the signal vanishes at $\omega = \omega_z$. This is typically phrased as the particle motion shorting the resonator's thermal noise to ground. The 3 dB width of this so-called *'dip'* signal is approximately equal to the cooling time constant γ for $\omega_z = \omega_R$. For a particle tuned off-resonance, $\omega_z \neq \omega_R$, the dip signal becomes highly asymmetrical. The theoretical detection signal is in a few ways an idealized version of the real signal. Most importantly, the theoretical line resembles the mean detected signal, while in reality an averaging of the spectrum is done only for a finite time. See Section A.5 for a theoretical derivation of a numerical generation of time domain and frequency domain detection signal. The consequences of this will also be discussed later in the investigation of systematic effects.

To gauge the scaling of the resolution $\sigma(\omega_z)$ with measurement time T it is important to note the incoherent nature of this detection method. The detected noise signal over arbitrary time intervals τ gives uncorrelated Fourier spectra. The independent fit values of ω_z with uncertainty $\sigma(\omega_z)$ thus average via the square root of the number of measurements, assuming no other sources that change ω_z. Therefore the uncertainty of the dip method scales as

$$\sigma(\omega_z)(T) \propto \frac{1}{\sqrt{T}}. \tag{2.54}$$

2.6. Excitations and mode coupling

Excitations and couplings of the motional modes are used for non-thermal detection methods and thermalization of modes that are not directly cooled. In the case of ions and typical Penning-trap parameters, all excitations and couplings are achieved by radio frequency (RF) signals. The corresponding wavelengths are much larger than any structure of the trap or motional amplitude, so they may be treated as constant in space.

2.6.1. Dipolar excitation

The simplest excitations of the harmonic motional modes correspond to applying sinusoidal driving forces close to the mode frequencies and in direction of the respective oscillations. For example, the eom of the driven and undamped oscillation of the axial mode are

$$\frac{\mathrm{d}}{\mathrm{d}t}\begin{pmatrix} z \\ \tilde{z} \end{pmatrix} = \begin{pmatrix} 0 & \omega_z \\ -\omega_z & 0 \end{pmatrix}\begin{pmatrix} z \\ \tilde{z} \end{pmatrix} + \begin{pmatrix} 0 \\ C\sin(\omega_{\mathrm{RF}}t + \phi) \end{pmatrix}, \tag{2.55}$$

with C defining the strength of the exciting force and ω_{RF}, ϕ the frequency and phase of the excitation, respectively. On resonance, $\omega_{\mathrm{RF}} = \omega_z$, the solution can be derived with the ansatz $z(t) = a\sin(\omega_z t) + b\cos(\omega_z t) + At\sin(\omega_z t) + Bt\cos(\omega_z t)$. The evolution, given an initial phase space point $(z_0, \tilde{z}_0)$, is

$$\begin{pmatrix} z(t) \\ \tilde{z}(t) \end{pmatrix} = E_z\begin{pmatrix} z_0 \\ \tilde{z}_0 \end{pmatrix} + \frac{C}{2\omega_z}\sin(\omega_z t)\begin{pmatrix} \cos(\phi) \\ \sin(\phi) \end{pmatrix} + \frac{C}{2}t\begin{pmatrix} -\cos(\omega_z t + \phi) \\ \sin(\omega_z t + \phi) \end{pmatrix}, \tag{2.56}$$

where E_z is the free evolution, Eq. (2.10). In order to investigate the change of the initial amplitude $\rho_{z,0}^2 = z_0^2 + \tilde{z}_0^2$ after a time $t = T$, it can be assumed that $\omega_z T = 2n\pi$ by arbitrarily changing

the zero time of $(z_0, \tilde{z}_0)$. This simplifies the above equation to

$$\begin{pmatrix} z(T) \\ \tilde{z}(T) \end{pmatrix} = \begin{pmatrix} z_0 \\ \tilde{z}_0 \end{pmatrix} + \frac{C}{2} T \begin{pmatrix} -\cos(\phi) \\ \sin(\phi) \end{pmatrix} \equiv \begin{pmatrix} z_0 \\ \tilde{z}_0 \end{pmatrix} + \vec{B}_z(C, T, \phi), \tag{2.57}$$

where $\vec{B}_z$ has units of amplitude and corresponds to a linear displacement in the phase space coordinates. The increase in amplitude is given by

$$\rho_z^2(T) = \rho_{z,0}^2 + \rho_{z,0} CT \cos(\varphi_z - \phi) + \frac{C^2 T^2}{4}, \tag{2.58}$$

where the phase φ_z of the initial point is defined through $(z_0, \tilde{z}_0) = \rho_{z,0}(\cos(\varphi_z), \sin(\varphi_z))$. For the random initial (thermal) value of $\rho_{z,0}$ and φ_z, the final amplitudes and phases will have a smaller relative distribution for larger excitations $|B_z| = \frac{CT}{2}$. On average, the square of the amplitude, or equivalently its energy, increases linearly with the square of the excitation amplitude and excitation time.

In the case of the radial modes, the same derivation holds for dipolar excitations with forces in the radial plane and frequencies at their respective eigenfrequencies. The off-resonant terms in the dipolar excitation at the non-targeted mode can be safely neglected due to the high frequency difference. Similar to the above, the displacement will be called $\vec{B}_\pm$ for the modified cyclotron and magnetron mode, respectively.

In practice, dipolar excitation signals are applied via RF excitations on the trap electrodes. For the axial mode, it is sufficient to apply the signal between any off-center electrode and ground to get an electric potential that has the desired linear dependence in the z-coordinate. In the case of the radial modes, electrodes split along the z-axis are used to generate electric potentials depending on the radial coordinates.

2.6.2. Quadrupolar excitation

Couplings between the three motional modes inside the Penning trap are typically achieved via quadrupolar excitations. Depending on the mode structure, couplings between the two radial modes or the radial modes and the axial mode are possible. Here, the quadrupolar excitation is used for thermalization and detection of the radial motion via the axial motion and resonator and no radial-to-radial coupling is required. The excitation field necessary for coupling the radial modes to the axial mode requires a quadrupole configuration orthogonal to the trap's static field. The force on the particle due to a particular such field may be written as

$$\vec{F} = m \,\mathrm{Re}(C e^{i\omega_{\mathrm{RF}} t}) \begin{pmatrix} z \\ 0 \\ x \end{pmatrix}, \tag{2.59}$$

where C is a complex amplitude of the excitation that incorporates its phase and ω_{RF} its frequency. To generate such a field, off-center split electrodes, as sketched in Figure 2.2, can be used.

It can be shown that for a particular choice of the real coordinates $r_\pm(t)$ that describe the modified cyclotron and magnetron motion, the coupling is described by the following eom [72]

$$\frac{\mathrm{d}}{\mathrm{d}t}\begin{pmatrix} z \\ \tilde{z} \\ r_+ \\ \tilde{r}_+ \\ r_- \\ \tilde{r}_- \end{pmatrix} = \begin{pmatrix} 0 & \omega_z & 0 & 0 & 0 & 0 \\ -\omega_z & 0 & 0 & 0 & 0 & 0 \\ 0 & 0 & 0 & \omega_+ & 0 & 0 \\ 0 & 0 & -\omega_+ & 0 & 0 & 0 \\ 0 & 0 & 0 & 0 & 0 & \omega_- \\ 0 & 0 & 0 & 0 & -\omega_- & 0 \end{pmatrix}\begin{pmatrix} z \\ \tilde{z} \\ r_+ \\ \tilde{r}_+ \\ r_- \\ \tilde{r}_- \end{pmatrix} + \mathrm{Re}(Ce^{i\omega_{\mathrm{RF}}t})\begin{pmatrix} 0 \\ \frac{r_+ + r_-}{\omega_z} \\ 0 \\ \frac{z}{\omega_+} \\ 0 \\ -\frac{z}{\omega_-} \end{pmatrix}, \tag{2.60}$$

where $\tilde{r}_\pm = v_{r_\pm}/\omega_\pm$. The general ansatz

$$\begin{aligned} z(t) &= \mathrm{Re}(P_z(t)e^{i\omega_z t}), \\ r_\pm(t) &= \mathrm{Re}(P_\pm(t)e^{i\omega_\pm t}), \end{aligned} \tag{2.61}$$

where P_i are complex amplitudes, is inserted into the eom to yield

$$\begin{aligned} \mathrm{Re}\left[(\ddot{P}_z + i2\dot{P}_z\omega_z)e^{i\omega_z t}\right] &= \mathrm{Re}(Ce^{i\omega_{\mathrm{RF}}t})\,\mathrm{Re}(P_+(t)e^{i\omega_+ t} + P_-(t)e^{i\omega_- t}), \\ \mathrm{Re}\left[(\ddot{P}_\pm + i2\dot{P}_\pm\omega_\pm)e^{i\omega_\pm t}\right] &= \pm\,\mathrm{Re}(Ce^{i\omega_{\mathrm{RF}}t})\,\mathrm{Re}(P_z(t)e^{i\omega_z t}). \end{aligned} \tag{2.62}$$

Inspecting the right-hand side of these equations shows that oscillating terms at the sum and difference frequencies of the eigenmotion frequencies and the excitation frequency occur. For the four combinations $\omega_{\mathrm{RF}} \in \{\omega_+ - \omega_z, \omega_z + \omega_-, \omega_+ + \omega_z, \omega_z - \omega_-\}$, a resonant oscillation with (one of) the terms on the left-hand side occurs. The non-resonant terms are dropped, which constitutes a classical rotating wave approximation. Further, it will be assumed that the amplitudes change slowly compared to the eigenmotions such that $\omega_i\dot{P}_i \gg \ddot{P}_i$ and $\ddot{P}_i$ can be dropped.

In the case of the two sideband excitations with the modified cyclotron motion $\omega_{\mathrm{RF}} = \omega_+ \pm \omega_z$, a comparison of coefficients before the sine and cosine parts yields

$$\frac{\mathrm{d}}{\mathrm{d}t}\begin{pmatrix} Z \\ \tilde{Z} \\ X^+ \\ Y^+ \end{pmatrix} = \frac{1}{4}\begin{pmatrix} 0 & 0 & \pm\frac{\mathrm{Im}(C)}{\omega_z} & \mp\frac{\mathrm{Re}(C)}{\omega_z} \\ 0 & 0 & -\frac{\mathrm{Re}(C)}{\omega_z} & -\frac{\mathrm{Im}(C)}{\omega_z} \\ \frac{\mathrm{Im}(C)}{\omega_+} & \mp\frac{\mathrm{Re}(C)}{\omega_+} & 0 & 0 \\ -\frac{\mathrm{Re}(C)}{\omega_+} & \mp\frac{\mathrm{Im}(C)}{\omega_+} & 0 & 0 \end{pmatrix}\begin{pmatrix} Z \\ \tilde{Z} \\ X^+ \\ Y^+ \end{pmatrix}, \tag{2.63}$$

where the amplitudes have been redefined in terms of their real and imaginary parts as $P_z = Z + i\tilde{Z}$, $P_+ = X_+ + iY_+$, compared with the original solutions of the Penning trap Eq. (2.10) and Eq. (2.14). This differential equation can be nicely integrated[2]

$$\begin{pmatrix} Z \\ \tilde{Z} \\ X^+ \\ Y^+ \end{pmatrix} = \begin{pmatrix} c_\pm(t) & 0 & \sqrt{\frac{\omega_+}{\omega_z}}\sin(\Phi)s_\pm(t) & \mp\sqrt{\frac{\omega_+}{\omega_z}}\cos(\Phi)s_\pm(t) \\ 0 & c_\pm(t) & \mp\sqrt{\frac{\omega_+}{\omega_z}}\cos(\Phi)s_\pm(t) & \mp\sqrt{\frac{\omega_+}{\omega_z}}\sin(\Phi)s_\pm(t) \\ \sqrt{\frac{\omega_z}{\omega_+}}\sin(\Phi)s_\pm(t) & \mp\sqrt{\frac{\omega_z}{\omega_+}}\cos(\Phi)s_\pm(t) & c_\pm(t) & 0 \\ \mp\sqrt{\frac{\omega_z}{\omega_+}}\cos(\Phi)s_\pm(t) & \mp\sqrt{\frac{\omega_z}{\omega_+}}\sin(\Phi)s_\pm(t) & 0 & c_\pm(t) \end{pmatrix}\begin{pmatrix} Z_0 \\ \tilde{Z}_0 \\ X_0^+ \\ Y_0^+ \end{pmatrix}, \tag{2.64}$$

[2] At this point the help of Mathematica [73] to symbolically exponentiate the matrix was appreciated.

where $c_+(t) = \cosh(\Omega t)$, $s_+(t) = \sinh(\Omega t)$, $c_-(t) = \cos(\Omega t)$, $s_-(t) = \sin(\Omega t)$, Φ is the phase of the excitation, and $(Z_0, \tilde{Z}_0, X_0^+, Y_0^+)$ is the initial point in phase space. The so-called Rabi frequency

$$\Omega = \frac{|C|}{4\sqrt{\omega_+ \omega_z}} \tag{2.65}$$

defines the strength of the coupling of the modified cyclotron to the axial mode. This rather complicated looking matrix signifies the full mixing of the initial phase space point of the two modes with the quadrupolar sideband drive.

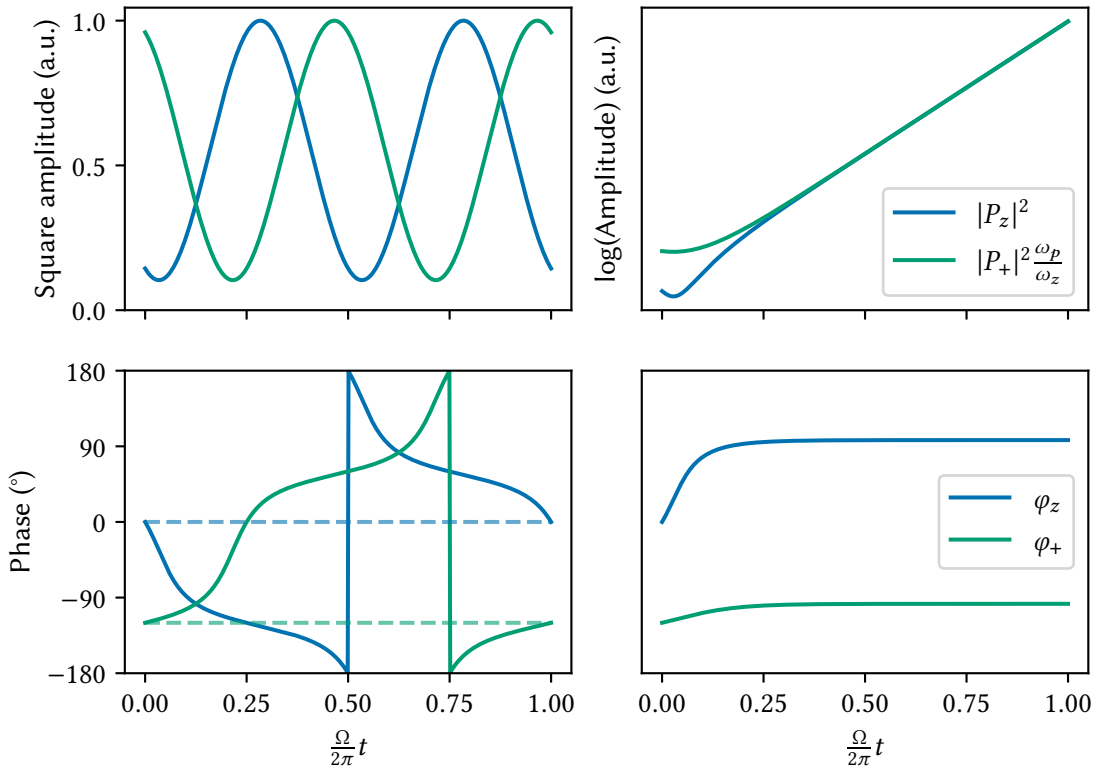

Figure 2.5: Quadrupole coupling of the modified cyclotron mode to the axial mode. The left and right hand side show the coupling with the sidebands $\omega_{\mathrm{RF}} = \omega_+ - \omega_z$ and $\omega_{\mathrm{RF}} = \omega_+ + \omega_z$, respectively. The phases are defined as $\varphi_z = \arctan\left(\tilde{Z}/Z\right)$ and $\varphi_+ = \arctan(Y^+/X^+)$.

Figure 2.5 shows the coupling for both the lower and upper sideband for an exemplary initial point and a drive with phase $\Phi = \pi/2$. The lower sideband solution has only oscillating terms and shows an exchange of amplitude and phase between the two modes. The square of the amplitudes oscillates at twice the Rabi frequency Ω and after a full cycle, the initial phases are restored. No additional energy is supplied to the modes with this coupling, as the sum of the square amplitudes is constant. In contrast, the upper sideband leads to an exponential increase in both mode amplitudes and both phases converge.

In the case of quadrupolar excitations at sidebands with the magnetron mode, the derivation follows identically. The solution differs by the change of hyperbolic and sinusoidal functions with the sign of the sideband. The hyperbolic functions appear with the negative sideband $\omega_{\mathrm{RF}} = \omega_z - \omega_-$ and the sine functions at the positive sideband $\omega_{\mathrm{RF}} = \omega_z + \omega_-$.

Applications of the sideband drives will be discussed in the following two sections.

2.7. Cooling and thermal detection of the radial modes

The axial mode is cooled to the ambient temperature of the detection system, as expressed by the thermal amplitude Eq. (2.48). To thermalize the radial modes to this bath as well, they are coupled to the axial mode via the quadrupolar excitation at the energy exchanging sidebands $\omega_+ - \omega_z$ and $\omega_z + \omega_-$ respectively. The energy that is transferred from the radial mode to the axial mode is then dissipated in the axial resonator. From the exemplary coupling in Figure 2.5 it can already be seen that the exchange of energy does not happen one-to-one but with a scaling factor. Indeed, both from quantum mechanical, see ref. [62] and classical derivations, see Section A.4.3, it can be shown that the couplings result in thermal amplitudes

$$\begin{aligned} E_{+,th} &= \frac{1}{2} m\omega_+^2 \rho_{+,th}^2 = \frac{\omega_+}{\omega_z} E_{z,th} = \frac{1}{2} m\omega_+^2 \left(\sqrt{\frac{\omega_z}{\omega_+}} \rho_{z,th} \right)^2 \\ E_{-,th} &= -\frac{1}{4} m\omega_z^2 \rho_{-,th}^2 = -\frac{\omega_-}{\omega_z} E_{z,th} = -\frac{1}{4} m\omega_z^2 \left(\sqrt{\frac{\omega_z}{\omega_+}} \rho_{z,th} \right)^2 , \end{aligned} \tag{2.66}$$

where both the thermal magnetron and modified cyclotron amplitude are identical provided the same approximation as in Eq. (2.15) is made. Cooling the radial modes via the sidebands is referred to as cyclotron and magnetron cooling, respectively.

If the amplitude evolution of the negative sideband, $\omega_{\mathrm{RF}} = \omega_+ - \omega_z$, Eq. (2.64), is combined with the fast evolution at the eigenfrequency Eq. (2.61), it becomes clear that the eigenfrequencies of the axial and cyclotron motion are split into two sidebands at $\omega_{z,1,2} = \omega_z \pm \Omega$. By allowing for a detuning of the sideband drive $\omega_{\mathrm{RF}} = \omega_+ - \omega_z + \delta$, a more general calculation shows that the two axial frequency components are [74]

$$\omega_{z,1,2} = \omega_z - \frac{1}{2} \left(\delta \pm \sqrt{4\Omega^2 + \delta^2} \right). \tag{2.67}$$

This allows to reproduce the modified cyclotron frequency via the relation

$$\omega_+ = \omega_{z,1} + \omega_{z,2} - \omega_z + \omega_{\mathrm{RF}}, \tag{2.68}$$

and similarly for quadrupole drives close to the positive magnetron sideband

$$\omega_- = -\omega_{z,1} - \omega_{z,2} + \omega_z + \omega_{\mathrm{RF}}. \tag{2.69}$$

The splitting of the frequencies has a minimum at $\delta = 0$ and follows the shape of an avoided crossing often encountered in coupled quantum mechanical two-level systems [75].

During thermal equilibrium, i.e. after a sufficiently long cooling and coupling time, the two axial eigenmotions produce individual dip signals at their respective frequencies [70]. The two

dip signals (‘*double dip*‘) superimposed on the thermal noise of the resonator are expressed through

$$|U(\omega)|^2 = |U_{th}(\omega)|^2 \frac{1}{1 + \left(\frac{\omega_R^2 - \omega^2}{\omega \Gamma_R} - \frac{\omega \gamma_{z,1}}{\omega_{z,1}^2 - \omega^2} - \frac{\omega \gamma_{z,2}}{\omega_{z,2}^2 - \omega^2} \right)^2}, \tag{2.70}$$

compare with Eq. (2.51) and see Figure 2.6. Here, the two dips may have different widths $\gamma_{z,1,2}$ which depend on the detuning of the quadrupolar drive δ. For the extraction of the frequencies via a fit to the measured spectrum, this is of no concern, as the widths $\gamma_{z,1,2}$ are fit separately. In Section B.3, a first-principle derivation of the double dip lineshape is done, which differs

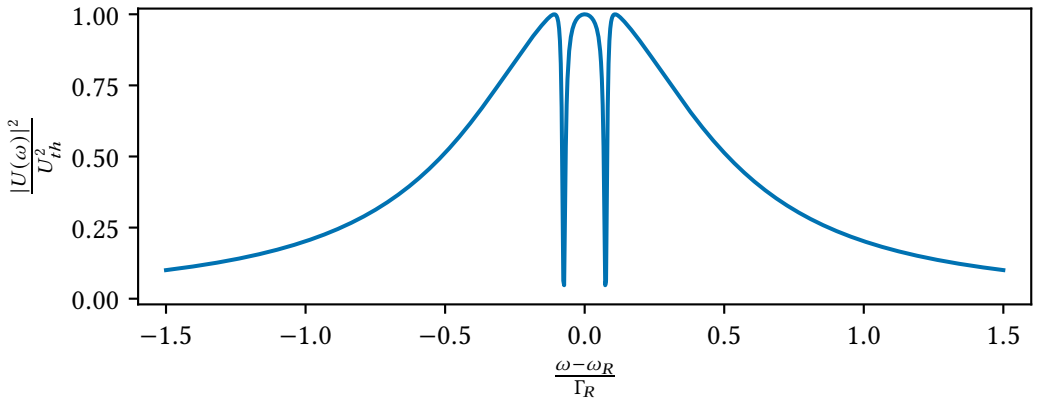

Figure 2.6: Double dip detection signal. Here $\omega_z = \omega_R$ and the detuning $\delta = 0$. The dips are thus split by the rabi frequency Ω and centered around the resonator.

slightly in its mathematical form, but does not, at least for the experiments performed here, lead to measurable consequences.

The detection of the modified cyclotron frequency via the double dip technique requires only the addition of the continuous quadrupolar drive and is thus fairly straightforward to implement. As the detection is done at thermal equilibrium, systematic shifts, as described in Section 2.3 and Eq. (2.40), are smaller than techniques using excited motions. The resolution of this technique is typically limited via the same effects as the measurement of the axial frequency through the single dip and scales only with the inverse of the square root of measurement time. While the uncertainty of the measured ω_z is suppressed in the determination of ω_c through the invariance theorem Eq. (2.6), compare Eq. (2.7), the modified cyclotron frequencies uncertainty contributes essentially one-to-one.

2.8. Phase-sensitive detection of the modified cyclotron mode

To improve on the double-dip technique, coherent detection techniques of the modified cyclotron frequency can be employed. The coherent detection relies on measuring the phase φ_+ of the motion at an initial time T_1 and at a final time $T_2 = T_1 + T_{\text{evol}}$ separated by a coherent

evolution of the oscillation. The acquired phase difference

$$\Delta\varphi_+ = \omega_+ T_{\text{evol}} - 2\pi N_+ \tag{2.71}$$

depends on the free evolution time T_{evol} and number of full evolutions N_+. Assuming no uncertainty of N_+, the uncertainty of the determined cyclotron frequency then scales directly with time

$$\sigma(\omega_+) = \frac{\sigma(\Delta\varphi_+)}{T_{\text{evol}}}. \tag{2.72}$$

2.8.1. Phase measurement sequences

First, a dipolar excitation pulse $\vec{B}_+$ is used to excite the modified cyclotron motion to a high amplitude and set the initial phase of the motion, compare Eq. (2.57). Opposed to the axial motion, the modified cyclotron motion is not coupled to a detector, meaning it evolves coherently. After the evolution time T_{evol}, a coupling pulse, using the quadrupolar excitation, transfers the phase information into the axial mode, where it can be read out using the axial detection system. Both the lower and the upper sideband can be used to transfer the phase.

Utilizing the lower sideband to transfer the phase is termed the Pulse and Phase (PnP) method and was first introduced in ref. [74]. Here a pulse of length $T_{\text{couple}} = \frac{\pi}{2}\frac{1}{\Omega}$ is used, which gives the following coupling matrix (for $\Phi = \pi/2$), compare Eq. (2.64):

$$C_{\text{PnP}} = \begin{pmatrix} 0 & 0 & \sqrt{\frac{\omega_z}{\omega_+}} & 0 \\ 0 & 0 & 0 & \sqrt{\frac{\omega_z}{\omega_+}} \\ \sqrt{\frac{\omega_+}{\omega_z}} & 0 & 0 & 0 \\ 0 & \sqrt{\frac{\omega_+}{\omega_z}} & 0 & 0 \end{pmatrix}. \tag{2.73}$$

The final phase space point of the axial motions amplitude depends only on the initial point of the modified cyclotron motion and has an identical phase, compare also the point of $t = \frac{1}{4}\frac{2\pi}{\Omega}$ in Figure 2.5.

Employing the upper sideband for the coupling is termed Pulse and Amplify (PnA) and was introduced in ref. [76]. Here, also for $\Phi = \pi/2$, the coupling matrix for a coupling time T_{couple} is

$$C_{\text{PnA}} = \begin{pmatrix} c_+(T_{\text{couple}}) & 0 & \sqrt{\frac{\omega_+}{\omega_z}}s_+(T_{\text{couple}}) & 0 \\ 0 & c_+(T_{\text{couple}}) & 0 & -\sqrt{\frac{\omega_+}{\omega_z}}s_+(T_{\text{couple}}) \\ \sqrt{\frac{\omega_z}{\omega_+}}s_+(T_{\text{couple}}) & 0 & c_+(T_{\text{couple}}) & 0 \\ 0 & -\sqrt{\frac{\omega_z}{\omega_+}}s_+(T_{\text{couple}}) & 0 & c_+(T_{\text{couple}}) \end{pmatrix}. \tag{2.74}$$

It is not directly obvious that this transfers the phase information. The final phase is given via the fraction

$$\frac{\tilde{Z}}{Z} = \frac{c_+\tilde{Z}_0 - \sqrt{\frac{\omega_+}{\omega_z}}s_+ Y_0^+}{c_+ Z_0 + \sqrt{\frac{\omega_+}{\omega_z}}s_+ X_0^+} = \frac{\eta\sin(\varphi_{z,0}) - \sin(\varphi_{+,0})}{\eta\cos(\varphi_{z,0}) + \cos(\varphi_{+,0})}, \tag{2.75}$$

where the parameter $\eta = \frac{|P_{z,0}|}{\sqrt{\frac{\omega_+}{\omega_z}}|P_{+,0}|}\coth\left(\Omega T_{\text{couple}}\right)$ is introduced and coth is the hyperbolic cotangent. Keeping in mind that $|P_{z,0}|$ and $|P_{+,0}|$ are the amplitudes of the axial and modified cyclotron motion before the coupling pulse, the axial motion is thermal $|P_{z,0}| = \rho_{z,th}$ and using Eq. (2.66), the expansion parameter can be rewritten as

$$\eta = \frac{\rho_{+,th}}{\rho_{+,\text{exc}}}\coth\left(\Omega T_{\text{couple}}\right), \tag{2.76}$$

where $\rho_{+,\text{exc}} = |P_{+,0}|$ is the amplitude of the modified cyclotron motion after the dipole excitation[3]. A series expansion of the phase $\varphi_z = \arctan\left(\tilde{Z}/Z\right)$ around the parameter $\eta < 1$ gives (Mathematica)

$$\begin{aligned}\varphi_z &= -\varphi_{+,0} + \sum_{k=1}^{\infty}\frac{(-1)^{k+1}\eta^k}{k}\sin\left[k(\varphi_{+,0}+\varphi_{z,0})\right] \\ &= -\varphi_{+,0} + \eta\sin[\varphi_{+,0}+\varphi_{z,0}] - \frac{1}{2}\eta^2\sin\left[2(\varphi_{+,0}+\varphi_{z,0})\right] + O(\eta^3).\end{aligned} \tag{2.77}$$

While the final phase depends φ_z also on the axial phase before the coupling pulse $\varphi_{z,0}$, the latter is randomly distributed over the full 2π range for individual PnA trials due to the coupling to the detection system. Therefore, the sin terms average to zero and the mean detected phase $\langle\varphi_z\rangle = -\langle\varphi_{+,0}\rangle$. However, the additional terms in Eq. (2.77) introduce a technical jitter for the PnA method, which scales with the parameter η, see also ref. [76] and the next section.

A single phase measurement is a chain of excitation $\vec{B}_+$ Eq. (2.57), free evolution E_+T_{evol} Eq. (2.14) with evolution time T_{evol} and coupling $C_{\text{PnA/P}}$ that transforms the initial (and thermally distributed) phase space point $\vec{X}_0 = (Z, \tilde{Z}, x_0^+, y_0^+)$ to the final point

$$\vec{X_f}(T_{\text{evol}}) = C_{\text{PnA/P}}E_+(T_{\text{evol}})(\vec{X_0} + \vec{B_+}). \tag{2.78}$$

In this notation, the matrices and vectors need to be appropriately expanded to the 4-D phase space. The free evolution of the phase during the excitation and coupling pulses was omitted, as it is common for each choice of T_{evol}.

For a better understanding, the PnA and PnP sequences are additionally visualized in Figure 2.7 and Figure 2.8. Initially, following a coupling of the cyclotron mode to the axial mode via the lower sideband, the amplitude and phase of both the axial and modified cyclotron mode are thermally distributed, compare Section A.4.3. The excitation pulse brings the modified cyclotron motion to a non-thermal amplitude and defines the starting phase with a phase uncertainty depending on the ratio of excitation to thermal amplitude. After a free evolution time, the modified cyclotron motion has phase φ_+. In the case of PnA, the coupling pulse excites both motions and after the pulse, the axial motion's phase is the negative of φ_+. In the case of PnP, the coupling pulse fully exchanges the phase space coordinates, thus giving the axial motion the defined phase φ_+ and leaving the modified cyclotron motion thermally distributed. The final amplitude and phase of the axial motion after the coupling pulse evolve according to the thermally driven detection system Eq. (2.47). Therefore, the phase uncertainty increases due to the thermalization of the axial mode.

[3] When using different heatbaths for the axial and modified cyclotron motion, i.e. a *cyclotron resonator*, the thermal amplitude $\rho_{+,th}$ in this formula always corresponds to the one from thermalization with the axial heatbath!

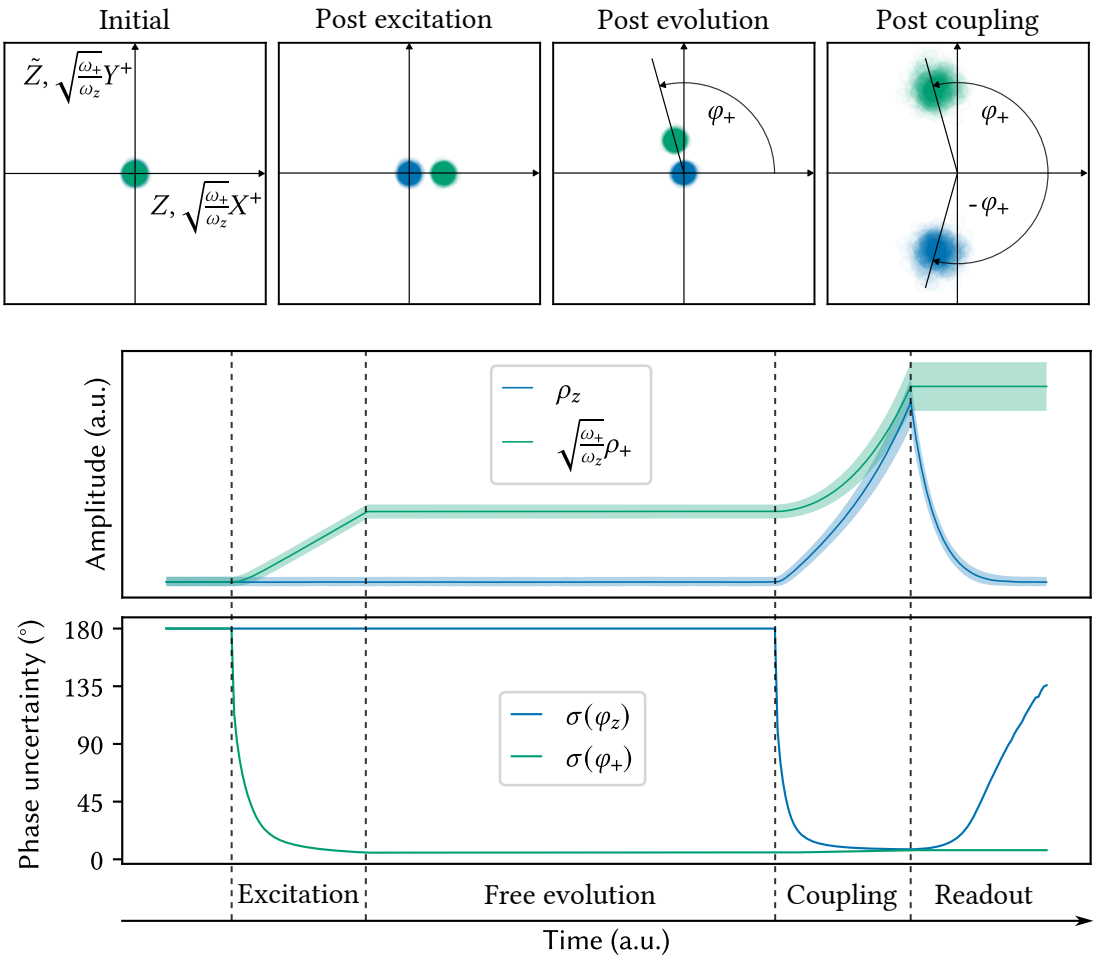

Figure 2.7: Visualization of an exemplary PnA sequence. The top row of plots shows the phase space of the axial(blue) and modified cyclotron(green) motion at different times of the sequence. In the second row, the amplitudes and their corresponding distribution, indicated by the $1-\sigma$ uncertainty bands, are shown. The lowest plot shows the phase uncertainties, where $180°$ corresponds to a fully random phase. Note that the phase uncertainties never fully go to zero and are a couple of degrees for the example here. For details on the generation of the data for this plot see Section A.5.2.

2.8.2. Phase uncertainty

After the coupling pulse, the non-thermal axial mode drives and transfers its energy to the resonator at frequency ω_z. Thus, the phase $\varphi_{\text{det}}(\omega_z) \equiv \varphi_{\text{det}}$ in the Fourier spectrum calculated from the detected resonator signal $\tilde{\zeta}$ depends on the phase of the axial mode after the coupling pulse, which in turn depends on the phase of the modified cyclotron mode φ_+. Generally, the detected phase φ_{det} in the Fourier spectrum of the detection signal may be expressed as

$$\varphi_{\text{det}} = (\pm\omega_+ T_{\text{evol}} + \delta\varphi_{\text{off}}) \bmod 2\pi \tag{2.79}$$

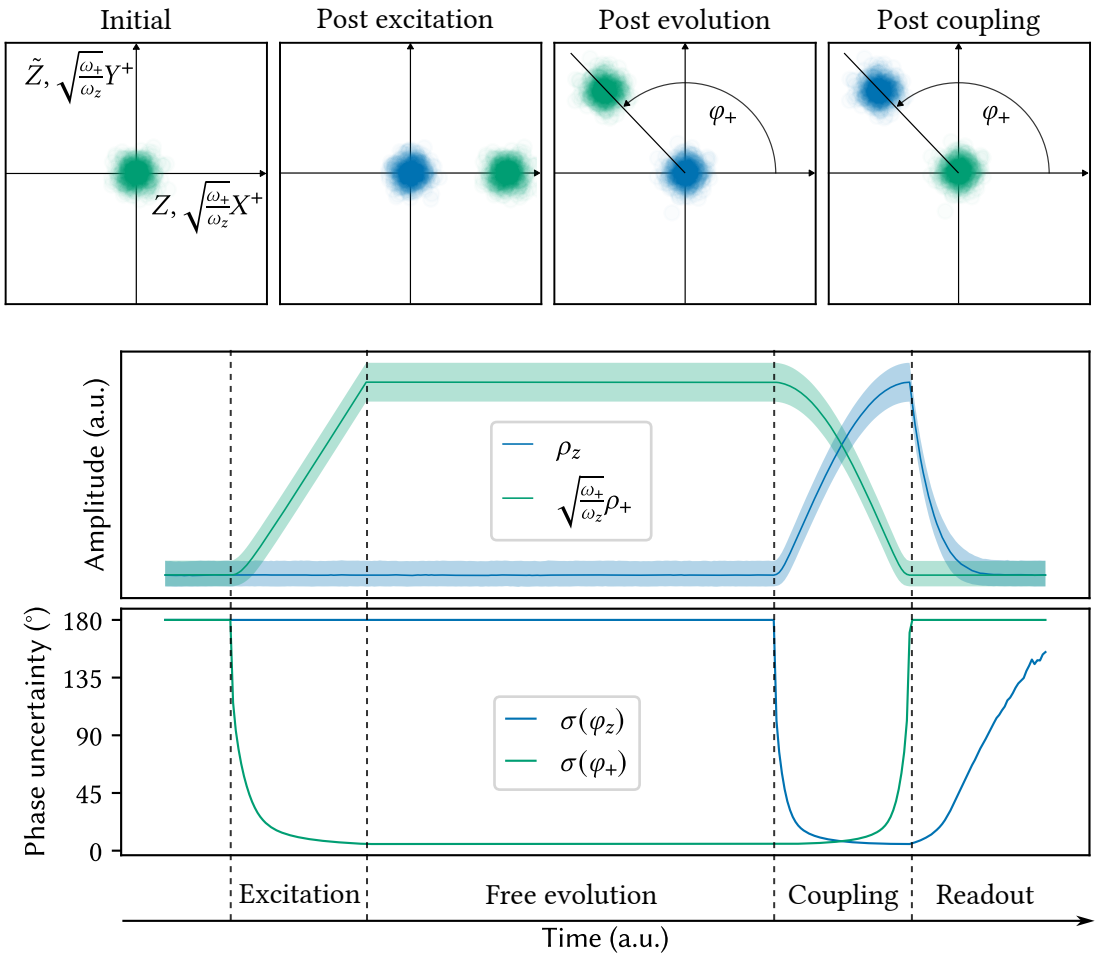

Figure 2.8: Visualization of an exemplary PnP sequence. For details see text and Figure 2.7.

where the mod 2π operation is meant to symbolically subtract $2\pi N$, where N is integer, such that a number between 0 and 2π is left. For PnP, the positive sign is used, while for PnA the negative sign is used. The uncertainty of the determined ω_+ is proportional to the phase uncertainty, often called *'phase jitter'*, $\sigma(\varphi_{\text{det}})$. In the following, common sources for the phase jitter are summarized.

Phase imprint jitter

The phase of the cyclotron motion imprinted by the dipolar excitation pulse $\vec{B}_+$ depends on the initial thermal phase, compare Eq. (2.57). The higher the excitation amplitude, the lower this dependence. The jitter is visualized through the finite size of the phase space circles in Figure 2.7 and 2.8. The expected phase-imprint jitter, given the thermal amplitude $\rho_{+,th}$ and excitation amplitude $|\vec{B}_+|$, can be easily numerically estimated. Adding the excitation $\vec{B}_+$ to phase space samples $\{(X_i^+, Y_i^+)\}$ taken from the thermal distribution, Eq. (A.38), allows to calculate

the phases via $\varphi_{+,i} = \arctan\left(X_i^+, Y_i^+\right)$. The jitter is then simply the (circular) standard deviation of these values. Figure 2.9 shows the phase-imprint jitter as a function of $\frac{|\vec{B}_+|}{\rho_{+,th}}$. Clearly,

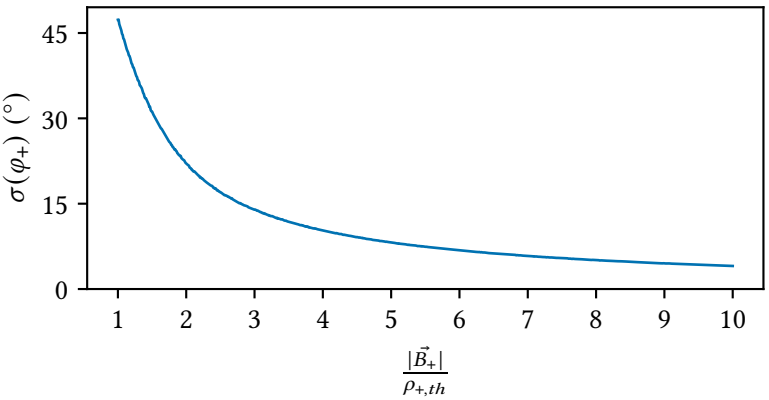

Figure 2.9: The jitter due to phase imprint. For details see text.

by increasing the excitation amplitude, the effect of the phase-imprint jitter can be minimized arbitrarily.

Field imperfection and relativistic jitter

As described in the previous sections, field imperfections and the relativistic shift of the cyclotron motion, in first-order, shift ω_+ depending on the square of the finite amplitude ρ_+. As the excited amplitude in the free evolution period is distributed due to the initial thermal amplitude, the modified cyclotron frequency will be slightly different in every run of the phase detection sequence. Using the formula for the amplitude after the dipolar excitation, compare Eq. (2.58), the frequency shift can be written as

$$\delta\omega_+ = D(\rho_+^2 + 2\rho_+ B_+ \cos(\varphi_+) + B_+^2), \tag{2.80}$$

where D is a constant depending on the field imperfections and the relativistic shift and $B_+ = |\vec{B}_+|$ is the excitation amplitude. Using the distribution of the amplitude and angle

$$p(\rho_+, \varphi_+) = \frac{\rho_+}{\pi\rho_{+,th}^2} \exp\left(-\frac{\rho_+^2}{\rho_{+,th}^2}\right), \tag{2.81}$$

compare Eq. (A.39) and Eq. (A.40), the mean and standard deviation can be calculated as[4]

$$\begin{aligned} \left\langle \delta\omega_+ \right\rangle &= D\left(B_+^2 + \rho_{+,th}^2\right), \\ \sigma(\delta\omega_+) &= D\rho_{+,th}\sqrt{2B_+^2 + \rho_{+,th}^2}. \end{aligned} \tag{2.82}$$

[4]Using the same approximation $\rho_{+,th} \ll B_+$ as done in ref. [77] Eq. (4.11)., the jitter derived here is smaller by a factor $1/\sqrt{2(1-\pi/8)} \approx 0.91$.

The jitter of the cyclotron phase (and thus the detected phase) scales with the evolution time T_{evol} as

$$\sigma(\varphi_+) = T_{\mathrm{evol}}\sigma(\delta\omega_+) = T_{\mathrm{evol}}D\rho_{+,th}\sqrt{2B_+^2 + \rho_{+,th}^2}, \tag{2.83}$$

where a jitter larger than π is to be interpreted as a fully random phase. Though field imperfections contributing to $|D|$ can be minimized experimentally, the relativistic jitter, compare Eq. (2.40),

$$\frac{\sigma(\delta\omega_+)}{\omega_+} = \frac{\omega_+^2}{2c^2}\rho_{+,th}\sqrt{2B_+^2 + \rho_{+,th}^2}, \tag{2.84}$$

can only be reduced by decreasing the cyclotron excitation radius B_+ or the thermal amplitude $\rho_{+,th}$. Due to the finite thermal amplitudes, the combined relativistic and phase-imprint jitter thus has an optimum and can not be tuned arbitrarily small. Figure 2.10 shows an exemplary

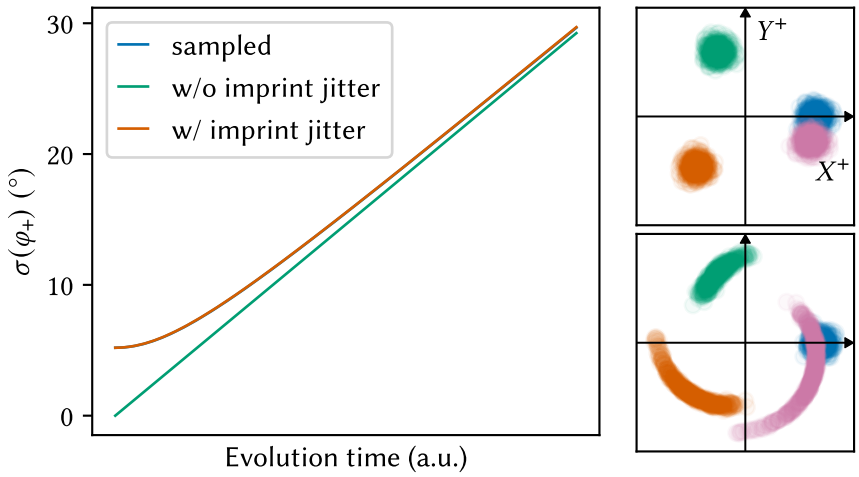

Figure 2.10: Exemplary jitter and phase space illustration due to field imperfections and the relativistic shift ($D > 0$). On the left-hand side, the jitter as a function of evolution time is plotted. The phase space sampled curve in blue, necessarily also includes the phase-imprint jitter. The green curve shows the jitter according to Eq. (2.83). To also include the phase imprint in the analytical solution it is added under the square root, see the orange curve. The orange and sampled curves coincide perfectly. The right-hand side shows the phase space for increasing evolution time, in the order (blue, green, orange, purple). For the upper plot, the systematic shifts of ω_+ were added only with the mean excited amplitude, resulting in a constant shift, but no additional jitter. For the lower plot, each phase space point evolves according to $\omega_+ + \delta\omega_+$, with $\delta\omega_+$ from Eq. (2.80), which results in the deformation of the phase space volume and the increased jitter.

plot of the jitter due to field imperfections and the relativistic shift and their effect on the phase space coordinates. As $D > 0$ was chosen here, the phase space points with higher amplitude, i.e. the ones further away from the center, experience a larger positive systematic shift and are thus faster, and the ones with lower amplitude lack behind.

Readout jitter

In addition to the axial oscillation signal which incorporates the phase information, the detection signal includes the full thermal noise spectrum of the resonator and the input noise of the cryogenic amplifier. The noise in a single Fourier frequency bin can be reduced by decreasing the bandwidth, compare Eq. (2.52), which requires increasing the measurement time of the detection signal. As the detection signal decays with the time constant $\frac{2\pi}{\gamma_z}$, there is a limit to this. This additional jitter thus scales with the signal-to-noise ratio (SNR) in the detected Fourier spectrum. For the PnP method, the final amplitude in the axial mode depends only on the initial amplitude of the modified cyclotron motion and thus on the excitation pulse $|B_+|$. In contrast, the PnA method allows to arbitrarily increase the amplitude of the axial motion after the coupling pulse, compare Figure 2.5, thus eliminating the SNR-dependent jitter and also removing the need to fine-tune the detection time. For PnA, the coupling itself adds another jitter as seen in Eq. (2.77), which can be evaluated (Mathematica) for the limiting case of large coupling pulses, $\coth\left(\Omega T_{\text{couple}}\right) \longrightarrow 1$, to be

$$\sigma(\varphi_z)_{\text{PnA}} = \sqrt{0.5\,\text{Li}_2\left[\left(\frac{B_+^2}{\rho_{+,th}^2} + 1.0\right)^{-1}\right]}, \tag{2.85}$$

where Li_2 is the Dilogarithm. This similarly depends on the ratio of amplitude of the cyclotron motion to the amplitude of the axial motion, which is thermally distributed, before the coupling pulse. In practice, the jitter of PnA and PnP are then mostly identical, see also Section A.5.2. Here, PnA is used over PnP primarily due to the ability to not have to tune the detection time. Figure 2.11 shows the PnA specific jitter Eq. (2.85) and the full thermal jitter of the PnA method, i.e. the phase imprint and readout jitter, calculated as explained in Section A.5.2.

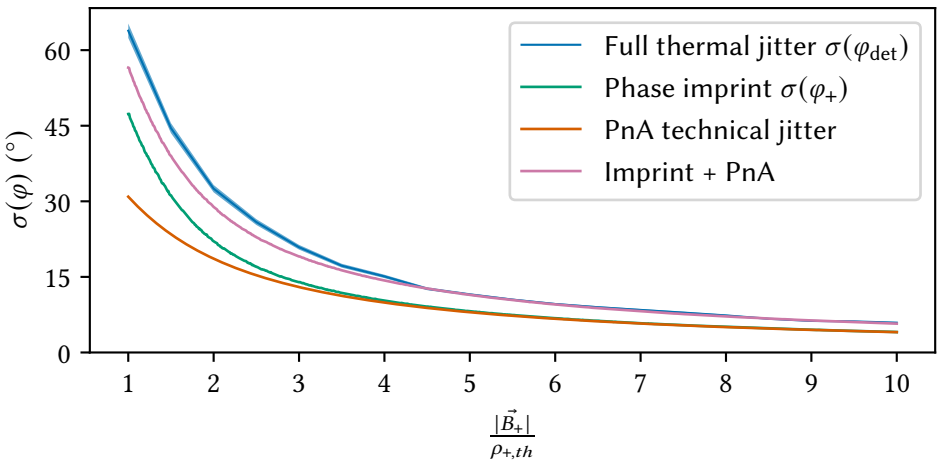

Figure 2.11: Exemplary jitter due to phase imprint and readout for PnA. The blue curve data is calculated from fully generated data of PnA cycles and has a small error bar due to the finite number of generated cycles. For PnA, the coupling time was chosen large enough to make the jitter for the different excitation amplitudes not limited by the detection time. Though the generation of the data relies on experimental parameters such as ω_R, Γ_R, γ_z etc., the full thermal jitter mostly only depends on the ratio $\frac{|\vec{B}_+|}{\rho_{+,th}}$. The orange line is the technical PnA jitter as calculated from Eq. (2.85) and the purple line is the squared sum under the square root of the phase imprint and technical jitter. The small difference of the blue to the purple line may be due to the definition of the circular standard deviation used to compute the jitter from the sampled data.

Chapter 3.

The Zeeman and hyperfine splitting

Due to its simplicity, a spin inside a magnetic field is often used as a model system for quantum mechanics [78]. In particular, spin-1/2 systems in magnetic fields, as described by the Zeeman effect, are ideal two-state quantum systems and their description is as fundamentally relevant for understanding basic quantum mechanics, as it is for state-of-the-art research. A typical next step in complexity concerns the description of interacting two-state systems. An ideal example of this is the Zeeman and hyperfine structure of the ground-state of hydrogen [79]. Any hydrogen-like atom in the ground state has a very similar and simple structure and Penning traps allow probing it in an ideal environment.

In the previous chapter, I introduced the theoretical groundwork and the experimental techniques of the Penning trap as a tool to measure the cyclotron frequency ω_c. Here, I will outline the quantum mechanical description of the combined Zeeman and hyperfine splitting in hydrogen-like ground-state systems and the intricacies of their spectroscopy in Penning traps. This includes the calculation of the transition frequencies, the transition rates, and a theoretical description of the transition probability lineshape. Following that, I discuss the influence of special relativity on the transition frequencies and the detection of spin states in Penning traps.

3.1. The Breit-Rabi equation

In the systems investigated here, only a single s-shell valence-electron with spin $S = 1/2$ is bound to the nucleus. In the case of a nuclear spin $I \neq 0$, there is a direct interaction between the nucleus and the electron due to their respective magnetic moments. Pictorially, the nucleus feels the strong magnetic field originating from the closely bound orbiting electron, which interacts with its magnetic moment. This leads to the system having two energy states, depending on the relative orientation of the electron and nucleus magnetic moments. If in addition, an external magnetic field is present, a Zeeman splitting of these two energy states depending on the orientation of the spins with respect to the magnetic field occurs. The initial two states are split into $4I + 2$ states.

The combined Zeeman and hyperfine splitting can be expressed through the non-relativistic

Hamiltonian in the dipole approximation [80]

$$\hat{H} = A\hat{\vec{S}} \cdot \hat{\vec{I}} - \mu_B g_e \vec{B} \cdot \hat{\vec{S}} - \mu_N g_I \vec{B} \cdot \hat{\vec{I}}. \tag{3.1}$$

The hyperfine constant A is a measure of the strength of the coupling of the electron and nucleus spin which are incorporated as the dimensionless spin operators $\hat{\vec{S}} = (\hat{S}_x, \hat{S}_y, \hat{S}_z)$ and $\hat{\vec{I}} = (\hat{I}_x, \hat{I}_y, \hat{I}_z)$, respectively. The Bohr and nuclear magneton μ_B and μ_N quantify the magnetic moment of an electron or proton for single angular momentum quantum numbers, respectively. The relation of the respective magneton to the charge e and masses m_e and m_p of the electron and proton are

$$\mu_B = \frac{e\hbar}{2m_e}, \quad \mu_N = \frac{e\hbar}{2m_p}, \tag{3.2}$$

where $\hbar$ is the reduced Planck constant. In the case of spin angular momenta, an additional factor, called the g-factor needs to be introduced. For the electron it is $g_e \approx -2$ and for nuclei it is typically of $O(1)$, e.g. for the proton $g_I \approx 5.6$. Due to the lower mass of the electron, its magnetic moment per quantum is much larger, e.g. $\mu_B/\mu_N = m_p/m_e \approx 1800$ [22].

In the following, a static field $\vec{B} = (0, 0, B_0)$ is chosen. The quantum eigenstates $|m_s, m_I\rangle = |m_s\rangle \otimes |m_I\rangle$, where $\otimes$ is the tensor product, of the uncoupled $A = 0$ system are expressed via the z-components m_s and m_I of their respective spins. The z-component quantum numbers range from $m_s = \pm 1/2$ and $m_I = \{-I, -I+1, \ldots, I\}$. The operators are defined via their action on the full basis set of the states $|m_s, m_I\rangle$. Similar to ref. [80] the ladder operators

$$S_\pm = S_x \pm iS_y, \quad I_\pm = I_x \pm iI_y \tag{3.3}$$

are defined. Using the angular momentum commutation relations $[S_i, S_j] = i \sum_k \epsilon_{ijk} S_k$, where ϵ_{ijk} is the Levi-Civita symbol, it can be shown that

$$S_\pm |m_s\rangle = \sqrt{S(S+1) - m_s(m_s \pm 1)}\, |m_s \pm 1\rangle\,, \tag{3.4}$$

where S is the total spin. Applying $S_\pm$ on states that have no higher/lower state annihilates the state, i.e. gives a zero for the prefactor. The same formula and argument holds for $I_\pm$ by replacing S with I and m_s with m_I. Substituting Eq. (3.3) into Eq. (3.1) results in

$$\hat{H} = AI_zS_z + \frac{A}{2}(I_+S_- + I_-S_+) - (\mu_B g_e S_z + \mu_n g_I I_z)B_0. \tag{3.5}$$

While the first and last terms do not change the z-projection quantum numbers, the second term leaves only their sum $m_F = m_s + m_I$ equal. Therefore, states with equal m_F quantum number form a submanifold of $\hat{H}_{m_F}$ with eigenstates only composed of superpositions of them. As the electron spin has only two possible values, it is sensible to form the states

$$|\pm\rangle_{m_F} = |m_s = \pm 1/2, m_I = m_F \mp 1/2\rangle\,, \tag{3.6}$$

which build the basis state of the submanifold. For the cases of $m_F = \pm(I + 1/2)$, only the $|-\rangle_{I+1/2}$ and $|+\rangle_{-I-1/2}$ exist, respectively, and they are eigenstates of the full Hamiltonian. Taking $|+\rangle_{m_F} = (1, 0)^T$ and $|-\rangle_{m_F} = (0, 1)^T$ allows expressing

$$\hat{H}_{m_F} = \begin{pmatrix} \frac{A}{2}(m_F - \frac{1}{2}) - \frac{1}{2}E_s + \frac{1}{2}E_I(1 - 2m_F) & \frac{A}{2}\sqrt{(I+1/2)^2 - m_F^2} \\ \frac{A}{2}\sqrt{(I+1/2)^2 - m_F^2} & \frac{A}{2}(-m_F - \frac{1}{2}) + \frac{1}{2}E_s + \frac{1}{2}E_I(-1 - 2m_F) \end{pmatrix}, \tag{3.7}$$

where

$$E_s = \mu_B g_e B_0 \quad \text{and} \quad E_I = \mu_N g_I B_0 \tag{3.8}$$

are the energy of the individual magnetic moments. The solution of the time-independent Schrödinger equation is given via the diagonalization of this matrix which yields the energies

$$\begin{aligned} E^{1,2}_{m_F} &= E_0 \pm \frac{A}{2}\sqrt{(I+1/2)^2 - m_F^2}\cosh(\theta), \\ E^{1}_{I+1/2} &= E_0 + \frac{A}{2}\left(I+\frac{1}{2}\right) + E_I - E_s, \\ E^{2}_{-I-1/2} &= E_0 + \frac{A}{2}\left(I+\frac{1}{2}\right) - E_I + E_s, \\ E_0 &= -\frac{A}{4} - m_F E_I, \end{aligned} \tag{3.9}$$

and normalized eigenstates

$$\begin{aligned} |1,2\rangle_{m_F} &= \frac{1}{\sqrt{2}}\left(\sqrt{1 \pm \tanh(\theta)}\,|+\rangle_{m_F} \mp \sqrt{1 \mp \tanh(\theta)}\,|-\rangle_{m_F}\right), \\ |1\rangle_{I+1/2} &= |m_s = 1/2, m_I = I\rangle\,, \\ |2\rangle_{-I-1/2} &= |m_s = -1/2, m_I = -I\rangle\,, \end{aligned} \tag{3.10}$$

where the mixing of states is quantified by

$$\sinh(\theta) = \frac{A m_F + E_I - E_s}{A\sqrt{(I+1/2)^2 - m_F^2}}. \tag{3.11}$$

The above equations of the energies of the combined Zeeman and hyperfine splitting are called the Breit-Rabi equation [81]. At zero magnetic field, $B_0 = 0$, the terms $E_s = E_I = 0$ and the energies are $E^{1,2}_{m_F} = A/2(-1/2 \pm 1/2 \pm I)$ and $E^{1}_{I+1/2} = E^{2}_{-I-1/2} = IA/2$. Therefore, only two different energy states exist at $B_0 = 0$ and they are spaced by the zero-field hyperfine splitting

$$E_{\mathrm{HFS}} = A\left(I+\frac{1}{2}\right). \tag{3.12}$$

In the literature, typically approximations based on the field strength B_0 are made to distinguish between the weak field and the strong field, the latter also called the Paschen–Back regime [82]. In the weak-field regime, the quantum number F of the approximately conserved total angular momentum $\vec{F} = \vec{S} + \vec{I}$ is introduced and the mixing of the states is large. In the strong field regime, the mixing due to the hyperfine splitting can be neglected and the eigenstates are equal to the ones at $A = 0$ i.e. $|m_s, m_I\rangle$. In the case of the measurements performed here, the mixing is typically small, as $|\sinh(\theta)| > 1 \Rightarrow |\tanh(\theta)| \gtrapprox 1$, but not negligible, so the full results derived above need to be used.

3.2. Transition rates and selection rules

Transitions between the states are driven with microwave radiation at frequencies corresponding to the energy difference between the states. Given a sinusoidal magnetic excitation, a term

$$\hat{H}_{\mathrm{MW}} = -(\mu_B g_e \hat{\vec{S}} + \mu_N g_I \hat{\vec{I}}) \cdot \vec{B}_{\mathrm{MW}} \cos(\omega_{\mathrm{MW}} t), \tag{3.13}$$

is added to the Hamiltonian Eq. (3.1). Here, $\vec{B}_{\mathrm{MW}}$ contains the direction and strength and ω_{MW} is the frequency of the exciting microwave field. Any spatial component of the exciting field is neglected, as the wavelength of the transitions in the Zeeman and hyperfine splitting for light ions at our magnetic fields is much larger, $\lambda \gtrapprox 1.5$ mm, than the ion's motional amplitudes, $\rho_i \ll 1$ mm.

In the following, the eigenstates, Eq. (3.10), are written as $|\Psi_k\rangle$ and the associated energies, Eq. (3.9), as E_k. The time-dependent Schrödinger equation of the general state $|\Psi\rangle$ is [83]

$$i\hbar \frac{\mathrm{d}}{\mathrm{d}t} |\Psi\rangle = (\hat{H} + \hat{H}_{\mathrm{MW}}) |\Psi\rangle . \tag{3.14}$$

Plugging in the Ansatz

$$|\Psi\rangle = \sum_k c_k(t) |\Psi_k\rangle e^{-i\frac{E_k}{\hbar}t} \tag{3.15}$$

yields the following differential equation for the amplitudes $c_m(t)$:

$$\dot{c}_m = i \sum_k \underbrace{\frac{1}{\hbar} \langle \Psi_m | (\mu_B g_e \hat{\vec{S}} + \mu_N g_I \hat{\vec{I}}) \cdot \vec{B}_{\mathrm{MW}} |\Psi_k\rangle}_{=:\Omega_{mk}} e^{i\frac{E_m - E_k}{\hbar}t} \frac{1}{2}(e^{i\omega_{\mathrm{MW}}t} + e^{-i\omega_{\mathrm{MW}}t}) c_k(t), \tag{3.16}$$

where the Rabi frequency Ω_{mk} was defined. If the excitation frequency ω_{MW} is close to a difference $\frac{E_m - E_n}{\hbar} =: \omega_{mn}$, a rotating wave approximation can be made to drop all terms with large frequencies [1]. This effectively reduces the system to a two-level system, which is described by a coupled differential equation

$$\begin{aligned} \dot{c}_m &= \frac{i}{2} \Omega_{mn} e^{-i\Delta_{mn}t} c_n(t) \\ \dot{c}_n &= \frac{i}{2} \Omega^*_{mn} e^{i\Delta_{mn}t} c_m(t), \end{aligned} \tag{3.17}$$

where $\Delta_{mn} = \omega_{\mathrm{RF}} - \frac{E_m - E_n}{\hbar}$. Solving for the probabilities reproduces the well-known Rabi cycle [84]

$$P_n(\Delta, t \mid \Omega) = c_n(t) c_n^*(t) = \frac{|\Omega_{mn}|^2}{|\Omega_{mn}|^2 + \Delta_{mn}^2} \sin^2\left(\frac{1}{2}\sqrt{|\Omega_{mn}|^2 + \Delta_{mn}^2}\, t\right), \quad P_m = 1 - P_n, \tag{3.18}$$

where the initial condition of being in the state m was taken. On resonance, $\Delta_{mn} = 0$, the probabilities evolve with the rate $|\Omega_{mn}|/2$ and have full contrast, i.e. range from zero to one.

[1] Note that this step is crucial. If the difference of some transition frequencies is of the order of the Rabi frequency, the rotating wave approximation may fail. This may introduce asymmetries in the observed resonance and lead to significant shifts.

Off resonance, the probabilities evolve faster and at a reduced contrast. The rate at which the transition is driven, given by the Rabi frequency, scales with the strength of the exciting field $\vec{B}_{\mathrm{MW}}$ and can thus be experimentally tuned.

To calculate the matrix element of the Rabi frequency Eq. (3.16) in the case of x and y components of the field $\vec{B}_{\mathrm{MW}}$, the x and y spin operators can be expressed via the ladder operators Eq. (3.3). As the ladder operators change the m_F quantum number by 1, the x and y components of $\vec{B}_{\mathrm{MW}}$ can only induce transitions between states with $\delta m_F = 1$. In the strong field limit, this selection rule becomes the stronger condition that either $\delta m_s = 1$ or $\delta m_I = 0$. For intermediate fields, couplings between states with high field quantum number differences of $\delta m_I = 2$ and $\delta m_s = 1$ are possible.

A z-component in $\vec{B}_{\mathrm{MW}}$ results in a coupling between states of equal m_F, as both S_z and I_z do not change m_F. In the strong field limit, this coupling vanishes as the states $|1, 2\rangle_{m_F}$, compare Eq. (3.10), are orthogonal eigenstates of S_z and I_z.

3.3. Transition probabilities

The goal of the experiment is to measure a set of transition frequencies ω_i corresponding to the energy differences in Eq. (3.9). To this end, the probability to drive the transition with irradiated microwaves at frequency ω_{RF} is measured. In principle, the Rabi cycle, Eq. (3.18), could be observed for varying ω_{RF} to fit the value of ω_i. Here, several effects that will alter the observed probability and a discussion of these follows.

3.3.1. Including the measurement uncertainty of the magnetic field

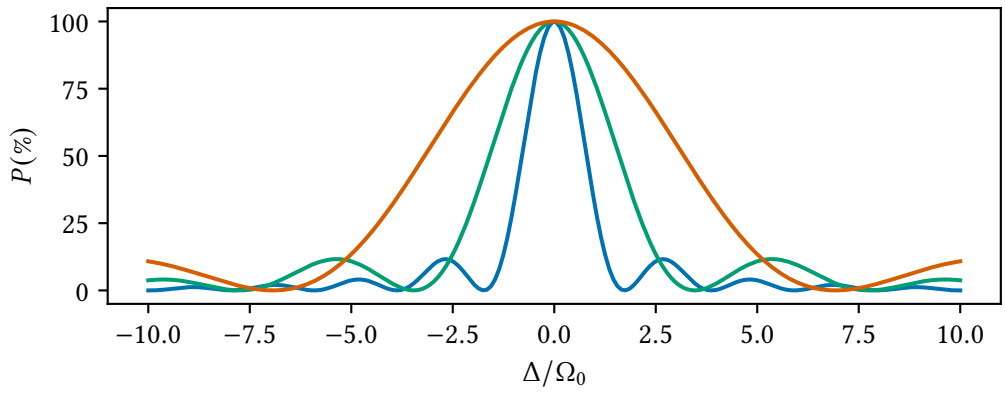

Figure 3.1: The probability to change the state for different Rabi frequencies is shown. The Rabi frequency Ω is Ω_0 for the blue line, $2\Omega_0$ for the green line, $4\Omega_0$ for the orange line. The time $t = \pi/\Omega$ is chosen such that a maximum at 0 occurs.

Figure 3.1 shows the Rabi cycle for different Rabi frequencies. In order to maximize the precision for the same number of recorded data points, the Rabi frequency should be reduced as far as possible. That, however, leads to a complication. The value of the real transition frequency

ω_i included in $\Delta_i = \omega_{\mathrm{MW}} - \omega_i(B_0)$ depends on the current magnetic field inside the Penning trap. As the magnetic field may drift and is only measured with a finite uncertainty during each excitation try, Δ_i is statistically distributed. If the width of this distribution approaches the Rabi frequency, the Rabi cycle's probability will be altered significantly.

Assuming normal distributed values of the measured magnetic field B_0 with standard deviation σ_B, the standard deviation of Δ for a particular transition with frequency $\omega(B)$ is to first order

$$\sigma_\omega(B_0 \mid \sigma_B) = \left|\frac{\partial\omega(B)}{\partial B}(B_0)\right| \sigma_B. \tag{3.19}$$

Given a single measured value of the magnetic field, the experimentally chosen detuning Δ is statistically distributed around the real value by Δ_B with a probability

$$P_B(\Delta_B \mid \sigma_\omega) = \frac{1}{\sqrt{2\pi\sigma_\omega^2}} e^{-\frac{1}{2}\Delta_B^2/\sigma_\omega^2}. \tag{3.20}$$

The observed probability after many experimental tries is thus the convolution

$$\begin{aligned} P_B(\Delta, t \mid \sigma_\omega, \Omega) &= P_B(\Delta \mid \sigma_\omega) * P(\Delta, t \mid \Omega) \\ &= \int_{-\infty}^{\infty} \mathrm{d}\Delta_B P(\Delta_B) \frac{\Omega^2}{\Omega^2 + (\Delta - \Delta_B)^2} \sin^2\left(\frac{1}{2}\sqrt{\Omega^2 + (\Delta - \Delta_B)^2}\, t\right) \end{aligned} \tag{3.21}$$

where Ω is the Rabi frequency of the transition.

Two cases need to be considered here. In the case of $t \gg \pi/\sigma_\omega$ and $\sigma_\omega \approx \Omega$, the sinusoidal term may be taken as the average value of $1/2$. The resulting probability lineshape is just the convolution of a normal distribution with width σ_ω and a Lorentzian function with width Ω and height 0.5. Such a lineshape is also known as a Voigt profile [85]. In the second case, σ_ω is significantly smaller, such that $t \gtrapprox \pi/\sigma_\omega$ and $\sigma_\omega \approx \Omega$. Here, the time dependence does not drop out, but for a fixed time, the oscillating variations with Δ are still smoothed out via the convolution. Figure 3.2 shows the probability lineshape for both cases.

3.3.2. Decoherence effects

Choosing the probability Eq. (3.18) for a single try assumes that, during the excitation time t, the magnetic field does not significantly change. If this were the case, the derivation of the transition probability done in the previous chapter would have to include the dynamics of the field resulting in the emergence of decoherence effects.

In the simplest case, noise in the magnetic field value will lead to decoherence. To include decoherence in the calculation of the transition probability, a pure wavefunction approach cannot be used. Instead, the quantum state is represented via a density matrix. It has been argued above, that the hyperfine structure can be reduced to two-level systems with ground and excited states when driving a specific transition. For a driven two-level system, the time evolution of the density matrix including decoherence can be rephrased as the time evolution of the so-called Bloch-vector $\vec{M}$ via the Bloch-equations [86]. The Bloch-equations for an excitation

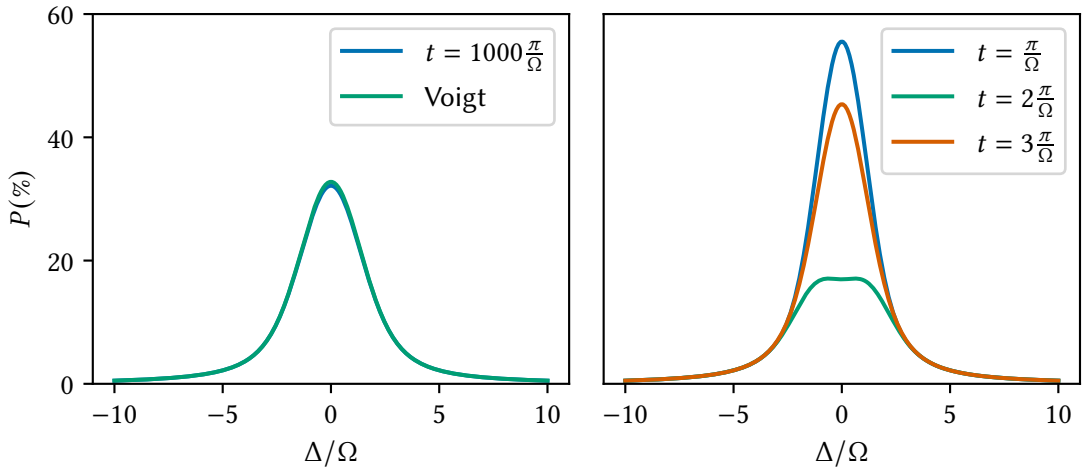

Figure 3.2: Rabi resonance with included B measurement uncertainty. For both plots $\Omega = \sigma_\omega$. On the left, the difference between the full probability at $t = 1000\frac{\pi}{\Omega}$ and the Voigt profile has nearly vanished. On the right, a clear dependence on irradiation time t is still visible. Note that in the experiment, the irradiation time t between both cases are kept similar and $\Omega = \sigma_\omega$ are vastly different.

$\vec{B}_{\mathrm{MW}} = (B_{\mathrm{MW}}, 0, 0)$ in the frame co-rotating with the excitation are

$$\frac{\mathrm{d}}{\mathrm{d}t}\begin{pmatrix} M_x \\ M_y \\ M_z \end{pmatrix} = \underbrace{\begin{pmatrix} -\gamma & \Delta & 0 \\ -\Delta & -\gamma & \Omega \\ 0 & -\Omega & 0 \end{pmatrix}}_{\Theta}\begin{pmatrix} M_x \\ M_y \\ M_z \end{pmatrix}, \tag{3.22}$$

where γ is a relaxation rate of x and y-components. The x and y-components of $\vec{M}$ are connected to the coherence of the superposition of excited and ground state, and the z-component, $M_z = 2P - 1$, reflects the probability P to be in the excited state. Certain types of magnetic field noise can be modelled via a dephasing rate γ of the superposition [86]. A direct relaxation rate of the z-component is ignored, as it is typically associated with spontaneous emission and physically not motivated here. Assuming to be in the ground state initially $\vec{M}_0 = (0, 0, -1)$, the probability is written via the matrix exponential

$$P(\Delta, t \mid \Omega, \gamma) = -\left(e^{\Theta(\Delta,\Omega,\gamma)t}\right)_{33}. \tag{3.23}$$

The measurement uncertainty of the magnetic field over several attempts of the drive has to be included here as well, which again gives the final probability as the convolution

$$P(\Delta, t \mid \sigma_\omega, \Omega, \gamma) = P_B(\Delta \mid \sigma_\omega) * P(\Delta, t \mid \Omega, \gamma). \tag{3.24}$$

The case of $\gamma = 0$ reproduces the probability Eq. (3.21).

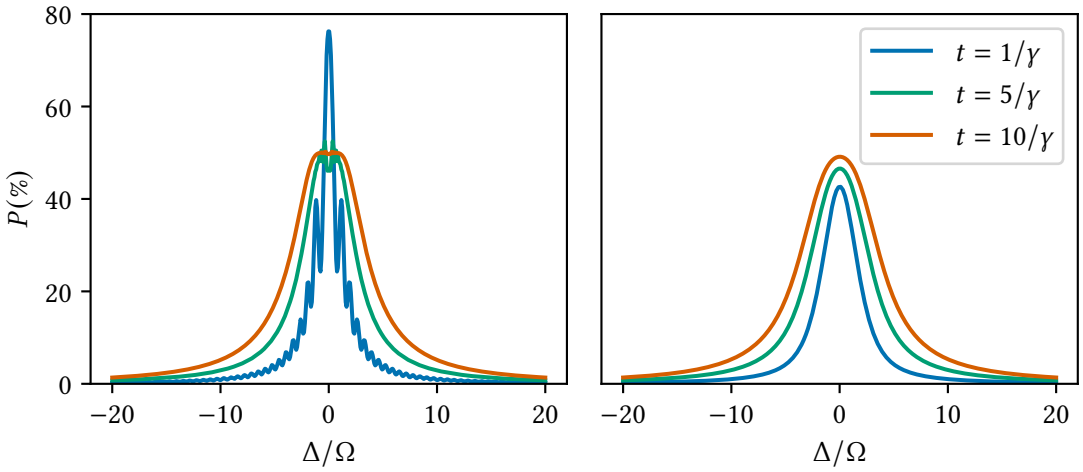

Figure 3.3: Rabi resonance with dephasing. The left-hand side shows the probability according to Eq. (3.23) and the right-hand side includes the convolution with the distribution due to measurement uncertainty Eq. (3.24). Here $\Omega = \sigma_\omega = 10\gamma$.

Figure 3.3 shows the resonance curves for the decoherent evolution with and without the measurement uncertainty. It is assumed that the dephasing rate due to field noise during a single attempt is much smaller than the measurement uncertainty over several attempts $\gamma \ll \sigma_\omega$. The plot shows a saturation effect due to the irradiation time t, while the previous consideration only showed saturation due to the power. For the probability Eq. (3.23), an oscillating structure still exists at times close to the dephasing timescale, but this structure is lost for large times. For large times, the probability further converges to $P_{\text{sat}} = 0.5$. The convolution with the measurement uncertainty removes the structure even for the smaller times, but still shows the saturation broadening effect and a lineshape reminiscent of a Voigt profile. The saturation effect with larger times leads to a worse statistical uncertainty on the determined frequency center. For the case of a fixed time t, the saturation broadening can be decreased by lowering Ω relative to σ_ω.

3.3.3. Asymmetry effects

The effects described above should be considered when choosing optimal experimental parameters, but the probability lineshapes are still symmetric and simply taking a Gaussian to fit the center would not lead to any systematic shifts. Previously, only the idealized effect of magnetic field fluctuations as a dephasing was discussed. If the fluctuations of the magnetic field were not symmetrically distributed, the resulting probability lineshape would inherit some of this asymmetry.

For non-perfect homogeneity of the magnetic field $B = B_0 + B(z)$, the thermal axial motion leads to a coupling of the particles observed magnetic field to the thermal heat bath of the detection system. The first inhomogeneity $B_1 z$ couples the symmetric normal distribution of the thermal variable z, compare Section A.4.2, to the magnetic field, so it does not lead to

asymmetry. In contrast, the square of the coordinate z appearing in the second inhomogeneity $B_2 z^2$, is distributed according to the asymmetric Maxwell distribution.

In ref. [87] the asymmetric lineshape due to B_2 has been derived for a spin-1/2 system by including the thermal motion in the transition frequency

$$\omega(t) = \omega_0 + 2\Delta\omega \frac{z^2}{\rho_{z,th}^2}, \tag{3.25}$$

where the linewidth parameter is defined as $\Delta\omega = \omega_0 \frac{B_2}{B_0} \frac{\rho_{z,th}^2}{2}$. This can be adapted for the combined Zeeman and hyperfine splitting by defining it via

$$\Delta\omega = \frac{\mathrm{d}\omega(B_0)}{\mathrm{d}B_0} B_2 \frac{\rho_{z,th}^2}{2}, \tag{3.26}$$

which is valid, because $\Delta\omega \ll \omega_0$. With these definitions, the mean $\langle\omega(t)\rangle = \omega_0 + \Delta\omega$. A statistical solution of the probability is derived via the evaluation of n-time correlation functions of the axial coordinate, which introduce the coupling time γ_z of the axial motion to the heat bath. The probability

$$P(\Delta, t \mid \Omega, \Delta\omega, \gamma_z) = 0.5 \left[1 - \exp\left(-\pi\Omega^2 t \chi(\Delta, \Delta\omega, \gamma_z)\right)\right], \tag{3.27}$$

is expressed via the lineshape function χ. This function will be called the Brown-Gabrielse line.

The general lineshape function derived in ref. [87] is

$$\begin{gathered}\chi(\Delta, \Delta\omega, \gamma_z) = \frac{4}{\pi} \mathrm{Re}\left[\frac{\gamma_z' \gamma_z}{(\gamma_z' + \gamma_z)^2} \sum_{n=0}^{\infty} \left(\frac{\gamma_z' - \gamma_z}{\gamma_z' + \gamma_z}\right)^{2n} \frac{1}{(n+\frac{1}{2})\gamma_z' - \frac{1}{2}\gamma_z - i\Delta}\right], \\ \gamma_z' = \sqrt{\gamma_z^2 + 4i\gamma\Delta\omega}.\end{gathered} \tag{3.28}$$

The derivation relies on the assumptions

$$t \gg 2\pi/\gamma_z, \quad t \gg 2\pi/\Delta\omega, \quad \Omega \ll \Delta\omega \ \text{ and } \ \Omega \ll \gamma_z. \tag{3.29}$$

As will be discussed later, for a set of transitions these assumptions are more or less fulfilled. The numerical studies performed in this work, see Section A.6, confirm the full probability Eq. (3.27) for the above assumptions and can even extend the calculations outside of them.

The lineshape function approaches a symmetric Lorentzian profile for the strong coupling case, $\gamma_z \gg \Delta\omega$, as the frequency $\omega(t)$ follows its average value very fast. In the case of weak coupling, $\gamma_z \ll \Delta\omega$, the oscillation frequency of the Bloch vector changes only over several cycles and the lineshape function reproduces the thermal Boltzmann distribution of the square axial amplitude. Figure 3.4 shows the different coupling regimes and the saturation effect of the Brown-Gabrielse line. Without saturation, the weighted centers of the probability

$$\Delta_0 = \left\langle\Delta\right\rangle = \frac{1}{\int \mathrm{d}\Delta P(\Delta)} \int \mathrm{d}\Delta P(\Delta)\Delta, \tag{3.30}$$

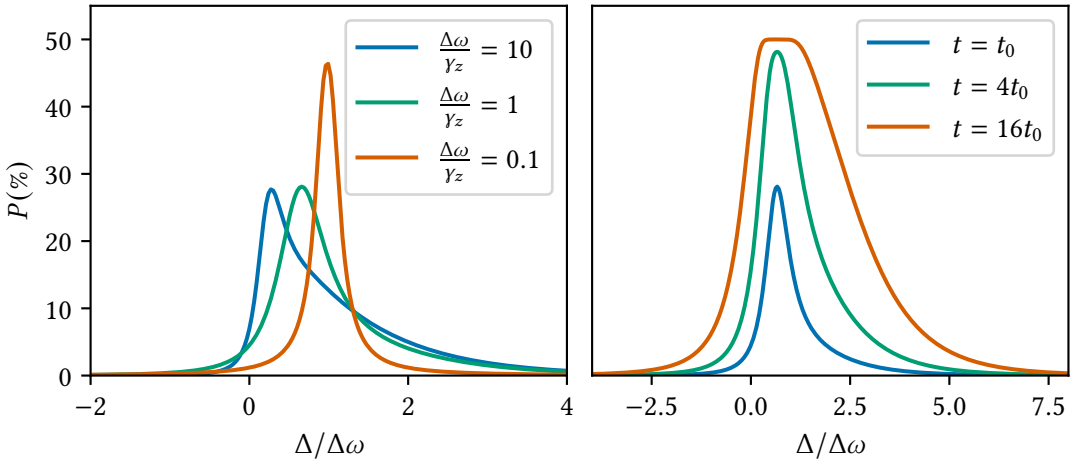

Figure 3.4: Brown-Gabrielse line. The left-hand side shows the unsaturated case of Eq. (3.27) for different ratios of $\frac{\Delta\omega}{\gamma_z}$ to illustrate the weak (blue), intermediate (green) and strong (orange) coupling. The right-hand side shows the saturation behaviour with increasing times for $\Delta\omega/\gamma_z = 1.0$. Equivalently the Rabi frequency could have been increased by the square roots of the factors to achieve the same effect.

even for the very asymmetric case at $\Delta\omega/\gamma_z = 0.1$, have a value very close to the average value in time $\Delta_0 \approx \langle\Delta(t)\rangle = \Delta\omega$. The saturation for large t or Ω not only leads to a broadening of the line but in the case of not too large $\Delta\omega/\gamma_z$, a shift of Δ_0 occurs due to asymmetric broadening.

In principle, the saturation and the associated shifts should become obvious due to the asymmetry in the recorded resonance. Including the shot-to-shot magnetic field uncertainty via the convolution

$$P(\Delta, t \mid \sigma_\omega, \Omega, \Delta\omega, \gamma_z) = P_B(\Delta \mid \sigma_\omega) * P(\Delta, t \mid \Omega, \Delta\omega, \gamma_z) \tag{3.31}$$

can cover up the asymmetry in the lineshape for σ_ω similar to $\Delta\omega$, but keep the mean shift due to the saturation, see Figure 3.5. This saturation shift due to the underlying asymmetric line has to be treated with care and can be minimized by reducing the saturation with the Rabi frequency as much as possible. The decrease of Rabi frequency leads to a worse statistic uncertainty on the determined center in this case, as the width of the resonance does not decrease with the maximum amplitude.

3.4. Relativistic shift of the levels

Treating the hyperfine and Zeeman splitting fully relativistic would need a relativistic quantum mechanical solution of the ion inside the magnetic field, compare the calculations for a simple spin-1/2 system in ref. [62]. Here, the spin of the nucleus may be larger than 1/2, and thus not even the Dirac equation would be sufficient to do these calculations. The two most important shifts, the Doppler shift and the shift due to the Thomas precession can be derived more easily.

Similar to the shift of the free cyclotron frequency, compare Eq. (2.40), the transitions of the

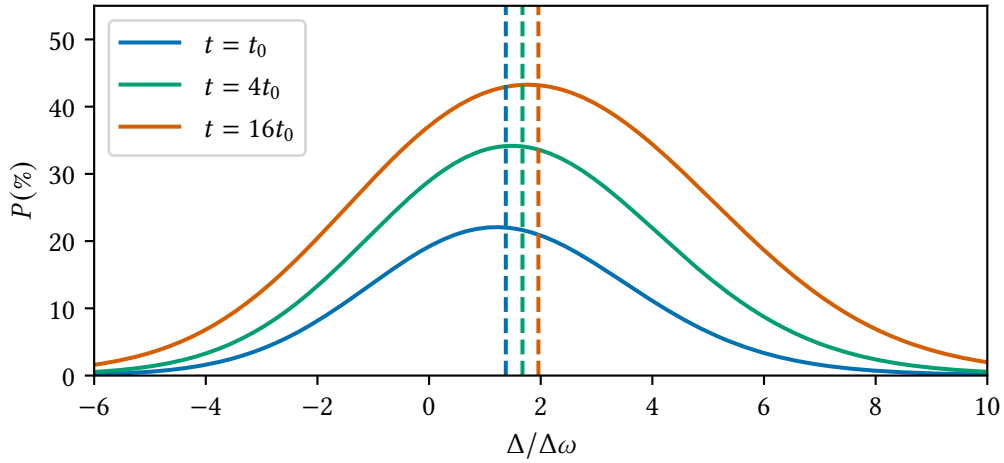

Figure 3.5: Brown-Gabrielse line with measurement uncertainty. Here $\sigma_\omega = 2\Delta\omega$ and $\Delta\omega = \gamma_z$. The asymmetric broadening of the underlying line is covered up by the measurement uncertainty, but the weighted center Δ_0, indicated by the dashed line, shifts with increasing saturation.

Zeeman and hyperfine splitting are Doppler shifted due to the fast cyclotron motion. Here, the shift of the relevant measurement quantity in the lab frame

$$\Delta(\omega_{\mathrm{MW}}, \omega_c) = \omega_{\mathrm{MW}} - \omega(\omega_c), \tag{3.32}$$

where the transition frequency ω is computed from the lab frame free cyclotron frequency ω_c, will be derived. The transition is resonantly driven, if the microwave irradiation frequency is equal to the transition frequency in the ion's rotating frame of reference, which will be denoted with primed quantities. In the ion frame, the lab frame magnetic field B_0 is boosted to

$$B_0^{'} = \gamma B_0, \tag{3.33}$$

where γ is calculated via Eq. (2.41). As the lab frame free cyclotron frequency also includes the factor γ via $\omega_c = \frac{q}{\gamma m} B_0$, the transition frequency in the ion frame is

$$\begin{aligned} \omega^{'} &= \omega(B_0^{'}) = \omega(\gamma^2 \frac{m}{q}\omega_c) \approx \omega(\omega_c) + \omega_c(\gamma^2 - 1)\frac{\mathrm{d}\omega}{\mathrm{d}\omega_c}(\omega_c) \\ &\approx \omega(\omega_c) + 2\omega_c(\gamma - 1)\frac{\mathrm{d}\omega}{\mathrm{d}\omega_c}(\omega_c), \end{aligned} \tag{3.34}$$

where $\gamma - 1 \ll 1$ was used. The magnetic field component which drives the transition is transversal to the direction of the ion's cyclotron motion thus giving a transversal Doppler shift $\omega_{\mathrm{MW}}^{'} = \gamma\omega_{\mathrm{MW}}$. Therefore

$$\Delta^{'} = \omega_{\mathrm{MW}}^{'} - \omega^{'} = \Delta(\omega_{\mathrm{MW}}, \omega_c) + (\gamma - 1)\left(\omega - 2\omega_c \frac{\partial\omega}{\partial\omega_c}(\omega_c)\right), \tag{3.35}$$

where $\omega_{\mathrm{MW}} \approx \omega$ was used in the correction term.

The Thomas precession is a relativistic effect that leads to an additional precession frequency that has to be added to the classical Larmor precession of a spin in a magnetic field [88]. To include the Thomas precession, the time evolution of the vector quantities $\hat{\vec{S}}$ and $\hat{\vec{I}}$ can be derived from the initial Hamiltonian, Eq. (3.1). In the Heisenberg picture this yields

$$\begin{aligned} \frac{d}{dt}\hat{\vec{S}} &= \frac{1}{\hbar}(A\hat{\vec{I}} - \mu_B g_e \vec{B}) \times \hat{\vec{S}}, \\ \frac{d}{dt}\hat{\vec{I}} &= \frac{1}{\hbar}(A\hat{\vec{S}} - \mu_N g_I \vec{B}) \times \hat{\vec{I}}, \end{aligned} \tag{3.36}$$

where $\times$ is the cross product. In ref. [89], leading to Eq. (11.107), it is explained that for the time evolution of any vector quantity $\vec{G}$, the Thomas precision has to be included to the time derivative via the addition of the term $\vec{\omega}_T \times \vec{G}$. The precession vector is given by

$$\vec{\omega}_T = \frac{\gamma^2}{\gamma + 1} \frac{\vec{a} \times \vec{v}}{c^2}, \tag{3.37}$$

where $\vec{a}$ and $\vec{v}$ are the acceleration and velocity of the ion, respectively. By adding these terms to the above equation, they can be reabsorbed into the initial Hamiltonian

$$\hat{H} = A\hat{\vec{S}} \cdot \hat{\vec{I}} - (\mu_B g_e \vec{B} - \hbar\vec{\omega}_T) \cdot \hat{\vec{S}} - (\mu_N g_I \vec{B} - \hbar\vec{\omega}_T) \cdot \hat{\vec{I}}. \tag{3.38}$$

This reproduces the Ansatz used in ref. [90] for the Thomas precession of the hyperfine structure in a storage ring. For $\vec{B} = (0, 0, B_0)$ and a pure cyclotron motion with velocity $\beta = v_c/c$, the Thomas precession frequency can be simplified to

$$\vec{\omega}_T = \frac{\gamma^2\beta^2}{\gamma + 1} \frac{q}{m} \vec{B} = (\gamma - 1) \frac{q}{m} \vec{B}. \tag{3.39}$$

Due to the factoring with $\vec{B}$, the Thomas precession can be integrated into the Breit-Rabi equation Eq. (3.9) by replacing the energy terms E_s and E_I with

$$\begin{aligned} E_s^{'} &= E_s - \hbar(\gamma - 1)\omega_c, \\ E_I^{'} &= E_I - \hbar(\gamma - 1)\omega_c. \end{aligned} \tag{3.40}$$

As a comparison, the correction term is equal to the correction of the cyclotron frequency, see Eq. (2.40), but $E_s \gg \hbar\omega_c$. In contrast, typically E_I is a lot smaller compared to E_s and of similar magnitude compared to $\hbar\omega_c$. The result derived here is also applicable to bound-electron g-factor measurements, where it reproduces the result given in ref. [91], and to bare nuclear magnetic moment measurements.

3.5. Detection of Zeeman states and the double-trap technique

The detection of the Zeeman eigenstates in the Penning trap can be achieved via the continuous Stern-Gerlach effect [92]. To this end, a large B_2 is intentionally introduced to couple the

Zeeman eigenstate of the particle to the axial motion. The energies of an eigenstate $E_m(B)$, compare Eq. (3.9), then depend on the square of the position z. This leads to the additional axial force

$$F_m = -\frac{\partial E_m(B_0 + B_2 z^2)}{\partial z} = -2zB_2 \frac{\partial E_m(B)}{\partial B}, \tag{3.41}$$

where the magnetic field derivative $\frac{\partial E_m(B)}{\partial B} \approx \frac{\partial E_m}{\partial B}(B_0)$ can typically be assumed to be constant as $|B_2 z^2| \ll |B_0|$ and $E_m(B)$ does not change fast. The state dependent axial force alters the axial oscillation frequency ω_z, compare Eq. (2.3), to

$$\omega_{z,m} = \sqrt{\omega_z^2 + 2\frac{B_2}{m}\frac{\partial E_m}{\partial B}} \approx \omega_z^2 + \frac{B_2}{m\omega_z}\frac{\partial E_m}{\partial B}. \tag{3.42}$$

A successfully driven transition from state m to n leads to a frequency shift

$$\delta\omega_{z,mn} = \frac{B_2}{m\omega_z}\frac{\hbar\partial\omega_{mn}}{\partial B}, \tag{3.43}$$

where the sign of $\hbar\omega_{mn} = E_m - E_n$ may be positive or negative. The size of the frequency shift depends not only on the size of B_2 and the mass of the ion m but also on the magnetic field dependence of the chosen transition ω_{mn}. The magnetic field dependence can vary by orders of magnitude for the different transitions, making some transitions impossible to use for the detection, as the axial frequency shift is below the detection limit.

The detection of the spin state through the continuous Stern-Gerlach effect requires large values of B_2, e.g. in our experiment $B_2 \approx 282$ kT/m^2. This couples the axial to the cyclotron mode, compare Eq. (2.35), to such a degree that the sideband coupling is neigh impossible and a precision measurement of ω_c is very difficult. Additionally, the transition resonance is significantly broadened by the linewidth parameter Eq. (3.26), which limits the statistical accuracy of the determination of the center frequency.

To overcome these limitations, the double-trap technique, first introduced in ref. [68], is used. In a precision trap (PT) with optimized electric harmonicity and magnetic homogeneity the high-precision measurement of the cyclotron frequency ω_c and the probe of the transition frequency is performed. The ion is then adiabatically transported to a trap with a large B_2 value, called the analysis trap (AT), where the spin state is determined. Afterwards, the ion is transported back to the PT to start a new measurement cycle.

Chapter 4.

The experimental setup

Parts of our experimental setup at the MPIK were originally based in large parts on the design of the Mainz proton g-factor experiment, see e.g. refs. [70, 93]. Construction of the setup started in 2018 at the MPIK and the original team consisted of group leader Andreas Mooser, who was previously part of the Mainz proton as well as the BASE antiproton g-factor experiments, Antonia Schneider as a Master student, and Alexander Rischka who helped as a post-doc. Initial efforts were focused on the in-trap production of ^{3}He and the design of a new analysis trap for the detection of spin-flips of $^3He^{2+}$, see refs. [94, 95]. I started one year later in early 2019 and worked on the millimeter microwave transmission required for the hyperfine structure measurement of $^3He^+$, see ref. [96]. The setup was ready to assemble at the start of 2020, with a few delays caused by the start of the pandemic. The commissioning of the experiment started in the late spring and the first measurements on $^3He^+$ quickly thereafter.

After the successful measurement of the hyperfine structure of $^3He^+$ outlined in the Ph.D. thesis of Antonia Schneider, see ref. [97], several upgrades to the experiment were implemented. Mainly, these upgrades were meant to advance our aims for future measurements with ions sympathetically cooled via coupling to $^9Be^+$ and improve our measurement precision. To this end, a laser alignment system for both an ablation and cooling laser for $^9Be^+$ was installed and the Penning-trap setup was changed significantly. After some initial, only in parts successful, efforts towards the measurement of the Zeeman splitting of $^3He^{2+}$, which included the commissioning of the new analysis trap and sympathetic laser cooling, it was decided to measure the hyperfine structure of $^9Be^{3+}$. In this chapter, I will give an overview of the experimental setup used for this measurement.

4.1. The superconducting magnet and (some of) its history

The perhaps most vital and unchanging part of many Penning-trap experiments is the superconducting magnet system inside which the experiments are performed. The 5.7 T magnet system used in this experiment has a long history in precision Penning-trap measurements. It was designed by R.S. Van Dyck in conjunction with the manufacturer Nalorac Cryogenic Corporation (NCC) with the aim of the highest possible temporal stability and spatial uniformity

of the field. In first measurements in 1998, see ref. [98], it was shown that the magnet performs exceptionally well, having unprecedented temporal stability of 17 parts per trillion (ppt) per hour. Later, mass measurements using this magnet were performed at the UW-PTMS[1] experiment in Seattle, where the stability was further improved to 2 ppt per hour [99]. The magnet was shipped to the MPIK in Heidelberg in 2008, where the Tritium-Helium Trap (THe-Trap) experiment was established with the goal to measure the mass difference of ^{3}H to ^{3}He. Several Ph.D. theses describe the magnet system and some of its history at the MPIK in detail, see for example refs. [100–103]. Since 2018, the magnet has been used for experiments investigating the Zeeman and hyperfine splittings of light ions.

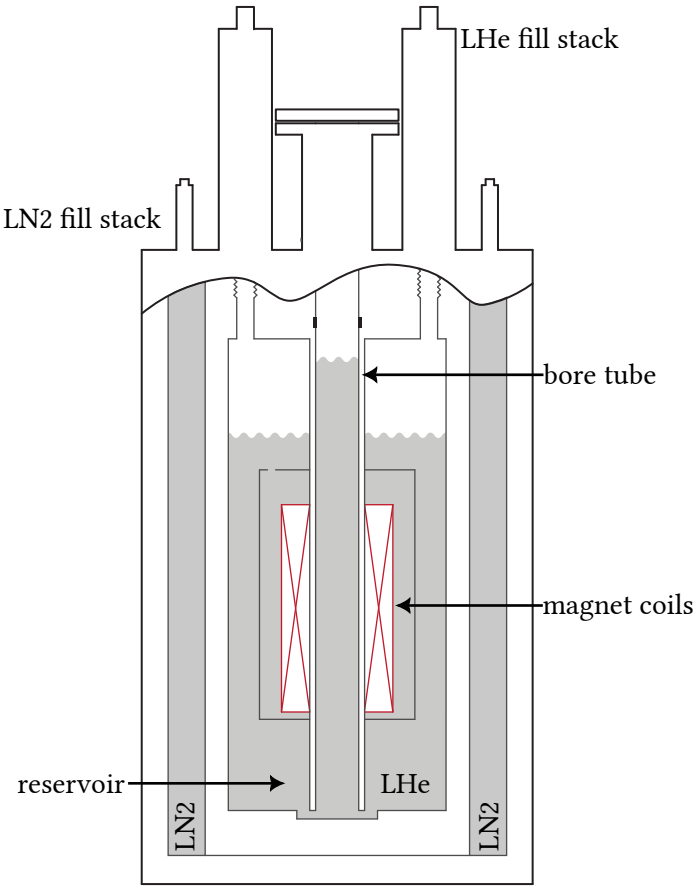

Figure 4.1: The superconducting magnet. Figure adapted from ref. [102].

Figure 4.1 shows a sketch of the superconducting magnet system. The magnet has a so-called cold bore, i.e. the bore is cooled to ~ 4.2 K by liquid helium (LHe) and serves directly as the cryostat for the inserted experiment. The reservoir, which is connected to the bore tube at the bottom of the magnet, is filled with LHe from the LHe fill stacks at the top. The reservoir and bore take approximately 160 l and 14 l of LHe, respectively. Both the bore tube and the reservoir have individual return lines connected at the top, which are merged on the outside in

[1]University of Washington Penning Trap Mass Spectrometer

the normal operation of the experiment. The reservoir is surrounded by an insulating vacuum and an outer liquid nitrogen (LN2) reservoir. Without an experiment inserted, the LN2 reservoir is refilled once per week and the LHe reservoir once every six weeks. The additional heat load of the inserted experiment roughly doubles the LHe usage.

4.2. The vacuum setup

The experimental setup is shown in Figure 4.2. The top, room temperature section is assembled from commercial, mostly CF100, vacuum parts, which include DC feedthrough flanges for biasing and coaxial feedthrough flanges for the detection- and excitation lines. The CF flanges are sealed via either copper gaskets or Viton seals. A CF60 turbopump is used to achieve a pressure of $\sim 10^{-7}$ mbar inside the prevacuum. At the top, a viewport for the microwave and laser transmission is installed, while the outward-facing sides feature viewports for the laser alignment. The room temperature section is mounted on top of the magnet and can be tilted via an adjustment CF-100 piece. The boiled-off LHe from the bore exits at the side of the adapter separating the bore volume from the experiment prevacuum.

The long section connecting the room temperature part of the experiment to the cryogenic part of the experiment serves to reduce the heat load and efficiently use the cooling potential of the LHe cryostat. To this end, four thin-walled tubes instead of a single big tube are used, and aluminum heat shields are attached to them. It is further of utmost importance to not only use the evaporation heat of the boiled-off LHe but also cool the experiment with the cold evaporated gas. Indeed, the energy needed for vaporizing helium is actually negligibly small compared to the energy needed to increase its temperature from 4.2 K to room temperature [104]. Cotton is wound around the connecting section such that the gaseous helium flow through the bore tube is restricted and cools the experiment efficiently.

All vacuum connections in the cryogenic part are sealed using custom indium gaskets. In the cryogenic prevacuum chamber, the Penning traps are placed in a separate copper vacuum chamber, called the trap chamber. At the bottom of the trap chamber, custom electrical feedthroughs manufactured by Kyocera (57 in total) and a central 1 mm diameter quartz glass window are soldered into a copper flange. Another set of windows for microwave and laser access is soldered into the top flange. With the experiment still outside the magnet, the trap chamber is pumped through a thin copper tube to a pressure of $\sim 10^{-6}$ mbar and subsequently pinched off to seal it. In the cryogenic environment, all residual gases freeze, or in the case of helium, build a monolayer on the surfaces. This gives essentially ideal vacuum conditions inside the trap chamber and ion storage times exceed the time needed to perform all measurements. For example, in the experiments with $^{9}Be^{3+}$, only a single ion was used in the whole one-year measurement campaign.

4.3. The trap tower

The trap tower, see Figure 4.3, is the cylindrical stack of electrodes inside the trap chamber. The electrodes are CNC turned from oxygen-free high thermal conductivity (OHFC) copper at the MPIK workshop to tolerances of a few μm and subsequently gold plated by Drollinger GmbH.

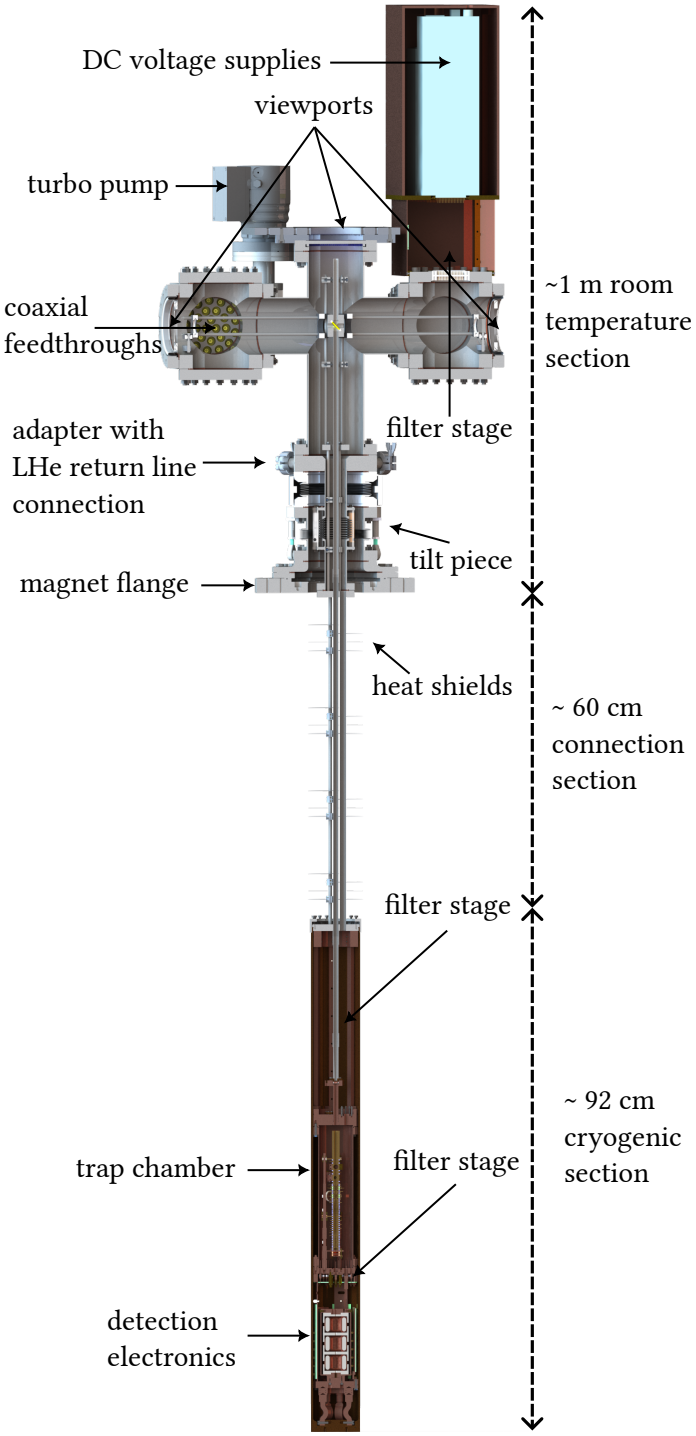

Figure 4.2: The vacuum setup. For details see text.

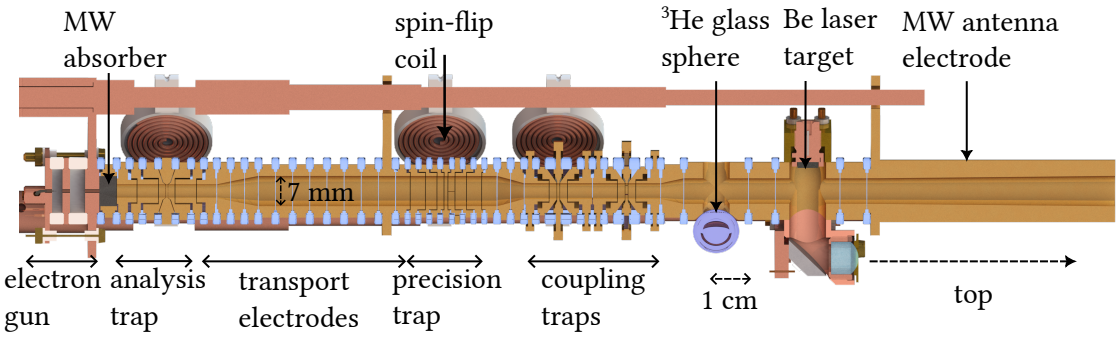

Figure 4.3: The trap tower. For details see text.

The machining tolerances of the sapphire spacers manufactured by Saphirwerk AG and used for isolating the electrodes at a distance of 0.14 mm are also specified at the µm regime. The gold-plated electrodes and sapphire spacers are typically so close to the specification dimensions, that individual pairs of fitting parts have to be chosen during the assembly. Starting at the bottom of the trap tower, the individual parts are discussed in more detail.

Electron gun

The electron gun emits electrons via field emission from a small tungsten tip, which is fabricated as explained in ref. [105]. The tungsten tip is placed on the axis of symmetry of the trap tower and connected to an electrode called the FEP (field emission point) electrode, which is the leftmost electrode in Figure 4.3. Ideally, the tungsten tip reaches just into the next electrode, called the HV (high voltage) electrode. To extract electrons with kinetic energy E_{kin}, the FEP electrode is biased to $V_{\mathrm{FEP}} = E_{\mathrm{kin}}/e$ and an extraction voltage on the HV electrode of typically up to 2 kV is needed. For details on the ion production, see the next chapter.

Analysis trap

The analysis trap (AT) is a 5-pole Penning trap with a small radius of 1.8 mm based on the design and optimizations performed in ref. [106]. The design of the AT ring electrode is optimized for a large value of B_2, which is achieved via optimizing the flare angle. This angle in conjunction with the comparably small radius and the 0.14 mm gaps leads to deviations from the idealized calculations outlined in Eq. (2.20). Therefore, the inner lengths, compare z_i in the calculations leading to Eq. (2.20), and the tuning ratio TR is optimized via finite element methods. While previously a Ni ring electrode with $B_2 \approx 110$ kT/m^2 was used, a stronger CoFe (*Vacuflux 50*) ring electrode to generate $B_2 \approx 282$ kT/m^2 was installed in this measurement campaign. The CoFe ring additionally decreases the magnetic field by about 0.7 T to around 5 T in the AT. An axial excitation line is connected to the lower endcap and the resonator is connected to the lower correction electrode. Excitations of spin transitions in the low GHz regime are possible with a so-called spin-flip coil fixated next to the trap, which consists of a few windings of copper wire terminated to ground [70]. The spin-flip coil is also used for excitations of and

couplings to the radial modes. The relevant trap parameters are listed in Table 4.1.

Transport section

To decrease the magnet field inhomogeneity in the PT, it has to be spatially separated from the AT. Next to the AT, three conical electrodes increase the radius to the 3.5 mm radius of the PT and, subsequently, a number of identical transport electrodes lead to the PT. The length of the transport electrodes should not be chosen too long, as this may lead to problems with the ion transport. The center of the PT is at a distance of about 6 cm from the PT, which decreases the inhomogeneities to $B_1 \approx 30$ mT/m and $B_2 \approx 1$ T/m^2.

Precision trap

During the measurement campaign of the $^3He^+$ hyperfine structure, some first attempts toward the phase-sensitive cyclotron measurements were unsuccessful. At the time, it was believed that this may have been due to frequency jitter from a too large uncompensated C_6 coefficient of the 3.5 mm 5-pole trap. As was argued in Section 2.2, a 7-pole trap always allows compensating C_4 and C_6 simultaneously, which triggered us to develop such a trap for the upgrade. For the optimization criteria of the 7-pole trap see Section 2.2. The combined orthogonality comes with some challenges, which will be discussed in the Section 5. An axial excitation line is connected to the uppermost correction electrode. The correction electrode above the ring electrode is split to allow for quadrupolar excitations. A spin-flip coil identical to the one in the AT is fixated next to the trap. In order to decrease d_{deff}, compare Eq. (2.44), and therefore increase the detection signal amplitude, the resonator is connected to two electrodes, e.g. the two lower correction electrodes. The PT is located at the center of the superconducting magnet, where the magnetic field homogeneity is ideal. The measured homogeneity around the central 10 mm of the magnet is about 1 µT [107]. The theoretical parameters of the new 7-pole PT are listed in Table 4.1.

Coupling traps

This pair of traps was originally designed to be used for the common endcap coupling technique, originally proposed in ref. [108], at the Mainz proton g-factor experiment, see ref. [109, 110]. In the top of the two traps, a cloud of laser-cooled beryllium ions would be stored, while the bottom trap stores the single target ion. Through the interaction of the induced image currents in the common endcap[2] the target ion's axial mode is sympathetically cooled to below the ambient 4 K. This required optimizing the traps for minimal capacitance from the common endcap to ground, which explains the larger sapphire spacers used here. Additionally, the upper trap has a ring electrode which is split into six parts, which serves a twofold function. By applying appropriately phase shifted RF signals, a rotating wall excitation can stabilize the beryllium clouds magnetron motion [111]. The split electrode has small gaps through which fluorescence electrodes hit silicon photomultipliers mounted around it, which can be used for

[2] As shown in Figure 4.3, the two traps have individual endcaps. The two endcaps are connected via capacitances to be common in their AC signal while allowing for individual DC biasing.

e.g. temperature measurements of the beryllium cloud [112]. The identical theoretical parameters of the two traps are listed in Table 4.1.

Table 4.1: Theoretical trap parameters. The two values of l_c and TR for the PT are the lengths and tuning ratios of the two correction electrode pairs of the 7-pole trap. For definitions of the variables see Section 2.2.

	AT	PT	CT
a_{el}/mm	1.8	3.5	2.0
l_r/mm	0.386	0.691	0.502
l_c/mm	1.359	(1.359, 2.307)	1.501
C_2/U_0 m^2	−114310	−23257	−93494
TR	0.879	(0.964, 0.815)	0.881
d_{eff}/mm	2.995	7.1	4.625

Sources

For production of ^{3}He, we use a gas-filled glass sphere, as described in ref. [94, 97]. The sphere is made from SO_2, has 1 cm diameter, 1 mm wall thickness and is filled with 5 mbar of ^{3}He gas. The sphere is mounted at the side opening of an electrode at the top of the trap tower. The

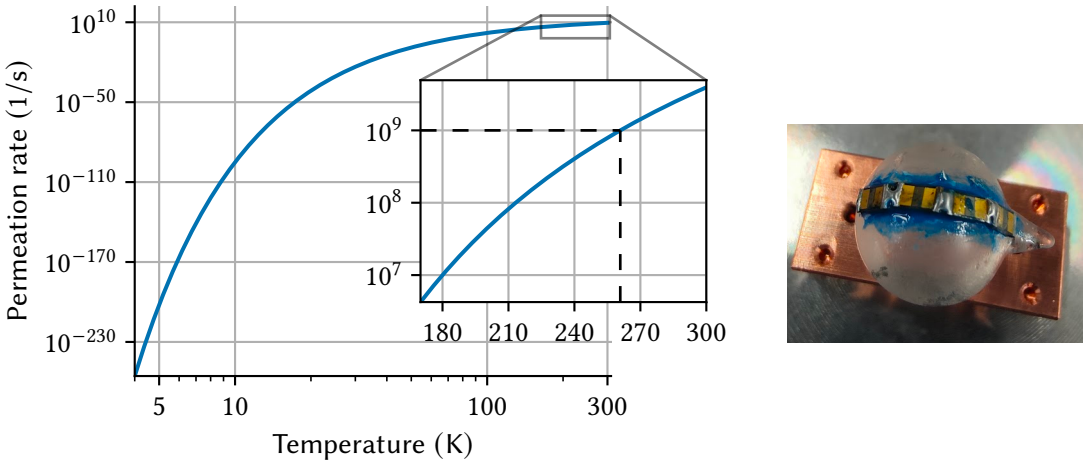

Figure 4.4: Left: Permeation rate of helium through the glass sphere. Right: Photograph of the glass sphere with the attached heating resistors. The heating resistors where actually changed from the ^{3}He$^+$ measurement, as the specific type used proved to be very ferromagnetic and lead to additional B_2 in the PT.

strong temperature dependence of the permeation can be used to produce ^{3}He gas via heating of the glass sphere with the attached resistors while simultaneously having no effect on the

vacuum conditions in normal operation, see Figure 4.4. For a theoretical description of the permeation rate see refs. [94, 113].

To estimate the required permeation rate and thus the temperature, the ionization rate in the trap volume needs to be calculated. Given the electron-impact cross-section σ_{EI}, see ref. [114] for a compilation of values, the rate of ionization is

$$R_{\mathrm{ion}} = \frac{\rho_{A,\mathrm{He}} \sigma_{\mathrm{EI}} I}{e}, \tag{4.1}$$

where $\rho_{A,\mathrm{He}}$ is the ^{3}He atom area density in units Number/Area and I the electron beam current inside the ionization volume and e is the elementary charge. In an equilibrium of production of ^{3}He via the permeation with rate R_{He} and loss of atoms via a loss rate R_{loss} inside the ionization volume, the area density is calculated as

$$\rho_{A,\mathrm{He}} = \frac{R_{\mathrm{He}}}{R_{\mathrm{loss}}} \frac{1}{A}, \tag{4.2}$$

where A is the area of the ionization volume, i.e. the trap's cross-sectional area $A = \pi a_{el}^2$. An upper bound for the loss rate is found by assuming a single horizontal crossing of the thermal atoms through the trap tower which gives $R_{\mathrm{loss}} = v_{th}/a_{el}$, where $v_{th} = \sqrt{k_B T/m}$ is the thermal velocity of the atoms with temperature T and mass m. In total, this gives an ionization rate of

$$R_{\mathrm{ion}} = \frac{R_{\mathrm{He}}}{\sqrt{k_B T/m}} \frac{1}{\pi a_{el}} \frac{\sigma_{\mathrm{EI}} I}{e}. \tag{4.3}$$

For electron beam currents of around 10 nA and a desired ionization rate of one ion per minute, the indicated permeation rate in Figure 4.4 of $R_{\mathrm{He}} = 10^9$ is estimated. This rate corresponds to a temperature of about 260 K.

While this source design can be applied identically to ^{4}He and maybe the neon isotopes, it would be harder to implement for nearly all other elements as they have much larger atomic (or molecular) size and thus much smaller permeation [3].

The production of beryllium ions is achieved via laser ablation from a solid target, which is mounted on another electrode with openings on the side. For details on the alignment of the laser, see the next Section. Inside the trap chamber, the laser pulse from the frequency-doubled Nd:YAG laser (Litron Nano 60-30) is first focused by a lens with a focal length of 25 mm and deflected by a mirror onto the ^{9}Be target. Above a threshold energy density on the surface of the material, atoms are evaporated and a plasma is formed [115]. In an appropriately biased trap, only the positively charged ions are then captured.

The experimental steps used for preparing ions are discussed in more detail in Section 5.

4.4. Laser and microwave access

The design of the millimeter microwave and the laser access to the trap chamber are described in detail in ref. [96] and ref. [116], respectively. Here, I will only give a short overview.

[3] They are also solid at 4 K, which might make things more difficult.

The millimeter microwaves needed for hydrogen- and lithium-like Zeeman splittings of light ions at the 5.7 T in the PT and 5 T in the AT span quite a large range. As a reference, the values for the bare electron spin-precession frequencies are $\sim$ 160 GHz and $\sim$ 140 GHz, in the AT and PT, respectively [22]. The additional hyperfine splitting further broadens the required frequency span. Microwave frequencies are classified by certain bands, in the case of the frequencies here, they fall into the D band, which spans 110-170 GHz, or in terms of wavelength 2.73 - 1.76 mm. For the transmission of these microwaves, the most important parameter is the required power in the AT, which is vastly higher than in the PT due to the broadening of the transition line profile from the high B_2. With the old Ni ring electrode, a required power of 15 nW at the ions position was estimated, which increases with the new CoFe ring by about a factor of 3 [96]. In this experiment, the D band microwaves are produced via frequency multiplication of an input 9.17-14.17 GHz signal by a factor of 12. The signal generator is a Rohde & Schwarz, model SMB100A, and it is connected via a coaxial cable to a two-state frequency multiplier/amplifier from Virginia Diodes, model WR6.5SGX, which outputs the D band microwaves with a typical output power of 8 dBm at a WR6 rectangular waveguide connector. The multiplier output signal is guided with a section of WR6 waveguides to a microwave antenna horn at the top viewport of the experiment stack, compare Figure 4.2. The microwaves travel a distance of about 3 cm through the window and free space and are picked up by a stainless steel pipe with 8 mm diameter acting as an oversized waveguide. The advantages of the oversized waveguide are the reduced losses compared to the WR6 waveguide and the ability to also guide the cooling laser through it. The disadvantages of oversized waveguides are mostly reflections and mode conversion at non-uniformities of the waveguide. The microwaves are guided through a uniform 1.5 m long oversized waveguide section to the top of the trap chamber, where they are picked up with a horn antenna electrode at the top of the trap tower, compare Figure 4.3.

$^9Be^+$ can be laser (Doppler) cooled via the transition $^2S_{1/2} \rightarrow {}^2P_{3/2}$ at $\sim$ 313 nm [117]. Here, the ultraviolet (UV) 313 nm beam is produced by a Toptica TA-FHG pro frequency quadrupled diode laser and needs to be guided centrally through the oversized waveguide. Additionally, the green Nd:YAG laser at 532 nm needs to be guided off-center into the trap chamber. As this experiment has access only from the top, compare Figure 4.1, the alignment of the lasers is challenging. As explained in ref. [116], the alignment of the UV beam is done via a first *rough* alignment to the experiment axis by use of a beam splitter and fluorescence plates inside the top of the experiment. A silicon photomultiplier (SiPM) is mounted below the 1 mm diameter window of the trap chamber and its signal is subsequently maximized for a more fine-tuned alignment. The green laser is aligned relative to the UV laser on the outside of the experiment on a long beam path. In practice, the alignment worked quite well but needed a couple of hours of trial and error until the UV laser was aligned properly. The alignment of the green laser was then typically no issue and laser ablation worked right away.

4.5. Detection systems

The detection technique for the ion motion described in Section 2.5 requires high-Q resonators that pick up the image current signal. The Q-value is defined via the 3 dB width Γ_R of the

resonator

$$Q \equiv \frac{\omega_R}{\Gamma_R} = \frac{R}{\omega_R L} = \omega_R RC. \tag{4.4}$$

The dimensionless Q-value in an RLC parallel circuit is the fraction of total energy to the energy lost per oscillation period of the electric signal in the resonator [118]. Through the parallel resistance R, it is directly connected to the width of the detected dip, which is the cooling time constant γ defined in Eq. (2.45). To be able to detect the axial frequency via the dip technique in a reasonable time, compare Eq. (2.51), the dip width γ should be $\gamma/2/\pi \gtrapprox 0.5$ Hz. For the typically low charge states and axial frequencies in the hundred of kHz regime, large Q-values above 1000 are required.

To this end, superconducting niob-titanium (Nb-Ti) coils are connected to the trap electrodes. The effective parallel capacitance comes mostly from the self-capacitance of the coil, the trap electrodes capacitance to ground, and the trap chamber feedthrough, compare ref. [119]. Understanding sources that influence the Q-value of the resonator is challenging, as effectively any kind of losses in the resonator will lower this value. Important effects include losses in the non-superconducting parts of the resonator, dielectric losses in the coil core, the non-ideal AC superconductivity, and flux creep leading to finite resistance in magnetic fields [120–122].

Here, the resonators are wound with 0.075 mm formvar-insulated Nb-Ti wire around a toroidal PTFE core. The superconducting coils are placed below the trap chamber inside a separate housing called the resonator chamber. There, one end of the resonator is connected to ground, while the other end is connected to the electrode. The connections to the electrodes are made with copper wire and a special, low dielectric loss sapphire feedthrough on the trap chamber feedthrough flange. For detection of the resonator signal, a connecting wire that leads to a cryogenic amplifier is soldered to the coil after a number of turns as seen from the electrode. The fraction of turns after the connection to the total windings of the coil defines a coupling factor. Typically, the amplifier will have a negative influence on the Q-value of the resonator. At the expense of detection signal amplitude, a lower coupling factor can be chosen to reduce this influence [123]. The relevant measured parameters of the three resonators are listed in Table 4.2.

For more details on the design of the detection electronics of this experiment, see refs. [11, 119].

Table 4.2: Approximate measured parameters of the resonators for the individual traps.

	AT	PT	CT
$\omega_R/2\pi$/kHz	798	484	470
Q	3000	6600	2700
L/mH	1.5	3.5	3.5

4.6. Wiring, filtering, and devices

The wiring, filtering, and the devices did not significantly change from the experimental setup described in ref. [97]. A short overview is given here, for more details and a wiring diagram see ref. [97].

Electrode biasing

To bias the electrodes, ultra-stable low-noise Stahl electronics UM-14-LN voltage supplies are used. They have three main channels labeled (A, B, C) and three primed main channels labeled (A', B', C'). Here, the ultra-stable main channels of the UM-14-LN are used for biasing the ring and correction electrodes, while the less stable and precise add-on channels are used for endcaps and transport electrodes. While the ion is in one of the traps, all electrodes connected to the add-on channels are switched to ground with relay switches in the room temperature section of the experiment[4].

A major source of fluctuations in the output voltage of the UM-14-LN can be ambient temperature fluctuations. To reduce these dependencies, the UM-14-LN should in principle be operated at a temperature around 25 °C, where the temperature coefficient of the output voltage is minimal [124]. Here, we place the three UM-14-LN inside a copper housing on top of the experiment to reduce the temperature fluctuations.

The electrode bias lines are filtered at three stages via RC low-pass filters. For the add-on channels, 4.7 nF capacitors and 820 kΩ resistors are used, while for the main channels 22 nF and the same resistors are used. This leads to time constants of about 3 ms and 18 ms of the filter, respectively. The first filter stage is directly below the voltage supply housing at room temperature. From there, the bias lines are connected to the experiment via a flange with three Sub-D 37 pins connectors. Three multi-wire cables (Manganin Cryoloom from CMR-Direct), connect the bias to the second filter stage, compare Figure 4.2, where identical parts are used. Another identical filtering occurs at the last filter stage, called the 4 K board, below the trap chamber. Inside the trap chamber, the DC connections are made with isolated copper cables.

Excitation lines

The motional excitations and coupling of the ion are produced with Agilent/Keysight 33600A Series Trueform Waveform Generators. Flexible coaxial cables at room temperature connect to coaxial feedthroughs into the experiment. Inside the experiment, cryo-optimized coaxial cables from GVL Cryoengeneering (GVLZ189) are used. These lead all the way to the 4 K board, where capacitive voltage dividers with 18 pF and 180 pF divide the amplitudes by a factor of 10 in order to suppress noise components.

For the low-frequency spin-transitions, the signal is generated with the Rohde & Schwarz SMB100A. To efficiently transmit the few GHz signals to the spin-flip coils, thin semirigid coaxial cables are used inside the experiment (CryoCoax 0.86mm Beryllium Copper), as the flexible cryo-coaxial cables have quite high losses at these frequencies. These signals are not filtered at the 4 K board.

[4] In fact, this is crucial for the endcaps, as the add-on channels seem to fluctuate even if set to zero volts.

All excitation lines are referenced to a GPS locked SRS FS725 rubidium standard.

Detection lines

The cryogenic axial resonator amplifiers each need four DC connections, i.e. for three transistor gates and one transistor drain. The bias lines for the gates are filtered identically to the electrode bias lines, while the biasing lines of the drains are filtered with 50 Ω resistors instead of the 820 kΩ ones. From the cryogenic axial resonator amplifiers, coaxial cables lead to the room-temperature coaxial flange. At room temperature, the signals are again amplified via Minicircuits ZFL low-noise amplifiers. The detection signals are then downmixed by several hundred kHz to frequencies in the audio regime. This is advantageous as the signal-to-noise ratio of the available analog to digital converters in the audio regime is typically superior. Here, the downmixed signals are detected with a National Instruments CompactDAQ (cDAQ) system with two NI-9250 modules. The NI-9250 modules have a 24 bit resolution and a sampling rate of 102400 Hz. The downmixers and the NI-9250 are locked to the rubidium standard as well.

Chapter 5.

Methods

With the introduction of phase-sensitive detection methods at our experiment during the course of my Ph.D. work, the statistical precision of the cyclotron frequency measurements was improved drastically compared to ref. [97]. In addition to the improved statistical precision, systematic effects needed to be understood better. To this end, new and robust methods to optimize and characterize the new 7-pole trap were implemented.

In this chapter, the experimental realization and evaluations of most of the general Penning-trap methods will be discussed. I will first give an overview of the processing of the detection signal in conjunction with the experimental control and basic ion work and loading and preparation of single ions. This is followed by an introduction to several statistical methods necessary to analyze the acquired experimental data. The dip and phase-sensitive detection methods are discussed next. Thereafter, the characterization and optimization of the analysis and precision trap are explained in detail. It must be noted that these methods were not developed in the order presented here, but rather developed and improved as the measurement campaign progressed. Here, I will give example evaluations of the methods used for different parts of the measurement. In the subsequent chapters, I will point out the methods and optimizations used for the individual measurements and discuss additional specific methods for the Zeeman and hyperfine splitting measurements.

5.1. Detection signal, experimental control and basic ion work

For the purpose of dip and non-thermal ion peak detection, the downmixed axial resonator signal needs to be Fourier transformed to a frequency spectrum, compare Section 2.5. To efficiently observe the ion's response to experimental changes, a computer program which continuously performs Fast Fourier transforms (FFT) of the signal was written in C++. It uses Welch's method to average the data and overlapping to increase the update rate [125]. The time signal length used for a single Fourier transform T_{FFT} defines the frequency bin width $\Delta f = 1/T_{\mathrm{FFT}}$ and the sampling rate f_s the maximum frequency $f_{\mathrm{max}} = f_s/2$ of the FFT. When recording dip signals, Δf is chosen to be at least a factor of 5 smaller than the dip width $\gamma_z/2\pi$. The averaging of the spectrum with a total time T_{avg} is typically done to increase the signal-to-noise ratio of

the detected ion signal.

The experiment is operated via a control system written in Python code. The Python code abstracts the individual traps as objects and the laboratory devices are accessed via high-level methods on these objects. A graphical user interface (GUI) displays the FFTs, all applied electrode voltages and the currently running signal generators. The direct control of the devices and running of measurement routines is done from the command line. For an example view of the GUI, see Figure 5.1.

During the first steps of commissioning the experiment, or working with a new ion species, the experimental work is a back-and-forth of user commands to the control system and direct user analysis of the detection signal. We call this part *ion work*.

Setting the trap potential

The trapping potential is set via the ring voltage U_0 and the tuning ratio TR, or in the case of the 7-pole trap, the two tuning ratios TR_1 and TR_2. The first starting point for setting the potential is to calculate the required U_0 to bring the ion into resonance with the resonator, compare Table 4.2, via Eq. (2.3) and the nominal C_2/U_0 value of the trap from Table 4.1. For example, using $q/m = 1/3\ e/m_u$ and the PT's $C_2/U_0 = -23257$ and $\omega_R/2\pi = 484$ kHz, the required voltage is $U_0 \approx -6.182$ V. Setting the PT potential with the Python control system is done via the command **pt.set_trap(-6.182, (0.964, 0.815))**.

Using excitations and couplings

The rough knowledge of the magnetic field inside the traps also allows to calculate the magnetron frequency, compare Eq. (2.4), sufficiently precise to do magnetron cooling via the upper sideband $\omega_z + \omega_-$. For a magnetic field of $B_{0,\mathrm{PT}} = 5.72$ T and $q/m = 1/3\ e/m_u$, the magnetron frequency is $\omega_-/2\pi \approx 4001.0$ Hz. The command to turn on the coupling continuously is e.g. **pt.exc_on("QUAD", -30, 484e3 + 4001.0)**. The first argument is an identifier for the quadrupolar excitation via the split electrode and the second argument is the excitation power in units of dBm.

For the purpose of dipolar excitations of the motional modes, typically fixed pulses and not continuous excitations are used. This is done e.g. by the command **pt.sinus_burst("QUAD", -30, 4001.0, 1000)**, where the last argument is the number of cycles.

Other typical ion work examples include the use of parametric excitation, compare ref. [76]. The parametric excitation at frequency $\omega_{\mathrm{RF}} \approx 2\omega_z$ locks the ion's axial frequency to half the excitation frequency. Compared to direct axial excitation at ω_z this has the advantage that the excitation signal itself is not present on the detection signal. If this excitation is turned on close to twice the resonator frequency and a peak signal is observed, it is thus a clear indicator that ions are present. Figure 5.2 shows an example signal obtained with parametric excitation.

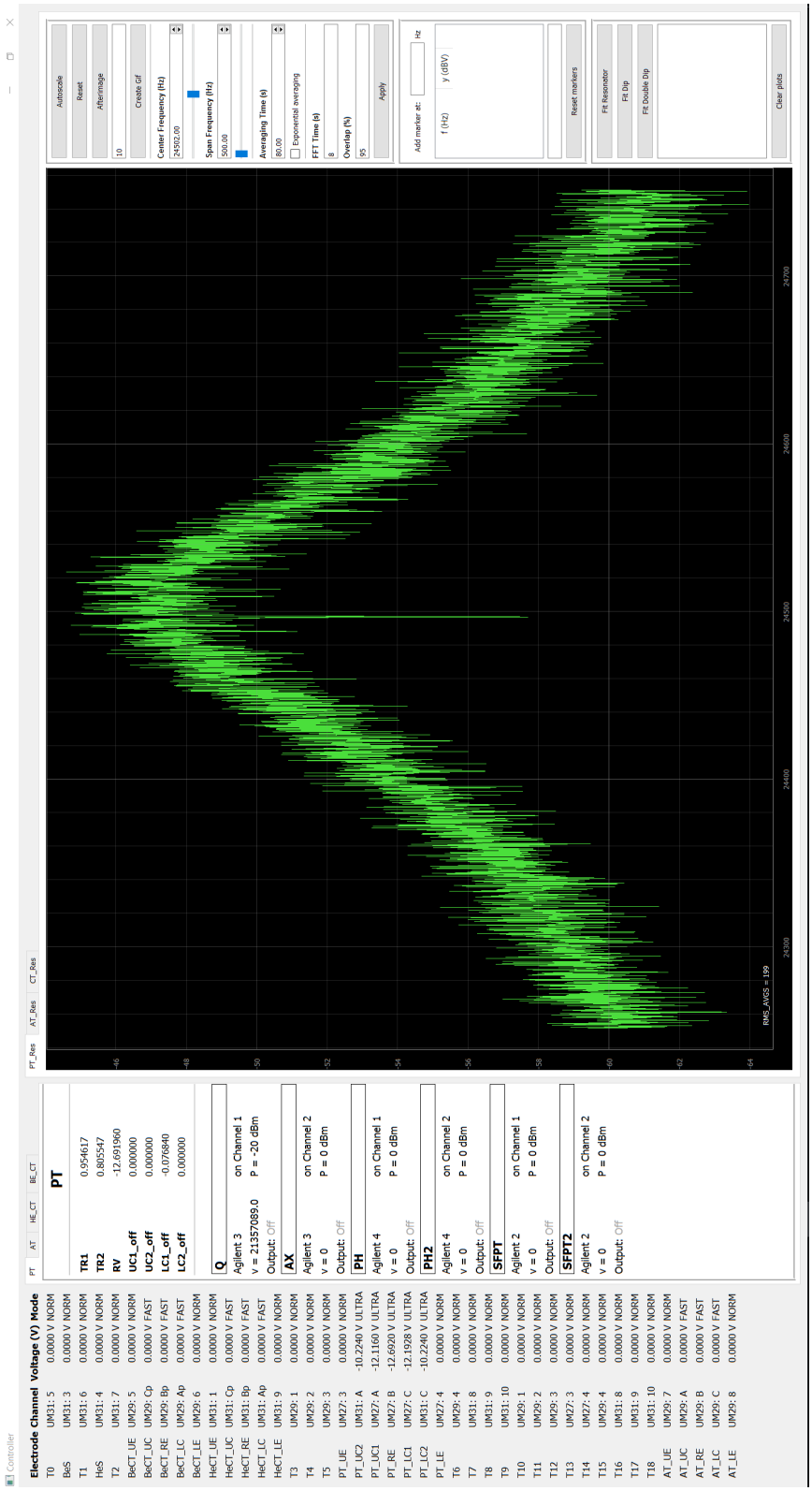

Figure 5.1: The GUI of the control system with a typical resonator and ion dip signal.

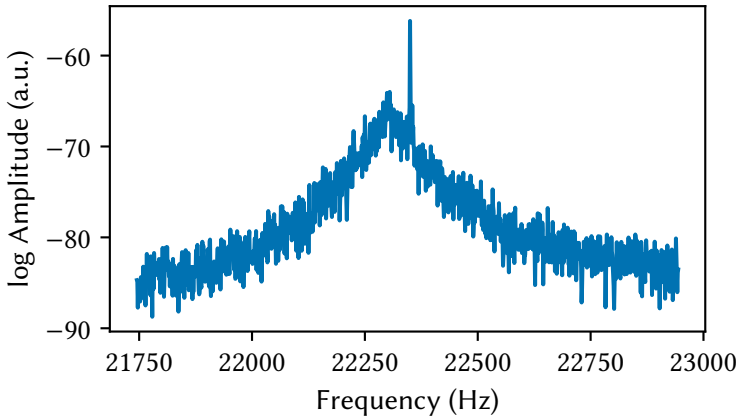

Figure 5.2: A parametric excitation peak. The x-axis is the downmixed frequency. The peak appears exactly at $\omega_{\mathrm{RF}}/2$ indicating that the ion's natural axial frequency is close.

5.2. Ion loading and preparation

As the loading of ^{3}He ions had already been done and worked reliably, as described in ref. [97], the very initial characterizations of the new traps in this campaign were also performed with $^3He^+$. Loading of $^3He^+$ directly into the PT worked with the following steps:

1. The PT is set to the theoretical tuning ratio and expected voltage to bring $^3He^+$ into (or close to) resonance.
2. The ^{3}He glass sphere is heated with $\sim$ 1 W of power.
3. Simultaneously, an electron beam is produced with the FEP by applying -100 volt at the FEP electrode and 1.7 kV on the HV electrode.
4. Both the heating and the beam are turned on for a maximum of 60 s.
5. Ideally, a hot (axial) ion signal can be observed in this timeframe and the FEP and heater are turned off before a second atom is ionized.

The hot ion signal stems from the axial energy deposited onto the resonator, but it typically chirps over the resonator and quickly disappears. In the still inhomogeneous trap, ω_z depends strongly on the motional radii and after the ion deposits energy into the resonator its frequency changes. The magnetron cooling sideband is turned on at $\omega_R + \omega_-$ and the voltage is varied in order to change to ion's axial frequency. If the ion's axial frequency is brought into resonance, $\omega_z \approx \omega_R$, the typically large magnetron energy is transferred to the axial mode and a *cooling peak* appears on the resonator. As ρ_- decreases, the axial frequency has to be adjusted until the magnetron mode is fully thermalized. In the case of $^3He^+$, this approach was sufficient to produce a dip signal of a single ion thereafter, see Figure 5.3.

Loading $^9Be^{3+}$ proved to be more challenging. The process started with loading $^9Be^+$ into the trap via laser ablation. First, the lasers were adjusted into the trap, see the previous chapter. While gradually increasing the power of the Nd:YAG pulses, the resonator detection signal was observed after every single pulse. Ion signals were observed abruptly at a large enough pulse power. This happens because the laser ablation requires a certain threshold power [115], and it seems that after this threshold is crossed, the number of trapped ions in this experiment is very large. The ablation produced $^9Be^+$ and $^9Be^{2+}$, but no $^9Be^{3+}$ was observed. This may simply be due to the much higher ionization energy of $^9Be^{3+}$ and no $^9Be^{3+}$ being produced in the ablation. Another possibility might be that the produced $^9Be^{3+}$ recombining with $^9Be^+$ inside the plasma to form two $^9Be^{2+}$ ions, as this is energetically more favorable. First attempts to subsequently ionize the trapped lower charge states with the FEP were not successful. It was suspected that either the maximally produced electron current of $\sim$ 100 nA was too small in combination with the lower ionization cross-section for $^9Be^{3+}$ or the trapped ^{9}Be ions' orbits and the electron beam simply had no overlap. To increase both the electron current and the overlap with the ions' orbits, the electron beam was reflected by applying a voltage equal to the FEP voltage to an electrode at the top of the trap tower. Reflecting the electron beam directly increases the current density and also leads to the build up of space charge which further broadens the beam [126]. Production of $^9Be^{3+}$ then followed these steps

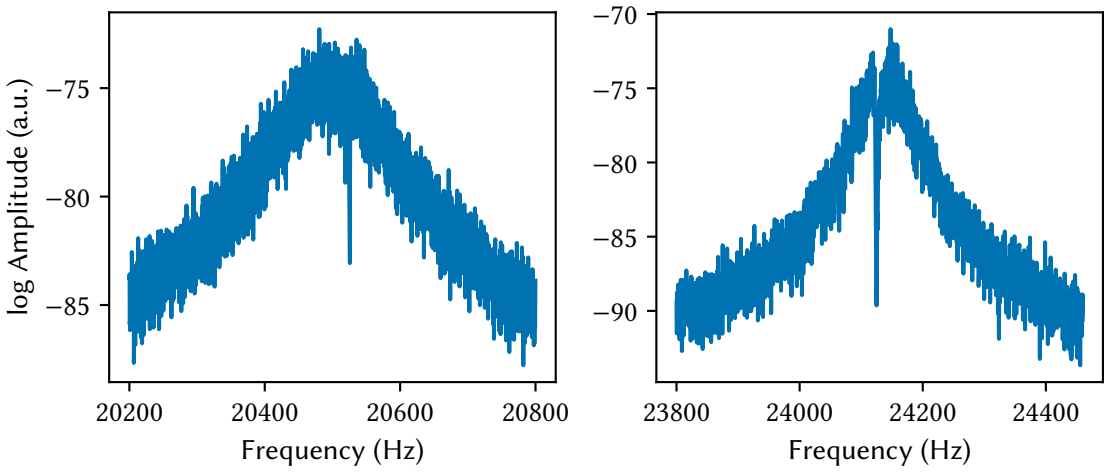

Figure 5.3: Dip signals after ion loading and initial preparation. The left-hand side shows a $^{3}He^{+}$ and the right-hand side a $^{9}Be^{3+}$ dip in the PT. The slightly different looking resonator background signal stem from changes to the downmix frequency and cryogenic amplifiers.

1. The PT was set as low as possible, i.e. −14 V on the ring electrode.
2. A cloud of $^{9}Be^{+}$ ions is produced via laser ablation.
3. The PT is set to the same parameters previously found for $^{3}He^{+}$ as it has the same q/m as $^{9}Be^{3+}$.
4. The FEP electrode is set to −250 V and the HV electrode to 1.8 kV.
5. The reflection electrode is set to −250 V for a couple of seconds.
6. A huge ion signal is observed.

This immediately produced a huge signal, which turned out to not only include $^{9}Be^{3+}$, but also $^{12}C^{4+}$ ions. Other charge states and protons were also observed at the respective ring voltages. Potentially, the widened electron beam removed and ionized contaminants from the surfaces inside the trap tower to produce these ions. Contaminant ions at different q/m were removed by keeping $^{9}Be^{3+}$ resonant and applying direct excitations at the predicted axial frequency of the other observed q/m ion species. Subsequently, the potential is made shallow for a short amount of time by putting U_0 close to zero. We call this a *'drop'* and typically do it for a few seconds to potentials of up to a few tens of negative mV. To remove the $^{12}C^{4+}$ ions, which are at the same q/m ratio, the method of SWIFT clean was used, see ref. [127]. A broadband excitation with a narrow *notch* directly around the resonator separately excites the just off-resonant $^{12}C^{4+}$ ions while excluding the $^{9}Be^{3+}$. Another subsequent drop removes some or all the ions. Removing the $^{12}C^{4+}$ required high amplitudes of the SWIFT and very shallow drops. Several attempts were needed, as the last step led to complete loss of all ions for the first few tries. Getting rid of all the contaminant ions and having only a single $^{9}Be^{3+}$ left was done only once, as the single prepared $^{9}Be^{3+}$ was actually stored for the whole measurement campaign.

5.3. Statistical methods

Often, the main goal of measurements in experimental physics is to infer the parameters of underlying theories. Specifically, in this experiment, the measurement of transitions of the Zeeman and hyperfine structure is used to infer the three independent parameters in the Breit-Rabi equation, compare Eq. (3.9). To give accurate values and meaningful uncertainties of these parameters, robust statistical methods are needed.

In this section, I will introduce a number of statistical methods needed for the evaluation of the optimization and characterization measurements, as well as the final resonance measurement.

5.3.1. Parameter inference

In statistics and probability theory, the most crucial part is, in my experience, asking the right questions. In the case of inferring the parameters of a model describing a set of measurements, the question is: Given the model, which set of its parameters would lead to observations most closely resembling the measurements? To answer this question, the model probability $P(\vec{y} \mid \vec{p})$ to observe a single measurement of a vector $\vec{y}$ given the set of parameters $\vec{p}$ needs to be calculated for the whole set of measurements $\{\vec{y}_i\}$. Assuming that individual measurements $\vec{y}_i$ are independent, the total probability of observing the measurements given the model and its parameters can be calculated via

$$\mathcal{L}(\vec{p}) \equiv P(\{\vec{y}_i\} \mid \vec{p}) = \prod_i P(\vec{y}_i \mid \vec{p}). \tag{5.1}$$

The function $\mathcal{L}(\vec{p})$ is called the likelihood function. The question is then answered by maximizing the likelihood, i.e. finding the set of parameters $\vec{p}_0$, which makes the measured data most likely to be observed given the model. This method is called maximum likelihood estimation (MLE). Equivalently to maximizing the likelihood, typically the negative log-likelihood is minimized.

The likelihood is related to the probability of the parameters via Bayes theorem [128]

$$P(\vec{p} \mid \{\vec{y}_i\}) = \frac{\mathcal{L}(\vec{p})P(\vec{p})}{P(\{\vec{y}_i\})}. \tag{5.2}$$

In the context of Bayesian statistics, the left-hand side is called the posterior probability, $P(\vec{p})$ the prior probability, and $P(\{\vec{y}_i\})$ the evidence. The probability density of the evidence $P(\{\vec{y}_i\})$ can typically not be calculated, but as it does not depend on the sought-after parameters $\vec{p}$ it is constant. For MLE, the prior distribution of the parameter is typically assumed to be uniform and is thus also constant. The $1-\sigma$ confidences of the parameters can be calculated by finding equipotential surfaces where $\mathcal{L}(\vec{p}) = 0.5\mathcal{L}(\vec{p}_0)$, see e.g. the ROOT MINUIT library [129]. A computationally much cheaper approach is to assume asymptotic normality of the likelihood and compute the covariance via the inverse Hessian matrix H of the log-likelihood [130]

$$\mathrm{cov}(\vec{p}_0) = (-H(\log \mathcal{L}))^{-1}, \quad H_{ij}(\log \mathcal{L}) = \frac{\partial^2 \log \mathcal{L}}{\partial p_i \partial p_j}(\vec{p}_0). \tag{5.3}$$

Maximum likelihood estimation and the calculation of the covariance matrix are typically done via numerical minimization and differentiation techniques.

Another approach to parameter inference is to directly sample from the unknown distribution of the parameters described by the unknown probability $P(\vec{p} \mid \{\vec{y}_i\})$, e.g.

$$\{\vec{p}_j\} \sim \Omega, \tag{5.4}$$

where Ω is the posterior probability distribution and the tilde ($\sim$) denotes *is sampled from*. Markov chain Monte Carlo (MCMC) methods can sample from the posterior distribution given a function proportional to the posterior probability density $P(\vec{p}\,|\,\{\vec{y}_i\})$ [131], e.g. the likelihood, compare Eq. (5.2). Given that the MCMC sampler has converged to the target distribution, it is straightforward to form mean values $\langle p_i \rangle$, variances and covariances $\mathrm{cov}(\vec{p}_0)$ from a sufficient number of N produced samples:

$$\begin{aligned} \langle p_i \rangle &= \frac{1}{N} \sum_{k=1}^{N} p_{i,k} \\ \mathrm{cov}(\vec{p})_{i,j} &= \langle p_i p_j \rangle - \langle p_i \rangle \langle p_j \rangle \end{aligned} \tag{5.5}$$

To account for asymmetric error intervals due to asymmetric posterior distributions, quantiles $p_{i,q}$ can be calculated from the samples. The quantile $p_{i,q}$ is the first sample value which is larger than $N \cdot q$ of the N parameter samples $\{p_{i,j}\}$. Confidence bands are calculated via the quantiles of the function values, i.e. for a function $f(\vec{x}, \vec{p})$ quantiles of the set $\{f(\vec{x}, \vec{p}_i)\}$ are used. Here, the 0.16, 0.5 and 0.84 quantiles corresponding to a $1 - \sigma$ interval of a normal distribution are used for all plotted confidence bands.

For low statistics measurements, the likelihood can be quite noisy. In this case, the statistic nature of the MCMC sampling can work much more robustly than the deterministic MLE approach. Additionally, while the use of a uniform prior probability $P(\vec{p})$ in an MLE approach to define broad parameter bounds works, bounds very close to the best fit parameters can lead to problems with the confidences, see e.g. the ion temperature measurement method in this chapter.

5.3.2. Probabilistic programming model

In this work, an analysis toolkit written in the Julia programming language and based on the probabilistic programming framework Turing.jl, see ref. [132], is used to solve many of the inference problems. Given a description of the model involving the computation of the probability $P(\vec{y}_i \mid \vec{p})$ for the measurement data, it can infer best-fit parameters and covariances by both MLE and MCMC sampling.

In the following, the framework is explained using the example of linear extrapolation of data. Consider a varied parameter x and measured parameter y with uncertainty σ_y. The data is described by the relation $y = ax + y_0$ and the objective is to find y_0, which is not measurable because $x = 0$ can experimentally not be chosen. The model definition is done with the following code:

```
@model function extrapolation(x⃗, y⃗, σ⃗_y, bounds)
```

```
    a ~ Uniform(bounds[1][1], bounds[1][2])
    y₀ ~ Uniform(bounds[2][1], bounds[2][2])

    ȳpredict = a x⃗ .+ y₀
    @. ȳ ~ Normal(ȳpredict, σ⃗y)
end
```

The first two lines in the model definition are the prior distributions of the model parameters a and y_0. For this problem they are assumed to be uniform distributions to account for fit bounds. Next, the predictions given the two model parameters and the x-values are computed. The measured values y are assumed to be normally distributed around the prediction[1]. The last line in the model defines the likelihood of the problem. Figure 5.4 shows an example dataset

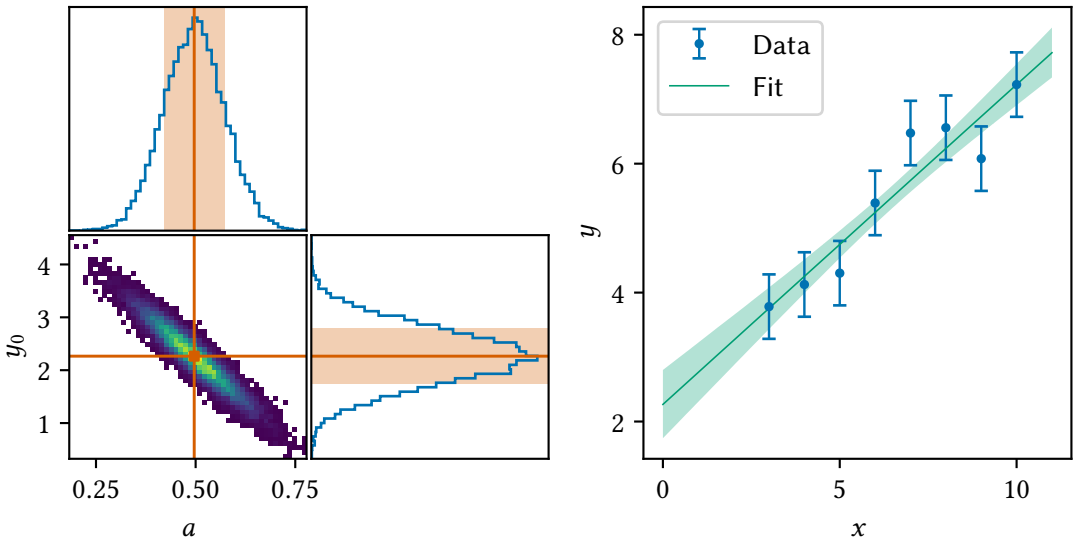

Figure 5.4: Example use of MCMC for linear extrapolation. The left-hand side shows histograms of the sampled parameters a and y_0 of the model. The $1-\sigma$ intervals of a and y_0 are indicated by the orange line and band, respectively. The right-hand side shows the data, the mean, and confidences of the fit.

that has truth values of $a = 0.5$ and $y_0 = 2.0$ and is fit with the above extrapolation model using MCMC sampling of the posterior distribution. The 0.5 quantile is used as the best fit value and the 0.18 and 0.84 quantile are used to give confidence intervals of the parameters. The 2-d histogram nicely shows the correlation between the two fit parameters a and y_0.

5.4. Dip detection

For the thermal dip detection technique, the detection signal is recorded after a sufficiently long cooling time of the ion in resonance with the detector. The sought-after axial frequency

[1]Here, the `@.` macro is used for element wise computation of the code.

ω_z, or in the case of a double dip $\omega_{z,1}$ and $\omega_{z,2}$, of the ion are determined from a non-linear least squares fit of the theoretical lineshape to the calculated spectrum. Generally, the fit function may be written as

$$f_{\text{fit}}(\omega \mid \vec{p}_{\text{tf}}, \vec{p}_{\text{dip}}) = f_{\text{tf}}(f_{\text{dip}}(\omega \mid \vec{p}_{\text{dip}}), \omega \mid \vec{p}_{\text{tf}}), \tag{5.6}$$

where f_{tf} together with $\vec{p}_{\text{tf}}$ transforms the detection signal described by the dip lineshape f_{dip} with parameters $\vec{p}_{\text{dip}}$.

The transfer function f_{tf}, in the simplest case, adds the white noise background of the input noise of the cryogenic amplifier, compare Section A.5.1, and transforms the signal to decibel units. Additionally, the amplification of the signal may include a non-uniform, in first-order linear dependence on the frequency. In total, this gives

$$f_{\text{tf}}(y(\omega), \omega \mid a_0, a_1, a_2) = 10 \log_{10}(a_0 + a_1 y(\omega) + a_2 \omega y(\omega)). \tag{5.7}$$

For the fit of the axial frequency ω_z, the parameters in $\vec{p}_{\text{dip}}$ and $\vec{p}_{\text{tf}}$ need to be either included in the fit or fixed beforehand. Here, the final fit of ω_z is performed after a number of preparatory steps.

1. First, a fit of the detection signal with the resonator lineshape, Eq. (2.53), is performed which gives first values for ω_R, Γ_R and $\vec{p}_{\text{tf}}$

2. Using the resonator lineshape and the previously determined parameters, a residual with the spectrum is calculated. From the residual, a rough dip location is determined simply by peak detection.

3. A span of a couple of dip widths γ_z is cut out around the rough dip location and a second fit of the resonator lineshape is performed to get better values for ω_R, Γ_R and $\vec{p}_{\text{tf}}$. This fit is performed inside a frequency span a couple of multiples of Γ_R.

4. Lastly, the dip parameters are fit with the dip lineshape while leaving the previously fit parameters fixed. This fit is performed inside a frequency span a couple of multiples of γ_z around the dip.

Figure 5.5 visualizes the steps. The procedure for fitting a double dip spectrum is very similar and only differs in that the two dips are cut out of the spectrum in the third step.

For the characterization of field imperfections or the detection of spin state changes in the AT via the continuous Stern-Gerlach effect, the measurement of the dip frequencies does not need to be highly accurate. In this case, it is sufficient to use the ideal dip or double dip signal, Eq. (2.51) and Eq. (2.70), and the transfer function Eq. (5.7) for fitting the frequencies. In contrast, for the high-precision measurements of the axial frequency ω_z and ω_+ via the double dip in the PT, the correct description of the detected dip signal is crucial. As the estimation of systematic shifts and uncertainties due to the dip signal lineshape is different for the double dip and phase-sensitive cyclotron frequency measurements, they will be discussed individually in the next chapters.

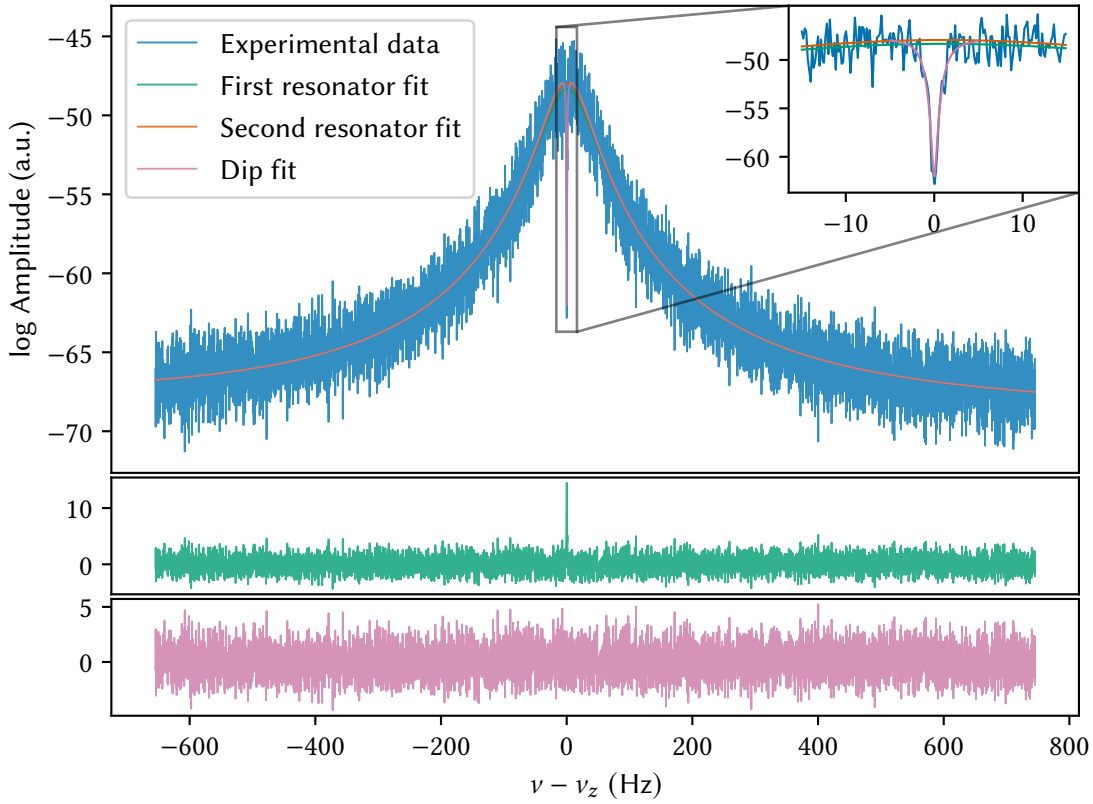

Figure 5.5: Dip fitting procedure. The top graph shows the various fits performed on the spectrum. Below the difference of the first resonator fit and the experimental data is plotted. The bottom shows the difference of the final dip fit and the experimental data. For details see text.

5.5. Phase methods

The phase-sensitive detection sequences are summarized in Eq. (2.78) and Figures 2.7 and 2.8. Experimentally, the sequences are implemented with the setup shown in Figure 5.6. All involved devices are frequency-locked via the 10 MHz outputs of the rubidium clock (SRS FS725). The trigger generator (SRS DG645) generates two TTL trigger pulses. First, one pulse triggers the signal generator (Agilent/Keysight 33600A) which generates the excitation and coupling pulse. The signal generator's first output directly generates the excitation pulse. Via an internal delay, the second output generates the coupling pulse after a time $T_{\text{couple}} = \Delta T_{\text{exc}} + T_{\text{evol}}$, where ΔT_{exc} is the length of the excitation pulse and T_{evol} the free evolution time. Both outputs of the signal generator are connected via a signal combiner. In this run of the experiment, the excitation line to the split electrode of the PT was broken and instead the PT spin-flip coil is used for driving radial dipole and radial quadrupole excitations. The second pulse from the DG645 at time $T_{\text{Readout}} = \Delta T_{\text{exc}} + T_{\text{evol}} + \Delta T_{\text{couple}} + \Delta T_{\text{off}}$, where ΔT_{Couple} is the length of the cou-

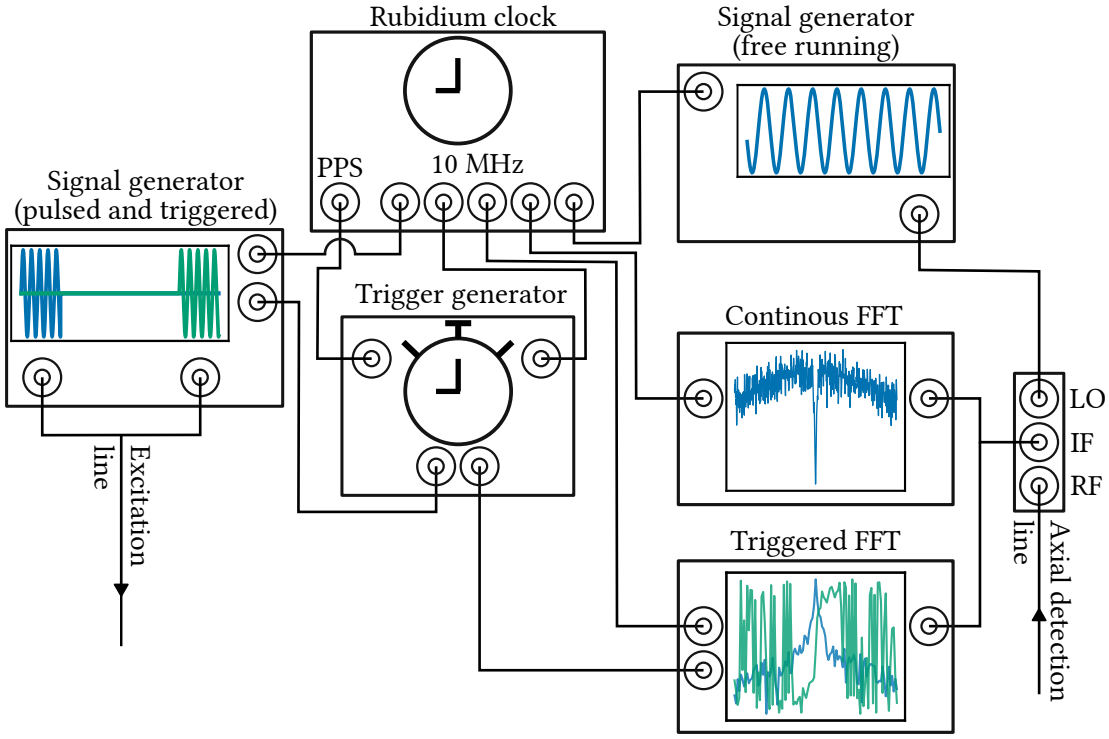

Figure 5.6: Setup used for the phase sensitive measurements. The straight lines represent the signal paths. Outputs are located at the bottom and inputs at the sides of the respective square symbols. The blue and green signal in the pulsed and triggered generator represent the excitation and coupling pulse, respectively. The blue and green signal in the triggered FFT represent the amplitude and phase of the spectrum, respectively. For details see text.

pling pulse and ΔT_{off} an additional offset, triggers the data acquisition of the FFT analyzer (SRS SR1). The offset ΔT_{off} is tuned to compensate for internal trigger delays of the FFT analyzer relative to the signal generator. The FFT phase and amplitude spectra of the hot ion signal measured by the SR1 are computed without averaging and a typical acquisition time $T_{\text{FFT}} \approx 2\pi/\gamma_z$. Because the detection signal needs to be down-mixed for the detection and thus depends on the relative phase of the local oscillator (LO), the LO would need to be triggered as well. Here, this additional trigger is circumvented by using integer Hz down-mix frequencies at the LO and starting the trigger sequence on the pulse per second (PPS) of the rubidium clock [77].

The constant phase offset $\delta\varphi_{\text{off}}$ in Eq. (2.79) is a sum of different components that occur due to several experimental reasons. For example, during the coupling pulse a free evolution phase is also acquired, compare Eq. (2.62), and due to the different internal trigger delays of the signal generator and the FFT analyzer, another offset is produced. The important requirement for $\delta\varphi_{\text{off}}$ is its independence of T_{evol} and of the final phase of the modified cyclotron motion. This independence can be experimentally verified, see the next chapters. To subtract the offset phase, a reference phase φ_{ref} with a short evolution time T_{ref}, here 0.1 s, is measured. With the definitions $\Delta\varphi = \pm(\varphi_{\text{det}} - \varphi_{\text{ref}})$, $\Delta T_{\text{evol}} = T_{\text{evol}} - T_{\text{ref}}$ and $\Delta N = N - N_{\text{ref}}$, where N_{ref} is

equivalently defined to bring φ_{ref} to the 2π range, the relation

$$\Delta\varphi = \omega_+ \Delta T_{\text{evol}} - 2\pi\Delta N \tag{5.8}$$

can be used to infer the cyclotron frequency, if the integer number ΔN is known.

The determination of the ω_+, including the full number of revolutions ΔN, is performed by measurement of phases $\{\Delta\varphi_i\}$ for a number of evolution times $\{\Delta T_{\text{evol},i}\}$. Due to the phase measurement uncertainty $\sigma(\Delta\varphi)$, care has to be taken to not make an error in the determination of the full number of cycles. One method is to sequentially increase the precision of ω_+ at a higher evolution time by using the previously less precise value to estimate and keep track of the full number of revolutions ΔN, see ref. [133]. Similar to ref. [134], the modified cyclotron frequency can also be calculated via a regression through the measured phases at the different evolution times. To this end, the loss function

$$f(\omega_+ \mid \{\delta\varphi_i\}, \{\Delta T_{\text{evol},i}\}) = \sum_i \left[(\omega_+ \Delta T_{\text{evol},i} - \Delta\varphi_i)/(2\pi) - \lfloor(\omega_+ \Delta T_{\text{evol},i} - \Delta\varphi_i)/(2\pi)\rceil\right]^2, \tag{5.9}$$

is minimized, where $\lfloor\rceil$ rounds to the nearest integer, resulting in the terms in the sum to be in the range $(-0.5, 0.5)$. Here, the idea is to bring the predicted phases $\omega_+ \Delta T_{\text{evol},i}$ as close to the measured phases $\Delta\varphi_i$ modulo 2π, compare Eq. (5.8). Figure 5.7 illustrates the absolute ω_+

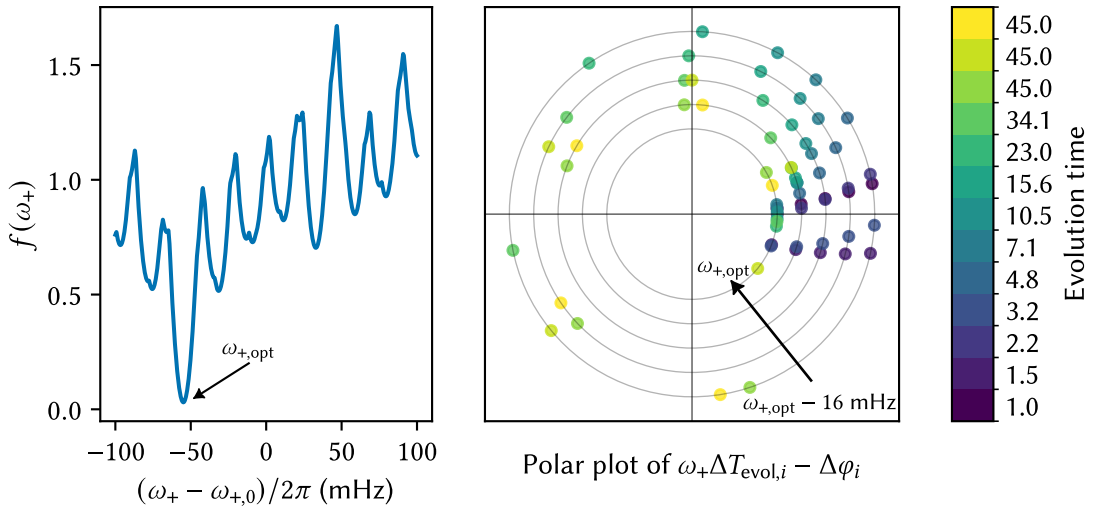

Figure 5.7: Exemplary determination of the absolute value ω_+ via regression. The left plot shows the value of the loss function around and in the range of an initial guess $\omega_{+,0}$ and its uncertainty which can be taken from e.g. a double dip measurement. A clear global minimum exists. The right plot shows polar plots of the difference of predicted absolute phase $\omega_+ \Delta T_{\text{evol},i}$ to the measured phase $\Delta\varphi_i$ for all individual evolution times and values of ω_+ (each ω_+ on an individual diameter) nearing the optimum value from the left plot. At the optimum, the differences between the predicted to the measured phases are clustered closely around zero.

determination through regression. The polar plot shows that the terms with higher evolution

time change to loss function more rapidly and thus have the most influence on the final $\omega_{+,\mathrm{opt}}$ value. In the sequential method, only the phase measured with the highest evolution time value contributes directly to ω_+ and its uncertainty, and all others just serve to determine ΔN. Here, the regression method is used in the same way[2]. From $\omega_{+,\mathrm{opt}}$ the final ΔN is determined and only the phases from the highest evolution time are used to calculate ω_+ from Eq. (5.8).

5.6. AT characterization

For the characterization of the AT, it is important to keep its purpose in mind. In the AT, the repeatable and unambiguous spin-state detection needs to be performed via the continuous Stern-Gerlach effect, compare Section 3.5. Therefore, only the detection of ω_z and resolving the changes $\delta\omega_{z,mn}$ due to a spin-state change, compare Eq. (3.43), are necessary, while the radial frequencies do not need to be detected precisely.

The main difficulties in working with the AT are due to its small size, $r_{\mathrm{AT}} = 1.8$ mm, and large nominal $B_2 \approx 282$ kT. The small size leads to large expansion coefficients C_k, compare Eq. (2.20), which in turn requires high voltage stability and very sensitive fine-tuning of the voltages to make the trap harmonic enough to detect ion signals. The large B_2 strongly shifts the ion's axial frequency depending even on thermally distributed cyclotron amplitudes, compare Eq. (2.35). The large B_2 also makes the detection and coupling to ω_+ via quadrupolar coupling impossible, as both axial and cyclotron frequency are coupled too strongly to the amplitudes. Additionally, the ferromagnetic ring electrode produces a large B_4 value. The B_4 leads to a shift $\delta\omega_z \propto B_4\rho_+^2\rho_z^2$, which compares to the shift due to C_4, $\delta\omega_z \propto C_4\rho_z^2$ [67]. The ideal tuning ratio which compensates the combined $B_4\rho_+^2$ and C_4 shift depends then on ρ_+ which is thermally distributed after a PT measurement [97].

Table 5.1: Experimentally determined parameters of $^9Be^{3+}$ in the AT. The values of ω_R, Γ_R and γ_z are formed via the mean over a dataset with 142 dip spectra. The range in U_0 corresponds to the typical spread of the ring voltage due to the thermal distribution of ρ_+ after coupling in the PT. For details see text.

$\omega_R/2\pi$	$\Gamma_R/2\pi$	U_0	TR	$\delta\nu_z/\delta U_0$	$\gamma_z/2\pi$
795.6406(6) kHz	235.6(6) Hz	(−3.398, −3.368) V	0.8885	113.8(2) Hz/mV	3.96(3) Hz

$\omega_c/2\pi$	$\omega_+/2\pi$	$\omega_-/2\pi$	B_0	B_2
25.427(2) MHz	25.414(2) MHz	12.46(1) kHz	4.9732(4) T	282.4(1) kT/m^2

Table 5.1 lists experimentally determined parameters of $^9Be^{3+}$ in the AT. The first row is determined via axial spectra, compare Figure 5.8. Additionally, the scheme to reproducibly center the ion's axial frequency on the resonator is illustrated in Figure 5.8.

[2]This helps to make both methods comparable. Additionally, having all phase values from the different evolution times contribute to ω_+ makes it much harder to argue that the magnetic field during the irradiation of the Zeeman transition is identical to the one that determines ω_+.

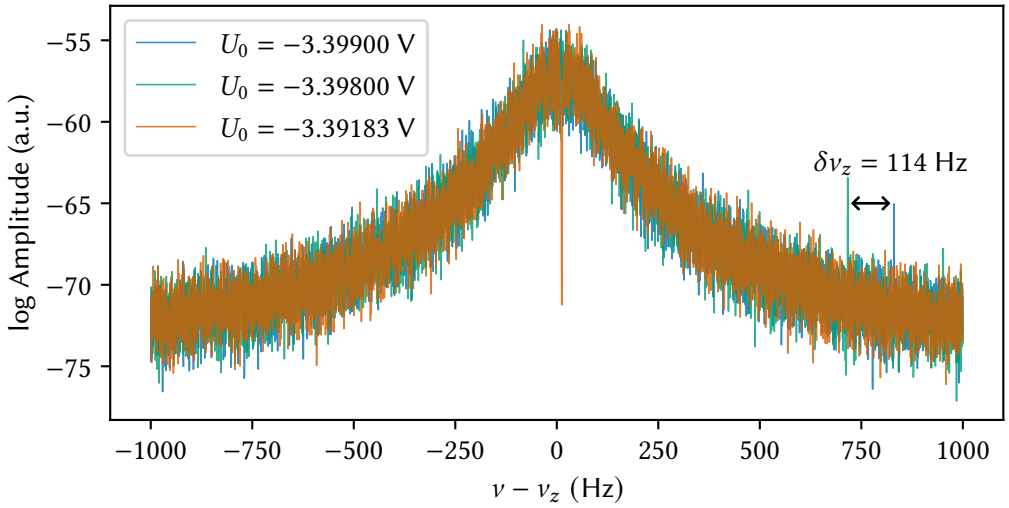

Figure 5.8: $^9Be^{3+}$ signal in the AT for different ring voltages. To bring the ion into resonance, the ring voltage is decreased in 1 mV steps. The ion signal is unambiguously identified if subsequently two peaks separated by $\delta\nu_z/\delta U_0 \approx 114$ Hz/mV appear. This allows to center the ion onto resonance $\nu_z \approx \nu_R$.

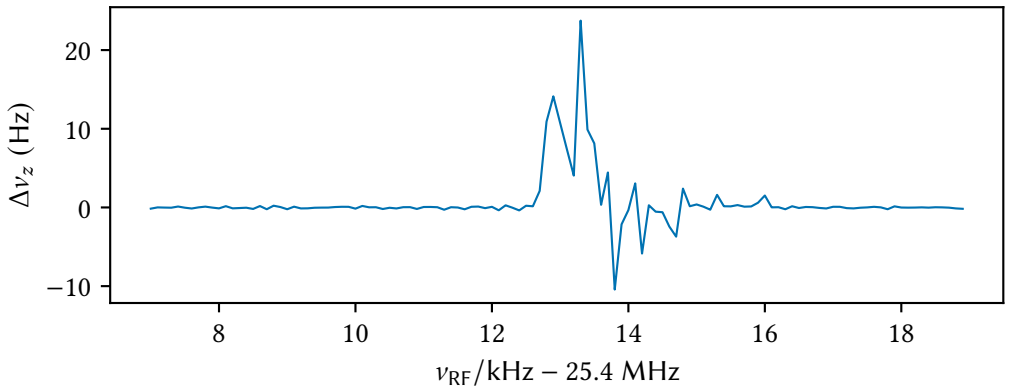

Figure 5.9: Determination of ω_+ in the AT with $^9Be^{3+}$. The data shows the change of the axial frequency after a weak dipolar excitation at frequency ν_{RF}. Close to resonance, the amplitude ρ_+ changes depending on the phase difference of excitation and motion, compare Eq. (2.58), which can lead to both positive and negative shifts of ν_z.

In order to calculate the spin transition frequencies in the AT, the magnetic field needs to be measured to a relative precision comparable to the linewidth parameter, compare Eq. (3.26). Here, this requires a precision $\sigma(B)/B \approx 10^{-4}$. While the magnetron frequency can be determined via a double-dip measurement, as described above, this is not possible for the modified cyclotron frequency. To determine ω_+, a weak direct dipolar excitation is used to excite the

motion and the shift Eq. (2.35) is detected afterwards, compare ref. [97]. Only close to resonance, $\omega_{\mathrm{RF}} \approx \omega_+$, a change of the amplitude occurs, see Figure 5.9. Using this measurement allows calculating ω_c and the magnetic field, see Table 5.1.

An experimental value of B_2 can be determined via the axial frequency changes due to the continuous Stern-Gerlach effect, compare Eq. (3.43). Using successive measurements of ω_z after changing the spin-state yields $B_2 = 282.4(1)\ \mathrm{kT/m^2}$, which is about 5 % lower than the calculated $B_2 = 298(5)\ \mathrm{kT/m^2}$ of the trap [28]. The calculated B_2 relies on the material's magnetic saturation, for which no data at 4 K exists, and a temperature dependence of 5 % seems reasonable.

5.7. PT optimization and characterization

The optimization and characterization of the PT is crucial for the high-precision measurement of the Zeeman and HFS transitions, as any errors in the determination of ω_c will propagate to the extracted parameters. In this section, the methods used to minimize or at least characterize the shifts discussed in Section 2.3 will be presented. For reference, Table 5.2 summarizes the experimental parameters of $^9\mathrm{Be}^{3+}$ in the PT. In this section, any measurement of ω_z is performed

Table 5.2: Experimentally determined parameters of $^9\mathrm{Be}^{3+}$ in the PT. The values of ω_R, Γ_R and γ_z are formed via the mean over a dataset with 142 dip spectra. The values for ω_c, ω_+ and B_0 are given without an error and 7 digits precision, as magnetic field drifts of this order of magnitude occur during the measurement campaign.

$\omega_R/2\pi$	$\Gamma_R/2\pi$	U_0	$(\mathrm{TR}_1, \mathrm{TR}_2)$	$\delta\nu_z/\delta U_0$	$\gamma_z/2\pi$
484.14549(5) kHz	78.6(9) Hz	−6.37 V	(0.95996, 0.80632)	37.8(1) Hz/mV	2.52(5) Hz

$\omega_c/2\pi$	$\omega_+/2\pi$	$\omega_-/2\pi$	B_0
29.254040 MHz	29.250034 MHz	4.0074(2) kHz	5.7218158 T

via a dip measurement with typically $T_{\mathrm{FFT}} = 6$ s and $T_{\mathrm{avg}} = 20 - 40$ s. This leads to a typical statistical uncertainty of less than $\sigma(\omega_z)/2\pi \approx 100$ mHz.

5.7.1. Trap symmetrization

The fields of the trap may be asymmetric due to e.g. machining tolerances of the electrodes and the sapphire spacers or surface contamination and patch potentials [91]. These asymmetries lead to large odd-order C_k coefficients, of which C_3 is the most problematic. In the 7-pole PT, the potential of the inner correction electrodes, being the closest to the ion, contributes the most to the symmetry of the field. Any effective (and unknown) offset δU on either the upper or lower correction electrode leads to a linear change $\delta C_2 = E_{1,2}\delta U$, compare Eq. (2.20), where $E_{1,2}$ is a parameter which is specific to the electrode, but equal for both the upper and lower, inner (1) correction electrode. Additionally, the first odd-order coefficients lead to the shift of

the zero position, compare Eq. (2.27), and an associated shift due to C_3

$$\delta C_2 = 3\delta C_3 \Delta z = -\frac{3\delta C_1 \delta C_3}{2C_2} = -\frac{3E_{1,1}E_{1,3}\delta U^2}{2C_2}, \tag{5.10}$$

where $E_{1,1}$ and $E_{1,3}$ are defined similar to $E_{1,2}$. Obviously, the asymmetric components have opposite sign for the upper and lower correction electrodes, but as they appear only as their product, the sign of the shift is equal for both cases. By asymmetrically applying an additional offset $\pm\delta U_a$ on the upper and lower correction electrode, respectively, such that the voltages of the trap are[3]

$$\vec{U} = (0, \mathrm{TR}_2 U_0, \mathrm{TR}_1 U_0 - \delta U_a, U_0, \mathrm{TR}_1 U_0 + \delta U_a + \delta U, \mathrm{TR}_2 U_0, 0) \tag{5.11}$$

this gives in total

$$\delta C_2(\delta U_a) = E_{1,2}(\delta U + \delta U_a - \delta U_a) - \frac{3E_{1,1}E_{1,3}}{2C_2}(\delta U + 2\delta U_a)^2. \tag{5.12}$$

This function is extremal at $\delta U_a = -\frac{1}{2}\delta U$, which makes the compensation of the offset via measurement of the axial frequency shifts

$$\delta\omega_z(U_a) = \omega_z \frac{\delta C_2(\delta U_a)}{2C_2} = -\omega_z \frac{3E_{1,1}E_{1,3}}{4C_2^2}(\delta U + 2\delta U_a)^2, \tag{5.13}$$

where the constant term $E_{1,2}\delta U$ was dropped, possible.

Figure 5.10 shows the result of the symmetrization in the PT and the fit of the above model. From the fit, the offset $\delta U = 86.35(8)$ mV and the product $E_{1,1}E_{1,3} = -727(9)\times10^6$ V^{-2}m^{-4}

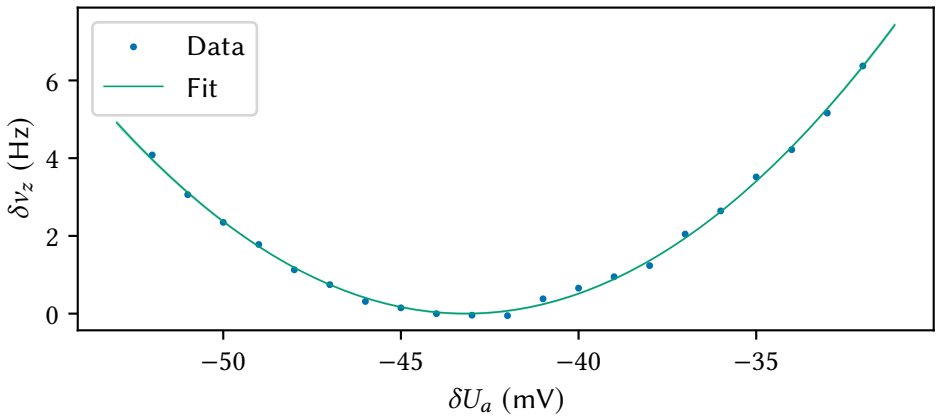

Figure 5.10: Symmetrization of the PT. The axial frequency values are taken via single axial dip measurements. For details see text.

are determined. The latter can be cross-checked with the value from trap theory $E_{1,1}E_{1,3} =$

[3] Assuming a single offset δU on either the upper or lower correction is indeed enough. Only the difference of their potential matters here, as the identical part is tuned with the tuning ratio optimization.

$-696\times10^6\ \mathrm{V^{-2}m^{-4}}$. Though the value shows disagreement with the experimental value, having a 5 % deviation for a geometrical trap parameter is not uncommon. In contrast, the measured offset is quite large and if not corrected, the resulting C_3 contributions are significant (see later), i.e. given the measured offset, the theoretical C_3/C_2 is

$$C_3/C_2 = -6.0(3)\ \mathrm{m^{-1}}, \tag{5.14}$$

where the 5 % deviation of $E_{1,1}E_{1,3}$ was applied as an error on C_3. Finally, for the compensation only a single correction offset of $-\delta U$ is applied to the upper correction electrode.

5.7.2. B_1 measurement

Though there are no direct systematic shifts due to B_1 on the determined spin transition frequencies, it is important to measure B_1 for the correct determination of other field imperfections. The measurement of B_1 is done by shifting the ion axially via an offset applied to a correction electrode and measuring the magnetic field via ω_c [135]. Offsets on a correction electrode lead to a C_1, which in turn shifts the position, compare Eq. (2.27). The magnetic field is then measured using the double-dip method.

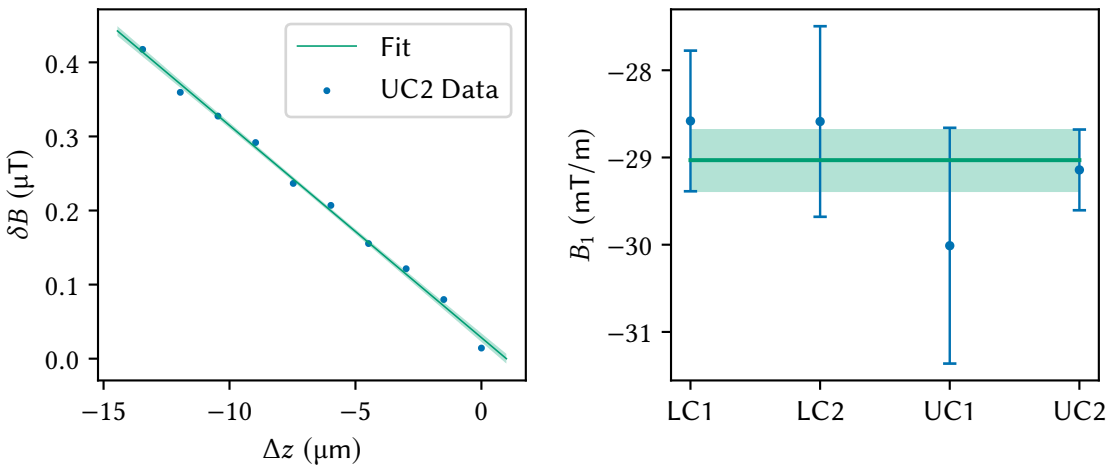

Figure 5.11: Measurement of B_1. The left plot shows the B_1 measurement exemplary using offsets on the outer upper correction electrode. The right-hand side shows the 4 individual results of B_1 measured via offsets on the individual correction electrodes. The weighted mean and its uncertainty band are plotted in green.

Figure 5.11 shows the results of the B_1 measurements. The 4 values measured by individually using all correction electrodes to shift the ion are consistent, and a weighted mean can be calculated to give

$$B_1 = -29(2)\ \mathrm{mT/m}. \tag{5.15}$$

Similar to the above arguments, additional to the statistical uncertainty, a 5 % uncertainty due to the dependence on the theoretical C_1 coefficients was included. The measured B_1 is vastly

larger than could be attributed to the superconducting magnet's inhomogeneity, which should be better than $|B_1| < 0.1\,\mathrm{mT/m}$, compare ref. [107]. A finite element calculation of the magnetic field change due to the ferromagnetic ring of the AT performed with COMSOL Multiphysics yields $B_1 =$ and fits quite well.

5.7.3. Tuning ratio optimization

The PT potential needs to be tuned to be as harmonic as possible. In particular, the first even anharmonicities C_4 and C_6 must be tuned as close to zero as possible. During the $^3He^+$ measurement, a 5-pole PT was used and only C_4 could be actively optimized [97]. For a small C_6, the design criterion $C_4(\mathrm{TR_{opt}}) = C_6(\mathrm{TR_{opt}}) = 0$ (*compensated*) of the trap needs to be fulfilled, which in practice is always broken to some degree. With the two tuning ratios of the new 7-pole PT, both C_4 and C_6 can be actively minimized, but the optimization is also more complex compared to the 5-pole trap.

The voltages of the 7 electrodes are expressed as

$$\vec{U} = (0, U_2, U_1, U_0, U_1, U_2, 0) \tag{5.16}$$

As given in Eq. (2.20), the C_k coefficients are linear in the voltages. It is helpful to write

$$C_k = E_{0,k}U_0 + E_{1,k}U_1 + E_{2,k}U_2, \quad E_{i,k} = \frac{\partial C_k}{\partial U_i}. \tag{5.17}$$

The axial frequency requirement $\omega_z \approx \omega_R$ fixes $C_2 = \frac{\omega_z^2}{2}\frac{m}{q}$ and the optimization requirement is summarized by

$$\begin{pmatrix} C_2 \\ C_4 \\ C_6 \end{pmatrix} = \begin{pmatrix} E_{0,2} & E_{1,2} & E_{2,2} \\ E_{0,4} & E_{1,4} & E_{2,4} \\ E_{0,6} & E_{1,6} & E_{2,6} \end{pmatrix} \begin{pmatrix} U_0 \\ U_1 \\ U_2 \end{pmatrix} \stackrel{!}{=} \begin{pmatrix} \frac{\omega_z^2}{2}\frac{m}{q} \\ 0 \\ 0 \end{pmatrix}. \tag{5.18}$$

If for some set of $\{U_0, U_1, U_2\}$ the condition is fulfilled and a different ion species with another q'/m' is to be brought into resonance, only the C_2 needs to be actively adjusted. By just scaling all voltages with a factor $q'/m' \cdot m/q$, this can be achieved while keeping $C_4 = C_6 = 0$. This motivates the use of ratios, e.g. setting $U_1 = \mathrm{TR}_1 U_0$ and $U_2 = \mathrm{TR}_2 U_0$. The theoretical values of these coefficients for the 7-pole PT are summarized in Table 5.3.

Table 5.3: Theoretical contributions of the individual voltages/electrodes to the C-coeffecients. While $E_{i,2}$ is similar in magnitude for all electrodes, the contribution to C_4 and C_6 are much reduced for the second and first pair of correction electrodes, respectively.

	$E_{i,2}/10^4$ $(\mathrm{m^{-2}V^{-1}})$	$E_{i,4}/10^8$ $(\mathrm{m^{-4}V^{-1}})$	$E_{i,6}/10^{12}$ $(\mathrm{m^{-6}V^{-1}})$
$i = 0$	−2.3257	24.414	−224.42
$i = 1$	−3.1231	−3.6527	242.65
$i = 2$	3.6903	−25.624	−11.491

While C_2 is effectively measured via ω_z, C_4 and C_6 are measured via the systematic shift of the axial frequency $\delta\omega_z(\rho_-)$ after an excitation of the magnetron amplitude ρ_-. While for C_4 the shift is $\delta\omega_z \propto C_4\rho_-^2$, compare Eq. (2.25), for C_6 a shift $\delta\omega_z \propto C_6\rho_-^4$ occurs [67]. By measuring the shift for different excitation amplitudes ρ_-, shifts from C_4 and C_6 can be discriminated. The final amplitude can be either tuned via the dipole pulse excitation strength, or its time, compare Eq. (2.58). Here, the excitation time in units of cycles N is used, as it is experimentally more robust compared to the excitation strength, which relies on a proper calibration of the function generator used for the dipole excitation. The polynomial

$$\delta\omega_z = aN^2 + bN^4 \tag{5.19}$$

is fit to the measured data. In order to optimize the trap, the measurement and fit of $\delta\omega_z(\rho_-)$ are performed for different tuning ratios.

For $^9Be^{3+}$, the tuning ratios found while previously working with $^3He^+$ in the same trap were used. For $^3He^+$, in turn, the initial tuning ratios were taken from theory, compare Table 4.1. The symmetrization explained in the previous section had not been performed yet. First, the combined tuning ratio TR_C was optimized. The combined tuning ratio changes both correction electrode pairs via $(TR_1', TR_2') = (TR_C TR_1, TR_C TR_2)$. The trap was designed so that TR_C does not change C_2, i.e. $TR_1 E_{1,2} + TR_2 E_{2,2} = 0$ at the optimal set of (TR_1, TR_2), which is the equivalent of the orthogonality condition of the 5-pole trap[4]. Experimentally, to keep the axial frequency centered on the resonator, the ring voltage had to be readjusted by $\delta U_0(TR_C) = 0.19(1.0 - TR_C)$ V, showing that the orthogonality is experimentally not quite given. Figure 5.12 shows the optimization of TR_C. From this optimization, the intercept $TR_{C,4} = 1.0006(1)$, where $\delta\omega_z(TR_{C,4})/N^2 = 0$, was fit using a linear regression. No statistically significant C_6 shifts were observed.

Around the new tuning ratios $(TR_1', TR_2') = (TR_{C,0} TR_1, TR_{C,0} TR_2)$, the dependence of the C-coefficients from changes of TR_2 was measured in the same way, see Figure 5.13. By only changing U_2, a very large shift of the axial frequency occurs and the retuning was done with the function $\delta U_0(\delta TR_2) = +10.4(\delta TR_2)$ V. Again, the intercept $TR_{2,4} = 0.8061(1)$, where $\delta\omega_z(TR_{2,4})/N^2 = 0$, was fit and no C_6 shifts could be observed at this level.

For TR_1, where the contribution to C_4 is much smaller, compare Table 5.3, it was decided to increase the dipole excitation pulse length to excite to higher radii. Here the readjustment of the ring voltage was performed with $\delta U_0(\delta TR_1) = -8.54\delta TR_1$ V. As seen in Figure 5.14, C_6 contributions could be resolved for this correction electrode pair. The intercept of the C_4 shift is at $TR_{1,4} = 0.96013(1)$ and the intercept of the C_6 shift is at $TR_{1,6} = 0.96001(5)$. Including shifts of order N^6 in the evaluation of the optimization of TR_1 significantly shifts the intercept of C_6 to $TR_{1,6} = 0.9591(5)$. In order to adjust both C_4 and C_6 closer to zero, TR_2 was readjusted slightly to compensate for C_4 close to $TR_{1,6}$. The final values for the tuning ratios used in (most) of the measurements are

$$(TR_1, TR_2) = (0.95996, 0.80632). \tag{5.20}$$

In the case of the initial optimization of the tuning ratios done with $^3He^+$, $TR_{1,4}$ and $TR_{1,6}$ were found to be a lot more different. Here, the measurement of both dependencies of C_4 on

[4]The orthogonality of the 5-pole trap is expressed as $E_{1,2} = 0$ for the single pair of correction electrodes.

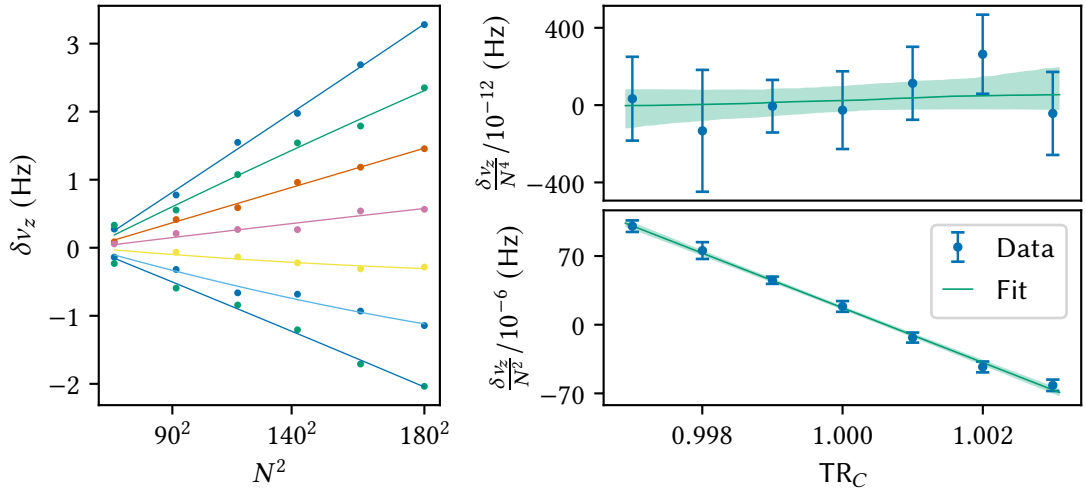

Figure 5.12: Optimization of TR_C. The left-hand side shows the individually measured curves $\omega_z(\rho_-)$ and the fit Eq. (5.19) for each of the applied values of TR_C. The right-hand side displays the quadratic (bottom) and quartic (top) coefficients of the polynomial fit against the tuning ratio and a linear fit through them. It is important to note that not only the tuning ratio changes, but also a readjustment of the ring voltage is done in order to keep the ion centered on the resonator.

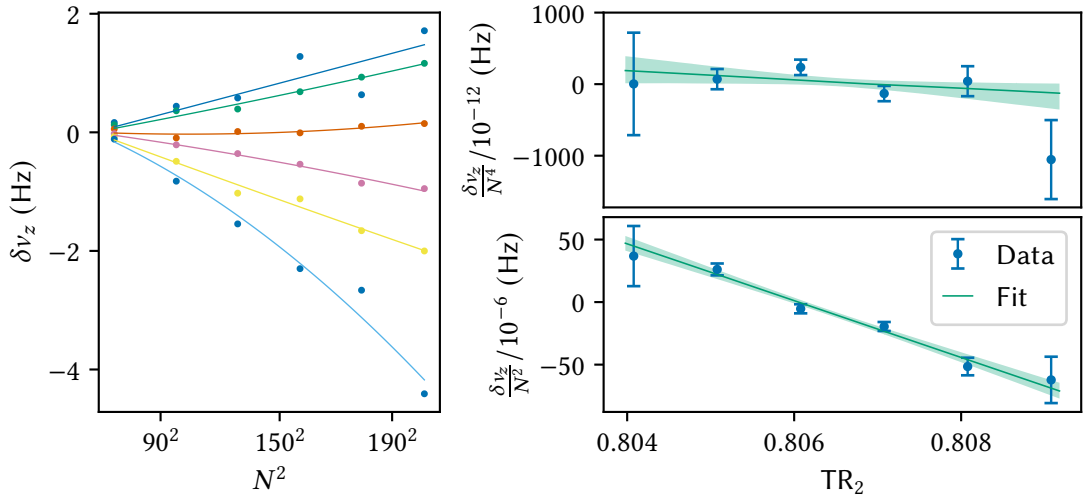

Figure 5.13: Optimization of TR_2. For details see Figure 5.12 and text.

the tuning ratios could be used to move on a line of $C_4 = 0$ by adjusting both TR_1 and TR_2 simultaneously. On this line C_6 can then be tuned to zero independent of C_4. In retrospect, the optimization of the tuning ratios would have profited from higher excitation radii (i.e. more cycles N), as especially for the optimization of TR_C and TR_2 the C_6 contributions were not

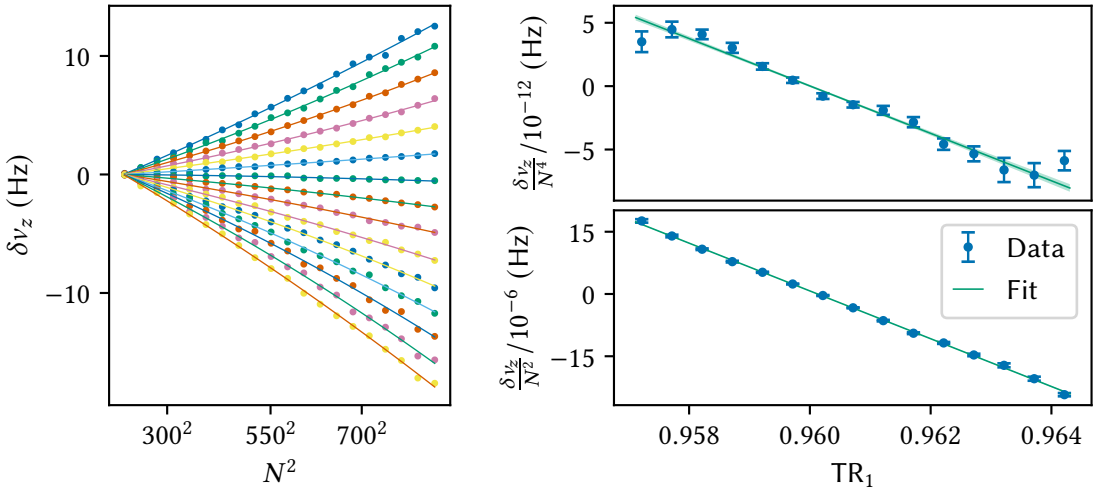

Figure 5.14: Optimization of TR_1. For details see Figure 5.12 and text.

resolved.

As a cross-check, a simultaneous evaluation of the three optimizations can be done by fitting the E-parameters, compare Eq. (5.18). From the measurements, the dataset $\omega_z(\vec{U})$, $\delta\omega_z(\vec{U}, N)$ can be formed. The data is fit to

$$\begin{aligned}\omega_z(\vec{U}) &= \sqrt{2\sum_{i=1}^{3} E_{i,2}U_i q/m} \\ \delta\omega_z(\vec{U}, N) &= \sum_{i=1}^{3}(F_{i,4}U_i N^2 + F_{i,6}U_i N^4 + F_{i,8}U_i N^6),\end{aligned} \tag{5.21}$$

where $E_{i,2}$ can be used directly, but the higher order terms would require the knowledge of ρ_- in absolute units, which at this point is unknown. Therefore, the generic expansion coefficients $F_{i,4/6}$ where introduced. Table 5.4 shows the result of this fit performed with the MCMC meth-

Table 5.4: Experimental determination of the parameters defined in Eq. (5.21). The coefficients of order N^6 for $i = 0$ and $i = 2$ were highly correlated and not statistically different from zero.

	$E_{i,2}/10^4$ ($m^{-2}V^{-1}$)	$F_{i,4}/2\pi/10^8$ (HzV^{-1})	$F_{i,6}/2\pi/10^{14}$ (HzV^{-1})
$i = 0$	−2.3311(1)	−60(5)	–
$i = 1$	−3.0278(1)	9.1(2)	2.5(8)
$i = 2$	3.6935(1)	64(6)	–

ods introduced in Section 5.3.2. For $E_{i,2}$, the deviations to the theoretical parameters in Table 5.3 are of the order of a few percent and thus similar to the deviations found for the symmetrization. While no direct comparison of the $F_{i,4/6}$ parameters can be made with theoretical values,

the two fractions $F_{0,4}/F_{1,4} = E_{0,4}/E_{1,4} = -6.6(5)$ and $F_{0,4}/F_{2,4} = E_{0,4}/E_{2,4} = -0.95(1)$ can be compared with the theoretical values of $E_{0,4}/E_{1,4} = -6.68$ and $E_{0,4}/E_{2,4} = -0.953$, respectively[5]. These values agree quite well.

This evaluation also presents an alternative way to directly derive optimal tuning ratios. For each MCMC sample of the expansion coefficients, Eq. (5.21) can be inverted for optimal voltages, i.e. $\omega_z(\vec{U}) = \omega_R$, $\sum_i F_{i,4}U_i = 0$ and $\sum_i F_{i,6}U_i = 0$. The distributions of the voltages yield the tuning ratios with uncertainties

$$(\mathrm{TR}_1, \mathrm{TR}_2) = (0.96014(3), 0.806283(1)). \tag{5.22}$$

The uncertainties of the tuning ratios obtained in this way only reflect the uncertainty of the optimum, but not the uncertainty of C_4 or C_6. This more mathematical way of optimizing tuning ratios of 7-pole Penning traps was not used during this measurement campaign but could be used in future measurements.

5.7.4. Field imperfections and amplitude calibrations

Here, a method to explicitly characterize the field imperfections will be presented in order to evaluate the systematic shifts and uncertainties of the final fit parameters. This also includes the calibration of the cyclotron amplitude ρ_+, which is needed for the PnA method.

The principle to determine the excited amplitude ρ_+ and the magnetic inhomogeneity B_2 is outlined in ref. [77]. In a trap with small field imperfections, the shift $\delta\omega_+(\rho_+)$ is dominated by the relativistic shift, Eq. (2.40). By varying the number of cycles of the dipole pulse N_+, and measuring $\delta\omega_+(N_+)$ a calibration $\rho_+ = K_+N_+$ can be extracted as the relativistic shift only has the amplitude as a possibly unknown parameter. In turn, the axial frequency shift $\delta\omega_z(N_+) \propto B_2\rho_+^2$ measures B_2, compare Eq. (2.35).

More generally, residual C_4, C_3 and B_1 field imperfections will also contribute to both the axial and modified cyclotron frequency shifts. In total, the theoretical systematic shifts of quadratic order in the amplitudes of the axial and modified cyclotron frequency can be summarized as

$$\begin{aligned}
&\delta\omega_z(\rho_+, \rho_-, \rho_z \mid C_4, C_3, B_2, B_1) = \\
&\qquad \sum_{\rho_i=\{\rho_+,\rho_-,\rho_z\}} \delta_{z,\rho_i}\rho_i^2 = \sum_{\rho_i=\{\rho_+,\rho_-,\rho_z\}} \left[\delta_{z,C_4,\rho_i} + \delta_{z,C_3^2,\rho_i} + \delta_{z,B_2,\rho_i} + \delta_{z,B_1^2,\rho_i} + \delta_{z,C_3B_1,\rho_i}\right]\rho_i^2, \\
&\delta\omega_+(\rho_+, \rho_-, \rho_z \mid C_4, C_3, B_2, B_1) = \\
&\qquad \sum_{\rho_i=\{\rho_+,\rho_-,\rho_z\}} \delta_{+,\rho_i}\rho_i^2 = \sum_{\rho_i=\{\rho_+,\rho_-,\rho_z\}} \left[\delta_{+,C_4,\rho_i} + \delta_{+,C_3^2,\rho_i} + \delta_{+,B_2,\rho_i} + \delta_{+,B_1^2,\rho_i} + \delta_{+,C_3B_1,\rho_i}\right]\rho_i^2 - \frac{\omega_+^3\rho_+^2}{2c^2},
\end{aligned} \tag{5.23}$$

where the terms $\delta_{z/+,X,\rho_i}$ are the prefactors of the systematic shift due to the field imperfection(s) X and amplitude ρ_i and the last term for ω_+ accounts for the relativistic shift, compare

[5] It might seem that the experimental error of the fraction $F_{0,4}/F_{2,4} = -0.95(1)$ are small compared to the values in Table 5.4. The reason for this is that the errors on the individual $F_{0,4}$ and $F_{2,4}$ are highly correlated and cancel to a large extend in the fraction.

Eqs.(2.25,2.30, 2.35, 2.37, 2.38, 2.39, 2.40). Not all systematic shifts X contribute, i.e. $\delta_{z/+,X,\rho_i}$ can be zero. Experimentally, the shift of the frequencies ω_z and ω_+ due to the different radii can be observed individually by measurement of the shift of the frequency at reference amplitudes to the shift at an excited amplitude in one of the modes, e.g. for shifts due to ρ_+

$$\begin{aligned}\omega_z(\rho_+,\rho_-,\rho_z) - \omega_z(\rho_{+,\mathrm{ref}},\rho_-,\rho_z) &= a_{z,\rho_+}(x_+^2 - x_{+,\mathrm{ref}}^2) + O(x^4) = \delta_{z,\rho_+}(\rho_+^2 - \rho_{+,\mathrm{ref}}^2) + O(\rho_+^4),\\ \omega_+(\rho_+,\rho_-,\rho_z) - \omega_+(\rho_{+,\mathrm{ref}},\rho_-,\rho_z) &= a_{+,\rho_+}(x_+^2 - x_{+,\mathrm{ref}}^2) + O(x^4) = \delta_{+,\rho_+}(\rho_+^2 - \rho_{+,\mathrm{ref}}^2) + O(\rho_+^4),\end{aligned} \tag{5.24}$$

where $a_{z/+,\rho_+}$ is the fit quadratic order dependence of the axial/modified cyclotron frequency on the experimental parameter x_+ which is proportional to $\rho_+ = K_+ x_+$. Similar definitions for the magnetron and axial motion give the system of 6 equations

$$\begin{aligned}a_{z,\rho_i} &= K_i^2 \delta_{z,\rho_i}(C_4, C_3, B_2, B_1),\\ a_{+,\rho_i} &= K_i^2 \delta_{+,\rho_i}(C_4, C_3, B_2, B_1),\end{aligned} \tag{5.25}$$

for $i = \{+,-,z\}$. As B_1 can be measured directly and independently from the systematic shifts, see Section 5.7.2, this leaves the 6 unknowns $\vec{p} = \{C_4, C_3, B_2, K_+, K_-, K_z\}$. While the shifts due to field imperfections always appear as a product of the imperfection parameter X with an amplitude calibration K_i, the relativistic shift of the cyclotron motion allows to remove this correlation.

For the modified cyclotron and magnetron motion, the number of cycles of a dipolar excitation $x_\pm$ is proportional to the final amplitude, assuming that $K_\pm x_\pm \gg \rho_{\pm,th}$, and the measurement of ω_z via the dip technique and ω_+ via phase sensitive methods is possible. The axial amplitude can not be changed easily, as the axial motion is coupled to the detector and thus constantly thermalized. Rather, the thermal amplitude $\rho_{z,th}$ is changed by using electronic feedback, see Section 5.8.2. With electronic feedback, the Q-value of the resonator is proportional to its temperature and the measure $x_z = \sqrt{Q/Q_0}$ gives the proportionality $\rho_{z,th} = \rho_{z,th,0} x_z = K_z \sqrt{Q/Q_0}$, where Q_0 and $\rho_{z,th,0}$ are the Q-value and thermal amplitude without feedback, respectively. The shifts of the axial frequency due to thermal axial amplitudes in a detected dip signal may increase by up to a factor of 2, depending on some experimental parameters, see ref. [136]. Therefore

$$a_{z,\rho_z} = C_z K_z^2 \delta_{z,\rho_z}(C_4, C_3, B_2, B_1), \tag{5.26}$$

with C_z between 1 and 2.

The individual measurements were performed in the following way:

```
for each amplitude
    N times
        With reference amplitude: measure ω_z with dip and δφ with PnA
        With excited amplitude: measure ω_z with dip and δφ with PnA
    end
end
```

Measuring at the same amplitude N times increases the statistical precision and further allows to fit the thermal radii from the distribution, see the next subsection. Performing the reference

measurement N times is used to compensate for drifts of ω_z, due to e.g. voltage drifts, and drifts of ω_+ due to magnetic field drifts. The model

$$\delta\omega_{z/+}(x_i \mid a_{z/+,\rho_i}) = a_{z/+,\rho_i} x_i^2 \tag{5.27}$$

is fit to the experimentally determined frequency shifts $\delta\omega_{z/+}(x_i) = \omega_{z/+}(x_i) - \omega_{z/+}(x_{\mathrm{ref}})$.

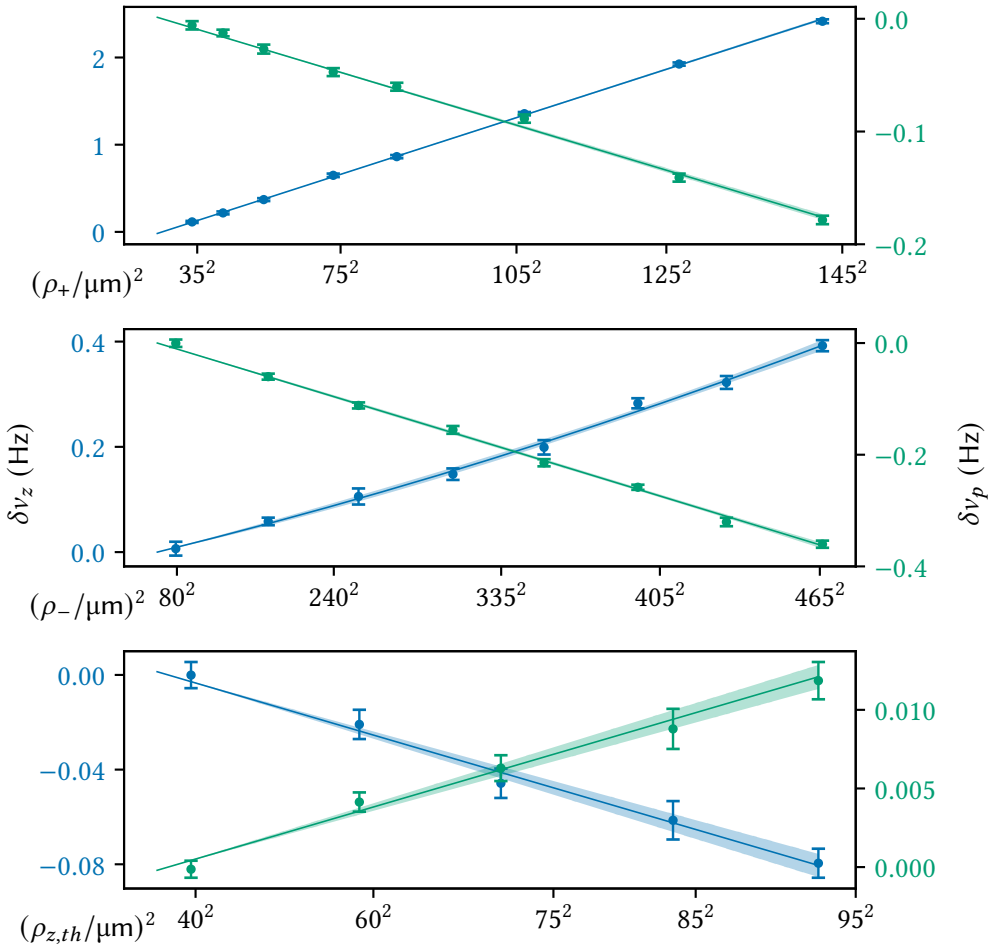

Figure 5.15: Measurement of the systematic shifts of the axial and modified cyclotron frequency for the three amplitudes ρ_+ (top), ρ_- (middle) and $\rho_{z,th}$ (bottom). For ρ_+ and ρ_-, this corresponds to the dipolar excitation amplitude, and the mean amplitude after excitation must additionally include the thermal amplitude, compare Eq. (2.58). The axial frequency is measured via an axial dip and the modified cyclotron frequency via PnA. The x-axis of the plots was scaled with the amplitude calibrations determined from the subsequent fit, see text and Table 5.5.

Figure 5.15 shows the measurements of the systematic shifts and the fits to extract a_{z,ρ_i} and a_{+,ρ_i}. While the shifts due to ρ_+ and ρ_z only have significant quadratic components, the

magnetron motion was also fit with quartic $b_{z,\rho_-} x_-^4$ and $b_{+,\rho_-} x_-^4$ components. Using the fit values of $a_{z/+,\rho_i}$ and their uncertainties, the inhomogeneities and amplitude calibrations are fit according to Eq. (5.25) and Eq. (5.33), see Table 5.5. In the MCMC fit, the parameter C_z,

Table 5.5: The determined field imperfections and amplitude calibrations from the measurement of systematic shifts to the axial and cyclotron frequency. The values of the amplitude calibrations K_+ and K_- depend on the used excitation power and the used excitation line. The lower table shows the Pearson correlation coefficient for the imperfections and the relevant coefficient for K_+. For details see text.

C_4/C_2 (m^{-2})	C_3/C_2 (m^{-1})	B_2 (Tm^{-2})	K_+ (μm/MCy)	K_- (μm/Cy)	K_z (μm)
27(6)	−6.2(6)	1.04(5)	40.8(7)	0.39(1)	36(1)

$\rho(C_4/C_2, C_3/C_2)$	$\rho(B_2, C_4/C_2)$	$\rho(B_2, C_3/C_2)$	$\rho(K_+, B_2)$
−0.998	−0.577	0.586	−0.781

compare Eq. (5.26), was left as a free parameter between 1 and 2 by sampling it from the prior distribution $C_z \sim \mathrm{Uniform}(1, 2)$. Similarly, the uncertainty of B_1 is included in the MCMC fit by sampling it from the prior probability distribution $B_1 \times \mathrm{m/mT} \sim \mathrm{Normal}(\mu = 29, \sigma = 2)$, compare Eq. (5.15). To signify the correlation between the determined parameters, the Pearson correlation coefficient

$$\rho(X, Y) = \frac{\mathrm{cov}(X, Y)}{\sigma(X)\sigma(Y)} \tag{5.28}$$

is given for a choice of relevant combinations, see Table 5.5. As will be explained in the next chapters, the full covariance matrix of the fit is used for the error and uncertainty propagation to the cyclotron frequency.

The values of C_3/C_2 and C_4/C_2 turned out to be rather large, as no symmetrization had been performed at the time. This consequently also leads to a large C_4/C_2, as the tuning ratio optimization alone can not discriminate between C_3 and C_4 and optimizes to

$$\frac{C_4}{C_2} = -\frac{3}{4}\left(\frac{C_3}{C_2}\right)^2, \tag{5.29}$$

compare Eq. (2.25) and Eq. (2.30). This is nicely reflected in Table 5.5[6]. In this method, the different dependencies of C_3 and C_4 shifts on the axial and magnetron radii allow to decorrelate their effects to a certain degree, as signified via the Pearson correlation coefficient $|\rho(C_4/C_2, C_3/C_2)| < 1$ and both values being significantly different from zero. Additionally, the estimate of C_3/C_2 obtained via the symmetrization shows perfect agreement, compare Eq. (5.14).

From the COMSOL calculation of the magnetic field change due to the AT ferromagnetic ring, the B_2 in the PT is expected to be $B_2 = 1.14$. Similar to B_1, this value fits relatively well with the measured value.

[6] Although the middle plot in Figure 5.15 clearly shows that the tuning ratio optimization is not ideal, $\delta\omega_z/\rho_-^2 \neq 0$, the shifts measured here would actually not be significant in the tuning ratio optimization. This is because the tuning ratio optimization does not use averaged values of ω_z and the amplitudes are significantly larger here.

Lastly, from the quartic components $b_{z,\rho_-}x_-^4$ and $b_{+,\rho_-}x_-^4$ and the determined K_-, C_6 can be estimated from the shifts [67]

$$\delta\omega_z = \frac{45}{16}\frac{C_6}{C_2}\omega_z\rho_-^4, \quad \delta\omega_+ = -\frac{45}{8}\frac{C_6}{C_2}\omega_-\rho_-^4 \tag{5.30}$$

This evaluates to the consistent values $C_6/C_2 = 1.2(5)\times10^6$ m^{-4} and $C_6/C_2 = 0(20)\times10^6$ m^{-4}, from $b_{z,\rho_-}x_-^4$ and $b_{+,\rho_-}x_-^4$, respectively. As the shifts due to C_6 scale relative to C_4 as

$$\frac{\delta\nu_i(C_6)}{\delta\nu_i(C_4)} \sim \frac{C_6}{C_4}\rho_j^2 < 10^{-4} \tag{5.31}$$

they are fully negligible at the amplitudes of the modes, $\rho_j < 40$ µm, during the measurements.

5.7.5. Measurement of the thermal amplitudes

The determination of the thermal amplitude of the axial motion is critical for the evaluation of the systematic shifts depending on the amplitudes. As the thermal amplitude of the axial motion is given via the temperature of the detection system, compare Eq. (2.48), it could ideally be calculated by assuming a temperature equal to that of the LHe cryostat at 4.2 K. The heat load at the detection system and possible noise or feedback characteristics of the cryogenic amplifiers typically lead to a slight increase of up to several K [91]. Therefore, the thermal amplitude needs to be explicitly measured and a couple of methods exist to do so.

Via the amplitude calibration

The previously described method already evaluates the thermal amplitude via the amplitude calibration using electronic feedback $K_z = \rho_{z,th} = 36(1)$ µm. Comparing with Eq. (2.48) the temperature of the detection system is evaluated to $T_z = 6.5(4)$ K. Here, this method works essentially via measuring the $B_2\rho_z^2$ associated shifts to ω_+ to determine $r_{z,th}$ together with the independently determined B_2. In a trap with lower B_2, explicitly detuning the trap to $C_4 \neq 0$ should enable the determination of $\rho_{z,th}$ via this method as well.

Via the distribution of frequency shifts after dipolar excitations

Similar to Eq. (2.82), the standard deviation of the shifts of the axial frequency after a dipolar excitation depend on the thermal amplitudes, and they can be fit as

$$\sigma(\delta\omega_z)(x_i \mid \sigma_i, \sigma_{0,i}) = \sqrt{\sigma_i^2 x_i^2 + \sigma_{0,i}^2}, \tag{5.32}$$

assuming a constant $\sigma_{0,i}$ which accounts for the measurement uncertainty. The fitted σ_i is connected to the thermal radius via

$$\sigma_i = \sqrt{2}K_i\delta_{z,\rho_i}\rho_{i,th}, \tag{5.33}$$

compare Eq. (2.82) and ref. [77].

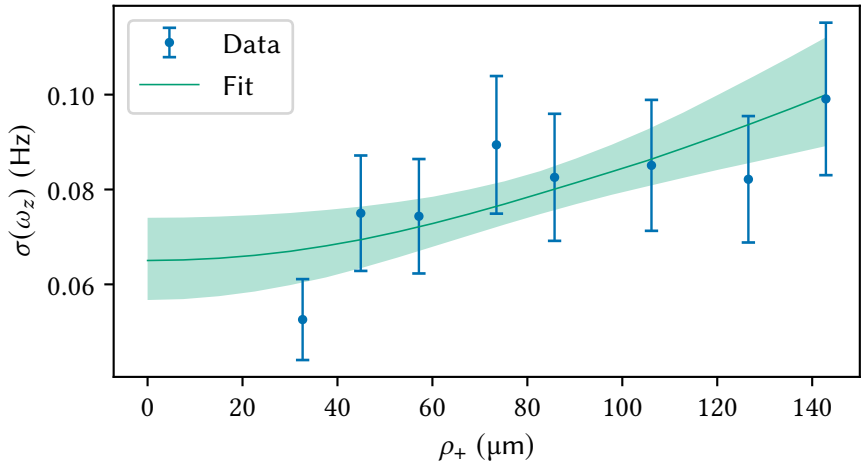

Figure 5.16: The standard deviation of the axial frequency following a dipole excitation of the modified cyclotron motion. The data is fit using Eq. (5.32).

Typically, this measurement is done by explicitly detuning the trap to $C_4 \neq 0$ and measuring $\delta\omega_z(\rho_+)$. Here, no explicit measurement with this technique was performed, but again the previous measurement can be used due to the large B_2 shift. Figure 5.16 shows to fit of $\rho_{+,th}$, which uses the same data as the middle plot in Figure 5.15. Clearly, the statistical significance of this measurement is not great. The extracted value, $\rho_{+,th} = 3.0(9)$ µm, reflects that. Calculating the corresponding axial amplitude via Eq. (2.66) gives $\rho_{z,th} = 24(7)$ µm and $T_z = 3(2)$ K, with a small tension to the previously determined value.

Via the distribution of ring voltages in the AT

The strong B_2 in the analysis trap leads to large axial frequency shifts $\delta\omega_z(\rho_+)$, compare Eq. (2.35), which allows to measure the thermal distribution of the modified cyclotron amplitude. After a thermalization of the modified cyclotron motion via the cooling sideband in the precision trap, the amplitude $\rho_{+,\mathrm{PT}}$ is distributed according to Eq. (A.39). The adiabatic transport from the PT to the AT conserves the angular momentum, i.e. the magnetic moment, compare Eq. (2.31),

$$\rho_{+,\mathrm{PT}}^2 \omega_{+,\mathrm{PT}} = \rho_{+,\mathrm{AT}}^2 \omega_{+,\mathrm{AT}}. \tag{5.34}$$

Using Eq. (2.35) the corresponding shift in the AT is

$$\delta\omega_{z,\mathrm{AT}} = \frac{\omega_{+,\mathrm{PT}}}{\omega_{z,\mathrm{AT}}} \frac{qB_{2,\mathrm{AT}}}{2m} \rho_{+,\mathrm{PT}}^2. \tag{5.35}$$

Even for thermally distributed $\rho_{+,\mathrm{PT}}$, the corresponding shifts are of the order of hundreds of Hz and the detection of the axial frequency would need to be performed far off-resonant the AT's axial detection system. Rather, the ring voltage in the AT is adjusted to center the ion $\omega_{z,\mathrm{AT}}(U_0) = \omega_{R,\mathrm{AT}}$ and the distribution of required ring voltages U_0 is measured. Using the experimental value $\delta\omega_{z,\mathrm{AT}}/\delta U_0 = 2\pi \cdot 113.8(2)$ Hz/mV, compare Table 5.1, the voltage shift

can be rewritten as $\delta U_0 = (\delta\omega_{z,\mathrm{AT}}/\delta U_0)^{-1}\delta\omega_{z,\mathrm{AT}}$. Comparing to Eq. (A.39), U_0 is distributed according to

$$p(U_0 \mid \beta(U_0), \sigma(U_0)) = \frac{\Theta(U_0 - \beta(U_0))}{\sigma(U_0)} \exp\left(-\frac{U_0 - \beta(U_0)}{\sigma(U_0)}\right), \tag{5.36}$$

where $\beta(U_0)$ is the voltage at zero amplitude and Θ is the Heaviside theta function. The parameter $\sigma(U_0)$ is connected to the thermal amplitude via

$$\begin{aligned} \sigma(U_0) &= (\delta\omega_{z,\mathrm{AT}}/\delta U_0)^{-1} \frac{\omega_{+,\mathrm{PT}}}{\omega_{z,\mathrm{AT}}} \frac{qB_{2,\mathrm{AT}}}{2m} \rho^2_{+,th,\mathrm{PT}}, \\ \Leftrightarrow \rho^2_{+,th,\mathrm{PT}} &= 4.288(8) \frac{\mu\mathrm{m}^2}{\mathrm{mV}} \sigma(U_0), \end{aligned} \tag{5.37}$$

where the systematic uncertainty is from the determination of measured AT quantities as given in Table 5.1.

The measurement is performed simply by repeating the sequence of cooling in the PT, transport to the AT and measurement of U_0. Figure 5.17 shows the binned data and a fit via MCMC

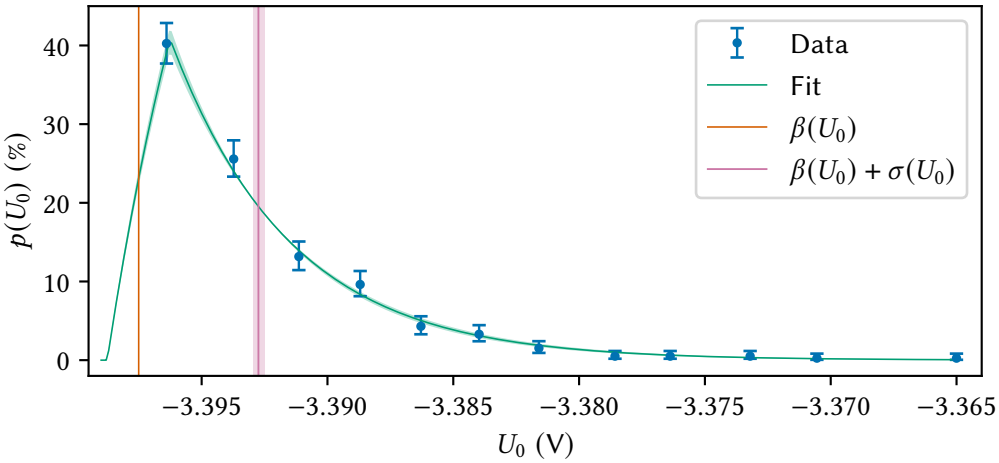

Figure 5.17: Fit of the distribution of voltages in the AT after thermalization of the modified cyclotron motion in the PT. The unbinned MCMC fit is performed with the model probability Eq. (5.36). For the visual representation of the fit, the probability needs to be adjusted by integrating over the bin width B, e.g. $p(U_0) \to \int_{U_0-B/2}^{U_0+B/2} p(U_0')\,\mathrm{d}U_0'$.

inference of the unbinned data and the probability Eq. (5.36). The extracted parameters are $\sigma(U_0) = 4.8(2)$ mV and $\beta(U_0) = -3.39751(1)$ V. Calculating the thermal radius via Eq. (5.37) gives $\rho_{+,th,\mathrm{PT}} = 4.5(1)$ µm. As above, Eq. (2.66) is used to convert to $\rho_{z,th,\mathrm{PT}} = 35.2(9)$ µm and $T_z = 6.2(3)$ K.

The double-trap technique, see Section 3.5, directly provides the data needed to evaluate the thermal amplitudes via this method, making it the preferable method regarding the systematic shift and uncertainty propagation. The comparison with the values from the two independent methods presented above serves as a cross-check.

5.8. Other experimental techniques

5.8.1. Ion transport

Transporting the ion from the PT to the AT and vice-versa is a crucial part of the measurement sequence. The transport routine utilizes the voltage ramping capabilities of the UM-14 voltage supply to continuously shift the potential well minimum from the center of one trap to the center of the other trap. First, in order to maximize the trapping depth, all electrodes of the trap tower (see Figure 4.3) excluding the ring and (inner) correction electrodes of the trap in which the ion resides are set to +14 V. For transports to the *right*, the initial trap potential is ramped to a configuration of $\{U_1 = 14\ \mathrm{V}, U_2 = -14\ \mathrm{V}, U_3 = -14\ \mathrm{V}, U_4 = 14\ \mathrm{V}\}$, where U_2 corresponds to the initial center electrode. Next, U_2 is ramped to +14 V, while U_4 is simultaneously ramped to −14 V. These steps then continue to the destination trap center, where in the last step the electrodes are ramped to the required voltage for a harmonic potential.

Typical difficulties of the transport are heating of the magnetron mode or even ion loss. A specific problem that occurred here and led to magnetron heating and sometimes ion loss was due to a large voltage settling time constant on one of the two lower correction electrodes of the PT. The large settling time was due to the cabling of the detection system to both lower correction electrodes which requires a large blocking resistor on one of them. To compensate, the ramping time constant had to be increased to be larger than the settling time while transporting through this electrode.

5.8.2. Electronic feedback

In Penning traps, feeding back the detection signal into the detection circuit has several applications [91, 137, 138]. Here, it is used to change the effective temperature of the detection system. To this end, the amplified detection signal is phase-shifted at room temperature, attenuated by a variable factor, and connected to an excitation line, which is coupled capacitively to the resonator coil. If there is no effective phase shift of the fed-back signal with respect to the resonator signal, the effective temperature is increased. For a shift of 180° the temperature is decreased. The magnitude of the increase or decrease depends on the amplitude of the fed-back signal. Phase shift values in between these two can be used to tune the resonator's frequency [139]. The correct applied phase shift for the two cases of 0° and 180° can be experimentally found by the two values where the resonance frequency is unchanged.

Ideally, the product of damping time constant $1/\Gamma_R$ (or equivalently the Q-value) and temperature T_z of the detector is constant and relates the feedback factor g via [91]

$$T_z/T_{z,0} = Q/Q_0 = g, \tag{5.38}$$

where $T_{z,0}$ and Q_0 are the temperature and Q-value without feedback. Negative feedback is achieved with $g < 1$ and positive feedback for $g > 1$. Due to noise of the cryogenic amplifiers, the relation for the temperature is practically limited to be

$$T_z = T_{z,0}\left(g + \frac{(g-1)^2}{g}K_g\right), \tag{5.39}$$

where K_g is related to the input noise of the resonator, while the relation for the Q-value is still valid, compare ref. [91].

Figure 5.19 shows dip spectra in the PT with applied positive and negative feedback. As

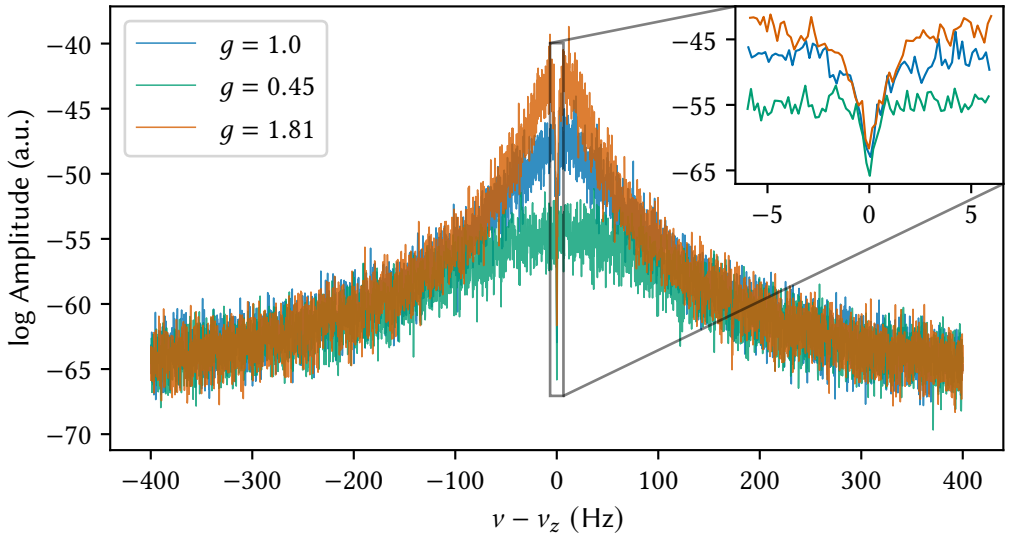

Figure 5.18: Dip spectra for different feedback factors g. The feedback factors are calculated via the ratio of the Q-value to the Q-value without feedback.

the Q-value change affects the effective parallel resistance, the cooling rate of the ion γ_z scales identically, compare Eq. (2.45) and see the plot. Figure 5.19 shows temperature measurements for the three different cases and a fit to the model Eq. (5.39). The fit returns $T_{z,0} = 5.8(4)$ K and $K_g = 0.5(4)$, so it is not quite able to resolve K_g sufficiently and more data points at lower g would have been helpful.

5.8.3. Magnetron frequency determination

When using the invariance theorem, Eq. (2.6), to determine the free cyclotron frequency, the magnetron frequency's accuracy is vastly less important than the axial frequency's and modified cyclotron frequency's. For the values of the eigenfrequencies for $^9Be^{3+}$, compare Table 5.2, an uncertainty of $\delta\omega_+ = 2\pi\times 1$ Hz corresponds to a fractional uncertainty of $\delta\omega_c/\omega_c \approx 5\times10^{-12}$. The determination via the magnetron double dip, compare Eq. (2.67), is in principle more than sufficient to get an uncertainty well below 100 mHz. Experimentally, an issue is that the sideband for the coupling $\omega_z+\omega_-$ is very close to the ion's axial frequency ω_z. Here, it was observed, that the determined magnetron frequency from the double dip depends on the amplitude of the coupling signal, which may be due to part of the coupling signal directly exciting the axial motion.

Figure 5.20 shows the magnetron frequency as a function of the coupling sideband's signal amplitude. A polynomial up to quadratic order in the amplitude is fit to the data to extrapolate to zero amplitude. The fit value of $\omega_-/2\pi = 4007.4(2)$ Hz is sufficiently accurate given the

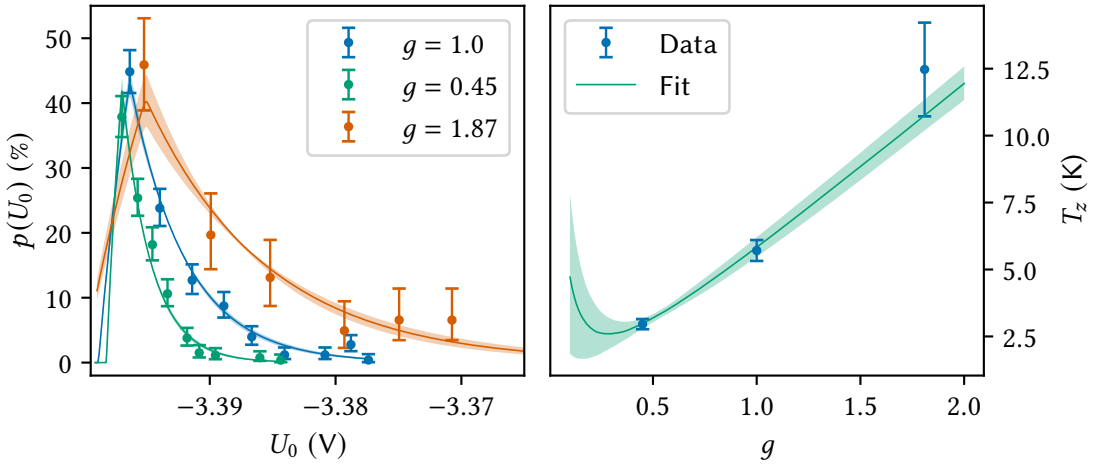

Figure 5.19: Temperature control via electronic feedback. The left-hand side shows the temperature measurements performed with the AT B_2 method, see the previous section. The right-hand side plots the temperature values T_z from the fits against the feedback factor g. The model Eq. (5.39) is fit to the data.

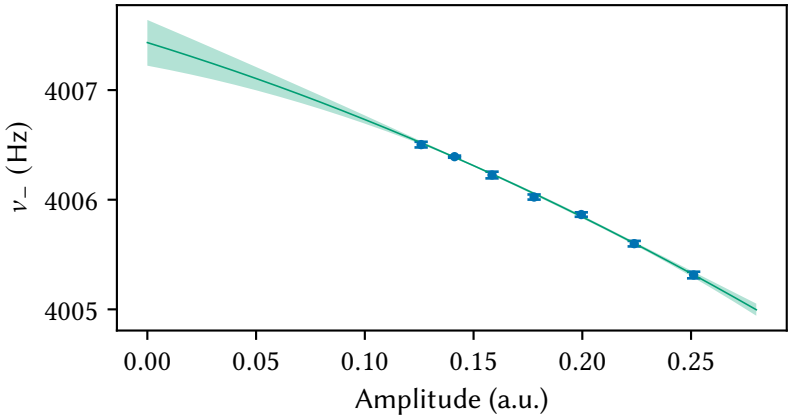

Figure 5.20: The magnetron frequency is determined by extrapolation to zero coupling strength of the quadrupole sideband. For details see text.

resulting uncertainty of $\delta\omega_c/\omega_c \approx 1{\times}10^{-12}$.

Chapter 6.

Measurement of nuclear properties

The measurement of the Zeeman and hyperfine splitting of the ground-state of $^9Be^+$ has been performed in a Penning trap using a cloud of ions and laser-fluorescence detection techniques as part of the earliest laser cooling experiments performed by Wineland *et al.* at the National Institute of Standards and Technology (NIST) [117, 140]. Additional to the ability to laser cool $^9Be^+$, the Zeeman structure of $^9Be^+$ includes two transitions which are first-order magnetic field independent at B-fields of 0.68 T and 0.82 T, respectively. This allowed measuring them with high resolution and extracting the nuclear to electron g-factor ratio and the zero-field hyperfine splitting with high accuracy [140]. Further, measuring the cyclotron frequency of the ion cloud and additional transition frequencies of the Zeeman structure, enabled the determination of mass ratios with high resolution via the electron g-factor [56]. More recently and also at NIST, the Zeeman and hyperfine splitting was remeasured at $\sim$ 4.5 T and confirmed a quadratic dependence of the zero-field splitting on the magnetic field [141].

For $^9Be^{3+}$, direct laser cooling is not possible which leads to a couple of key differences compared to the measurements performed on $^9Be^+$. Laser-cooled $^9Be^+$ close to the Doppler limit of 0.5 mK has very small motional amplitudes. In contrast, the motional modes of $^9Be^{3+}$ are only cooled resistively close to 4.2 K and are thus much larger. Therefore, any field imperfections will have a much larger impact on the systematics evaluation. Additionally, the relativistic shift will prove to be more significant. The spin-state detection also has to rely on the continuous Stern-Gerlach effect using single ions instead of fluorescence detection of many ions used, which dramatically increases the measurement time.

In this chapter, I will outline the measurement of transitions of the Zeeman and hyperfine splitting which are sensitive to the magnetic properties of the nucleus. A publication presenting the results of this measurement is in preparation [142]. To set the foundation for the following experimental work, the theory outlined in Section 3 is applied to hydrogen-like $^9Be^{3+}$. Preparatory steps necessary for the measurement of the Zeeman transitions, like the characterization of the double-dip magnetic field measurement and the spin-state preparation, are discussed next. The measurement sequence used for acquiring the transition resonances is discussed before moving along to the results. The determination of the results from the measurement of the frequencies of the Zeeman and hyperfine structure is complex and requires a careful prop-

agation of uncertainties. Here, I introduce a general approach to error propagation for Zeeman and hyperfine structure measurements in Penning traps which uses the full propagation of covariances. Lastly, I will present the results and discuss their relevance in the context of tests of the calculation of hyperfine splittings and diamagnetic shielding parameters.

6.1. The Zeeman and hyperfine splitting of $^9Be^{3+}$

The goal of the measurement is to fit the three independent parameters of the Zeeman and hyperfine splitting which are connected to the nuclear g-factor g_I, the electron g-factor g_s, and the zero-field splitting A. From here on, instead of g_e and g_I, the bound-electron g-factor g_s and shielded nuclear g-factor g'_I are used. These account for changes of the free parameters due to the binding Coulomb potential and their theory description is discussed in Section 6.6. The three independent parameters, compare Eq. (3.1), are defined via

$$\Gamma_e = \frac{g_s}{2}\frac{e}{q}\frac{m}{m_e}, \quad \Gamma_I = \frac{g'_I}{g_s}\frac{m_e}{m_p}, \quad \nu_{\mathrm{HFS}} = A/h, \tag{6.1}$$

where m is the mass of the $^9Be^{3+}$ ion and h is Planck's constant. Γ_e is defined in conjunction with bound-electron g-factor measurements, where $\Gamma_e = \nu_L/\nu_c$, with ν_L being the Larmor frequency of the bound electron [76]. Γ_I is defined as the scaled g-factor ratio, in the same way as in the publication for $^9Be^+$, ref. [141]. The definition $\vec{p} = (\Gamma_e, \Gamma_I, \nu_{\mathrm{HFS}})$ allows calculating $\nu_i(\nu_c \mid \vec{p})$ without use of any additional (external) parameters. For reference, the Hamiltonian, Eq. (3.1), as a function of these parameters and ν_c, and in units of frequency is

$$H = \nu_{\mathrm{HFS}}\hat{\vec{S}} \cdot \hat{\vec{I}} - \Gamma_e \nu_c \hat{S}_z - \Gamma_e\Gamma_I \nu_c \hat{I}_z. \tag{6.2}$$

Like ^{3}He, ^{9}Be has a negative nuclear spin g_I and thus also a negative hyperfine splitting constant A [34]. Though the nuclear magnetic moment of ^{9}Be is quite a bit smaller than that of ^{3}He, $g_I(^9\mathrm{Be})/g_I(^3\mathrm{He}) \approx -0.785/-4.255 \approx 0.184$, the zero-field splitting ν_{HFS} in $^9Be^{3+}$ is larger due to the higher charge. In ref. [143], the value $\nu_{\mathrm{HFS}}(^9Be^{3+}) \approx -12.800$ GHz is given with 5 significant digits. For comparison, $\nu_{\mathrm{HFS}}(^3He^+)/\approx -8.6656$ GHz. ^{9}Be has nuclear spin $I = 3/2$ which leads to 8 states in the Zeeman and hyperfine structure. The energies of the states are calculated via Eq. (3.9) and visualized in a so-called Breit-Rabi diagram in Figure 6.1. At the magnetic field of $B_0 \approx 5.72$ T, the mixing of the m_F substates, compare Eq. (3.10), is only $\sim 0.5\%$. While using the high-field quantum numbers for referring to the states is thus justified, it must be noted that the finite mixing is still highly relevant, as will be discussed further.

Table 6.1 lists the transitions possible with a magnetic radial dipole field, compare Section 3.2. In the following, the six low-frequency transitions are termed nuclear transitions, as only the nuclear spin changes in the high-field quantum numbers. Similarly, the four high-frequency transitions that only change the electron spin will be called electron transitions. Additionally, two transitions that change both the nuclear and electron spin are possible and will be called double spin transitions. For determining the three parameters independently, the measurement of three independent transitions is necessary. In the case of $^3He^+$, which has nuclear spin $I = 1/2$, only four dipole transitions are possible, compare ref. [97], and only any choice of

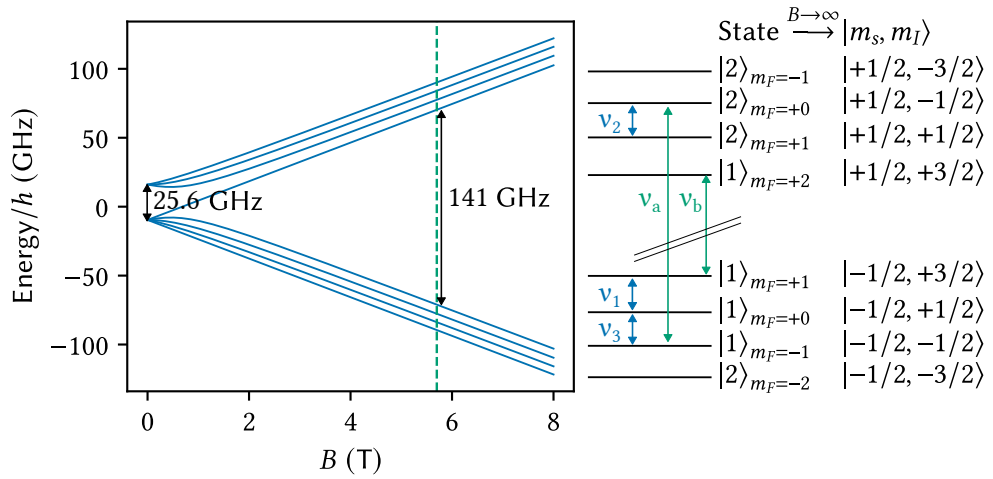

Figure 6.1: Breit-Rabi diagramm of $^9Be^{3+}$. The magnetic field in the PT at $B_0 \approx 5.72$ T is indicated by the green dashed line. The states are given via the same notation as in Eq. (3.9) and via the high-field limit quantum numbers m_s and m_I. The three measured nuclear transitions are marked in blue. The two measured electron spin transitions relevant to the next chapter are marked in green. Note that the order of the nuclear spin quantum number is reversed between positive and negative energy states due to the negative $\nu_{\mathrm{HFS}}(^9Be^{3+})$.

three is independent. Here, a larger choice of transitions exists. To find optimal transitions, which enable the highest resolution for these parameters, the sensitivities

$$\kappa(p) = \left| p \frac{\partial \nu}{\partial p} \left(\nu_c \frac{\partial \nu}{\partial \nu_c} \right)^{-1} \right| \tag{6.3}$$

are calculated for Γ_e, Γ_I and ν_{HFS}. In Section 3.3, it was shown that the reached precision to determine the center frequency of a transition ν via a resonance is directly related to the magnetic field measurement precision $\sigma(B) \sim \sigma(\nu_c)$. A sensitivity of 1 is a one-to-one correspondence of magnetic field uncertainty to the (statistical) uncertainty of the determination of the parameter. This is the case for bound-electron or the proton and antiproton g-factor measurements, as the Larmor frequency is just proportional to both the g-factor and the magnetic field. Γ_e behaves identically here, compare Table 6.1. In contrast, the two transitions $|-\frac{1}{2}, +\frac{1}{2}\rangle \rightarrow |-\frac{1}{2}, +\frac{3}{2}\rangle$ and $|+\frac{1}{2}, -\frac{1}{2}\rangle \rightarrow |+\frac{1}{2}, +\frac{1}{2}\rangle$, which in the following will be called ν_1 and ν_2, respectively, are preferred for determining the nuclear term Γ_I and the zero-field splitting ν_{HFS}. They are marked in Figure 6.1 and Table 6.1. Additional to the two transitions ν_1 and ν_2, being the most sensitive to the nuclear parameters, a third transition ν_3 is measured to independently determine Γ_e.

6.2. Preparatory steps

In this section, the specifics of the magnetic field measurement used for measuring the nuclear transitions, initial spin flips with $^9Be^{3+}$ in the AT, and a method to vastly decrease the state

Table 6.1: Radial dipole transitions of the hyperfine and Zeeman splitting of $^9Be^{3+}$ in the PT. The Rabi frequency Ω is given relative to the driving field amplitude B_x. The nuclear transitions measured with high precision and relevant to this chapter are marked in blue (correspondingly marked ν_1, ν_2, ν_3 in Figure 6.1). The electron transitions relevant to the next chapter are marked in green (correspondingly marked ν_a, ν_b in Figure 6.1). The two transitions marked in orange, change both the nuclear and electron spin. For details see text.

Transition	ν (GHz)	$\frac{\partial\nu}{\partial B}$ (GHz/T)	$\kappa(\Gamma_e)$	$\kappa(\Gamma_I)$	$\kappa(\nu_{\mathrm{HFS}})$	Ω/B_x (Hz/nT)
$\lvert-\frac{1}{2},-\frac{3}{2}\rangle \rightarrow \lvert-\frac{1}{2},-\frac{1}{2}\rangle$	5.7270	0.1195	1.0	0.050	7.38	5.64
$\lvert+\frac{1}{2},-\frac{3}{2}\rangle \rightarrow \lvert+\frac{1}{2},-\frac{1}{2}\rangle$	6.0569	0.0558	1.0	0.107	18.0	5.55
$\lvert-\frac{1}{2},-\frac{1}{2}\rangle \rightarrow \lvert-\frac{1}{2},+\frac{1}{2}\rangle$	6.1254	0.0678	1.0	0.088	14.8	6.99
$\lvert+\frac{1}{2},-\frac{1}{2}\rangle \rightarrow \lvert+\frac{1}{2},+\frac{1}{2}\rangle$	6.5528	−0.0257	1.0	0.233	45.6	6.90
$\lvert-\frac{1}{2},+\frac{1}{2}\rangle \rightarrow \lvert-\frac{1}{2},+\frac{3}{2}\rangle$	6.6213	−0.0137	1.0	0.437	85.5	6.57
$\lvert+\frac{1}{2},+\frac{3}{2}\rangle \rightarrow \lvert+\frac{1}{2},+\frac{1}{2}\rangle$	7.1941	−0.1616	1.0	0.037	8.78	6.53
$\lvert-\frac{1}{2},+\frac{3}{2}\rangle \rightarrow \lvert+\frac{1}{2},+\frac{3}{2}\rangle$	141.94	27.86	1.0	1×10^{-6}	0.11	87.8
$\lvert+\frac{1}{2},-\frac{1}{2}\rangle \rightarrow \lvert-\frac{1}{2},+\frac{3}{2}\rangle$	155.68	27.67	1.0	4×10^{-4}	0.02	0.52
$\lvert-\frac{1}{2},+\frac{1}{2}\rangle \rightarrow \lvert+\frac{1}{2},-\frac{1}{2}\rangle$	155.75	27.69	1.0	3×10^{-6}	0.02	87.5
$\lvert+\frac{1}{2},-\frac{3}{2}\rangle \rightarrow \lvert-\frac{1}{2},+\frac{1}{2}\rangle$	168.36	27.72	1.0	4×10^{-4}	0.06	0.44
$\lvert-\frac{1}{2},-\frac{1}{2}\rangle \rightarrow \lvert+\frac{1}{2},-\frac{1}{2}\rangle$	168.43	27.73	1.0	2×10^{-6}	0.06	87.6
$\lvert-\frac{1}{2},-\frac{3}{2}\rangle \rightarrow \lvert+\frac{1}{2},-\frac{3}{2}\rangle$	180.21	27.90	1.0	1×10^{-6}	0.13	87.8

preparation as well as the transition center search time are discussed.

6.2.1. Double-dip measurement

Even though the superior ν_+ measurement via the phase-sensitive methods was already working at the time, the nuclear transition measurements were performed with the double-dip method. The nuclear transitions ν_1 and ν_2 feature a vastly reduced relative magnetic field dependence compared to the electron transitions, compare Table 6.1. E.g., for ν_1 the relative dependence is reduced by a factor of about 100 compared to the electron transitions, which is directly reflected in the sensitivity to the zero-field splitting $\kappa(\nu_{\mathrm{HFS}})$. The double-dip technique reaches $\sigma(B)/B \approx 10^{-9}$ (ppb) uncertainty via a single measurement [28, 97]. This gives an expected statistical uncertainty of ν_1 and ν_2 within the single-digit parts per trillion range. In comparison, the relativistic Doppler shift of ν_1 and ν_2, compare Eq. (3.35), at thermal modified cyclotron amplitude, $\rho_+ = 4.5(1)$ µm, is $\sim$ 4 ppt. Choosing the coherent methods to measure ν_+ would lead to even smaller statistical uncertainties but a larger relativistic shift due to the required non-thermal amplitudes. The uncertainty of the relativistic shift would also grow and thus limit the determination of ν_1 and ν_2 via the systematic uncertainty. Measuring frequencies at relative precision at or below 10^{-12} is also not possible with the current frequency standard, as the Rubidium standard's long-term stability is limited at 10^{-12} relative precision, even locked via GPS [144].

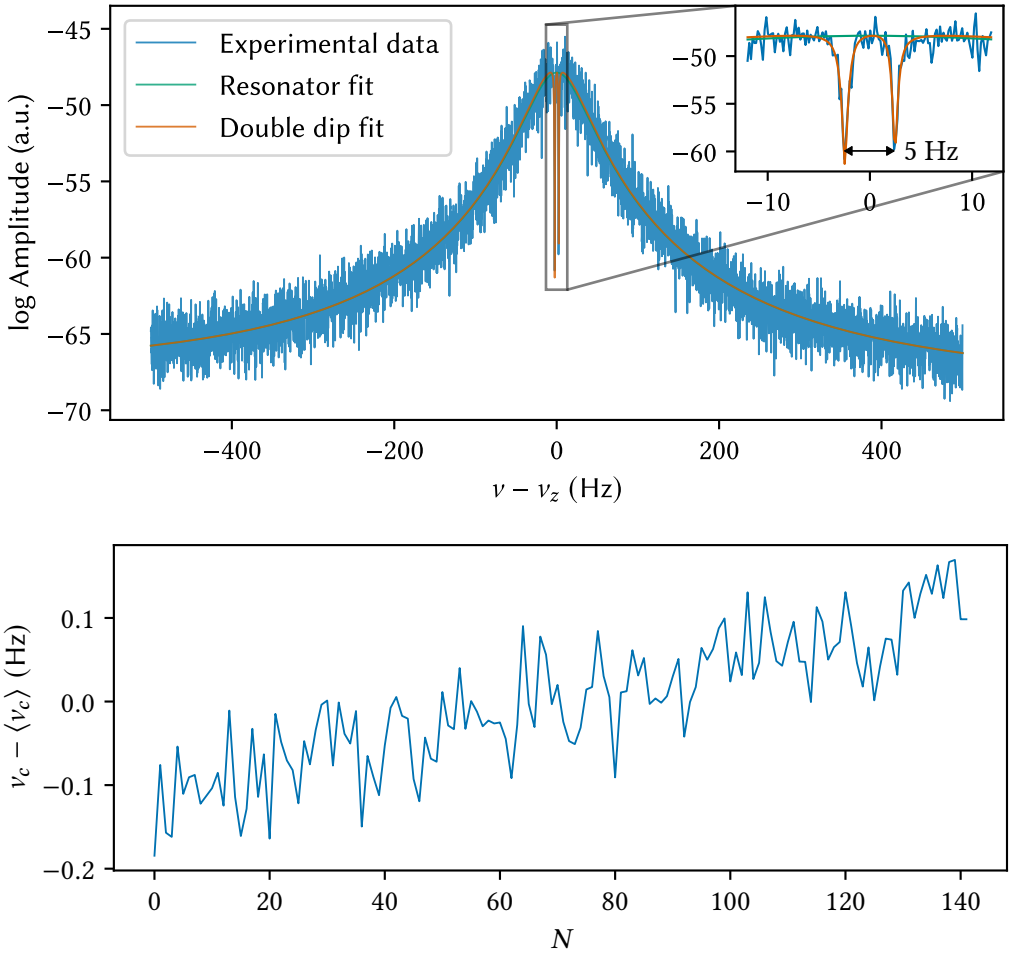

Figure 6.2: Cyclotron double-dip measurement with $^{9}Be^{3+}$ in the PT. The top graph shows a typical cyclotron double-dip signal and the fit to extract the two frequency components $\nu_{z,1}$ and $\nu_{z,2}$. The fit model is described in Section B.2. The bottom graph shows successive cyclotron frequency measurements.

Figure 6.2 shows a typical cyclotron double-dip spectrum with a Rabi frequency splitting of about 5 Hz. The continuous measurement of ν_c is achieved by alternating the modified cyclotron and axial frequency dip measurement and calculating ν_c via the invariance theorem, Eq. (2.6) (the magnetron frequency is taken from Section 5.8.3). The averaging time for the double dip is 60 s compared to the 40 s for the axial dip. The achieved single shot precision $\sigma(\Delta\nu_c)/\sqrt{2} \approx 38$ mHz, where $\Delta\nu_c$ is the difference of successive measurements, corresponds to 1.3 ppb.

6.2.2. Detection of nuclear transitions and spin flips in the AT

Due to the much-reduced dependence of the nuclear transitions on the magnetic field, their direct detection via the continuous Stern-Gerlach effect, Eq. (3.43), is much more challenging compared to the electronic transitions. Similarly, in measurements of the proton and antiproton g-factor [28, 70, 145], the small derivative $\partial\nu/\partial B \approx 42.6$ MHz/T requires a large B_2 to resolve the change $\delta\nu_z$ against e.g. voltage fluctuations during the axial detection time. The large B_2 not only increases $\delta\nu_z$ due to a spin-state change but also increases the change of the axial frequency due to the change of a single quantum of the modified cyclotron motion [70]. These single quantum jumps of the modified cyclotron motion occur at a rate that is proportional to the energy of the mode [146]. To be able to resolve spin flips, the modified cyclotron motion needs to be cooled stochastically [93] which takes a long time.

Here, the ν_1 transition, which has the smallest dependence on magnetic field of the nuclear transitions, would result in a tiny axial frequency change of $\delta\nu_z \approx 6$ mHz. Compared

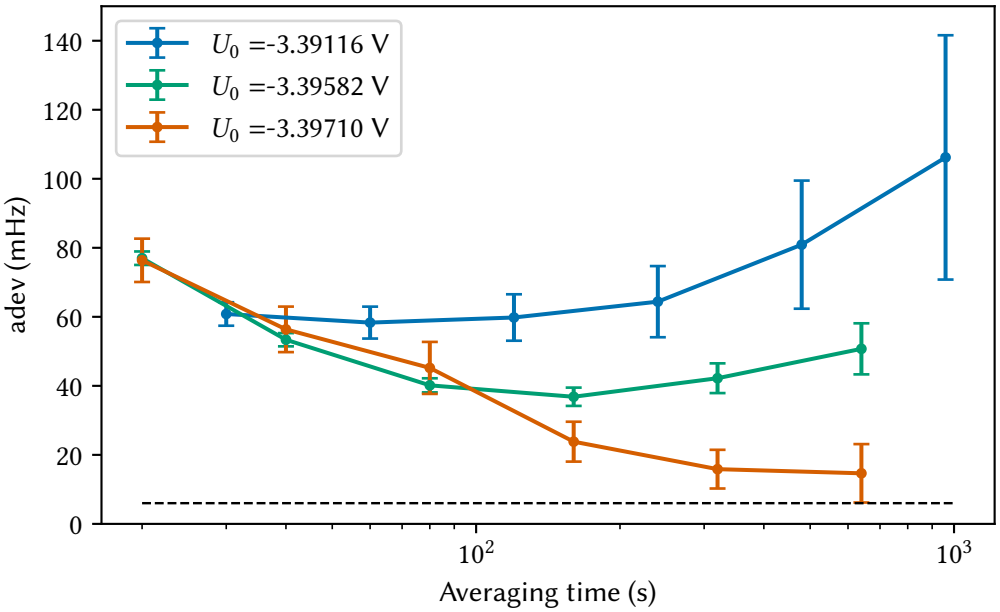

Figure 6.3: Axial frequency stability in the AT for different thermal amplitudes of the modified cyclotron motion. The different temperatures are expressed via the required ring voltages U_0, compare Section 5.7.5. The Allan deviation adev is the frequency stability for different averaging times [147]. The axial frequency shift due to transition ν_1 is shown by the dotted line.

to the achieved axial frequency stability in the AT, see Figure 6.3, this can not be resolved with the thermal distribution of modified cyclotron amplitudes in this experiment. In contrast, the change $\delta\nu_z \approx 11$ Hz for electron spin transitions can be resolved in a few seconds of averaging via the dip detection. To bypass the challenging direct detection of nuclear transitions, instead, the electron-spin transitions can be used for their detection [11]. For a nuclear transition $|m_s, m_I\rangle \rightarrow |m_s, m_I'\rangle$, the two detection transitions $|m_s, m_I\rangle \rightarrow |m_s', m_I\rangle$ and

$|m_s, m'_I\rangle \rightarrow |m'_s, m'_I\rangle$ are used. These two transitions are cycled until one of them produces a detectable spin-state change. This fully identifies the state as either m_I or m'_I. The scheme is visualized in Figure 6.4.

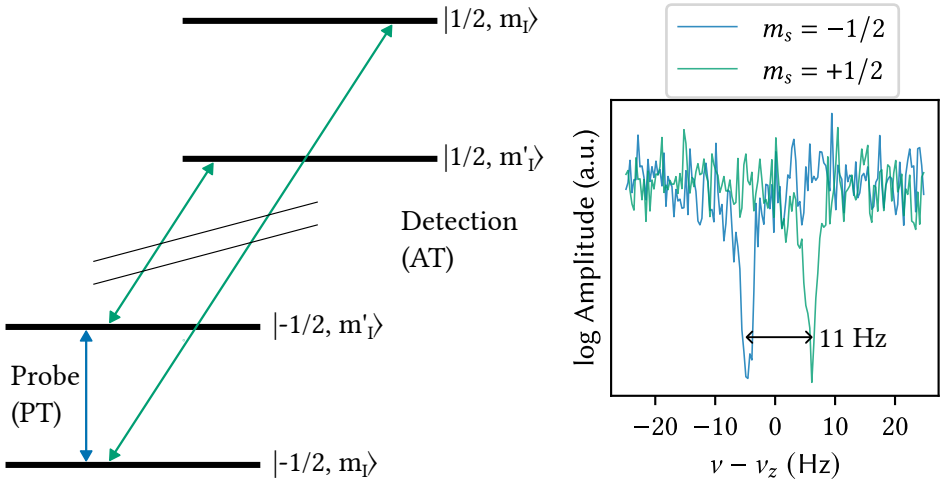

Figure 6.4: Detection of the spin state in the AT after probing an exemplary nuclear transition in the PT. Left-hand side: The nuclear probe transition driven in the PT is indicated in blue. The two electron transitions (green) are cycled in the AT until either produces a detectable electron spin-state change via the change of the axial frequency (right-hand side).

After the initial preparation of the $^9Be^{3+}$ ion, its spin state was unknown. In the AT, the electron transitions are broadened due to the large B_2, Eq. (3.26), to about $\Delta\nu \approx 1.5$ MHz, assuming a 4.2 K resonator. The magnetic field was determined as explained in Section 5.6, and the initial ~ 1 MHz uncertainties due to the value of $A(^9Be^{3+})$ were not critical. While alternating all four electron transitions, a spin flip was first detected via the $|-\frac{1}{2}, +\frac{3}{2}\rangle \rightarrow |+\frac{1}{2}, +\frac{3}{2}\rangle$ transition. A resonance of this transition was taken in the AT, see Figure 6.5. To this end, the frequency of the millimeter microwaves irradiated via the waveguide was varied over the calculated center frequency $\nu(B_{0,\mathrm{AT}} = 4.9732(4)) = 121.11(1)$ GHz, where the uncertainty is dominated by the magnetic field measurement in the AT. After irradiating at a frequency ν_{MW} for 20 s, an axial frequency spectrum was taken and compared to the previous spectrum to check whether a spin-state change occurred. The unbinned data was fit with the lineshape Eq. (3.27), which closely resembles the saturated Boltzmann distribution due to the large linewidth parameter. For details of the fit procedure see Section 6.4. The free parameters of the fit are the center of the resonance Δ_0, the linewidth parameter $\Delta\nu$ (see above), and the squared Rabi frequency Ω^2. From $\Delta\nu = 3.6(5)$ MHz, the thermal amplitude $\rho_{z,th,\mathrm{AT}} = 30(2)$ µm and the temperature of the detection system $T_{z,\mathrm{AT}} = 12(2)$ K were determined, compare Eqs. (3.26, 2.48). The temperature is significantly larger than the ambient 4.2 K, which could be due to feedback of the amplifier.

The resonance frequencies of the other electron transitions in the AT were found by manual searches around the predicted frequencies.

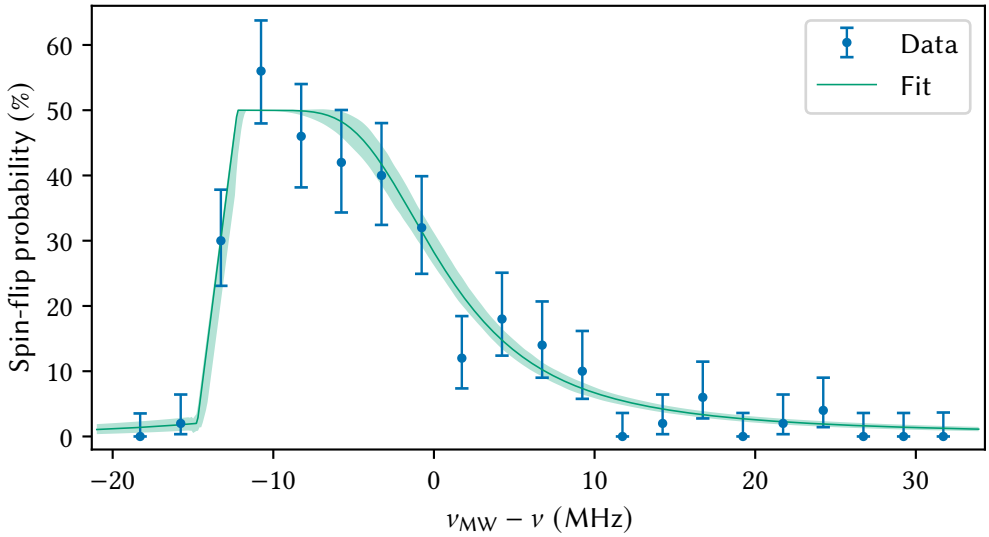

Figure 6.5: Resonance of the $|-\frac{1}{2},+\frac{3}{2}\rangle \rightarrow |+\frac{1}{2},+\frac{3}{2}\rangle$ transition in the AT. The unbinned data was fit with the lineshape Eq. (3.27). The fit curve and confidence band include the binwidth via averaging over the lineshape.

6.2.3. Adiabatic fast passage

Initially, the limited precision of the value $\nu_{\mathrm{HFS}}(^9\mathrm{Be}^{3+})$ from ref. [143] corresponded to MHz uncertainties on the transition frequencies. In contrast, the expected unsaturated widths of the resonances in the PT, as calculated via Eq. (3.19), are all below 1 kHz. To triangulate a precise transition center, saturated measurements with decreasingly smaller saturation widths could be used. However, this approach would be rather time-consuming, as even a partial resonance measurement requires at least a day of measurement time.

Adiabatic fast passage (AFP) is a method that can achieve 100 % spin-flip probability without precise knowledge of the transition center [148]. AFP is achieved by sweeping the excitation over the resonance center, which allows to adiabatically change the spin state. The requirement for AFP reads [149]

$$\gamma \ll \frac{1}{\Omega}\left|\frac{\mathrm{d}}{\mathrm{d}t}\Delta\right| \ll \Omega, \tag{6.4}$$

where γ, Ω and Δ, defined identically for the Bloch equation Eq. (3.22), are the dephasing rate, Rabi frequency and $\Delta = (\nu_{\mathrm{MW}} - \nu)$ in Hz. The sweep of Δ over $\Delta = 0$ relative to the Rabi frequency needs to be faster than the dephasing time, while at the same time, the strength of the coupling (expressed via the Rabi frequency) needs to be strong enough to keep up with the sweep. AFP has been done in a Penning trap via a sweep of the magnetic field with the use of large external magnetic field coils to change the resonance frequency $\nu(B)$ [150]. Here, instead, a linear sweep of the microwave frequency, which is possible with the frequency modulation capabilities of the SMB100A generator, was used. The dephasing rate, following similar arguments as in ref. [87], can be taken as the B_2 linewidth parameter $\Delta\nu$. As $\Delta\nu \propto \partial\nu/\partial B$, the

condition Eq. (6.4) can be met much easier with the nuclear transitions.

AFP was investigated first on the ν_1 transition, which has an expected width of below 1 Hz. The microwave frequency was swept in the PT and subsequently, the spin state was detected in the AT. To characterize AFP, initially, the frequency was swept over a span of 20 kHz in 400 s to produce 8 spin-state changes out of 8 tries. Another characterization measurement produced 60 spin-state changes out of 61 tries with a sweep span of 400 Hz and 14 s of sweep time. This corresponds to a spin-flip probability of $98^{+1}_{-4}\%$. Subsequently, a single cycle was typically enough to determine whether the transition center was inside the sweep span, which allowed a fast triangulation of the transition center. AFP was also successively used for the ν_2 transition.

Before taking the final resonances, the microwave amplitude had to be reduced to decrease the resonance width via the Rabi frequency, compare Section 3.3. To this end, partial resonances had to be taken in order to find a rough calibration of the Rabi frequency in dependence of the microwave amplitude. The final amplitude was chosen, such that Rabi frequency is roughly equal to the magnetic field measurement width $\sigma_\nu \approx \Omega$.

6.3. Measurement sequence

Here, the measurement scheme used for the nuclear transitions ν_i, $i = \{1, 2, 3\}$ is outlined.

The first and all subsequent cycles started in the AT. While the ion is in the AT, a resonator spectrum of the PT was taken. The free resonator spectrum without a dip can be used to better understand systematic effects related to the axial frequency determination. Due to the finite cyclotron temperature, the AT dip signal needed to be centered, compare Figure 5.8. Following, the spin state $|m_s, m_I\rangle$ was determined, compare Figure 6.4. After the detection of the nuclear spin state via the electron transition, the electron spin was reverted to its original orientation by another successful electron transition. The ion was then transported to the PT, compare Section 5.8.1. After the transport, the voltages were allowed to settle with a first waiting time of 100 s. An initial dip spectrum was taken, after which the ion was centered on the resonator $\nu_z = \nu_R$, where ν_R was taken from the fit of the resonator from the free resonator spectrum taken previously. This step required only tiny voltage adjustments, and an additional wait time of 60 s was done. Following, the magnetron mode was cooled via the upper sideband. Next, the precision measurement of the cyclotron frequency with the double-dip method was performed. Starting with an axial dip, a total of five axial frequency spectra, each taking 40 s, and three double-dip spectra, each taking 60 s, were taken alternately. After each double dip, an additional cooling of the magnetron mode was done. The axial dip prior and after a double dip were averaged and used to calculate a single ν_z, which in first-order accounts for axial frequency drifts, i.e. the time average of the axial frequency coincided with the time average of ν_+ as measured from the double dip. Therefore, a first cyclotron frequency measurement $\nu_{c,1}$ was finished after the second axial dip. This frequency was used to calculate the instantaneous transition frequency $\nu_i(\nu_{c,1})$. During the double-dip measurement of the second cyclotron frequency determination $\nu_{c,2}$, microwaves at $\nu_{\mathrm{MW}} = \nu_i(\nu_{c,1}) + \Delta_x$, where the random number $\Delta_x \sim \mathrm{Uniform}(\pm\mathrm{supp}(\Delta_i)/2)$ was drawn from the uniform distribution with a span $\mathrm{supp}(\Delta_i)$, were irradiated. After the third cyclotron frequency measurement $\nu_{c,3}$, the ion

was transported back to the AT. The total time for a single cycle was on average 18 minutes.

6.4. Statistical and systematic evaluation

To summarize, the relevant data taken during the measurements are the spin state $|m_s, m_I\rangle$ determined in the AT, the three individual cyclotron frequencies $\{\nu_{c,1}, \nu_{c,2}, \nu_{c,3}\}$, and the irradiated microwave frequency ν_{MW}. From the individual spin states, the spin state changes to the following cycle Δm_I, where either $\Delta m_I = 1$ or $\Delta m_I = 0$ are calculated[1]. Additionally, all measured FFT spectra of the resonator are saved for further analysis. In total, each resonance includes several hundred cycles.

In the following, the steps of the statistical and systematic analysis of the fit parameters $\vec{p}$, compare Eq. (6.1), are outlined.

6.4.1. Statistical analysis

Let $\Delta_{i,k}(\vec{p}) = \nu_{\mathrm{MW},i,k} - \nu_i(\nu_{c,i,k} \,|\, \vec{p})$, be defined as the difference of the irradiated microwave and predicted transition frequency for each transition measurement i and cycle k. The cyclotron frequency $\nu_{c,i,k}$ is taken as the mean value of the three individually measured values in each cycle. The spin-state change Δm_I for each transition i and cycle k is labelled $F_{i,k}$. The transition probabilities $P(\Delta_{i,k} \,|\, \vec{p}_{\mathrm{ls},i})$, additional to the parameters $\vec{p}$ of the Zeeman and hyperfine splitting, depend on the parameters of the probability lineshape $\vec{p}_{\mathrm{ls},i}$. Here, a Voigt lineshape is used, compare Eq. (3.21), and the discussion in the systematics section. Therefore, $\vec{p}_{\mathrm{ls},i} = (A_i, \sigma_i, \Omega_i)$, where A_i is an amplitude, σ_i the Gaussian and Ω_i the Lorentzian width. As a single spin-state change is either 0 or 1, it is Bernoulli distributed

$$F_{i,k} \sim \mathrm{Bernoulli}[P(\nu_{\mathrm{MW},i,k}, \nu_{c,i,k} \mid \vec{p}, \vec{p}_{\mathrm{ls},i})], \tag{6.5}$$

where the dependence of $\Delta_{i,k}(\vec{p})$ in P was rewritten to better discriminate between measured values $(\nu_{\mathrm{MW},i,k}, \nu_{c,i,k})$ and fit values $(\vec{p}, \vec{p}_{\mathrm{ls},i})$. The above statement, Eq. (6.5), allows calculating the full likelihood of the measurement and thus to fit the 3 parameters of the Zeeman any hyperfine splitting $\vec{p}$ simultaneously with the 9 parameters of the lineshape $\vec{p}_{\mathrm{ls},i}$, compare Section 5.3. As the likelihood does not factorize for the three measurements, having to simultaneously fit the 3 resonance measurements and their 12 free parameters is a complex task and obscures how the individual resonance measurements contribute.

To remedy this, instead an approach similar to non-linear least squares can be taken. Given an initial guess $\vec{p}_0$, the resonances are fit individually via

$$F_{i,k} \sim \mathrm{Bernoulli}[P(\nu_{\mathrm{MW},i,k} - \nu_i(\nu_{c,i,k} \mid \vec{p}_0) - \Delta_{0,i} \mid \vec{p}_{\mathrm{ls},i})], \tag{6.6}$$

where $\vec{p}_0$ is fixed and additional to $\vec{p}_{\mathrm{ls},i}$ the center of the resonance $\Delta_{0,i}$ is fit. Given the three fit values of $\Delta_{0,i}$, fitting $\vec{p}$ is possible by solving the system of equations

$$0 \stackrel{!}{=} \Delta_{0,i} + \nu_i(\nu_{c,0}, \vec{p}_0) - \nu_i(\nu_{c,0}, \vec{p}) \approx \Delta_{0,i} - \left(J_\nu(\nu_{c,0}, \vec{p}_0)\,(\vec{p} - \vec{p}_0)\right)_i, \tag{6.7}$$

[1] In order to answer the question: Did irradiating microwaves $\nu_{\mathrm{MW},k}$ in cycle k change the spin state? $\Delta m_{I,k} = 1$: Yes. $\Delta m_{I,k} = 0$: No.

where $\nu_{c,0}$ can be taken as the mean cyclotron frequency and

$$J_\nu(\nu_{c,0}, \vec{p}_0)_{ij} = \frac{\partial \nu_i(\nu_{c,0})}{\partial p_j}(\vec{p}_0) \tag{6.8}$$

is the Jacobian matrix of the transitions. These steps require two conditions. First, the range of cyclotron frequencies ν_c from all measurements may only result in small changes of the Jacobian matrix, such that $J_\nu(\nu_c, \vec{p}_0)\left(\vec{p} - \vec{p}_0\right)$ does not significantly vary. Secondly, the initial guess $\vec{p}_0$ must be close enough to justify the linearized approximation performed in Eq. (6.7). The linear system of equations Eq. (6.7) is solved by inversion of the Jacobian

$$\vec{p} = \vec{p}_0 + J_\nu^{-1}\vec{\Delta}_0, \tag{6.9}$$

where $\vec{\Delta}_0 = (\Delta_{0,1}, \Delta_{0,2}, \Delta_{0,3})$. Given an (approximate) normality of the distribution of $\Delta_{0,i}$, the propagation of uncertainties via the covariance matrices can be performed [151],

$$\mathrm{cov}(\vec{p}) = J_\nu^{-1}\mathrm{cov}(\vec{\Delta}_0)\left(J_\nu^{-1}\right)^T. \tag{6.10}$$

The statistical uncertainties of the individually fit centers $\Delta_{0,i}$ are not correlated, therefore the covariance matrix is $\mathrm{cov}(\vec{\Delta}_0) = \mathrm{diag}(\sigma^2(\Delta_{0,1}), \sigma^2(\Delta_{0,2}), \sigma^2(\Delta_{0,3}))$. Thus, this treatment allows to directly connect the statistical precision of each measurement $\sigma(\Delta_{0,i})$ with the precision of the extracted parameters and give the correlation of the extracted parameters via the covariances. Additionally, the steps taken here are easily adopted for the propagation of systematic shifts and uncertainties, see the next section.

6.4.2. Systematic analysis

The goal is to fully propagate the systematic effects and their covariances to the fit parameters, i.e.

$$\vec{p}^{\,\prime} = \vec{p} + \delta\vec{p}. \tag{6.11}$$

Here, the real parameters $\vec{p}$ are shifted due to systematic shifts $\delta\vec{p}$ to the observed fit parameters $\vec{p}^{\,\prime}$. Similar to the arguments from the previous chapter, considering the systematic shifts on the determined center frequency of the fit Eq. (6.6)

$$\begin{aligned}\Delta_{0,i}^{\prime} - \Delta_{0,i} &= \nu_i(\nu_{c,0}, \vec{p}^{\,\prime}) - \nu_i(\nu_{c,0}, \vec{p}) \\ &= \left(J_\nu \delta\vec{p}\right)_i\end{aligned} \tag{6.12}$$

greatly simplifies their treatment. Again, inversion of the Jacobian yields

$$\delta\vec{p} = J_\nu^{-1}\delta\vec{\Delta}_0, \tag{6.13}$$

where $\delta\vec{\Delta}_0 = \vec{\Delta}_0^{\,\prime} - \vec{\Delta}_0$. The first order treatment allows to evaluate the Jacobian J_ν at the initial parameters $\vec{p}_0$ and $\nu_{c,0}$. As in Eq. (6.10), the covariance is propagated by

$$\mathrm{cov}(\vec{p}) = J_\nu^{-1}\mathrm{cov}(\delta\vec{\Delta}_0)\left(J_\nu^{-1}\right)^T. \tag{6.14}$$

While the relativistic shift was already given via the shift of the resonance center, Eq. (3.35), all shifts related only to the determination of the magnetic field and thus the cyclotron frequency are not. Given the shifted, observed, cyclotron frequency $\nu_c' = \nu_c + \delta\nu_c$ from which the transition frequency is calculated as ${\nu_i}'(\nu_c') = \nu_i(\nu_c) + (\partial\nu_i/\partial\nu_c)\delta\nu_c$, a shift of the observed resonance occurs to

$$\delta\Delta_{0,i} = -\frac{\partial\nu_i}{\partial\nu_c}\delta\nu_c. \tag{6.15}$$

For the covariances $\mathrm{cov}(\delta\vec{\Delta}_0)$, common and individually evaluated systematic effects need to be differentiated. For example, the image charge shift, Eq. (2.43), can be assumed identical for each resonance $\delta\nu_{c,i} = \delta\nu_c$. In this case, the covariance simplifies to

$$\mathrm{cov}(\delta\Delta_{0,i})_{i,j} = \sigma(\delta\nu_c)^2 \frac{\partial\nu_i}{\partial\nu_c}\frac{\partial\nu_j}{\partial\nu_c}. \tag{6.16}$$

Interestingly, in this case and for the choice of parameters $\vec{p}$ used here, the propagated shift Eq. (6.13) and covariance Eq. (6.14), are non-zero only for Γ_e. This is clear from the definition of the Hamiltonian as a function of ν_c and the parameters $\vec{p}$ in Eq. (6.2), as any systematic shift of ν_c may be directly integrated into Γ_e. Thus, common shifts of the cyclotron frequency just contribute one-to-one to Γ_e.

In the more general cases, the approaches as for example given in ref. [151] must be applied.

6.5. Evaluation of results

First, the three resonance measurements corresponding to the transitions with frequencies ν_1, ν_2 and ν_3 used for the final analysis will be presented. Additional resonances were recorded for the systematics investigations and will be presented there.

6.5.1. Resonances

The final resonances were taken back-to-back, in the order ν_2, ν_1, ν_3, from the 1st to the 19th of December 2022. Each resonance consisted of roughly 400 cycles and took around 5 to 6 days to measure. Details of the three measurements and the fit results are tabulated in Table 6.2 and the resonances are visualized via binned data and the fit confidences in Figure 6.6. The fits are performed via the model Eq. (6.5) and a Voigt lineshape profile. For fitting, the probabilistic programming model, compare Section 5.3.2, is used together with the emcee MCMC sampler [153]. For comparison, the fits were also performed with another MCMC sampler, called NUTS (No-U-Turn Sampler, ref. [154]) and simply via MLE. All approaches produced consistent results, with deviations between the determined center frequencies at least an order of magnitude lower than the uncertainties. The uncertainties on the center frequencies $\sigma(\Delta_{0,i})$ are identical for both MCMC samplers and a few percent smaller for MLE. The uncertainties for ν_1, ν_2, and ν_3, as well as the fit Gaussian widths follow their dependence on the magnetic field, compare Table 6.1.

From the statistical result, the parameters $\vec{p} = (\Gamma_e, \Gamma_I, \nu_{\mathrm{HFS}})$ and covariances are calculated according to Eq. (6.9) and Eq. (6.10), respectively. The required Jacobian matrix is calculated

Table 6.2: Data of the nuclear-spin transition resonances and fit results. The fit center Δ_0 depends on the initial guess $\vec{p}_0$. The full width at half maximum (FWHM) and its uncertainty is directly calculated from the MCMC samples of σ and Ω according to ref. [152]. The second number for $\sigma(\Delta_0)$ is the fractional uncertainty to the average, absolute, transition frequency.

Transition	$\boldsymbol{\nu}_1$	$\boldsymbol{\nu}_2$	$\boldsymbol{\nu}_3$
Number of cycles	381	404	374
Number of spin flips	48	41	43
Range of ν_c/ Hz	29254040.2 ± 0.4	29254040.3 ± 0.2	29254040.4 ± 0.5
Range of ν_{MW}/ Hz	6619883119 ± 2	6551416300 ± 2	6124160824 ± 9
Δ_0/Hz	0.593	1.132	−0.711
$\sigma(\Delta_0)$/mHz	17 \ (2.6 ppt)	26 \ (4.0 ppt)	88 \ (14 ppt)
Gaussian width σ/Hz	0.06(3)	0.11(4)	0.5(2)
Lorentzian width Ω/Hz	0.08(3)	0.07(4)	0.2(2)
FWHM/Hz	0.26(5)	0.35(6)	1.3(2)
Amplitude	0.7(1)	0.47(8)	0.43(8)

accurately by use of forward-mode automatic differentiation, ref. [155]. The approach is justified, as both conditions explained in Section 6.4.1 are met. As shown in Table 6.2, the cyclotron frequency spread is below 1 Hz, resulting in insignificant changes to the product $J_\nu^{-1}(\nu_c)\vec{\Delta}_0$. Additionally, the initial parameter guess $\vec{p}_0$ resulted only in small $|\Delta_{0,i}| < 1.2$ Hz compared to the absolute frequencies $\nu_i > 6$ GHz and a closer initial guess does not significantly alter the results. The statistical results are (for the final analysis two significant digits are given for the uncertainties)

$$\begin{aligned} \Gamma_{e,\mathrm{stat}} = -5479.8633446(11) \setminus (0.2\ \mathrm{ppb}), \quad \Gamma_{I,\mathrm{stat}} = 2.1354753839(11)\times10^{-4} \setminus (0.5\ \mathrm{ppb}), \\ \nu_{\mathrm{HFS,stat}} = -12796971342.569(49)\ \mathrm{Hz} \setminus (4\ \mathrm{ppt}), \\ \rho(\Gamma_e,\Gamma_I)_{\mathrm{stat}} = 0.48, \quad \rho(\Gamma_e,\nu_{\mathrm{HFS}})_{\mathrm{stat}} = 0.80, \quad \rho(\Gamma_I,\nu_{\mathrm{HFS}})_{\mathrm{stat}} = 0.60, \end{aligned} \tag{6.17}$$

where the number behind the backslash gives the fractional uncertainty of the result. The relative fractional uncertainties of Γ_I, Γ_e, and ν_{HFS} are in agreement with the expectation from the sensitivities, compare Table 6.1. The Pearson coefficients $\rho(X, Y)$ as defined in Eq. (5.28) show that the results are quite correlated which justifies the rigorous treatment of the propagation of the covariances.

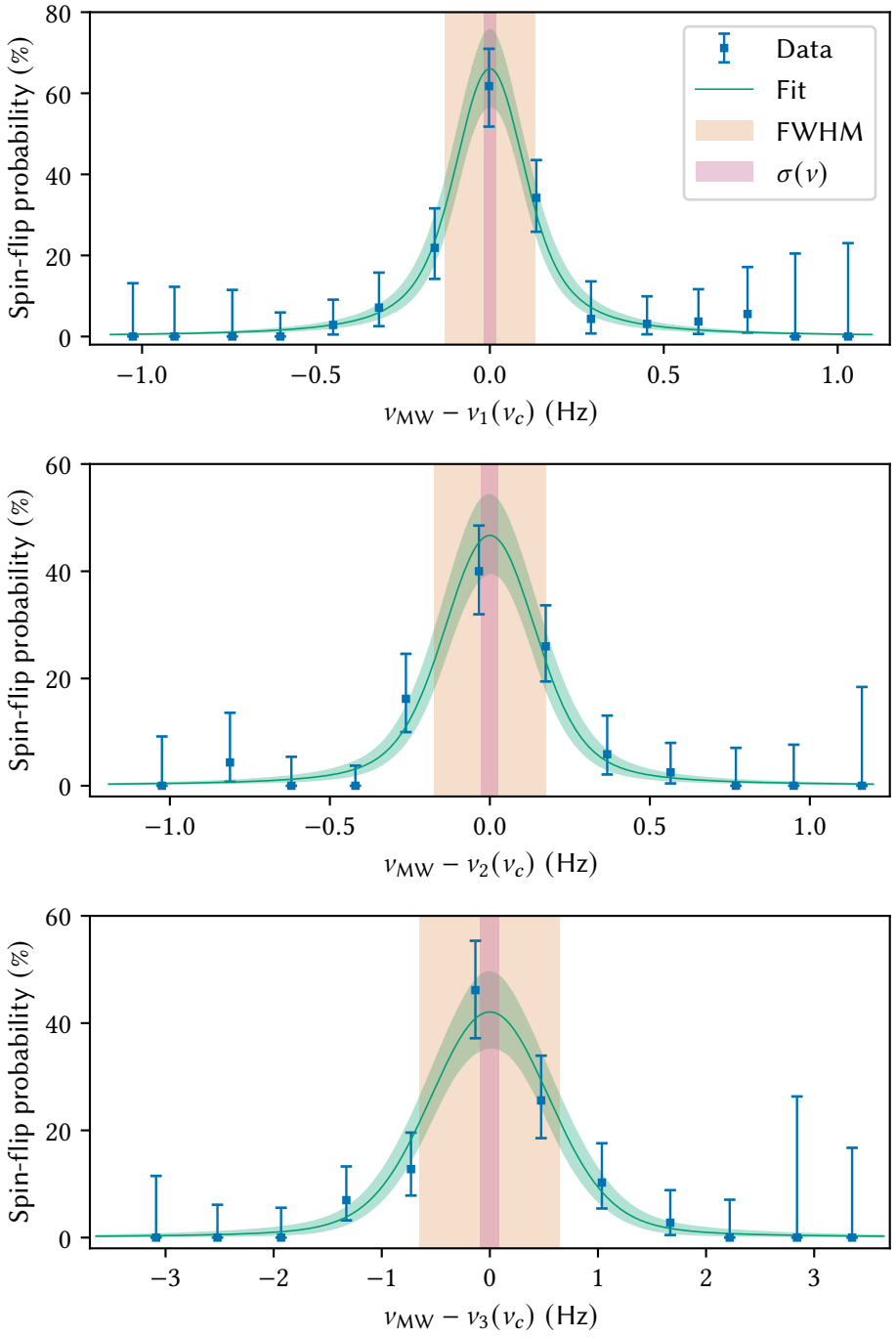

Figure 6.6: Nuclear-spin transition resonances. The frequencies $\nu_i(\nu_c \mid \vec{p})$ are calculated with the statistical fit result of $\vec{p}$. For details on the fit procedure see text. The plotted, binned, data are the number of spin-state changes divided by the total number of tries in that bin, and the error bars are the binomial confidences.

6.5.2. Systematics and error budget

Here, a full account of all relevant systematic shifts and uncertainties is given.

Probability lineshape

The probability lineshapes as discussed in Section 3.3 may influence the determined center frequencies if they include any asymmetries. The B_2 asymmetry, as described by the linewidth parameter $\delta\nu$, Eq. (3.26), is very small for the nuclear transitions, due to their reduced dependence on the magnetic field. The linewidths are 8.6, 16, and 43 mHz for ν_1, ν_2, and ν_3, respectively, about a factor of two smaller than the achieved statistical uncertainties of the centers. In the context of the Brown-Gabrielse treatment of the lineshape, see Section 3.3.3 and refs.[62, 87], $\delta\nu$ needs to be compared to the axial resonator coupling constant (i.e. the dip width), $\gamma_z = 2.52(5)$ Hz. This is firmly in the weak coupling regime, $\gamma_z \gg \delta\nu$, where no asymmetry is expected. Additionally, to further exclude such effects and as the asymmetry-induced shifts of the center are expected to scale with the irradiated microwave amplitude, the ν_2 transition was measured for three different microwave powers, see Figure 6.7. The fit value of the linear

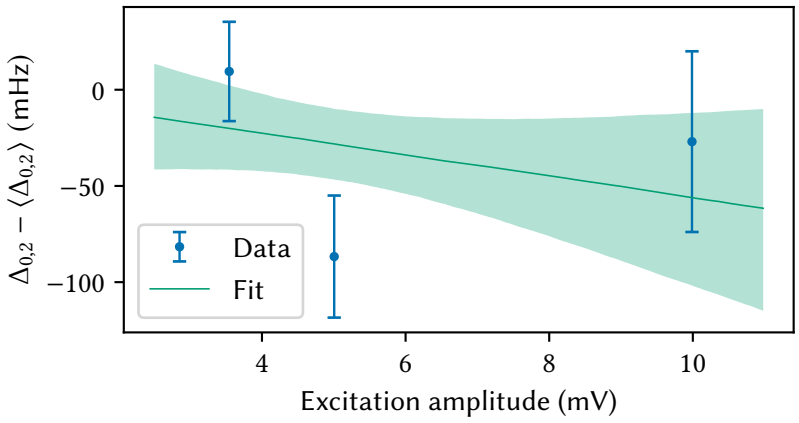

Figure 6.7: The fitted resonance center of the ν_2 transition for three different excitation amplitudes. The value with the lowest amplitude is the one used for the statistical analysis.

dependence is consistent with zero, indicating no scaling with the microwave amplitude.

Another indicator that the probability lineshape has no asymmetry rooted in any decoherent saturation effect, compare Figure 3.5, is that the measurement is, in fact, not decoherent. Already, the amplitude of the ν_1 transition is significantly above the decoherent saturation probability $P = 0.5$, see Table 6.2. To further investigate this, a Rabi flopping experiment was performed. To this end, for several times t of the microwave excitation at frequency $\nu_{\mathrm{MW}} = \nu_1(\nu_c)$ a few cycles ($\sim$ 18) were measured, see Figure 6.8. The lineshape Eq. (3.21) describes the Rabi cycle together with the magnetic field measurement uncertainty $\sigma(\nu_c)$. It fits the data well, indicating no saturation/decoherence effects and the reduction in contrast is fully due to the magnetic field determination uncertainty. The extracted Rabi frequency is

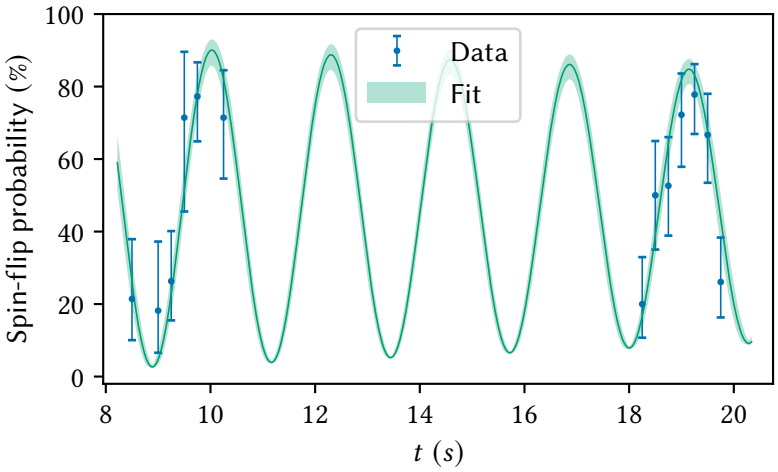

Figure 6.8: Time dependence of the transition probability. The y-data are the number of spin-state changes divided by the total number of tries at the given excitation time t. The fit uses the lineshape Eq. (3.21), which is numerically integrated.

$\Omega = 0.436(4)$ Hz. Using the excitation amplitude for this measurement gives the calibration $\Omega = 6.92(6)\ \mathrm{Hz} \times U_{\mathrm{MW}}/\mathrm{V}_{\mathrm{RMS}}$, where U_{MW} is the voltage amplitude at the microwave generator.

No shift or uncertainty is thus assigned to any asymmetry of the lineshape and using the Voigt lineshape as an approximation of Eq. (3.21) is sufficient.

Field imperfections and relativistic shift

The treatment of all shifts depending on the motional amplitudes is performed simultaneously to account for all relevant correlations. All motional amplitudes are thermalized to the axial resonator and thus related to the thermal axial amplitude $\rho_{z,th}$ via Eq. (2.66). For each individual resonance measurement, $\rho_{z,th}$ is determined from the parameter $\sigma(U_0)$, compare Eq. (5.37). The determined values are $\sigma(U_{0,1}) = 4.8(2)$ mV, $\sigma(U_{0,2}) = 4.7(2)$ mV and $\sigma(U_{0,3}) = 5.1(3)$ mV for ν_1, ν_2 and ν_3, respectively. For the evaluation of the shifts, a mean $\sigma(U_0)$ value is taken and assigned with a conservative, uncorrelated statistical uncertainty of the maximum deviation of the three values. In addition to the uncorrelated uncertainty, the systematic uncertainty of the prefactor in Eq. (5.37) may be taken as a fully correlated uncertainty. In total, $\rho^2_{z,th,i} = 1255(2)_{\mathrm{correlated}}(104)_{\mathrm{uncorrelated}}\ \mu\mathrm{m}^2$, i.e. the correlated uncertainty is basically negligible.

The following shifts from field imperfections contribute to the cyclotron frequency as determined from the invariance theorem, Eq. (2.6),

$$\delta\nu_{c,\mathrm{fields},i} = \rho^2_{z,th,i} \begin{pmatrix} C_3^2/C_2^2 \\ C_4/C_2 \\ B_2/B_0 \\ B_1/B_0 \cdot C_3/C_2 \end{pmatrix} \cdot \begin{pmatrix} -\frac{15}{8}\nu_- \\ -\frac{3}{2}\nu_- \\ \frac{1}{2}\nu_z \\ -\frac{3}{4}\nu_z \end{pmatrix} \equiv \rho^2_{z,th,i}\vec{K}\cdot\vec{L}, \tag{6.18}$$

where some appropriate approximations were made and all shifts which stem from effective

magnetic field shifts were excluded, compare Section 2.3. The vector $\vec{K}$ incorporates all field imperfection parameters. These were measured explicitly and evaluated in a combined way to yield all relevant covariances $\mathrm{cov}(\vec{K})$, compare Section 5.7.4[2]. Numerically, this shift amounts to $\delta\nu_{c,\mathrm{fields},i} = -0.5(1)$ mHz $\setminus -18(4)$ ppt for the cyclotron frequency.

The relativistic Doppler shift on the fitted center frequencies is

$$\delta\Delta_{0,\mathrm{rel},i} = -\rho_{z,th,i}^2 \frac{2\pi^2 \nu_+ \nu_z}{c^2} \left(\nu_i - 2\nu_c \frac{\partial \nu_i}{\partial \nu_c} \right), \tag{6.19}$$

where the opposite sign compared to Eq. (3.35) is due to the changed definition of the primed quantities. The relative relativistic shift of the cyclotron frequency is just the prefactor in front of the parentheses, compare Eq. (2.40), and amounts to $-3.9(2)$ ppt. This is completely insignificant for the double-dip measurements with its 1 ppb single-shot accuracy. For the nuclear transitions, the second term in the parentheses is mostly negligible against the first term, so the relative shift of the center is identical to the cyclotron frequency's. However, as the increased relative precision reached with the nuclear Zeeman and hyperfine transitions is in the low ppt regime, compare Table 6.2, this a very significant systematic.

Using the methods from Section 6.4.2, the shifts on the fit parameters are evaluated as

$$\begin{aligned}
\delta\Gamma_{e,\mathrm{amps}}/10^{-7} &= -1.0(2)_{\mathrm{fields}} - 0.2(3)_{\mathrm{rel}} = -1.2(4) \setminus 22(7)\ \mathrm{ppt}, \\
\delta\Gamma_{I,\mathrm{amps}}/10^{-14} &= 0.0(1)_{\mathrm{fields}} + 0.0(1.1)_{\mathrm{rel}} = 0.0(1.1) \setminus 0(52)\ \mathrm{ppt}, \\
\delta\nu_{\mathrm{HFS,amps}}/\mathrm{mHz} &= 0.0(4)_{\mathrm{fields}} + 50.0(2.6)_{\mathrm{rel}} = 50.0(2.7) \setminus -3.9(2)\ \mathrm{ppt}.
\end{aligned} \tag{6.20}$$

In total, the shifts and uncertainties due to the fields are basically negligible compared to the statistical uncertainties. However, the fractional relativistic shift on ν_{HFS} is very significant and equals exactly $1-\gamma = -3.9(2)$ ppt. This was anticipated, as ν_{HFS} does not depend on the magnetic field and $1-\gamma$ is just the expected Doppler shift. Additionally, the systematic uncertainty of the relativistic shift on Γ_I is amplified to 52 ppt, solidifying the argument for using the thermal double-dip method over the non-thermal phase-sensitive methods. With the latter, assuming $\rho_+ \approx 4\rho_{+,th}$, the uncertainty would increase by at least the same factor to 200 ppt, completely limiting the increased statistical precision which would be reached with the phase sensitive methods.

Thomas precession

The shift due to the Thomas precession, Eq. (3.40), is evaluated directly as a shift on Γ_e and Γ_I. For Γ_e, the ratio of electron Larmor frequency to the ion's cyclotron frequency greatly reduces the shift to $\delta\Gamma_e/\Gamma_e \approx (\gamma-1)/\Gamma_e \approx 10^{-15}$. For Γ_I, the ratio of the nucleus Larmor frequency to the cyclotron frequency is of the order of 1, and the shift $\delta\Gamma_I/\Gamma_I \approx 0.85 \cdot (\gamma-1) \approx 3.3$ ppt is much larger. Still, compared to the statistical precision of Γ_I, this shift is negligibly small. However, for future, more precise measurements of nuclear magnetic moments using the non-thermal, phase-sensitive methods where γ is larger, this shift will have to be taken into account.

[2] During this measurement, no trap symmetrization had yet been performed, and the trapping potential is identical to the one in Section 5.7.4.

Image charge shift

The image charge shift as given in Eq. (2.43) is common for all cyclotron frequency measurements as it depends only on the trap geometry. The 5 % uncertainty is therefore fully correlated, which makes Eq. (6.16) applicable, and the image charge shift only affects Γ_e

$$\delta\Gamma_{e,\mathrm{img}}/10^{-7} = -5.3(3) \setminus 96(5)\ \mathrm{ppt}, \tag{6.21}$$

while both Γ_I and ν_{HFS} neither experience a shift nor a systematic uncertainty.

Dip lineshape

The discussion of the theory description of the observed, thermal, axial detection spectrum and uncertainties of the extracted axial frequency associated with it has several important points. Even for the phase-sensitive methods, where it only contributes via the axial frequency in the invariance theorem, the typically conservative error estimates, see e.g. refs. [76, 156], can lead to significantly large uncertainties. The dip lineshape used here, and the assigned systematic uncertainty are discussed in Section B. In summary, the effective shifts of the determined cyclotron frequency depend on a systematic difference of the axial frequency to the measured resonator frequency $\nu_z - \nu_R$. Here, the resonator frequency is determined with each spectrum, compare Section 5.4, thus the statistical, uncorrelated, uncertainty of ν_R is included implicitly in the data of ν_c. Systematic, correlated, shifts are evaluated conservatively to $\sigma(\delta\nu_c) = 10$ mHz, see Section B. Similar to the image charge shift, this results only in a systematic effect for Γ_e, compare Eq. (6.16),

$$\delta\Gamma_{e,\mathrm{dip}}/10^{-7} = 0(19) \setminus 0.0(3)\ \mathrm{ppb}. \tag{6.22}$$

The uncertainty of 0.3 ppb is larger than the statistical uncertainty of Γ_e, highlighting the need for a thorough understanding of the axial detection signal when using the thermal detection techniques. However, as the results derived from Γ_e play only a secondary role in this measurement, the conservative uncertainty estimate is sufficient here.

Time reference

When measuring frequency ratios ν_1/ν_2, systematic offsets of the time reference $\delta\nu_{\mathrm{ref}}$ cancel, i.e.

$$\frac{\nu_1\left(1+\frac{\delta\nu_{\mathrm{ref}}}{\nu_{\mathrm{ref}}}\right)}{\nu_2\left(1+\frac{\delta\nu_{\mathrm{ref}}}{\nu_{\mathrm{ref}}}\right)} = \frac{\nu_1}{\nu_2}. \tag{6.23}$$

This is the case for bound-electron g-factor measurements without nuclear spin, where ν_L/ν_c is measured, as well as mass ratio measurements, where $\nu_{c,1}/\nu_{c,2}$ is measured[3]. Here, additional care has to be taken due to the large contribution of the constant frequency ν_{HFS} to the measured transition frequencies. Generally, the shift of the center is evaluated as

$$\Delta'_{0,\mathrm{rel},i} = \left(1+\frac{\delta\nu_{\mathrm{ref}}}{\nu_{\mathrm{ref}}}\right)\nu_{\mathrm{MW}} - \nu_i\left(\left(1+\frac{\delta\nu_{\mathrm{ref}}}{\nu_{\mathrm{ref}}}\right)\nu_c\right) = \Delta_{0,i} + \left(\frac{\delta\nu_{\mathrm{ref}}}{\nu_{\mathrm{ref}}}\right)\left(\nu_i - \frac{\partial\nu_i}{\partial\nu_c}\nu_c\right). \tag{6.24}$$

[3] However, this may become relevant when large temporal drifts of the reference occur therefore leading to different shifts for ν_1 and ν_2.

The time reference used here is a GPS locked Rubidium standard (SRS FS725), which has a long-term Allan deviation of just below ~ 1 ppt for days to weeks of integration time, compare ref. [144]. Therefore, a common systematic shift of the reference and a shift between the measurements of the three resonances must be included at this level. Given a correlated as well as uncorrelated uncertainty of $\sigma\left(\frac{\delta\nu_{\mathrm{ref}}}{\nu_{\mathrm{ref}}}\right) = 10^{-12}$, yields the following uncertainties

$$\begin{aligned} \delta\Gamma_{e,\mathrm{ref}}/10^{-7} &= 0.0(1.0) \setminus 0(19)\ \text{ppt}, \\ \delta\Gamma_{I,\mathrm{ref}}/10^{-14} &= 0.0(3.2) \setminus 0(0.15)\ \text{ppb}, \\ \delta\nu_{\mathrm{HFS,ref}}/\mathrm{mHz} &= 0(15) \setminus 0.0(1.2)\ \text{ppt}. \end{aligned} \tag{6.25}$$

The uncertainty on Γ_I is quite significant and comes from the uncorrelated uncertainty of the time reference, whereas the uncertainty on ν_{HFS} is mainly from the correlated uncertainty.

Corrections to the Breit-Rabi energies

Corrections in the form of quadratic Zeeman shifts [157] have been known for a long time and lead to a quadratic B-field dependence in the Hamilton Eq. (3.1). However, the correction term is zero for the angular momentum-free S-states. Nevertheless, for $^9\mathrm{Be}^+$, a dependence of the zero-field splitting $\nu_{\mathrm{HFS}}(^9\mathrm{Be}^+)$ on the external magnetic field was found [141]. Additionally, in systems like ^{85,87}Rb a dependence on the external magnetic field of the extracted g-factor ratio, i.e. Γ_I, has been observed [158] and attributed to shielding effects due to the nuclear quadrupole moment Q present when $I > 1/2$. In ref. [159], second-order effects in the Breit-Rabi energies are evaluated explicitly for hydrogen-like $1S$ systems. Indeed, for $^9\mathrm{Be}^{3+}$, using these formulas with $Q = 0$ gives identical energies to Eq. (3.9), but a significant shift occurs when using the quadrupole moment $Q(^9\mathrm{Be}) = 0.0529(4)\times10^{-28}\mathrm{m}^{-2}$ [160]. The corresponding shifts of the frequencies are $\nu_{Q,1} - \nu_1 = -36.4(3)$ mHz, $\nu_{Q,2} - \nu_2 = 5.69(4)$ mHz and $\nu_{Q,3} - \nu_3 = 4.36(3)$ mHz, where the Q subscript indicates the calculation via the formulas from ref. [159]. Propagating to the parameters gives

$$\begin{aligned} \delta\Gamma_{e,\mathrm{Q}}/10^{-7} &= -4.68(4) \setminus 85.5(6)\ \text{ppt}, \\ \delta\Gamma_{I,\mathrm{Q}}/10^{-14} &= -14.94(11) \setminus -0.700(5)\ \text{ppb}, \\ \delta\nu_{\mathrm{HFS,Q}}/\mathrm{mHz} &= 10.89(8) \setminus -0.851(6)\ \text{ppt}. \end{aligned} \tag{6.26}$$

Here, the significant and negative shift of Γ_I is due to the aforementioned additional shielding effect via the electric quadrupole moment[4].

Summary

All systematic shifts are summarized and corrected for in Table 6.3. Due to the systematic effects, the correlations as expressed by the Pearson correlation coefficients,

$$\rho(\Gamma_e, \Gamma_I) = 0.24, \quad \rho(\Gamma_e, \nu_{\mathrm{HFS}}) = 0.38, \quad \rho(\Gamma_I, \nu_{\mathrm{HFS}}) = 0.56, \tag{6.27}$$

[4]Indeed, the correction depends on the magnetic field. For lower magnetic fields all corrections would be smaller as well.

Table 6.3: Statistical results and error budget. For details see text.

	Γ_e	Γ_I	ν_{HFS}
Statistical result	−5479.8633446(11)	$2.1354753839(11)\times10^{-4}$	−12796971342.569(50) Hz
Systematic shifts	$/10^{-7}$	$/10^{-14}$	/mHz
Field imperfections	−1(< 1)	0(< 1)	0(< 1)
Relativistic	0(< 1)	0(1)	50(3)
Image charge	−5(< 1)	-	-
Dip	0(19)	-	-
Time reference	0(1)	0(3)	0(15)
Quadrupole moment	−5(< 1)	−15(< 1)	11(< 1)
Total shifts	−11(19)	−15(3)	61(15)
Corrected result	−5479.8633435(22)	$2.1354753854(11)\times10^{-4}$	−12796971342.630(52) Hz
Fractional uncertainty	0.39 ppb	0.54 ppb	4.0 ppt

are altered compared to the statistical result, Eq. (6.17). The individual systematic shifts and uncertainties that are significant vary quite a bit over the three fit parameters. For Γ_e, a couple of systematics contribute as significant shifts, while only the dip increases the uncertainty. In the case of Γ_I, only the correction due to the quadrupole moment is significant and the time reference uncertainty contributes slightly. For ν_{HFS} the largest contribution by far is the relativistic shift, followed by a significant shift due to the quadrupole moment, while the time reference uncertainty gives the largest systematic uncertainty.

6.6. The nuclear magnetic moment of ^{9}Be and a first precision test of multi-electron diamagnetic shielding calculations

Here, the measurement of Γ_I is used together with the theory calculation of the bound-electron g-factor and the shielding of $^9Be^{3+}$ to evaluate the bare-nuclear g-factor. The theory calculations of the hydrogen-like system have been performed in the division of Christoph Keitel at the MPIK by Bastian Sikora *et al.* Subsequently, via comparison to $^9Be^+$, a first test of multi-electron diamagnetic shielding calculations is performed.

The nuclear g-factor

The calculation of bound-electron g-factors of hydrogen-like ions in the light-Z regime is performed via a perturbative approach in both the fine structure constant α, via the number of loops in the Feynman diagram and the binding interaction with the parameter $Z\alpha$ [45]. Here, the calculations include corrections of the leading (relativistic) Dirac value by the finite mass (recoil) term, 1-loop QED up to order $(Z\alpha)^5$, 2-loop QED up to $(Z\alpha)^2$ and the leading, $(Z\alpha)^0$, 3-loop term. For the bound-electron g-factor, the finite size of the nucleus contributes only at 5×10^{-11}. The corrections evaluate as [142]

$$g_s(^9Be^{3+}) = 2.0017515747(5). \tag{6.28}$$

The diamagnetic shielding parameter σ [5] incorporates the binding corrections to the bare nuclear g-factor in the composite system,

$$g_I' = g_I(1-\sigma). \tag{6.29}$$

The leading non-relativistic value σ_0 of the shielding in hydrogen-like ions scales with the nuclear charge Z and is given by [40].

$$\sigma_0 = \frac{Z\alpha^2}{3}. \tag{6.30}$$

For $^9Be^{3+}$, this evaluates to about $\sigma_0 \approx 71$ ppm. Similar, to the electron g-factor, relativistic, QED, recoil and finite size effects alter the result. The calculations performed in ref. [142] reveal

$$\sigma(^9Be^{3+}) = 71.15396(18)\ \text{ppm}. \tag{6.31}$$

The uncertainty splits about evenly between the finite size and QED effects. Interestingly, for $^9Be^{3+}$, the QED correction, $\sigma_{\text{QED}}(^9Be^{3+}) = 0.23(13)$ ppb, is very small, owing to a cancellation of different contributions, compare ref. [39]. Given these two theoretical values and the experimental value of the proton-to-electron mass ratio [22], $m_p/m_e = 1836.15267343(11)$, the bare nuclear g-factor can be evaluated

$$g_I = \frac{m_p}{m_e}\frac{g_s(^9Be^{3+})\Gamma_I(^9Be^{3+})}{1-\sigma(^9Be^{3+})} = -0.78495442295(42)_{\text{exp}}(24)_{\text{theo}}, \tag{6.32}$$

where the theoretical uncertainty is in equal parts from $\sigma(^9Be^{3+})$ and the $g_s(^9Be^{3+})$. The total fractional uncertainty corresponds to 0.61 ppb, making this value the second most accurately measured nuclear magnetic moment after the proton [28]. The value given here improves the uncertainty of the previous best value, which was derived from the measurements on $^9Be^+$, see refs. [117, 161], $g_I = 0.784954393(2)$, by a factor of 30. The two values have only a slight tension of 1.5 σ.

Testing diamagnetic shielding parameters

As was outlined in Chapter 1, an experimental verification of the calculation of diamagnetic shielding parameters is necessary to establish their use in precision physics. Here, this is possible via the comparison of the bare-nuclear magnetic moments as extracted from the spectroscopy on $^9Be^{3+}$ and $^9Be^+$. The experimental value of the scaled g-factor ratio from the low B-field measurements, ref. [117], is $\Gamma_I(^9Be^+) = 2.134779853(2)\times10^{-4}$. In the determination of the bare-nuclear g-factor, this 1 ppb uncertainty is dominated by the 30 ppb uncertainty of the calculated shielding parameter, compare ref. [161]. Using the two measurements, the comparison

$$1-\sigma(^9Be^+) = (1-\sigma(^9Be^{3+}))\frac{\Gamma_I(^9Be^+)}{\Gamma_I(^9Be^{3+})}\frac{g_s(^9Be^+)}{g_s(^9Be^{3+})} \tag{6.33}$$

[5] Yes another σ. Please do not confuse it with an uncertainty or standard deviation.

yields an experimental value of the shielding [142]

$$\sigma(^9\mathrm{Be}^+) = 141.8821(11)_{\mathrm{exp}}(12)_{\mathrm{theo}}\ \mathrm{ppm}, \tag{6.34}$$

by use of the theoretical values of the bound-electron g-factors and the shielding in the hydrogen-like charge state. The theoretical uncertainty is limited by the bound-electron g-factor $g_s(^9\mathrm{Be}^+) = -2.0022621287(24)$, which is calculated identically to ref. [161], but includes the updated nuclear recoil correction from ref. [162]. The shielding parameter determined here is a factor of 25 more precise and agrees with the theory value, $\sigma(^9\mathrm{Be}^+) = 141.85(3)$ ppm, ref. [161] on the ppb level, making this a first high-precision test of the calculation of multi-electron diamagnetic shielding parameters.

Compared to calculations of shielding parameters in hydrogen-like systems, the calculation in multi-electron systems is more involved. A fully relativistic value of the hydrogen-like shielding value can be calculated analytically from the single-electron wavefunction obtained by solving the Dirac equation. This value can then be corrected for by binding-QED effects similar to calculations of the bound-electron g-factor [163]. In contrast, for multi-electron systems, approximate wavefunction solutions have to be used. For low-Z lithium-like atoms, fully correlated (Hylleraas) wavefunctions are used to calculate a non-relativistic leading value, which is then corrected for by a relativistic estimate and a recoil term [161, 164]. For helium-like atoms, the calculations are performed similarly by use of correlated wavefunction [165], however, a lot more corrections have been evaluated, including first-order QED and finite size effects [39, 40]. The latter calculations allow giving uncertainties for the ^{3}He atomic shielding much lower than the 0.7 ppb fractional experimental uncertainty [11]. Recently, it was pointed out, ref. [166], that these calculations can be extended to $^9\mathrm{Be}^+$. The experimental value determined here would then serve as an ideal benchmark at the single-digit ppb level, reaching the accuracy required for the ^{3}He atomic nuclear magnetic moment.

6.7. The HFS and effective Zemach radius

The hyperfine splitting ν_{HFS}, for zero angular momentum of the electron, arises from the magnetic dipole-dipole interaction of the nuclear and electron spin. This interaction scales as $1/r^3$, where r is the distance between the electron and nucleus [29]. As s-state electrons have a finite probability density inside the nucleus, the hyperfine splitting is very sensitive to the magnetic structure of the nucleus. It is reasonable to represent it as [52]

$$\nu_{\mathrm{HFS}} = \underbrace{\frac{E_F}{(I+1/2)h}}_{\equiv h\,\nu_{\mathrm{HFS},0}}(1 + a_e + \delta_{\mathrm{pt}} \underbrace{-2Z\tilde{r}_Z/a_0}_{\equiv\delta_{\mathrm{ns}}}), \tag{6.35}$$

where a_e is the electron's magnetic moment anomaly and a_0 the Bohr radius. The term E_F, called the Fermi contact term [29], is the classically calculated zero-field splitting. The term δ_{pt} summarizes all binding corrections which can be calculated from a point-nucleus model. The last term sums up all nuclear structure contributions δ_{ns} via the effective Zemach radius $\tilde{r}_Z$. The effective Zemach radius derives from the most significant contribution of nuclear structure

effects, called the Bohr-Weisskopf effect [167]. Here, the Zemach radius, which is defined by the average length scale of the convolution of the charge $\rho_e(\vec{r})$ and magnetization distribution $\rho_m(\vec{r})$,

$$r_Z = \int r\rho_e(\vec{r}-\vec{s})\rho_m(\vec{s})\,\mathrm{d}\vec{s}\,\mathrm{d}\vec{r} \tag{6.36}$$

contributes as the shift $-2Zr_Z/a_0$ [41]. From a theoretical perspective, two difficulties arise. Firstly, nuclear structure theory cannot predict the Zemach radius with sufficient accuracy, e.g. the best values are currently available for the proton via lattice quantum chromodynamics (QCD) and give a 1% fractional uncertainty [168]. Instead of calculating the Zemach radius them from theory, accurate measurements of the formfactors of nuclei can be used to infer it, e.g. for the proton, ref. [169]. However, the contribution of the polarization of the nucleus in the presence of the orbiting electron is not negligible, e.g. for hydrogen, it contributes another 5% of the leading Bohr-Weisskopf effect [170]. These contributions are currently very hard to evaluate and can instead be absorbed in the definition of the effective Zemach radius [171]. While not a pure property of the free nucleus anymore, this contribution can be assumed equal for different hyperfine splittings with the same nucleus [54]. Therefore, a measurement of the HFS in the hydrogen-like 1s system, which allows the best prediction of the point-nucleus contributions, is ideally suited to extract the effective Zemach radius with the best accuracy and use it as a reference to calculate the nuclear structure contributions to hyperfine splittings in other electronic configurations.

The Fermi energy is directly proportional to the nuclear g-factor [171] and for $^9Be^{3+}$ evaluates to

$$\nu_{\mathrm{HFS},0} = \frac{8}{3}Z^3\alpha^2R\frac{m_r^3}{m_e^3}\frac{m_e}{m_p}g_I = -12779407.7658(39)_\alpha(78)_{g_I}\ \mathrm{kHz}, \tag{6.37}$$

where $m_r = m_e m/(m_e+m)$ is the reduced mass of the electron, and the Rydberg frequency R, all required masses and α were taken from the latest CODATA evaluation [22]. Here, the fine-structure constant α, and the bare g_I of ^{9}Be contribute on similar levels. For $^9Be^{3+}$, the point-nucleus contribution is calculated with corrections due to QED, recoil effects, and also significant hadronic and muonic vacuum polarization contributions. Similary, these calculations were performed by Bastian Sikora *et al.*, and evaluate to [142]

$$\delta_{\mathrm{pt}} = 826.65(28)\ \mathrm{ppm},\quad \delta_{\mathrm{pt}}\nu_{\mathrm{HFS},0} = -10564.1(3.5)_{\mathrm{theo}}\ \mathrm{kHz}, \tag{6.38}$$

where the uncertainty is limited by radiative recoil calculations. The nuclear structure contribution is evaluated from Eq. (6.35),

$$\begin{aligned}\delta_{\mathrm{ns}} = \frac{\nu_{\mathrm{HFS,exp}}}{\nu_{\mathrm{HFS},0}} - (1+a_e+\delta_{\mathrm{pt}}) = -611.94(28)_{\mathrm{theo}}\ \mathrm{ppm},\\ \delta_{\mathrm{ns}}\nu_{\mathrm{HFS},0} = 7820.2(3.5)_{\mathrm{theo}}\ \mathrm{kHz},\end{aligned} \tag{6.39}$$

using the experimental value of $\nu_{\mathrm{HFS,exp}}$, the experimental value of a_e, ref. [22], and the calculated E_F and δ_{pt}. The experimental uncertainty due to $\nu_{\mathrm{HFS,exp}}$ is more than four orders of magnitude smaller than the theoretical uncertainty. The nuclear structure contribution itself is nearly equal in magnitude to the binding corrections to the HFS, and a factor of 10^7 larger than

the nuclear structure contributions to the bound-electron g-factor, highlighting the sensitivity of the HFS to nuclear structure. Using the definition of the effective Zemach radius, compare Eq. (6.35), gives

$$\tilde{r}_Z = -\frac{\delta_{\mathrm{ns}}}{2Z} a_0 = 4.0423(18)_{\mathrm{theo}}\ \mathrm{fm}. \tag{6.40}$$

Compared to the value evaluated from the measurement on the lithium-like $^9Be^+$, refs.[117, 172], $\tilde{r}_Z = 4.07(5)_{\mathrm{theo}}(2)_{g_I}$, this constitutes an improvement in accuracy by a factor of about 25[6]. The increased accuracy is made possible by the much better theory calculation of δ_{pt} possible in $^9Be^{3+}$, where no multi-electron calculations need to be performed. The two values are consistent, which indicates agreement of the multi-electron theory in $^9Be^+$.

Regarding future improvements of the hydrogen-like theory, the uncertainty of the bare-nuclear g-factor may become relevant, compare Eqs. (6.37, 6.38). Here, the uncertainty of g_I would limit only after a more than two orders of magnitude improvement. In contrast, for ^{6,7}Li the current fractional uncertainties on the nuclear magnetic moments of 460 and 170 ppb are already close to limiting the extraction of the effective Zemach radius [54]. Similarly, the current best test of the HFS at high Z with ^{209}Bi is strongly limited by the nuclear magnetic moment which is only known with 500 ppm uncertainty.

HFS comparison

Similar to the comparison done for $^{209}Bi^{80+,82+}$ [37, 38], forming a specific difference of the lithium-like to the hydrogen-like HFS to test the lithium-like theory is now possible. In ref. [142], the weighting factor $\xi = \nu_{\mathrm{HFS},0}(^9Be^+)/\nu_{\mathrm{HFS},0}(^9Be^{3+}) = 0.04881891046$ is derived which cancels the nuclear structure contributions in the difference

$$\Delta\nu_{\mathrm{HFS}} = \nu_{\mathrm{HFS}}(^9Be^+) - \xi\nu_{\mathrm{HFS}}(^9Be^{3+}), \tag{6.41}$$

compare Eq. (6.35). This cancels the leading contributions, but also some bound-state corrections such that the difference

$$\Delta\nu_{\mathrm{HFS,theo}} = -271.4(3.6)\ \mathrm{kHz} \tag{6.42}$$

is rather small. The remaining contributions are relativistic corrections of order α^6 and QED corrections of order α^7 [172]. Using the experimental value from ref. [141], $\nu_{\mathrm{HFS}}(^9Be^+) = -625008.837044(12)$ kHz, which accounts also for the B-field dependence of $\nu_{\mathrm{HFS}}(^9Be^+)$, the experimental difference is

$$\Delta\nu_{\mathrm{HFS,exp}} = -274.638909(12)\ \mathrm{kHz}, \tag{6.43}$$

where the uncertainty is limited by $\nu_{\mathrm{HFS}}(^9Be^+)$. The experimental value has a vastly smaller uncertainty compared to the theory value, highlighting the precision achievable in Penning-trap measurements of hyperfine splittings. The experimental and theoretical values agree, therefore confirming the calculations performed in ref. [172] and identical calculations used for ^{6,7}Li [54].

[6] The uncertainty of g_I could in principle be removed by using the value of g_I derived here.

6.8. The atomic mass of ^{9}Be

Lastly, the atomic mass of ^{9}Be may be derived from Γ_e, compare Eq. (6.1),

$$m(^9\mathrm{Be}) = \frac{q}{e}\frac{2}{g_s} m_e \Gamma_e + 3m_e - \Delta m_{\mathrm{binding}} = 9.0121830344(35)\ \mathrm{u}, \tag{6.44}$$

using the electron mass in atomic units [22], the mass equivalent of the ionization energies $\Delta m_{\mathrm{binding}} = 194.773164(44)$ pu, refs. [173–175], and the theory value of $g_s(^9\mathrm{Be}^{3+})$, Eq. (6.28). This value is in agreement with the accepted value, $m(^9\mathrm{Be}) = 9.01218306(8)$ [176] and improves on its uncertainty by a factor of 20.

Chapter 7.

Measurement of bound-electron g-factor resonances

In this chapter, the superior phase-sensitive detection of the modified cyclotron frequency is used to determine

$$\Gamma_e = \frac{g_s}{2}\frac{e}{q}\frac{m}{m_e} \tag{7.1}$$

with the highest possible precision. In the following, this type of measurement will also be referred to as 'bound-electron g-factor measurement'. Such a determination has two prominent applications. Given a similarly precise value of the ion-to-electron mass ratio, the bound-state QED contributions to the bound-electron g-factor can be tested. Especially for medium to high Z ions where the bound-state QED contributions are large, QED is tested with high stringency [5, 17, 18]. For light hydrogen-like ions, $Z \leq 6$, the calculation of bound-electron g-factors is believed to be correct with fractional uncertainties below 10 ppt and thus, in turn, the ion-to-electron mass ratio can be determined with high precision [20]. For example, the measurement of $g_s(^{12}C^{5+})$ allowed to directly determine the electron mass in atomic mass units with an, at the time, more than one order of magnitude improved precision [23].

While in principle all transitions of the Zeeman and hyperfine splitting are equally sensitive to Γ_e, compare Table 6.1, the nuclear spin transitions have a similarly large sensitivity to Γ_I and increased sensitivity to ν_{HFS}. Therefore, an improved determination of Γ_e from a nuclear-spin transition would require an increased precision on Γ_I and ν_{HFS} as well. That is not the case for the electron spin transitions, where the precision of Γ_I and ν_{HFS} as determined in the last chapter, does not limit the extraction of Γ_e.

First, I will discuss the characterization of the phase-sensitive detection of the modified cyclotron frequency including potential pitfalls which need to be accounted for. Next, several measurements of electron-spin transition resonances that profit from a more than two times improved resonance width when compared to any other bound-electron g-factor resonance to date will be presented. Thereafter, systematic effects will be discussed. Lastly, the results will be put into a broader perspective.

7.1. Characterization and optimization of the phase-sensitive detection of ν_+

While the measurements of nuclear-spin transitions may currently not benefit from the phase-sensitive detection of ν_+, measurements of electron spin transitions have no such limitations. Both the Doppler shift and the time reference, in contrast to the nuclear-spin transitions, do not contribute significantly to the uncertainty budget, as will be discussed in the systematics section.

The theoretical description of the phase-sensitive detection of ν_+ and the associated statistical precision due to various effects is given in Section 2.8. An overview of the experimental setup and the determination of absolute frequencies is given in Section 5.5. Here, a number of characterization measurements relevant to the phase-sensitive detection of ν_+ will be presented. At last, the phase-sensitive ν_+ detection will be compared to the double-dip measurement, highlighting the vastly improved measurement precision.

7.1.1. Initial optimizations

Firstly, measuring stable phases for short evolution times is required, i.e. successive phase measurements should be distributed around a center value and not uniformly distributed on the circle. This indicates that both the phase imprint of the dipole excitation pulse is strong enough and that the coupling pulse transfers the phase to the axial mode, compare Section 2.8.2. Optimizing the dipole excitation pulse separately is easier with PnP because the coupling pulse parameter $T_{\text{couple}} = \frac{\pi}{2}\frac{1}{\Omega}$ can be directly calculated from the Rabi frequency Ω of the measured splitting of the double dip. The dipole excitation pulse length or amplitude is then increased while monitoring the detected Fourier transform signal after the PnP sequence. A clear peak signal above the resonator's noise signal indicates a sufficient excitation amplitude and a coherent, stable, phase. After optimizing the dipole pulse with PnP, similarly, the coupling pulse amplitude or length can be optimized for PnA. In the next step, the amplitude calibration of ρ_+ can be performed, compare Figure 5.15 and Table 5.5. With the knowledge of the excited and thermal amplitudes, the phase uncertainty can be estimated, compare Section 2.8.2, and optimal parameters can be chosen for the dipole excitation pulse.

The chosen dipole excitation pulse length of $T_{\text{exc}} = 0.3$ MCyc gives an excitation amplitude of $B_+ = 12.2(2)$ µm compared to the thermal amplitude $\rho_{+,th} = 4.5(1)$ µm (Section 5.7.5). The expected PnA phase jitter for a short evolution time, where no systematic frequency shifts or magnetic field drifts contribute, can be calculated as shown in Figure 2.11 and amounts to about $\sigma(\varphi_{\text{ref}}) \approx 25°$. The measured reference phase jitter, chosen here with $T_{\text{ref}} = 0.1$ s, is a bit larger with $\sigma(\varphi_{\text{ref}}) = 29(1)°$. This difference may be due to a residual readout jitter from the detection system, compare Section 2.8.2. While the reference phase measurement is needed to account for the ab-initio unknown phase offset, compare Eq. (2.79), the phase measurement with the longest possible evolution time $T_{\text{evol, max}}$ defines the achievable precision to determine ν_+, compare Eq. (2.72). Here, it was possible to use a maximum evolution time $T_{\text{evol, max}} = 45.1$ s. With this value, the measured phase jitter is consistently $\sigma(\varphi_{\text{max}}) < 50°$ ensuring a sufficiently stable phase readout. However, the measured phase jitter was not constant. While it could be as low as $\sigma(\varphi_{\text{max}}) = 32(1)°$ for a few days, it also increased to close to $\sigma(\varphi_{\text{max}}) \approx 50°$ at other

times. To estimate the jitter contributions from systematic effects, the calculation Eq. (2.83) is used. Using the field imperfections, Table 5.5, and the relativistic shift of ν_+, Eq. (2.40), the total systematic contribution is $\sigma(\varphi_{\text{syst}})/T_{\text{evol}} = 0.237(4)^\circ\, s^{-1}$. For $T_{\text{evol, max}} = 45.1$ s this evaluates to $\sigma(\varphi_{\text{max, syst}}) = 10.7(2)^\circ$. From the experimental measurements, the minimal increase in jitter is $\sqrt{\sigma(\varphi_{\text{max}})^2 - \sigma(\varphi_{\text{ref}})^2} = \sqrt{(31(1)^\circ)^2 - (29(1)^\circ)^2} = 11(4)^\circ$. Therefore, for the minimal experimental jitter at the maximum evolution time, the expected increase is explained by the jitter due to systematic effects. The additional increase at times with higher phase jitter is thus possibly from real magnetic field fluctuations. Other Penning trap experiments also face limitations of their measurement uncertainty which are not explainable by their systematic effects, see for example Alphatrap [19] and the free electron g-factor experiment [177].

7.1.2. Non-zero phase residuals during N-determination

During the very first attempts with the phase-sensitive detection of ν_+, the residuals of the N-determination scheme, compare Eq. (5.9), clearly deviated from zero, see Figure 7.1. This was

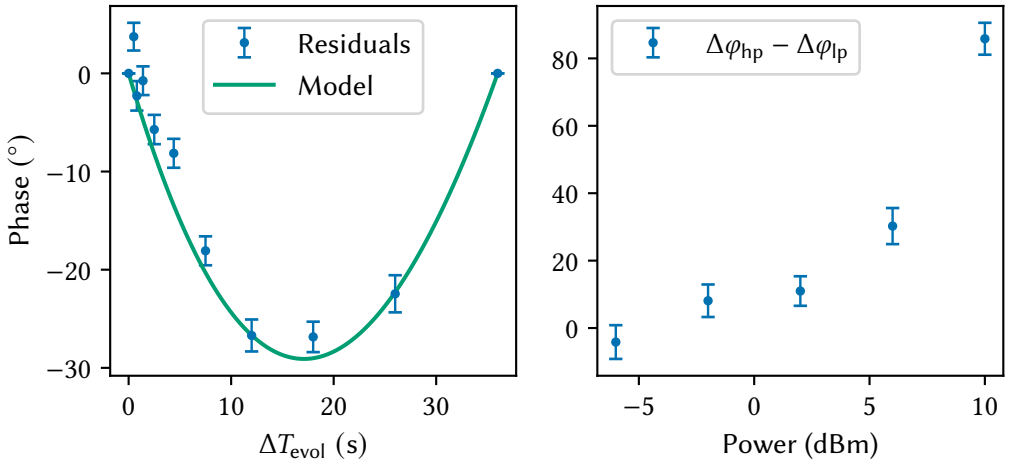

Figure 7.1: The left plot shows the residuals $2\pi\nu_+\Delta T_{\text{evol}} - \Delta\varphi - 2\pi N$ in the N-determination scheme, compare Eq. (5.9). A simple model is shown alongside the data, for details see text. The plot on the right-hand shows the difference of the measured phase for $\Delta T_{\text{evol}} = 30$ s for increasing power of the modified cyclotron cooling sideband $\Delta\varphi_{\text{hp}}$ to a reference measurement at low power $\Delta\varphi_{\text{lp}}$.

concerning, as it implied an evolution time dependence of the determined ν_+. Several effects may cause this dependence. For example, a mismatch between the trigger pulses of the delay generator and the programmed delay between the excitation and coupling pulse in the signal generator could result in effectively slightly different values of T_{evol} for both devices. As both are locked to the same 10 MHz reference, this would require an unexplained hardware effect. Precise oscilloscope measurements of the trigger and signal generator pulses could exclude this effect. Another plausible effect would be an induced frequency drift due to the involved pulses.

Assuming a simple exponential response to ν_+

$$\nu_+'(\tau) = \nu_+ + \delta\nu_+ e^{-t/\tau}, \tag{7.2}$$

with $\tau = 60$ s and $\delta\nu_+ = -60$ mHz results in very similar shape of the residuals, see Figure 7.1[1]. Here, after some investigations, the relatively large power of the cyclotron cooling sideband was found to lead to heating of a few mK of our cryogenic setup, which was detected with a temperature probe close to the trap chamber. This is most likely amplified by the use of the spin-flip coil for the quadrupolar excitations (as pointed out before, the split electrode excitation was broken). Compared to excitations over the split electrode, more power was needed for the same coupling Rabi splittings. Cyclotron cooling is performed before each PnA cycle, and the heating likely leads to a direct magnetic field response and thus the observed residuals. A direct measurement of this effect as a function of the power of the cooling sideband confirmed this, see the second plot of Figure 7.1.

To eliminate this effect, the power of the cooling sideband was reduced by 20 dB to −10 dBm, and a 10 s delay after cooling and before starting the PnA sequence was introduced. From combining the N-determination measurements of a number of electron-spin resonances, Figure 7.2, the residual effect can be conservatively estimated to be smaller than 2°. This corresponds to a 4 ppt uncertainty.

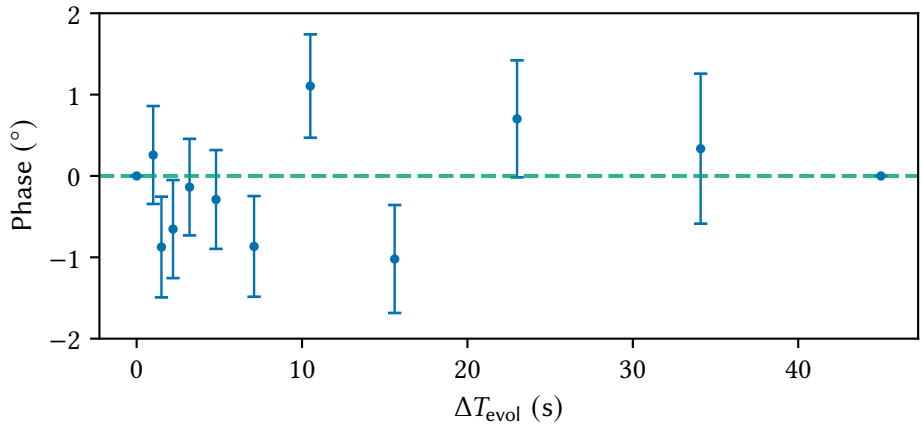

Figure 7.2: The phase residuals are greatly reduced compared to Figure 7.1 by lowering the cooling sideband power and using a delay.

7.1.3. Non-linear phase transfer

Another possible systematic effects is explained in ref. [133] Section 5.2. A residual dipole contribution at frequency ν_+ of the coupling pulse would lead to a non-linearity of the transferred modified cyclotron to the axial phase. To exclude such an effect, the PnA cycle is performed with short evolution times which scan the full 360° of φ_+. Here, 6 steps separated by 5 ms starting from $T_{\mathrm{evol}} = 1.0$ s were chosen. The phase residuals $\varphi - a(T_{\mathrm{evol}} - b)$, where a and b are

[1] A fit was not possible as it diverged for both $\delta\nu_+$ and τ. Very likely the response is more complex.

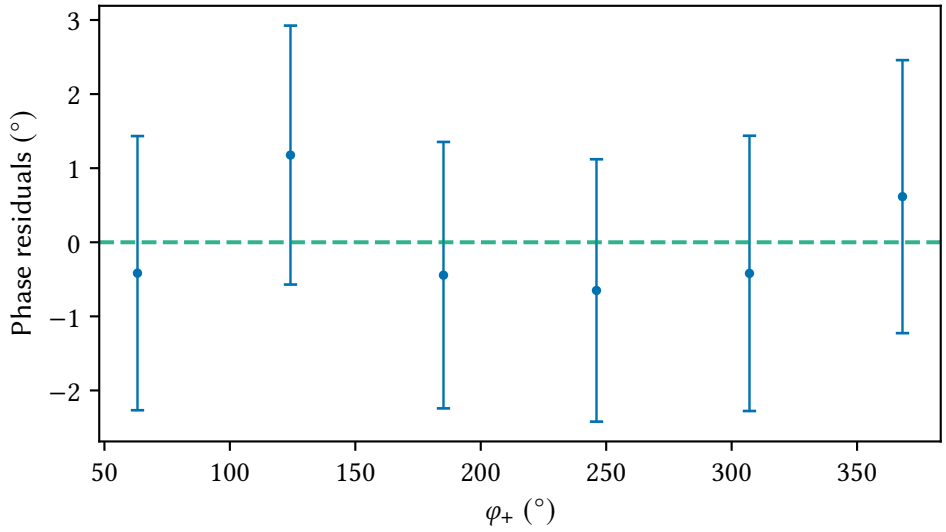

Figure 7.3: Shown are the residuals of the detected phase to a linear fit. The residuals are consistent with zero.

fit, are all consistent with zero and exclude non-linearities to below 3°, compare Figure 7.3.

7.1.4. Pressure dependence of the magnetic field

Though the superconducting magnet system used in this experiment has been designed to be largely unaffected by environmental influences [98], at the highest precision possible with the phase-sensitive detection they may still play a major role. It is well known that the magnetic field in superconducting magnets depends on the pressure of the LHe reservoir, see e.g. ref. [178]. This is explained by the induced changes to the boil-off temperature of the liquid helium, which indirectly leads to magnetic field changes. In normal operation of the superconducting magnet used here, the boiled-off LHe just exits into the atmosphere, flowing only through a passive check valve. The pressure inside the magnet reservoir thus directly follows the ambient air pressure changes. Using the PnA method, the cyclotron frequency was measured continuously over many hours while monitoring the ambient pressure in the magnet room, see Figure 7.4. Assuming a simple proportionality of the cyclotron frequency changes to the changes of the ambient pressure $\Delta\nu_c = a\Delta P$ fits the data perfectly, and only a comparably small drift of ν_c remains in the residuals. The proportionality amounts to

$$a = 0.3967(3)\ \text{mHz/pa} \mathrel{\hat{=}} 77.60(6)\ \text{pT/pa}, \tag{7.3}$$

where the uncertainty is only statistical and systematic uncertainties of the pressure sensor (BMP380) may be larger. Incidentally, this dependence has been measured with this magnet before, albeit with a completely different cryogenic insert, see ref. [101]. The value $a = 92(14)$ pT/pa is consistent with the one measured here.

Thus, by stabilizing the boil-off pressure of LHe in the magnet system the temporal stability of the magnetic field would vastly increase. As part of the PhD thesis of Marius Müller, a

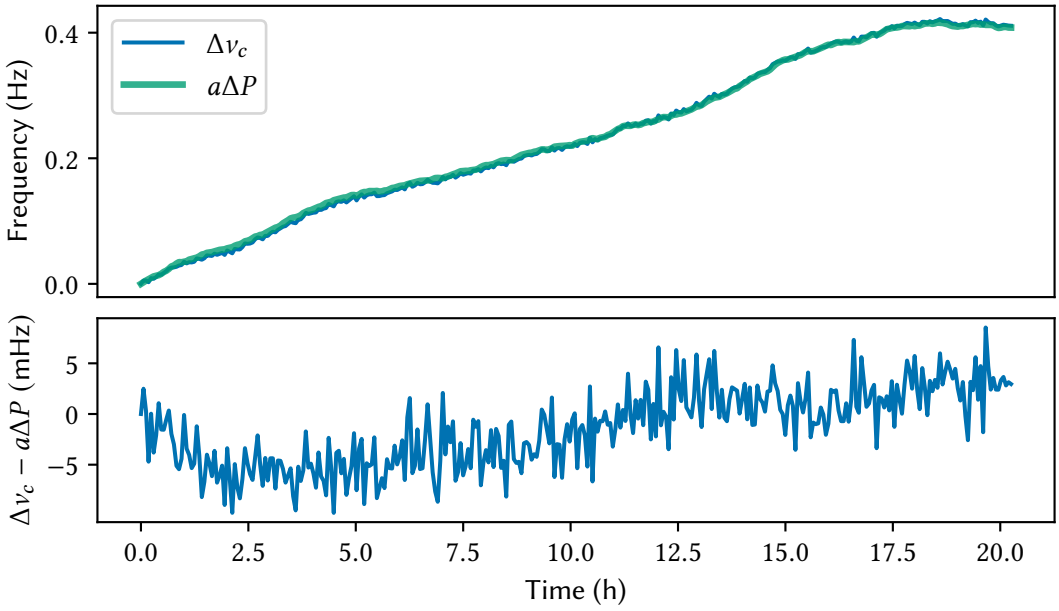

Figure 7.4: Pressure dependence of the magnetic field. The top shows the measured changes of the cyclotron frequency and the scaled changes of the ambient pressure. The scaling factor is fit via least squares estimation. The bottom shows the residuals. In the residuals, the range of the drift is reduced from 0.4 Hz to less than 10 mHz; a reduction by a factor of 40.

pressure stabilization system was developed, which is used for the measurements performed in this chapter. In short, a PID controller calculates the error signal from the measured pressure in the boil-off volume and then adjusts the pressure by regulating the flow of the boiled-off helium with a digital flow controller.

The long-term stability of the magnetic field reached by accounting for the pressure's influence is already at a level that will not influence the statistical precision, see also the next section. Investigations of other environmental influences on the relative stability of the magnetic field would require more thorough systematic measurements. Potentially, the effect that limits the jitter of the modified cyclotron frequency, compare Section 7.1.1, could be identified and accounted for.

7.1.5. Comparison to double-dip and magnetic field stability

For comparing the performance of the double-dip to the PnA method and analyzing the magnetic field stability, the data taken during electron-spin transition resonances can be used. Here, the cyclotron frequency is measured with the double-dip method and PnA method consecutively every $\sim$ 30 minutes over the span of several days, see also the next section[2]. For the double dip, the averaging time is 60 s, and for PnA the evolution time is $\Delta T_{\mathrm{evol}} = 45.0$ s. Fig-

[2]For the comparison performed here, ν_c is calculated from a single double-dip and PnA measurement, respectively, and not from the averages used for the resonance analysis.

ure 7.5 shows such data for a resonance with 252 cycles. The shot-to-shot stability, which cor-

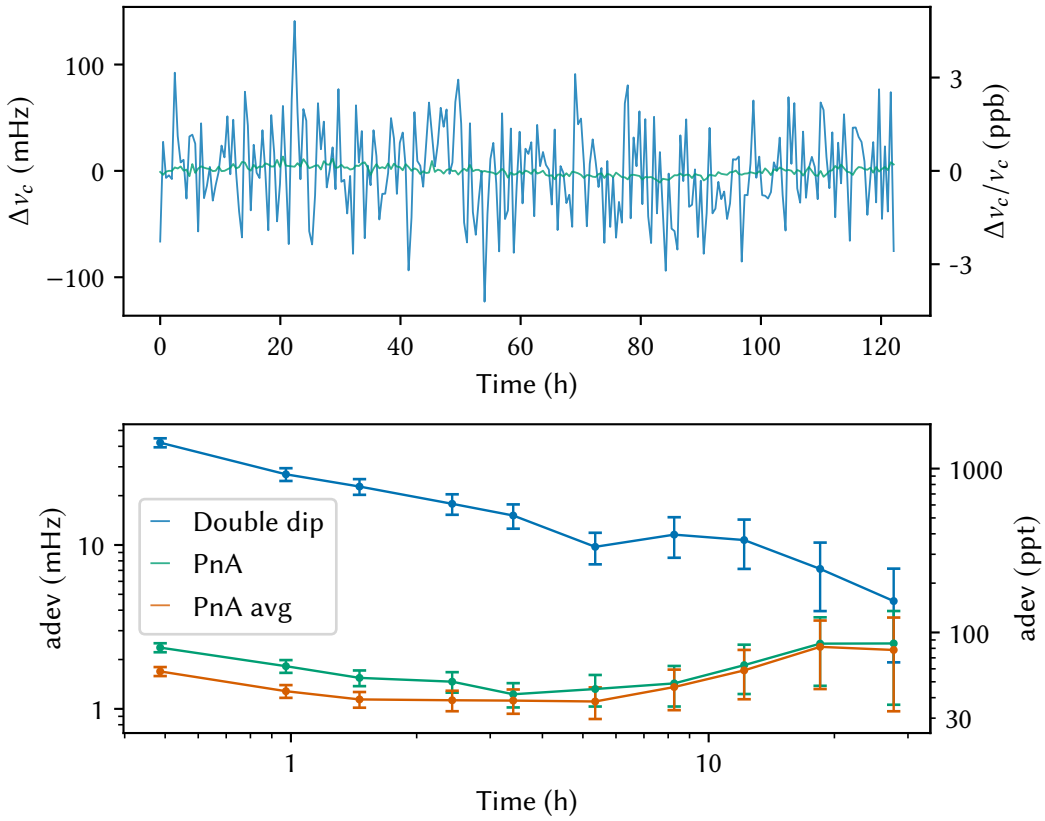

Figure 7.5: Measured cyclotron frequency with the double-dip and PnA method with active pressure stabilization. The data is taken from an electron-spin resonance measurement, where ν_c is measured with the double-dip and the PnA method consecutively every $\sim$ 30 minutes. The top plot shows the cyclotron frequency changes to the mean value and the bottom plot shows the Allan deviation. For details see text.

responds to the first data point in the Allan deviation, is improved by a factor of nearly 20 with the phase-sensitive detection of ν_+. Expressed differently, about 400 double-dip measurements would need to be averaged to match the single-shot precision of the phase-sensitive method. From the last point of the Allan deviation, the long term drift of the cyclotron frequency can be estimated as

$$\sigma(\nu_c)_{\text{drift}}/\nu_c = 3(2)\ \text{ppt/h}. \tag{7.4}$$

The small drift allows to average several measurements of ν_c in a single cycle of the transition measurements to improve its precision and thus the width of the resonance, compare Section 3.3. Therefore, three ν_c measurements with PnA are performed each cycle, see the Allan deviation of the average in Figure 7.5.

As an interesting side note, the magnetic field trend features a distinctive, repeatable, kink about 10 days after filling the magnet with LHe, see Figure 7.6. For future, further improved

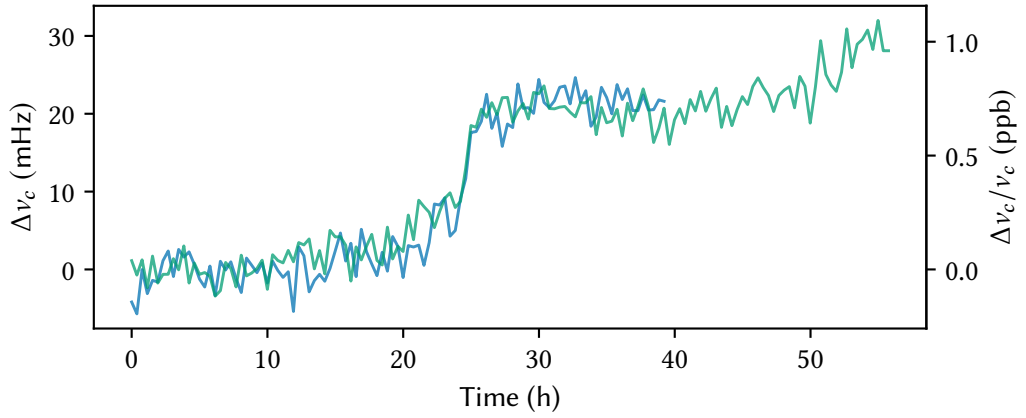

Figure 7.6: The cyclotron frequency (magnetic field) trend features a distinctive 'kink' which occurs repeatably about 10 days after filling the magnet with LHe, i.e. between the blue and green curve the magnet was filled with LHe. After this kink occurs, the cyclotron frequency features a small drift (only visible for the green curve here).

measurements, it might be advantageous to restrict data taking to the times before the kink occurs, as also the shot-to-shot uncertainty seems to increase slightly afterwards.

7.2. Measurement sequence

The measurement sequence of a single cycle is similar to the nuclear spin transition measurements, Section 6.3, and summarized in Figure 7.7. Some specifics to this sequence are summarized below.

Spin-state detection

In contrast to the detection of the nuclear spin state, no double-resonance detection was necessary. The same electron-spin transition driven in the PT was used in the AT for detection. Here, the sign of the axial frequency jump identified the electron-spin orientation, compare Eq. (3.43) and the right-hand plot in Figure 6.4, and only a single electron-spin flip needed to be detected in the AT.

PnA measurements

Prior to triggering any PnA sequence, the modified cyclotron mode was cooled for 5 s which was followed by a 10 s waiting time, compare Section 7.1.2. Additionally, as the double-dip measurements use the same drive as the cyclotron cooling, 60 s of wait time were used to settle any potential drifts. Before the N-determination sequence and the three individual PnA sequences with the longest evolution time, the magnetron mode was cooled for 10 s followed by a 10 s waiting time. For the N-determination, first, the reference phase at 0.1 s was measured

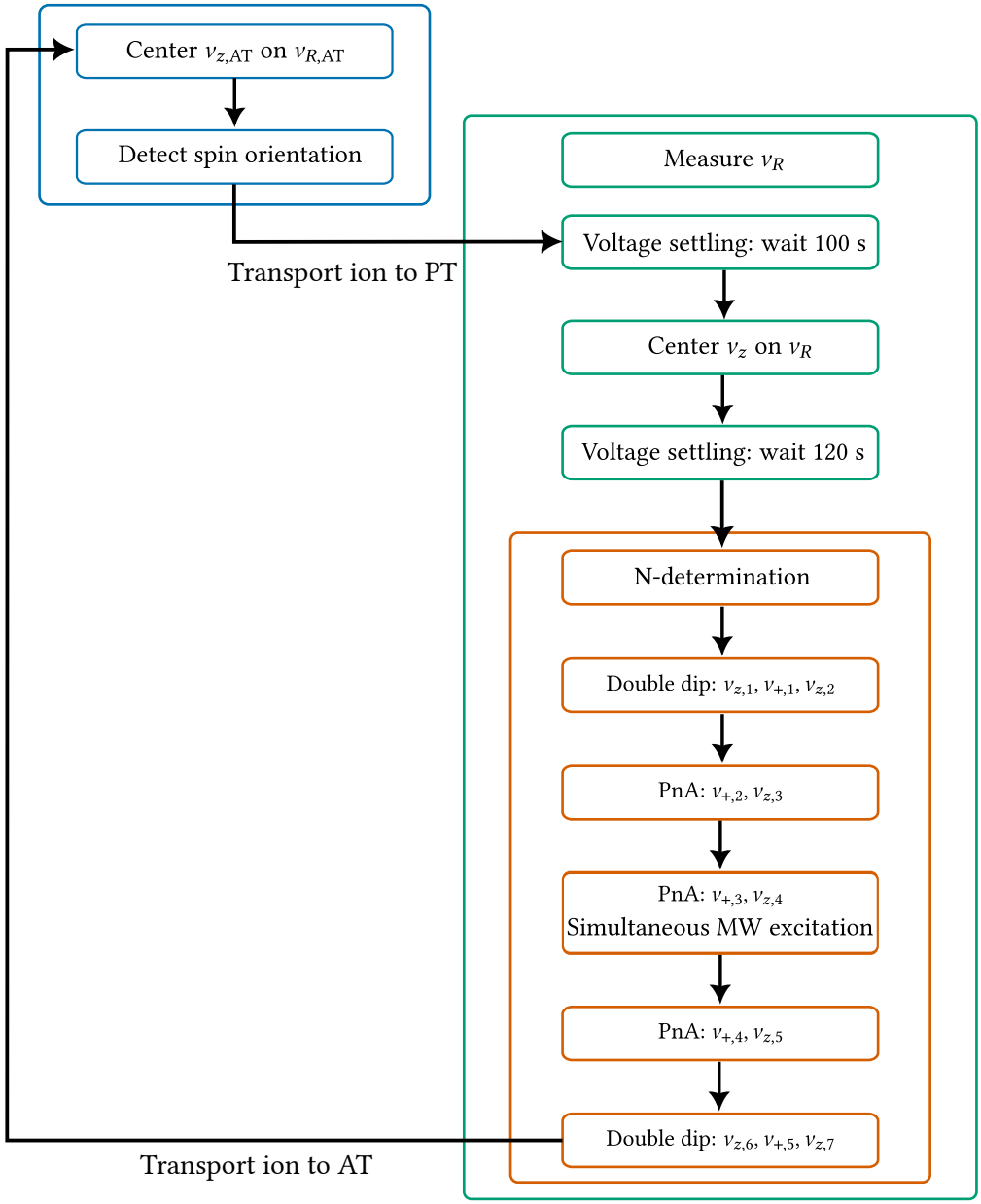

Figure 7.7: Measurement scheme for electron-spin transitions. The blue box indicates measurements in the AT, the green box measurements in the PT, and the orange box the high-precision frequency measurements. For details see text.

four times and averaged. A total of 10 increasing evolution times

$$T_{\text{evol}} = \{1.1, 1.6, 2.3, 3.3, 4.9, 7.2, 10.6, 15.7, 23.1, 34.2\}\ \text{s}, \tag{7.5}$$

were used to determine N together with the double-dip measurement $\nu_{+,1}$ performed afterwards. During the free evolution of the phase-measurements with the longest evolution time, $T_{\text{evol}} = 45.1$ s, ν_z measurements via an axial dip were performed.

Microwave excitation

Due to the vastly different power requirements to drive the electron-spin transition in the AT and the PT, compare ref. [96], a programmable waveguide attenuator (Mi-Wave 511) was used. In the AT the attenuation was set to 0 dB, while in the PT it was set to around 55 dB. Similar to the nuclear-spin transition measurements, the attenuation value for the PT had to be optimized with partial resonance measurements. Using the guess frequency $\nu_i(\nu_c)$, where ν_c is calculated from $\nu_{+,2}$ and $\nu_{z,3}$, the microwave excitation of the transition in the PT was performed during the free evolution time of the second PnA measurement $\nu_{+,3}$.

Cycle time

The spin-state detection procedure in the AT required on average $\sim$ 3 minutes. The transport to the PT, centering and voltage settling required 5 minutes. During the following precision determinations of ν_c, 17 phases, 7 axial dips, and two double dips were measured, totaling close to 20 minutes. The average time per cycle was just below 30 minutes.

7.3. Statistical and systematic evaluation

The statistical and systematic analysis uses the same concepts as outlined in Section 6.4. The free cyclotron frequency used for the analysis is calculated from the average values

$$\begin{aligned} \nu_+ &= \frac{1}{3}(\nu_{+,2} + \nu_{+,3} + \nu_{+,4}), \\ \nu_z &= \frac{1}{4}(\nu_{z,1} + \nu_{z,2} + \nu_{z,6} + \nu_{z,7}), \end{aligned} \tag{7.6}$$

compare Figure 7.7. The axial frequencies during the free evolution time, $\nu_{z,3}, \nu_{z,4}, \nu_{z,5}$, are shifted by the increased cyclotron amplitude and were instead used to rule out any drifts of ν_z.

Similar to the nuclear-spin transitions, a Voigt lineshape is used for the statistical analysis of the resonances. However, for the electron-spin transitions, the asymmetric lineshape due to B_2, compare Section 3.3.3, is potentially relevant. Due to the relatively large B_2 in the PT, the linewidth parameter, Eq. (3.26), of the electron-spin resonances,

$$\Delta\nu_{a,b} = 18(1) \text{ Hz}, \tag{7.7}$$

is similar in magnitude to the expected Gaussian width $\sigma_{\nu_{a,b}} = \left|\frac{\partial\nu_{a,b}}{\partial\nu_c}\right|\sigma(\nu_c) \approx 9$ Hz, compare Eq. (3.19), of the resonances. This leads to a broadening of the resonance. Additionally, the relation $\Delta\nu_{a,b}/\gamma_z \approx 7$ puts the resonances into the weak coupling regime, where the Brown-Gabrielse line approaches the asymmetric Boltzmann distribution, compare Figure 3.4. As visualized in Figure 3.5, this may lead to significant shifts of the resonance center, when fitting

with a symmetric lineshape (e.g. the Voigt-profile). Therefore, additional to the Voigt-profile, the Brown-Gabrielse line is used for fitting the resonances.

For the electron-spin transitions it is sufficient to only fit $p = \Gamma_e$ and use Γ_I and ν_{HFS} from the results of the previous chapter. The covariance of the determined center Δ_0 of the electron spin-resonances due to the covariance of $\vec{q}_0 = (\Gamma_I, \nu_{\mathrm{HFS}})$ is

$$\mathrm{cov}(\Delta_0)_j = \left(\nabla_{\vec{q}}\nu_j(\vec{q}_0)\right)^T \mathrm{cov}(\vec{q}_0)\nabla_{\vec{q}}\nu_j(\vec{q}_0), \tag{7.8}$$

where $\nabla_{\vec{q}}\nu_j(\vec{q}_0)$ is the gradient of the two transitions $j = \{a, b\}$ with respect to $\vec{q}$. Using the covariance from the last chapter, this corresponds to $\sigma(\Delta_{0,a}) \approx 39$ mHz and $\sigma(\Delta_{0,b}) \approx 71$ mHz. Propagating to Γ_e gives systematic uncertainties of less than 0.5 ppt, which is fully negligible compared to the statistical uncertainty, see the next section.

Therefore, the statistical fit, compare Eqs. (6.9, 6.10), is simply given by the scalar equation

$$\Gamma_e = \Gamma_{e,0} + \left(\frac{\partial\nu_j}{\partial\Gamma_e}\right)^{-1}\Delta_{0,j}, \quad \sigma(\Gamma_e) = \left(\frac{\partial\nu_j}{\partial\Gamma_e}\right)^{-1}\sigma(\Delta_{0,j}). \tag{7.9}$$

Similarly, for the systematic shift propagation, compare Eqs. (6.13, 6.14),

$$\delta\Gamma_e = \left(\frac{\partial\nu_j}{\partial\Gamma_e}\right)^{-1}\delta\Delta_{0,j}, \quad \sigma(\Gamma_e) = \left(\frac{\partial\nu_j}{\partial\Gamma_e}\right)^{-1}\sigma(\delta\Delta_{0,j}). \tag{7.10}$$

For reference, the fractional proportionalities

$$\left(\frac{\partial\nu_a}{\partial\Gamma_e}\right)^{-1}/\Gamma_e \approx 6.30\ \mathrm{ppt/Hz}, \quad \left(\frac{\partial\nu_b}{\partial\Gamma_e}\right)^{-1}/\Gamma_e \approx 6.27\ \mathrm{ppt/Hz}, \tag{7.11}$$

allow to easily map the result of the resonance center to Γ_e. For systematic effects on ν_c, compare Eq. (6.15), the correspondence

$$\frac{\delta\Gamma_e}{\Gamma_e} = \left(\frac{\partial\nu_j}{\partial\Gamma_e}\right)^{-1}\frac{\partial\nu_j}{\partial\nu_c}\frac{\nu_c}{\Gamma_e} = -\frac{\delta\nu_c}{\nu_c} \tag{7.12}$$

is exactly one-to-one.

7.4. Electron-spin transition measurements

In principle, the measurement of a single electron-spin resonance with the phase-sensitive detection would enable a large statistical improvement in the determination of Γ_e. Nevertheless, to further investigate systematic effects influencing the determination of Γ_e within this mostly uncharted regime of 10^{-11} relative precision, additional transition measurements were carried out. Compared to systems without nuclear spin, where only the transition with the Larmor frequency of the bound-electron exists, $^9Be^{3+}$ has 4 electron-spin transitions. Here, the two transitions $\nu_a \approx 168$ GHz and $\nu_b \approx 142$ GHz, as indicated in Figure 6.1 and Table 6.1, were probed[3]. Additionally, after performing the trap symmetrization, compare Section 5.7.1, another ν_b resonance was taken. At last, after discarding the $^9Be^{3+}$ ion which was used for nearly one year of measurements, a Γ_e resonance was taken with hydrogen-like $^{12}C^{5+}$.

[3]The choice was made due to the maximally different absolute frequency. The ~ 180 GHz transition could not be addressed as it was outside our available range (110 − 170 GHz) of microwave frequencies.

7.4.1. ν_a and ν_b resonances

First, a double-dip resonance of the transition with the higher frequency, ν_a, was measured in the last week of December 2022, just after finishing the nuclear-spin resonances. Resonances with the phase-sensitive detection required further optimizations. A high-statistics measurement of the ν_a transition was taken from the 30th of January to the 14th of February of 2023. A ν_b resonance was taken from the 11th to 16th of May. The resonances measurements and fits are summarized in Table 7.1 and visualized in Figures 7.9 and 7.8. For calculating $\nu_{\mathrm{MW}} - \nu_j(\nu_c \,|\, \vec{p}_0)$,

Table 7.1: Data of the electron-spin transition resonances and fit results. For definitions see Table 6.2 and for details see text. The fit center depends on the initial guess $\vec{p}_0 = (\Gamma_e, \Gamma_I, \nu_{\mathrm{HFS}})$ from Table 6.3.

Transition	$\boldsymbol{\nu_a}$ (Double dip)	$\boldsymbol{\nu_a}$	$\boldsymbol{\nu_b}$
Number of cycles	363	672	251
Number of spin flips	39	56	32
Range of ν_c/ Hz	29254040.1 ± 0.3	29254041.4 ± 0.1	29254041.22 ± 0.01
Range of ν_{MW}/ kHz	168428737 ± 3	168428744.7 ± 0.4	141940861.2 ± 0.1
Voigt lineshape			
Δ_0/Hz	−63(42)	−35.2(3.0)	−34.9(3.6)
Gaussian width σ/Hz	190(60)	12(5)	17(5)
Lorentzian width Ω/Hz	90(60)	12(5)	6(5)
FWHM/Hz	560(90)	43(7)	46(7)
Amplitude	0.42(7)	0.32(5)	0.43(5)
Brown/Gabrielse lineshape			
Δ_0/Hz	–	−36.5(3.0)	−37.2(3.0)
Gaussian width σ/Hz	–	13(4)	6(4)
Rabi frequency Ω/Hz	–	0.27(3)	0.36(6)

the initial parameters $\vec{p}_0 = (\Gamma_e, \Gamma_I, \nu_{\mathrm{HFS}})$ from the previous chapter, see the corrected parameters in Table 6.3, were used (compare also the discussion in the previous section).

The improvement due to the phase-sensitive technique is highlighted by the decrease of the FWHM by a factor of more than 10 compared to the double-dip resonance. Using the correspondence of 6.3 ppt/Hz, Eq. (7.11) and the value FWHM = 43 Hz for the PnA resonances gives a relative width of 270 ppt. This is an improvement by a factor of 2.2 compared to the previously best bound-electron g-factor resonances [5, 23] and enables similar statistical precision with a much lower amount of acquired data.

7.4.2. ν_b resonance with symmetrized trap potential

Before doing any of the resonance measurements, attempts to symmetrize the trapping potential failed because it was not clear to me how to apply the scheme known for 5-pole Penning traps, see e.g. ref. [70], to a 7-pole trap. Olesia Bezrodnova from the LIONTRAP experi-

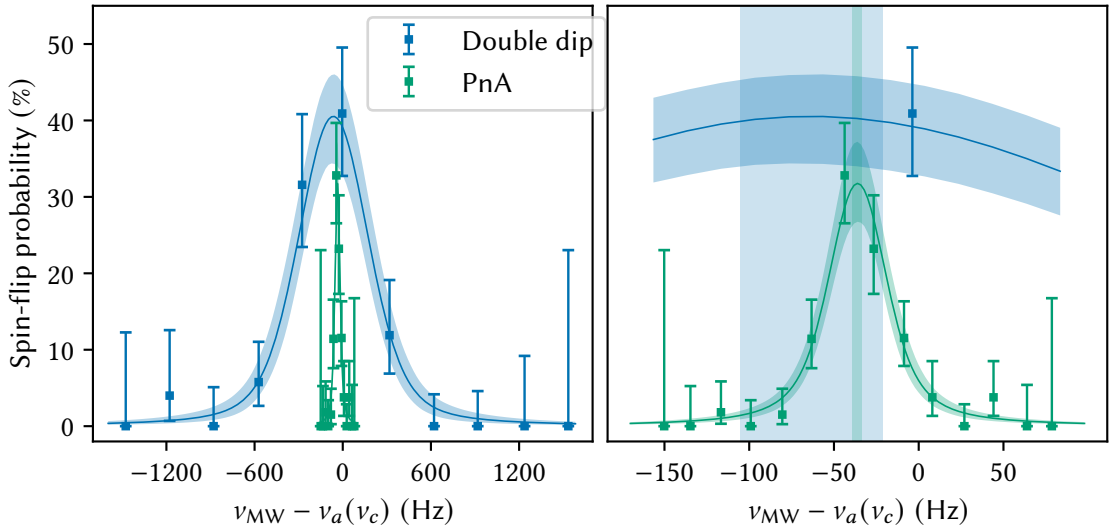

Figure 7.8: Comparison of resonances taken with the double-dip and PnA technique. The right-hand side shows a zoomed in view of the left-hand side, highlighting the much smaller resonance width achieved with the phase-sensitive detection. The vertical bars are 1-σ confidences of the determined center frequencies Δ_0.

ment pointed out to me that asymmetrically applied offsets make the symmetrization possible. Thereafter, I applied this scheme, compare Section 5.7.1, at our experiment to exclude any (unexplained) effects due to the relatively large C_4 and C_3 without the symmetrization.

Subsequently, the PT was optimized and the imperfections were measured according to Section 5.7.4. The inhomogeneities $C_3/C_2 = 0(2)$ m^{-1} and $C_4/C_2 = 3(2)$ m^{-2} were significantly reduced compared to the unsymmetrized case, Table 5.5. With the symmetrized fields, a resonance of ν_b was taken from the first to the 6th of June 2023, see Table 7.2 and Figure 7.10.

Table 7.2: Data and fit results of the ν_b transition resonances with symmetrized trapping fields.

Number of cycles	214
Number of spin flips	36
Range of ν_c/ Hz	29254037.96 ± 0.02
Range of ν_{MW}/ kHz	141940843.4 ± 0.2
Voigt lineshape	
Δ_0/Hz	−28.9(4.2)
Gaussian width σ/Hz	12(7)
Lorentzian width Ω/Hz	19(7)
FWHM/Hz	57(10)
Amplitude	0.45(4)

Brown/Gabrielse lineshape	
Δ_0/Hz	−36.4(4.2)
Gaussian width σ/Hz	14(7)
Rabi frequency Ω/Hz	0.6(1)

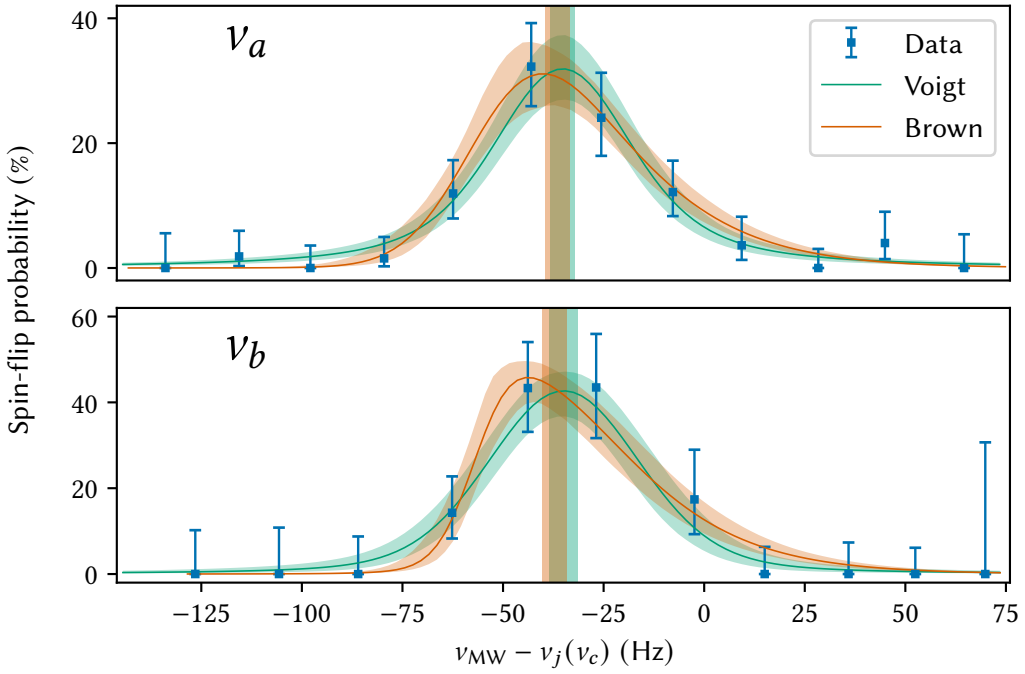

Figure 7.9: Electron-spin transition resonances. The frequencies in $\nu_{MW} - \nu_j(\nu_c \,|\, \vec{p}_0)$ are calculated with the corrected parameters from Table 6.3. The vertical bars show the 1-σ confidence of the transition center Δ_0.

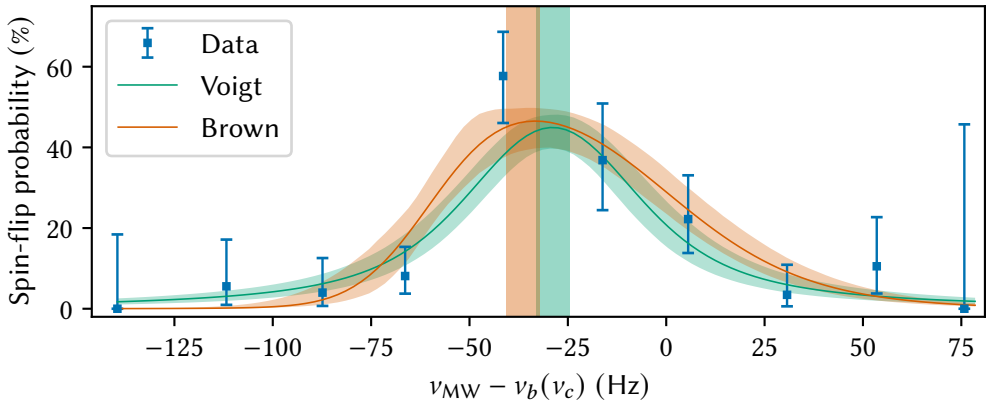

Figure 7.10: Resonance of ν_b with a symmetrized trap.

7.4.3. $^{12}C^{5+}$ resonance

A measurement of Γ_e with $^{12}C^{5+}$ is an ideal cross-check for any experiment-specific systematics, as it has been measured before with a combined fractional uncertainty of 28 ppt. Also, $^{12}C^{5+}$ has no nuclear spin and no hyperfine splitting, therefore only requiring the measurement of a

single transition - the electron's Larmor frequency. For calculating the Larmor frequency ν the simple relation

$$\nu = -\Gamma_e \nu_c \tag{7.13}$$

greatly simplifies the treatment of systematic effects.

After finishing with $^9Be^{3+}$, a $^{12}C^{5+}$ ion was loaded into the trap with a scheme similar to Section 5.2, but without using laser ablation. This works, because the surfaces inside the trap chamber hit by the expanding electron beam may have contaminants which include carbon, e.g. CO_2. After initial preparation, the PT was symmetrized, optimized, and the field imperfections were measured, compare Section 5.7. With the larger q^2/m, the dip width $\gamma_z \approx 5.4$ Hz is expectedly larger than for $^9Be^{3+}$. The magnetron frequency $\nu_- = 3200.92(7)$ Hz of $^{12}C^{5+}$ was determined via extrapolation, compare Section 5.8.3. The measured field imperfections are $C_3/C_2 = 0(2)$ m^{-1}, $C_4/C_2 = 2(7)$ m^{-2} and $B_2 = 1.0(1)$ m^{-2}. The latter value is consistent with the previous determination, $B_2 = 1.04(5)$ Tm^{-2}. Further, the modified cyclotron amplitude calibration $K_+ = 43(1)$ µm/Mcyc was determined. For the phase-sensitive detection, $N_+ = 0.278$ MCyc was used, resulting in an excitation amplitude of $B_+ = 11.9(4)$ µm. The highest evolution time with PnA during the resonance measurements was $T_{\mathrm{evol}} = 40.1$ s, slightly smaller than for $^9Be^{3+}$, however, due to the larger $\nu_c \approx 36$ MHz, the reached fractional precision was similar.

A resonance was recorded from the 16th to 23rd of June 2023, see Table 7.3 and Figure 7.11. For determining the resonance center, $\Gamma_{e,0} = -4376.210500872$ from ref. [179] was used.

Table 7.3: Data and fit results of the $^{12}C^{5+}$ resonance.

Number of cycles	273
Number of spin flips	33
Range of ν_c/ Hz	36618730.44 ± 0.05
Range of ν_{MW}/ kHz	160251272.68 ± 0.3
Voigt lineshape	
Δ_0/Hz	7.4(3.8)
Gaussian width σ/Hz	11(6)
Lorentzian width Ω/Hz	12(6)
FWHM/Hz	43(11)
Amplitude	0.33(7)

Brown/Gabrielse lineshape	
Δ_0/Hz	4.8(3.9)
Gaussian width σ/Hz	14(5)
Rabi frequency Ω/Hz	0.33(6)

7.4.4. Summary of statistical results

The statistical results for Γ_e are listed in Table 7.4.

7.4.5. Systematics and error budget

Here, a full account of all relevant systematic shifts and uncertainties is given. Some discussions are shortened when the arguments for the nuclear-spin transition resonances are applicable, see Section 6.5.2.

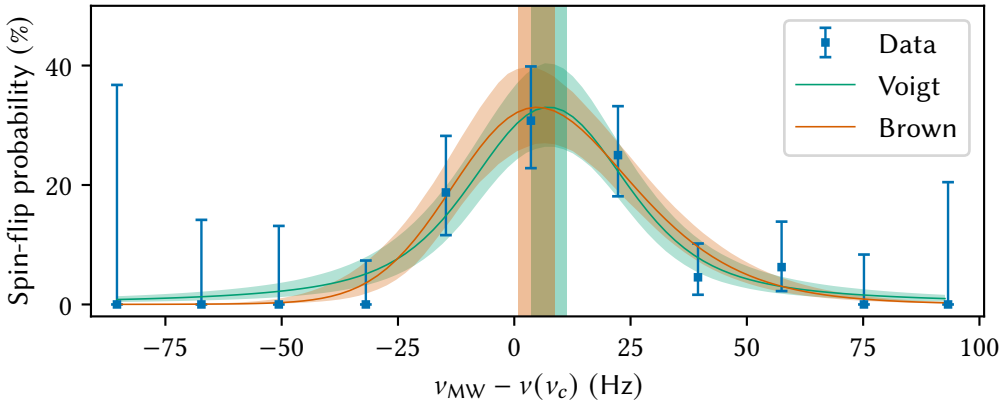

Figure 7.11: Larmor frequency resonance of $^{12}C^{5+}$ with a symmetrized trap. For details see text.

Table 7.4: Statistical result of Γ_e for the different resonances.

Γ_e	Voigt fit	Brown-Gabrielse fit
ν_a	−5479.86334228(10) \ 19 ppt	−5479.86334224(10) \ 19 ppt
ν_b	−5479.86334230(12) \ 23 ppt	−5479.86334222(10) \ 19 ppt
ν_b (sym)	−5479.86334251(14) \ 26 ppt	−5479.86334225(14) \ 26 ppt
$^{12}C^{5+}$	−4376.21050107(10) \ 24 ppt	−4376.21050100(11) \ 24 ppt

Probability lineshape

The asymmetric lineshape, Eq. (3.31), is fit with three free parameters, the resonance center Δ_0, the Gaussian width σ and the Rabi frequency Ω, according to

$$P(\nu_{MW} - \nu(\nu_c) - \Delta_0 \mid \sigma, \Omega) = P(\nu_{MW} - \nu(\nu_c) - \Delta_0 + \Delta\nu, T_{MW} \mid \sigma, \Omega, \Delta\nu, \gamma_z), \tag{7.14}$$

where T_{MW} is the length of the microwave excitation. The asymmetric lineshape accounts directly for the shifted center of the resonance due to B_2 by the linewidth parameter $\Delta\nu$, see Figure 3.4. However, as the measured ν_c is shifted in the same way and identically accounts for this via $\nu(\nu_c)$, the linewidth parameter $\Delta\nu$ is added in the transition probability. The linewidth parameter $\delta\nu$ is calculated with Eq. (3.26) using the experimental B_2 value and the dip width is taken as the axial cooling rate γ_z. The uncertainties of $\Delta\nu$ and γ_z are included in the fit model via a Gaussian prior.

The extracted fit parameters, Table 7.1, are compatible with the requirements of the Brown-Gabrielse line, compare Eq. (3.29). Furthermore, the numerical integration of the transition probability using these parameters, see Section A.6, shows good agreement with the Brown-Gabrielse line, solidifying its use. Ideally, an experimental verification of the probability lineshape would be performed, but the acquired statistics of the resonances are too low to discriminate between the two models and no significant asymmetry can be observed in the resonance data. Moving forward, the resonance center values determined with the Brown-Gabrielse line

will be used, but the difference to the value obtained with the Voigt profile will be included as a systematic lineshape uncertainty.

The shifts between the resonance centers using the two models are below 1-σ of the statistical uncertainty for the two initial resonances and the $^{12}C^{5+}$ resonance summarized in Table 7.1 and Table 7.3, respectively. However, the ν_b resonance with symmetrized potential, see Table 7.2 and Figure 7.10, has a much larger shift, which is due to the higher saturation by the larger Rabi frequency. While the output microwave power for this resonance was identical to the initial ν_b resonance, the effective power at the ion's position may be different due to the ion's slightly shifted axial position in the symmetrized potential, resulting in the larger Rabi frequency.

Field imperfections and relativistic shift

The shifts of ν_c from field imperfections and the relativistic shift are slightly different from the case of the nuclear-spin transitions due to the non-thermal modified cyclotron motion. In addition to Eq. (6.18), a contribution from the excitation $B_+ = K_+ N_+$, where N_+ is the number of cycles of the dipole excitation (for the resonances above, $N_+ = 0.3$ MCyc) and K_+ is taken from Table 5.5, needs to be included. However, as the axial frequency ν_z is separately measured with thermal amplitudes, only the shifts of ν_+ are relevant. For the fields, the only additional contribution is due to C_4,

$$\delta\nu_{c,\text{fields}} = \rho_{z,th}^2 \begin{pmatrix} C_3^2/C_2^2 \\ C_4/C_2 \\ B_2/B_0 \\ B_1/B_0 \cdot C_3/C_2 \end{pmatrix} \cdot \begin{pmatrix} -\frac{15}{8}\nu_- \\ -\frac{3}{2}\nu_- \\ \frac{1}{2}\nu_z \\ -\frac{3}{4}\nu_z \end{pmatrix} + \frac{3}{2}\frac{C_4}{C_2}\nu_- B_+^2 \equiv \rho_{z,th}^2 \vec{K}\cdot\vec{L} + \frac{3}{2}\frac{C_4}{C_2}\nu_- B_+^2, \tag{7.15}$$

as, again, no shifts that correspond to effective shifts of the magnetic field need to be included. The additional relativistic shift of the resonance center is more significant, Eq. (3.35),

$$\delta\Delta_{0,\text{rel}} = -\left(\frac{\nu_z}{\nu_+}\rho_{z,th}^2 + B_+^2\right)\frac{2\pi^2\nu_+^2}{c^2}\left(\nu_j - 2\nu_c\frac{\partial\nu_j}{\partial\nu_c}\right). \tag{7.16}$$

Using K_+ and C_4/C_2 from Table 5.5, the predicted shifts due to the dipole excitation are

$$\delta\Delta_{0,a}/N_+^2 = 45(2)\ \text{Hz/MCyc}^2, \quad \delta\Delta_{0,b}/N_+^2 = 54(2)\ \text{Hz/MCyc}^2, \tag{7.17}$$

for ν_a and ν_b, respectively. The included C_4 contribution amounts to only $-1.5(3)$ Hz/MCyc^2 and the difference of the two values is due to the larger relativistic shift of ν_b.

As a cross-check for potential unknown systematic effects at the non-thermal modified cyclotron amplitude, compare refs. [23, 91], resonances of the ν_a transition with additional excitation amplitudes were recorded, see Figure 7.12. From the linear fit to the data, the extrapolated resonance center at thermal modified cyclotron amplitude

$$\Delta_{0,a,\text{th}} = -37.7(2.8)\ \text{Hz} \tag{7.18}$$

and the scaling of the shift

$$\delta\Delta_{0,a}/N_+^2 = 46(4)\ \text{Hz/MCyc}^2 \tag{7.19}$$

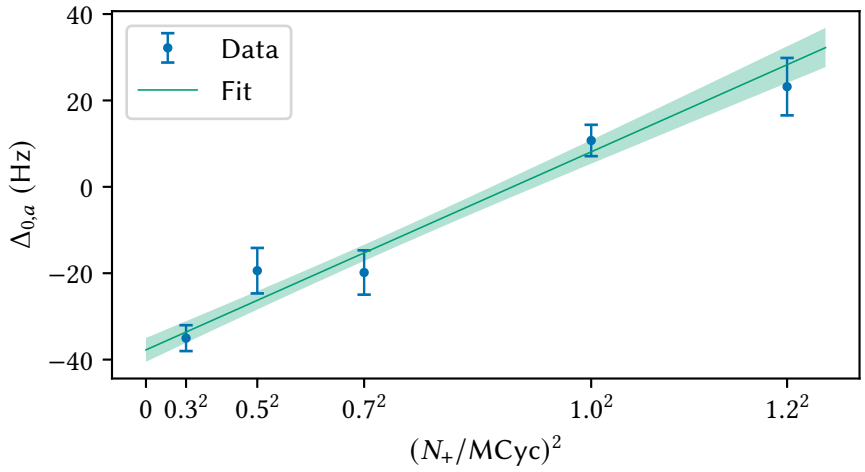

Figure 7.12: Extrapolation of the resonance center of ν_a to thermal modified cyclotron amplitude. Resonances of the transition are taken with larger modified cyclotron amplitude by increasing the dipole excitation $B_+ = K_+ N_+$. For the extrapolation all resonance fits are performed with the Voigt profile.

are extracted. The scaling of the shift perfectly fits with the previously calculated expected value, Eq. (7.17), from the amplitude calibration, indicating no further unknown effects.

For calculating the thermal contribution to the shifts, the thermal amplitudes are determined via the AT method from each resonance measurement individually, see Section 5.7.5. They are

	ν_a	ν_b	ν_b (sym)	$^{12}C^{5+}$
$\rho^2_{z,\mathrm{th}}/\mu\mathrm{m}^2$	1233(47)	1142(73)	1306(91)	917(55)

In total, the shifts due to the fields are

	ν_a	ν_b	ν_b (sym)	$^{12}C^{5+}$
$\delta\Gamma_{e,\mathrm{fields}}/10^{-8}$	−9(2)	−8(2)	0(1)	0(1)
$\delta\Gamma_{e,\mathrm{fields}}/\Gamma_e$ (ppt)	17(4)	15(4)	0(2)	0(2)

The symmetrized potential used for the last two resonances reduces the shift below the significant digit and the uncertainty is also decreased by a factor of 2. The relativistic shift of the resonances requires the thermal amplitudes as well as the amplitude calibration K_+, see Table 5.5 for $^9Be^{3+}$ and Section 7.4.3 for $^{12}C^{5+}$. The thermal (th), excited (exc), and total (tot) contributions are

	ν_a	ν_b	ν_b (sym)	$^{12}C^{5+}$
$\delta\Gamma_{e,\mathrm{rel,\,th}}/10^{-8}$	−1.97(8)	−2.2(1)	−2.5(2)	−1.56(9)
$\delta\Gamma_{e,\mathrm{rel,\,exc}}/10^{-8}$	−14.5(5)	−17.1(6)	−17.1(6)	−18(1)
$\delta\Gamma_{e,\mathrm{rel,\,tot}}/10^{-8}$	−16.5(5)	−19.3(6)	−19.6(6)	−20(1)
$\delta\Gamma_{e,\mathrm{rel,\,tot}}/\Gamma_e$ (ppt)	30(1)	35(1)	36(1)	46(3)

Thomas precession

The Thomas precession is negligible, compare the discussion in Section 6.5.2.

Image charge shift

The image charge shift amounts to the same value as for the nuclear-spin transition measurements and a slightly larger value for $^{12}C^{5+}$,

$$\begin{aligned} {}^{9}Be^{3+}: &\quad \delta\Gamma_{e,\mathrm{img}}/10^{-8} = -53(3) \setminus 96(5)\ \mathrm{ppt}, \\ {}^{12}C^{5+}: &\quad \delta\Gamma_{e,\mathrm{img}}/10^{-8} = -56(3) \setminus 128(6)\ \mathrm{ppt}. \end{aligned} \tag{7.20}$$

Dip lineshape

The influence of the dip lineshape is suppressed for the phase measurements compared to the double-dip measurements, as it only affects the ν_z determination. Thus, the uncertainty contribution to ν_c via the invariance theorem Eq. (2.6), directly decreases by $\sigma(\nu_c) = \sigma(\nu_z)\nu_z/\nu_c$. Assuming the estimate $\sigma(\nu_z) \approx 23$ mHz, see Section B.1, the systematic uncertainty due to the axial dip is

$$\begin{aligned} {}^{9}Be^{3+}: &\quad \sigma(\Gamma_{e,\mathrm{dip}})/10^{-8} = 7 \setminus 13\ \mathrm{ppt}, \\ {}^{12}C^{5+}: &\quad \sigma(\Gamma_{e,\mathrm{dip}})/10^{-8} = 4 \setminus 8\ \mathrm{ppt}. \end{aligned} \tag{7.21}$$

For $^{12}C^{5+}$, the larger cyclotron frequency further reduces the contribution of the axial frequency.

Time reference

The influence of the time reference, Eq. (6.24) is greatly suppressed for the electron-spin transitions, because the transition frequencies are determined with less fractional precision. Assuming $\sigma\left(\frac{\delta\nu_{\mathrm{ref}}}{\nu_{\mathrm{ref}}}\right) = 10^{-12}$, the fractional uncertainty on $\sigma(\Gamma_e)/\Gamma_e < 0.2\times10^{-13}$ calculated via Eq. (6.24) is negligible. For $^{12}C^{5+}$, no uncertainty due to the time reference occurs.

Corrections to the Breit-Rabi energies

As the correction required for $^{9}Be^{3+}$ from ref. [159] are effectively a shielding of the nuclear magnetic moment, the influence on the electron-spin transitions is suppressed. The frequencies are shifted by $\nu_{Q,a} - \nu_a = -37.2(3)$ mHz, $\nu_{Q,b} - \nu_b = 36.7(3)$ mHz, which results in negligible shifts smaller than 1 ppt on Γ_e.

Magnetron frequency

As pointed out before, Section 5.8.3, the uncertainty of the magnetron frequency of $^{9}Be^{3+}$, $\nu_- = 4007.4(2)$ Hz, contributes about 1 ppt to ν_c. For $^{12}C^{5+}$, the contribution of $\nu_- = 3200.92(7)$ Hz is even smaller, amounting to less than 0.2 ppt. Because the magnetron frequency determined by the extrapolation was done only once, this requires that it stays constant. From the relation

$\nu_- = \frac{1}{2}\nu_z^2/\nu_+$ an upper bound for the change ν_- over the whole $^9Be^{3+}$ campaign gives $\Delta\nu_- < 0.2$ Hz, which is estimated by the maximum deviation $\Delta\nu_z \approx 20$ Hz. This results in a combined uncertainty of $\sigma(\nu_-) = 0.3$ Hz and only a slightly larger 1.4 ppt uncertainty for ν_c. For $^{12}C^{5+}$, the measurement campaign was very short and no drift was observed.

Summary

All relevant systematic shifts are summarized and corrected for in Table 6.3.

Table 7.5: Statistical results and error budget for Γ_e. For the statistical result, the Brown-Gabrielse line is used. The difference of the results from the Brown-Gabrielse line to the Voigt profile is given by $\delta\Gamma_{e,\mathrm{ls}}$ and taken as the lineshape uncertainty σ_{ls} for the end results.

	ν_a	ν_b	ν_b (sym)	$^{12}C^{5+}$
Statistic Γ_e	−5479.86334224(10)	−5479.86334222(10)	−5479.86334225(14)	−4376.21050100(11)
$\delta\Gamma_{e,\mathrm{ls}}/10^{-8}$	4	8	26	7
		Systematic shifts$/10^{-8}$		
Fields	−9(2)	−8(2)	0(1)	0(1)
Relativistic	−17(1)	−19(1)	−20(1)	−20(1)
Image charge		−53(3)		−56(3)
Dip		0(7)		0(4)
ν_-		0(1)		–
Total shifts	−79(8)	−81(8)	−72(8)	−76(5)
Corrected Γ_e	−5479.86334145(13)	−5479.86334141(13)	−5479.86334153(16)	−4376.21050024(12)
without σ_{ls}	24 ppt	24 ppt	29 ppt	29 ppt
Corrected Γ_e	−5479.86334145(14)	−5479.86334141(15)	−5479.86334153(31)	−4376.21050024(14)
with σ_{ls}	26 ppt	27 ppt	57 ppt	32 ppt

As argued above, the statistical result is taken from the Brown-Gabrielse line fit of the resonances. A separate lineshape uncertainty σ_{ls} is introduced as the difference of the statistical result from both methods and included in the last given total uncertainty. It is significant only for the ν_b resonance measurement with symmetrized potentials, where a large difference between the fit resonance centers exists.

The most significant systematic shift is due to the image charge effect. Compared to ref. [23], in this experiment it is reduced by about a factor of 2 due to the larger magnetic field, compare Eq. (2.43). The uncertainty due to the dip contributes more than the uncertainty due to the image charge shift. For any improved measurement with a larger trap to reduce the image charge shift and with better statistics, understanding the dip lineshape will thus be crucial.

7.5. Evaluation of results and discussion

Summarizing, the statistical precision has been improved vastly by use of the phase-sensitive detection techniques. In our experiment, this allowed measuring bound-electron g-factor resonances with a currently unmatched relative width of $\sim$ 270 ppt. A detailed evaluation of systematic effects and several cross-checks have been performed showing no limiting factors

at the 10^{-11} level. The three results of $\Gamma_e(^9\mathrm{Be}^{3+})$ are internally consistent within their respective 1-σ uncertainties. Additionally, they agree with the result $\Gamma_e(^9\mathrm{Be}^{3+}) = -5479.8633435(22)$ from the previous chapter, but are more precise by a factor of up to 18. Expressed differently, this constitutes a consistency check of the Breit-Rabi formula at the level of the uncertainties of the five measured transition frequencies each of which is better than 30 ppt.

Following is a preliminary discussion of the results currently under ongoing investigation in our group.

The value $\Gamma_e(^{12}\mathrm{C}^{5+}) = -4376.21050024(14)$ can be directly compared to the experimental result from ref. [179] $\Gamma_{e,0}(^{12}\mathrm{C}^{5+}) = -4376.21050087(12)$. Surprisingly, even though both values were measured by nearly identical techniques at two different Penning trap experiments, a fractional difference of

$$\frac{\Gamma_e(^{12}\mathrm{C}^{5+}) - \Gamma_{e,0}(^{12}\mathrm{C}^{5+})}{\Gamma_{e,0}(^{12}\mathrm{C}^{5+})} = -144(42)\ \text{ppt}, \tag{7.22}$$

corresponding to nearly 3.5 combined standard deviations, was found.

To include the $^9\mathrm{Be}^{3+}$ measurements into this discussion, the values of $\Gamma_e(^9\mathrm{Be}^{3+})$ can be linked to $\Gamma(^{12}\mathrm{C}^{5+})$ via a rescaling factor R,

$$\Gamma_e(^{12}\mathrm{C}^{5+}) = \underbrace{\frac{m(^{12}\mathrm{C}^{5+})}{m(^9\mathrm{Be}^{3+})}\frac{q(^9\mathrm{Be}^{3+})}{q(^{12}\mathrm{C}^{5+})}\frac{g_s(^{12}\mathrm{C}^{5+})}{g_s(^9\mathrm{Be}^{3+})}}_{R}\Gamma_e(^9\mathrm{Be}^{3+}), \tag{7.23}$$

compare Eq. (7.1). This requires both precise values of the mass ratio $m(^9\mathrm{Be}^{3+})/m(^{12}\mathrm{C}^{5+})$ and the bound-electron g-factors.

The former has been determined at the Penning-trap mass spectrometer PENTATRAP [180] via the comparison $m(^9\mathrm{Be}^{3+})/m(^{12}\mathrm{C}^{4+})$. At PENTATRAP, mass-ratios of light and heavy ions can be measured with an unparalleled fractional precision surpassing 5 ppt [18, 181]. The preliminary value in atomic mass units,

$$m(^9\mathrm{Be}^{3+}) = 9.010537487225(90)\ \text{u}, \tag{7.24}$$

features a 10 ppt uncertainty [182]. It is important to emphasize that performing mass measurements at this level of precision demands experimental efforts comparable to those of the bound-electron g-factor measurements conducted here.

Extended, state-of-the-art, calculations of the bound-electron g-factor (preliminary)

$$g_s(^9\mathrm{Be}^{3+}) = -2.0017515746590(19) \tag{7.25}$$

were performed in the Keitel division by Bastian Sikora *et al.* [183]. For $^9\mathrm{Be}^{3+}$, the lower Z compared to $^{12}\mathrm{C}^{5+}$ allows an improved precision of the bound-electron g-factor. The mass $m(^{12}\mathrm{C}^{5+}) = 11.9972576802917(13)$ u and bound-electron g-factor $g_s(^{12}\mathrm{C}^{5+}) = -2.0010415901798(47)$ are taken from the publication of $\Gamma_{e,0}(^{12}\mathrm{C}^{5+})$, ref. [179]. The rescaling factor

$$R = 0.7985984736590(82) \tag{7.26}$$

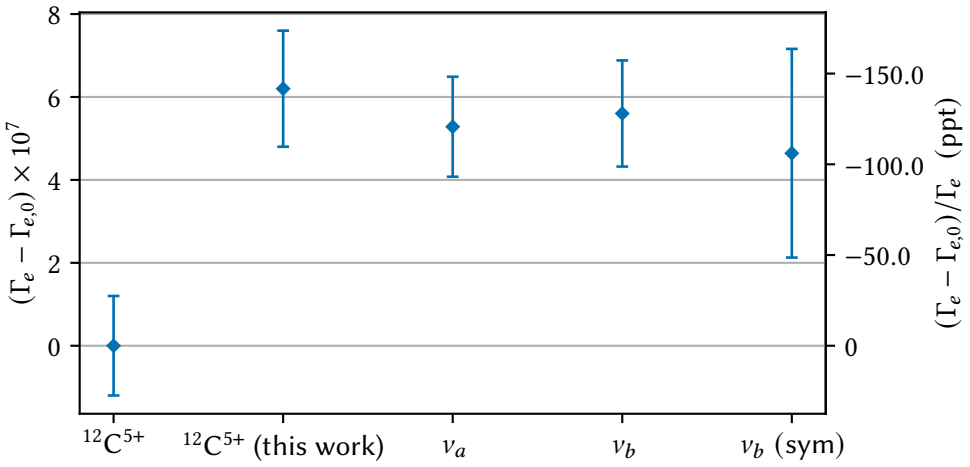

Figure 7.13: Comparison of bound-electron g-factor measurements. For details see text.

has a relative uncertainty of 10 ppt, which is smaller by a factor of about 2 compared to the experimental uncertainty reached here.

Finally, the comparison of the bound-electron g-factor measurements is visualized in Figure 7.13. As a whole, all measurements performed here, the bound-electron g-factor calculations, and the mass $m(^9Be^{3+})$ from PENTATRAP, are internally consistent. Thus, most likely, the discrepancy lies in either a common source of undiscovered systematic errors in the measurements performed here or in the previous measurements of $\Gamma_e(^{12}C^{5+})$. At the time of writing this thesis, no conclusive explanation had been found. The discussion of possible explanations and future prospects continues in the next chapter.

Chapter 8.

Outlook and summary

In this chapter, I will give an overview of current and ongoing projects at our experiment, which is now being called

Magnetic moment (μ)-Trap-Experiment: μTEx.

This includes a new coupling trap for sympathetic laser cooling, prospective measurements of nuclear magnetic moments and hyperfine splittings, and ongoing bound-electron g-factor measurements. Lastly, I will give a summary of the work performed throughout this thesis.

8.1. Sympathetic laser cooling via direct Coulomb coupling

In the case of ^{3}He, the main goal was the direct determination of its bare nuclear magnetic moment, which was determined at μTEx via spectroscopy of the combined hyperfine and Zeeman splitting in $^3He^+$ [11]. Choosing spectroscopy on $^3He^+$ over spectroscopy on the bare helion was a matter of the detection of the spin states, which is much more challenging for the bare system and requires advanced techniques for cooling the ion's trapping modes [184]. However, the direct measurement of bare nuclear magnetic moments or the magnetic moments in helium-like systems such as $^{6,7}Li^{2+}$ remain intriguing options for directly testing diamagnetic shielding in two-electron systems [185]. Additionally, measurements of various other interesting transitions would benefit from the reduced Doppler shift and broadening due to the smaller amplitudes [186]. Therefore, the aim towards advanced cooling techniques is still highly relevant.

One approach is to use sympathetic laser cooling, which has been shown to work to great success in e.g. RF ion traps [187] or for neutral atoms [188]. To this end, an ion species that is laser-addressable with available laser sources is used to sympathetically cool the ion of interest. The laser cooling of $^9Be^+$ ions with a 313 nm UV laser was already shown to work here, see ref. [116]. For coupling the motional modes in Penning traps, several approaches were envisaged in ref. [108]. The initial approach to be used at μTEx, called the common-endcap coupling, uses the interaction of image currents induced in a shared electrode. However, even with the optimized trap geometry, see Figure 4.3, coupling rates are very small resulting in very difficult experimental constraints [109]. In another approach, the ions' axial motions are coupled

via their image currents over a common axial detection system, which enhances the coupling rate. This coupling has been shown in ref. [186] for highly charged ions and has been used to sympathetically cool a proton [189]. A limitation of this approach is, however, the necessary coupling to the thermal heat bath of the resonator, which counteracts the laser cooling and effectively limits the ion temperature.

8.1.1. Concept and trap optimization

At μTEx, a new Penning trap design was developed, which allows to use the direct Coulomb interaction between laser-cooled ions and the ion of interest to mediate the cooling. The design was initially developed in ref. [124], but partly changed afterwards.

A schematic of the design is shown in Figure 8.1. The general concept revolves around a

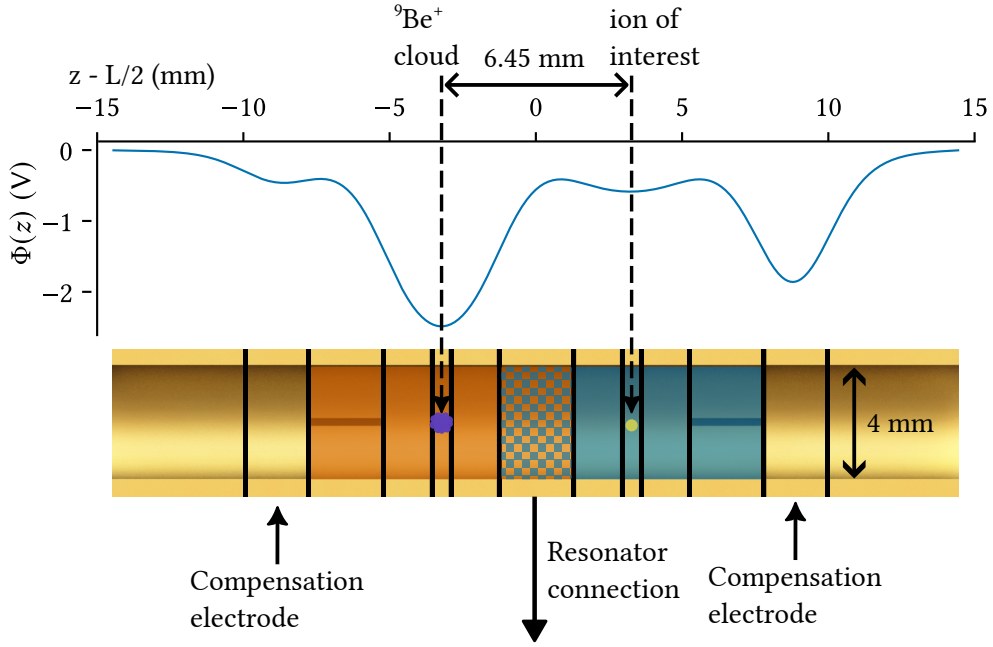

Figure 8.1: Bottom: The two traps, indicated by the red and blue shading, share a common, center endcap. Additional electrodes adjacent to the two trap compensate the potential of the opposite trap. The top graph shows the potential for ^{9}Be$^+$ ions in the left trap and an ^{3}He^{2+} ion in the right trap at $\omega_z/2\pi = 400$ kHz.

compromise between coupling strength and ease of optimization of the traps. Therefore, two close, but individually orthogonal and compensated 5-pole traps with a 2 mm radius are used to store a cloud of ^{9}Be$^+$ and the ion of interest, respectively. Still, the distance of 6.45 mm between the trap centers requires compensating the influence of one trap's electrostatic potential on the others. This compensation is (mostly) done by two additional compensation electrodes adjacent to the traps. On both ends, additional endcap electrodes are set to ground potential.

A main challenge in optimizing the trap voltages is the large q/m mismatch between ^{9}Be$^+$ and most (hydrogen-like or bare) ions of interest. As the Coulomb coupling only works ef-

ficiently on resonance $\omega_z = \omega_l = \omega_r$, where ω_l and ω_r indicate the axial frequencies in the left and right trap, respectively, the deep confining potential for $^9Be^+$ strongly influences the shallow potential of the ion of interest. To outline the calculation of the ideal trap potential, the applied voltages of the eleven electrodes (excepting the grounded endcaps) are defined as

$$\vec{U} = (W_C, 0, V_1, V_2, V_3, 0, W_1, W_2, W_3, 0, V_C)^T, \tag{8.1}$$

where V_i refers to voltages of the left trap and W_i of the right trap. For the compensation electrodes, the applied voltage depends mostly on the opposite trap potential, justifying the choice of the above notation. The primary influence of the other traps are the odd-order coefficients C_1 and C_3. Thus, the optimization criteria

$$\begin{gathered} C_1(z_{0,l}) = C_1(z_{0,r}) = C_3(z_{0,l}) = C_3(z_{0,r}) = C_4(z_{0,l}) = C_4(z_{0,r}) = 0, \\ C_2(z_{0,l}) = \frac{\omega_z^2}{2}\frac{m_l}{q_l}, \quad C_2(z_{0,r}) = \frac{\omega_z^2}{2}\frac{m_r}{q_r}, \end{gathered} \tag{8.2}$$

where $z_{0,l}$ and $z_{0,r}$ are the geometrical trap centers of the left and right trap and $\frac{m_{l,r}}{q_{l,r}}$ are the mass-to-charge ratios of the left and right ion species, were chosen[1]. Using the methods developed in Section 2.2, these 8 constraints yield a unique solution for the 8 voltages via inversion of a linear system of equations. In Table 8.1, the computed voltages for $\omega_z/2\pi = 400$ kHz, $^9Be^+$ in the left and $^3He^{2+}$ in the right trap, are given. The axial potential in the trap given these voltages is shown in Figure 8.1. In this example, the differences between the correction electrodes voltages, $V_1 - V_3$ and $W_1 - W_3$, are well below 1 mV. Therefore, working with tuning ratios, e.g. $V_1 = V_3 = \mathrm{TR}_V V_2$, is still possible. Additionally, the voltages which need to be applied to the compensation electrodes are close to the ring voltage of the opposite trap, i.e. $W_C \approx W_2$ and $V_C \approx V_2$. In total, this reduces the number of required voltages that need to be tuned separately in the initial optimization.

Table 8.1: . Required voltages $\vec{U}_f$ for the coupling trap with $\omega_z/2\pi = 400$ kHz, $^9Be^+$ in the left and $^3He^{2+}$ in the right trap. The voltages for using the traps individually, i.e. the other trap at zero potential, are given by $\vec{U}_i$.

	W_C	V_1	V_2	V_3	W_1	W_2	W_3	V_C
$\vec{U}_f$/V	−0.705	−2.819	−3.187	−2.819	−0.653	−0.682	−0.653	−3.055
$\vec{U}_i$/V	-	−2.764	−3.142	−2.764	−0.461	−0.524	−0.461	-
$(\vec{U}_f - \vec{U}_i)$/V	−0.705	−0.055	−0.045	−0.055	−0.193	−0.158	−0.193	−3.055

8.1.2. Coulomb coupling

The Coulomb potential, see e.g. ref [89], between an ion in the left trap and the right trap is

$$\Phi = \frac{q_l q_r}{4\pi\epsilon_0}\frac{1}{|\vec{r}_l - \vec{r}_r|} \approx \Phi_0 + \underbrace{\frac{q_l q_r}{2\pi\epsilon_0 d_0^3}}_{K}\frac{(z_l - z_r)^2}{2}, \tag{8.3}$$

[1]The C_1 condition ensures that the ions' equilibrium positions are in the geometrical centers of the individual traps.

where $d_0 = |z_{0,l} - z_{0,r}|$. For the approximation, the potential was expanded around the trap equilibrium positions $z_{0,l}$ and $z_{0,r}$ with the displacements z_1 and z_2. This assumes that the equilibrium positions are essentially unshifted by the weak Coulomb coupling and that the radial components are negligible small compared to d_0. The additional force on the ions is given by

$$F_{l,r} = -\frac{\partial \Phi}{\partial z_{l,r}} = -K(z_{l,r} - z_{r,l}). \tag{8.4}$$

Integrating this into a coupled differential equation of the axial motions z_l and z_r without a connected resonator or laser cooling, compare Eq. (2.8), gives

$$\frac{\mathrm{d}}{\mathrm{d}t}\begin{pmatrix} z_l \\ \tilde{z}_l \\ z_r \\ \tilde{z}_r \end{pmatrix} = \begin{pmatrix} 0 & \omega_l & 0 & 0 \\ -\omega_l - \frac{K}{m_l\omega_l} & 0 & \frac{K}{m_l\omega_l} & 0 \\ 0 & 0 & 0 & \omega_r \\ \frac{K}{m_r\omega_r} & 0 & -\omega_r - \frac{K}{m_r\omega_r} & 0 \end{pmatrix}\begin{pmatrix} z_l \\ \tilde{z}_l \\ z_r \\ \tilde{z}_r \end{pmatrix}. \tag{8.5}$$

From the eigenvalues of the above matrix, the coupling rate on resonance $\omega_l = \omega_r = \omega_z$ is calculated as

$$\Omega_K = \sqrt{K\left(\frac{1}{m_l} + \frac{1}{m_r}\right) + \omega_z^2} - \omega_z \approx \frac{K}{2\omega_z}\left(\frac{1}{m_l} + \frac{1}{m_r}\right), \tag{8.6}$$

where the last step is possible for small coupling $K \ll m_{l,r}\omega_z^2$. For the same example of coupling $^3He^{2+}$ to $^9Be^+$, $d_0 = 6.45$ and $\omega_z/2\pi = 400$ kHz, $\Omega/2\pi \approx 30$ mHz. While this is a small rate, it is larger than the rates achieved with other sympathetic coupling schemes for Penning traps (respectively for a single ion), refs. [109, 186, 190].

To increase the coupling rate, instead of a single ion, a cloud of n $^9Be^+$ ions can be used. Assuming a common motion of the cloud, this can be included by rescaling the mass and charge $m_l \to nm_l$ and $q_l \to nq_l$, respectively. This modifies the coupling rate to

$$\Omega_K(n) \approx \frac{K}{2\omega_z}\left(\frac{1}{m_l} + \frac{n}{m_r}\right), \tag{8.7}$$

giving a proportional increase for large n. For $n = 50$, a coupling rate of $\Omega/2\pi \approx 1.1$ Hz is reached.

8.1.3. Cooling

To couple the ions, the axial frequencies need to be resonantly matched. This requires connecting an axial detection system to the coupling trap, which acts as a heat bath at 4 K with a time constant of γ_z, counteracting the sympathetic cooling. However, it is possible to switch the detector's resonance frequency, see e.g. ref. [191]. After matching the frequencies, it is thus possible to significantly reduce the coupling to the resonator's heat bath. Here, a single, switchable, resonator is connected to the center endcap electrode, making the simultaneous detection of the axial frequencies of the ions in both traps possible.

A complete description of the two axial motions with n on-axis laser-cooled $^9Be^+$ ions, and the resonator motion is given by

$$\frac{\mathrm{d}}{\mathrm{d}t}\begin{pmatrix} z_l \\ \tilde{z}_l \\ z_r \\ \tilde{z}_r \\ \zeta \\ \tilde{\zeta} \end{pmatrix} = \underbrace{\begin{pmatrix} 0 & \omega_l & 0 & 0 & 0 & 0 \\ -\omega_l - \frac{K}{m_l\omega_l} & -\Gamma_D & \frac{K}{m_l\omega_l} & 0 & 0 & \frac{e\omega_R}{q_l\omega_l}\gamma_l \\ 0 & 0 & 0 & \omega_r & 0 & 0 \\ \frac{nK}{m_r\omega_r} & 0 & -\omega_r - \frac{nK}{m_r\omega_r} & 0 & 0 & -\frac{e\omega_R}{q_r\omega_r}\gamma_r \\ 0 & 0 & 0 & 0 & 0 & \omega_R \\ 0 & -\frac{nq_l\omega_l}{e\omega_R}\Gamma_R & 0 & \frac{q_r\omega_r}{e\omega_R}\Gamma_R & -\omega_R & -\Gamma_R \end{pmatrix}}_{A}\begin{pmatrix} z_l \\ \tilde{z}_l \\ z_r \\ \tilde{z}_r \\ \zeta \\ \tilde{\zeta} \end{pmatrix} + \begin{pmatrix} 0 \\ \Gamma_D\tilde{z}_{D,\mathrm{th}}(t) \\ 0 \\ 0 \\ 0 \\ \Gamma_R\tilde{\zeta}_{\mathrm{th}}(t) \end{pmatrix}, \tag{8.8}$$

where $\gamma_{l,r} = \frac{q_{l,r}^2 R}{m_l d_{\mathrm{eff}}^2}$ is defined for single ions for both $^9Be^+$ and the ion of interest. The Doppler laser cooling is included via the cooling rate Γ_D and the thermal noise $\tilde{z}_{D,\mathrm{th}}(t)$[2], which is linked to the minimum achievable temperature, called the Doppler temperature T_D. For $^9Be^+$, $T_D \approx 0.5$ mK, which can be converted to the thermal axial amplitude of the $^9Be^+$ ions

$$\rho_{z,l,D}^2 = \frac{1}{n}\frac{2k_B T_D}{m_l\omega_l^2} \tag{8.9}$$

via Eq. (2.48). The factor $1/n$ is due to the uncorrelated Doppler cooling of the n $^9Be^+$ ions. Following the formalism from Section A, the matrix B has two non-zero entries $B_{22} = \Gamma_D\rho_{z,l,D}^2/2$ and $B_{66} = \Gamma_R\rho_{\zeta,\mathrm{th}}^2/2$. The matrices A and B allow to calculate the achievable equivalent temperature

$$T_r = \frac{m_r\omega_r^2\langle z_l^2(t)\rangle}{2k_B} \tag{8.10}$$

of the ion of interest via the solution outlined in Section A.1.

Figure 8.2 shows the achieved temperature of the target ion after 100 s of sympathetic cooling as a function of the detuning from the resonator and the detuning between the ions. Additional parameters are found in the caption of the figure. The main takeaway from the figure is, that sympathetically cooling the target ion's axial motion to the Doppler temperature of the laser-cooled $^9Be^+$ ions is possible with reasonable experimental parameters. The further the detection system's resonance frequency is detuned from the ions' axial frequencies, the lower the achievable temperature, and a frequency switching of 30 kHz on top of 400 kHz is possible. Ideally, the $^9Be^+$ ions' axial frequency needs to be detuned by the coupling frequency $\nu_l - \nu_r = \Omega_K(n = 50)/2\pi \approx 1.1$ Hz and the matching of the frequencies should be better than 1 Hz. Both conditions pose no major challenge.

8.1.4. Status of the coupling trap

During the course of this work and in cooperation with the workshop at the MPIK, the electrodes for this new Penning trap were designed and later manufactured. Figure 8.3 shows a picture of the assembled trap. Now, it has replaced the old coupling trap in the trap tower, compare Figure 4.3, and is ready for commissioning.

[2]For Doppler cooling, this noise is the deflection of the ions due to the spontaneous emission.

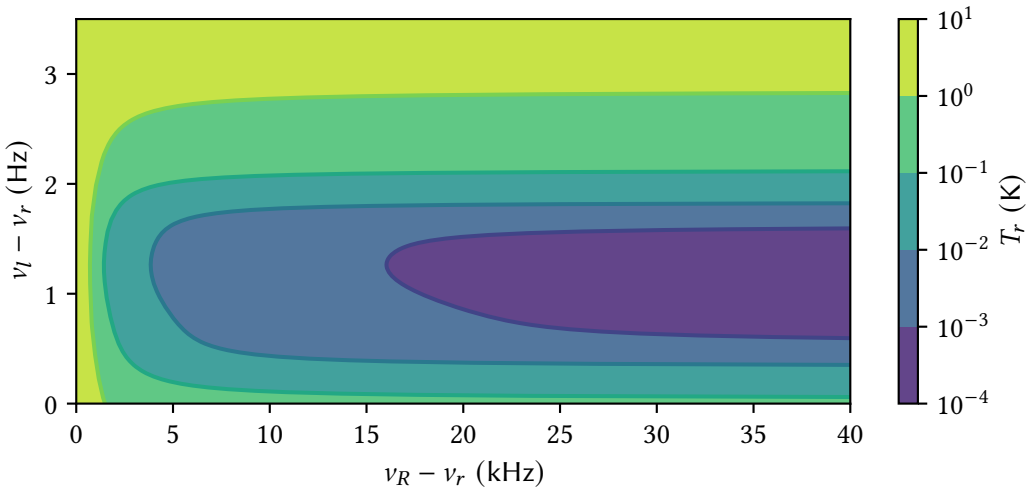

Figure 8.2: Achievable temperatures after 100 s of coupling $^3He^{2+}$ to laser-cooled $^9Be^+$ ions. The lowest values of T_r are only slightly larger than $T_D = 0.5$ mK. For this plot, the resonator Q-value $Q = 10000$, $d_{\text{eff}} = 13.45$ mm, and $n = 50$. The axial frequency of the target ion $\omega_r/2\pi = 400$ kHz is fixed. The laser cooling rate is set to the Rabi frequency $\Gamma_D = \Omega_K$ (higher values will lead to overdamping).

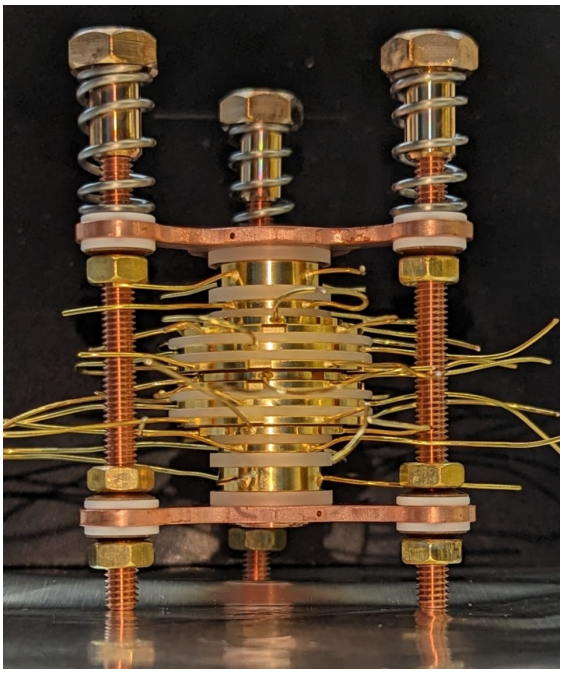

Figure 8.3: Picture of the assembled Penning trap for sympathetic laser cooling via direct Coulomb coupling.

8.2. HFS and nuclear magnetic moment measurements

At µTEx, high-precision measurements of the combined Zeeman and hyperfine splitting have now been performed for $^3He^+$, ref. [11] and $^9Be^{3+}$, see Chapter 6. These measurements enabled the determination of nuclear magnetic moments with relative precision below 1 ppb, and measurements of the 1*s* HFS at the ppt level.

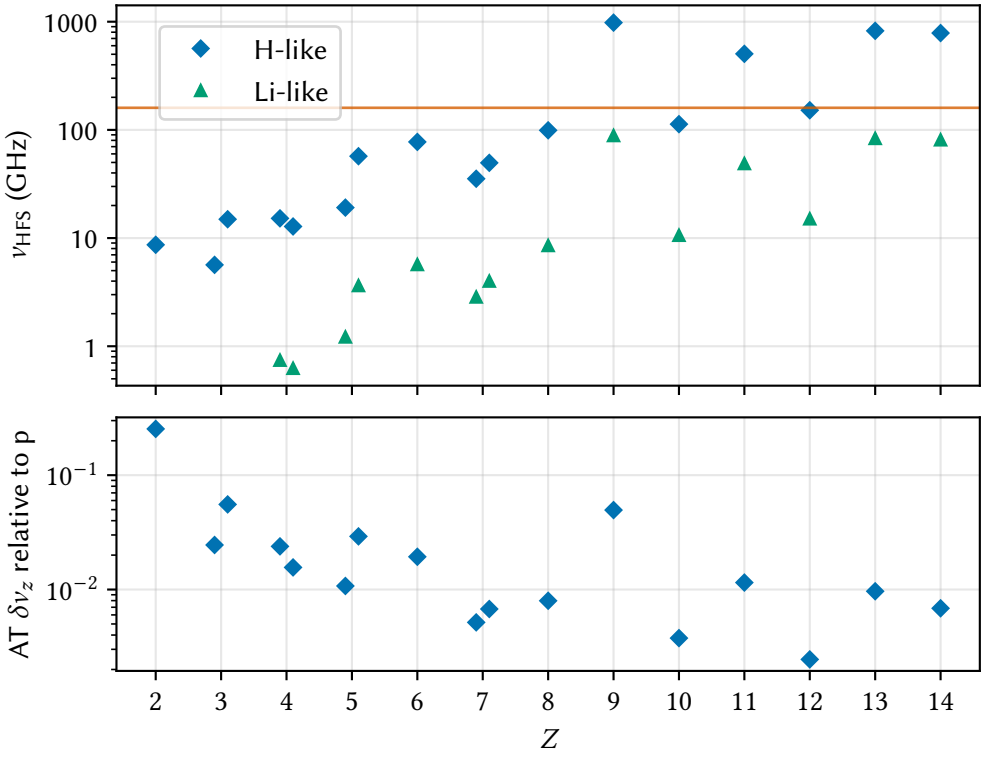

Figure 8.4: Visualization of conceptual HFS and nuclear magnetic moment measurements of light ions with nuclear charge Z (at the same Z, the isotopes are sorted left to right by mass). The top graph shows the zero-field splitting in the *s*-state of hydrogen-like and lithium-like systems [143]. For reference, the Larmor frequency of electrons at $B = 5.7$ T is indicated by the orange line. In the bottom plot, the fraction $\delta\nu_z/\delta\nu_{z,\mathrm{p}}$, where p is the proton, is shown for bare nuclei. Here, $\delta\nu_z$ is the axial frequency jump in the AT due to spin-flips of the nucleus according to Eq. (3.43). Data for the required nuclear magnetic moments is taken from ref. [33].

In the top of Figure 8.4, the hyperfine splitting ν_{HFS} is plotted for light, $Z \leq 14$, hydrogen- and lithium-like ions. As ν_{HFS} scales with the third power of Z, compare Eq. (6.37), it quickly rises to values similar to the electron Larmor frequency of $\nu \approx 160$ GHz at 5.7 T. In the past, microwave equipment in the high GHz (mm-Wave) to the low THz regime was essentially unavailable (called the terahertz gap [192]). Now, frequency multipliers with reasonably large output power are commercially available [193] enabling the spectroscopy of the hydrogen-like

Zeeman and hyperfine splitting up to the low THz regime. At these higher nuclear charges, tests of the HFS via the specific difference method used in Section 6.7 would be much more sensitive to bound-state QED contributions scaling with $(\alpha Z)^n$.

Concerning measurements of bare-nuclear magnetic moments, the bottom plot of Figure 8.4 shows the relative frequency jump

$$\delta\nu_z/\delta\nu_{z,\mathrm{p}} = \frac{m}{m_p}\frac{g_I}{g_p}, \tag{8.11}$$

where $g_p \approx 5.6$ is the proton g-factor. With the parameters from this measurement campaign, the frequency jump due to a spin-flip of a proton is

$$\delta\nu_{z,\mathrm{p}} \approx 150\ \mathrm{mHz}, \tag{8.12}$$

much smaller than the frequency jumps of about 10 Hz which were required to be detected in the measurements performed here. To be able to detect the even smaller frequency jumps of heavier ions, many challenging steps need to be taken. One is the implementation of advanced cooling techniques, see the previous section, to suppress frequency drifts due to cyclotron quantum jumps, compare ref. [146] and see Figure 6.3. Another is the required stability $\sigma(U_0)$ of the ring voltage U_0 which directly influences the axial frequency stability $\sigma(\nu_z) = \sigma(U_0)/2$, compare Eq. (2.3). Resolving e.g. $\delta\nu_z = 10$ mHz on top of $\nu_z \approx 800$ kHz would require voltage stability of better than 25 ppb. To this end, a Josephson voltage standard has recently been used to bias the ring electrode of the analysis trap at this experiment, and shown to improve on current commercial state-of-the-art voltage supplies. A publication [194] of these results, which are part of the PhD thesis of Annabelle Kaiser, is currently in the process of being published.

As an example, performing Zeeman and hyperfine spectroscopy on ^{6,7}Li in different charge states presents an intriguing option. With the hydrogen-like system, comparisons to measurements on the helium-like systems [52, 53] would enable tests of two-electron hyperfine splittings, where calculations have progressed further than for lithium-like systems [54, 59]. Additionally, measurements of the nuclear magnetic moments in the bare and helium-like system could be used to directly test the calculation of diamagnetic shielding parameters of helium-like systems, such as ^{3}He [185]. The development of an in-trap ^{6,7}Li target (amongst other candidates) has been the topic of a recent Bachelor thesis at μTEx [195].

8.3. Bound-electron g-factor measurements

Following the measurements performed in Chapter 7 and the discrepancy within $\Gamma_e(^{12}C^{5+})$, continued efforts were taken towards minimizing systematic effects. Specifically, the magnetostatic imperfection $B_2 \approx 1\ \mathrm{Tm}^{-2}$ and the associated linewidths $\Delta\nu(^9Be^{3+}) \approx 18$ Hz and $\Delta\nu(^{12}C^{5+}) \approx 13$ Hz, corresponding to about 100 ppt relative to the transition frequencies, were concerningly large. While the resulting asymmetric lineshape does not lead to significant contributions and has been cross-checked in this work by numerical integration, see Section A.6, the latter still shares some assumptions with the formal derivation from ref. [62].

To mitigate any potential asymmetry due to B_2 and cross-check the results obtained in this work, efforts towards reducing the B_2 in the PT have been pursued. Now, measurements of

the bound-electron g-factor of $^4He^+$ with significantly reduced B_2 (and B_1) are currently being performed as part of the PhD thesis of Marius Müller. With $^4He^+$, the theory uncertainty of the bound-electron g-factor is additionally suppressed [20], making it an ideal candidate to determine the electron mass via the mass ratio $m(^4He^+)/m_e$, compare Eq. (7.1), and a complementary measurement of the mass of $m(^4He^+)$ in atomic mass units. The latter has recently been performed in a Penning trap with 12 ppt relative uncertainty [196]. Here, with the already shown improvement of the statistical precision, the goal is a measurement of $m(^4He^+)/m_e$ with a relative uncertainty of better than 10 ppt.

8.4. Summary

The beginning of my PhD work coincided with the start of the assembly of the initial setup used for the following measurement of the $^3He^+$ magnetic moments [11]. While contributing to the assembly, commissioning, and spectroscopy measurements, with a focus on programming the experimental control software and co-analyzing the data, I concentrated on efforts towards the measurement of the bare nuclear magnetic moment of $^3He^{2+}$. For the latter, two major upgrades were envisaged. Firstly, a new analysis trap with a larger B_2 to increase the detection signal for the small nuclear magnetic moment, designed by Antonia Schneider [95], was supposed to replace the old AT design. Secondly, with the goal of eventually using sympathetic laser cooling, I designed the laser alignment stages inside the vacuum apparatus for both the ablation of ^9Be and the 313 nm cooling laser. After the measurements on $^3He^+$ were finished, the setup was thus modified to a large extent. In addition to the laser alignment stages, this included a complete reassembly of the trap tower with the new AT, the new 7-pole PT, designed by Marius Müller, and the first design of the coupling traps. Following, initial attempts at laser ablation and Doppler cooling of $^9Be^+$ were successful with the new setup, ref. [194]. However, after performing laser cooling measurements for a while, complications arose due to large axial frequency drifts, probably caused by induced surface charges from the UV laser. Additionally, the strong experimental constraints required for the common-endcap coupling, which includes frequency matching, made us abandon sympathetic laser cooling efforts with the current setup.

Measurements with $^9Be^{3+}$

Nevertheless, the in-trap production of ^9Be ions presented the prospect of performing Zeeman and hyperfine spectroscopy on hydrogen-like $^9Be^{3+}$. Here, by comparison to the measurements performed on $^9Be^+$, ref [117, 141], the goal was to perform the first high-precision comparison of such measurements across different charge states.

Towards performing and evaluating these measurements, I implemented and developed various improvements to the previously employed Penning-trap techniques. Here, the implementation of phase-sensitive detection of the modified cyclotron motion stands out. Directly, this allowed to drastically improve the magnetic field measurement uncertainty by more than an order of magnitude. Additionally, with the methods I developed to measure field imperfections and the motional amplitudes, the corresponding systematic shifts on ν_c could be robustly evaluated with uncertainties well below 10 ppt.

The measurement of nuclear-spin transition frequencies in $^{9}Be^{3+}$ was evaluated to determine nuclear properties. Specifically, the nuclear magnetic moment and the effective Zemach radius were determined, improving on the uncertainty of previous determinations with $^{9}Be^{+}$ by more than one order of magnitude. Now, the nuclear magnetic moment of ^{9}Be, determined with 0.6 ppb uncertainty, is the second most precise such value after the proton's [28]. Additionally, the comparison to the measurements performed on $^{9}Be^{+}$ serves as a crucial test of how nuclear properties transfer across different charge states. As such, the first test of the calculation of multi-electron diamagnetic shielding parameters was performed with 30 ppb precision, limited by the current theoretical calculations. Given the experimental uncertainty, future improved theoretical values can be tested with 1 ppb precision.

Using the phase-sensitive detection, I measured electron-spin resonances with full width at half maximum below 0.3 ppb, better by a factor of two compared to any currently published bound-electron g-factor measurement. Statistical uncertainties of around 20 ppt on Γ_e could be reached with relatively low statistics. Additionally, many cross-checks were performed to check systematic effects at the 10 ppt level. While currently an unexplained discrepancy between our Γ_e determinations exists to the previous determination, the measurements performed here pave the way towards a determination of the electron mass in atomic units with better than 10 ppt uncertainty.

List of publications

1. A. Schneider, B. Sikora, **S. Dickopf**, M. Müller, N. S. Oreshkina, A. Rischka, I. A. Valuev, S. Ulmer, J. Walz, Z. Harman, C. H. Keitel, A. Mooser and K. Blaum. *Direct measurement of the $^3He^+$ magnetic moments*, *Nature* **606**, 878-883 (2022). Cited as [11]

2. **S. Dickopf**, B. Sikora, A. Kaiser, M. Müller, S. Ulmer, V. A. Yerokhin, Z. Harman, C. H. Keitel, A. Mooser and K. Blaum. *Precision spectroscopy on ^9Be challenges limitations of nuclear structure*, *Submitted to Nature* (2024). Cited as [142]

3. A. Kaiser, **S. Dickopf**, M. Door, R. Behr, U. Beutel, S. Eliseev, A. Kaushik, K. Kromer, M. Müller, L. Palafox, S. Ulmer, A. Mooser, and K. Blaum. *Josephson voltage standards as ultra-stable low-noise voltage source for precision Penning-trap experiments*, *Submitted to APL* (2024). Cited as [194]

Bibliography

1. Gaillard, M. K., Grannis, P. D. & Sciulli, F. J. *The standard model of particle physics. Rev. Mod. Phys.* **71,** S96–S111 (1999).
2. Jaeckel, J. & Ringwald, A. *The Low-Energy Frontier of Particle Physics. Annual Review of Nuclear and Particle Science* **60,** 405–437 (2010).
3. Beacham, J. *et al. Physics beyond colliders at CERN: beyond the Standard Model working group report. Journal of Physics G: Nuclear and Particle Physics* **47,** 010501 (2019).
4. Kozlov, M. G., Safronova, M. S., Crespo López-Urrutia, J. R. & Schmidt, P. O. *Highly charged ions: Optical clocks and applications in fundamental physics. Rev. Mod. Phys.* **90,** 045005 (2018).
5. Morgner, J. *et al. Stringent test of QED with hydrogen-like tin. Nature* **622,** 53–57 (2023).
6. Smorra, C. *et al. A parts-per-billion measurement of the antiproton magnetic moment. Nature* **550,** 371–374 (2017).
7. Smorra, C. *et al. Direct limits on the interaction of antiprotons with axion-like dark matter. Nature* **575,** 310–314 (2019).
8. Borchert, M. J. *et al. A 16-parts-per-trillion measurement of the antiproton-to-proton charge–mass ratio. Nature* **601,** 53–57 (2022).
9. Sailer, T. *et al. Measurement of the bound-electron g-factor difference in coupled ions. Nature* **606,** 479–483 (2022).
10. Door, M. *et al. Search for new bosons with ytterbium isotope shifts.* 2024.
11. Schneider, A. *et al. Direct measurement of the* $^3He^+$ *magnetic moments. Nature* **606,** 878–883 (2022).
12. Gerlach, W. & Stern, O. *Der experimentelle Nachweis der Richtungsquantelung im Magnetfeld. Zeitschrift für Physik* **9,** 349–352 (1922).
13. Dirac, P. A. M. & Fowler, R. H. *The quantum theory of the electron. Proceedings of the Royal Society of London. Series A, Containing Papers of a Mathematical and Physical Character* **117,** 610–624 (1928).
14. Aoyama, T., Kinoshita, T. & Nio, M. *Theory of the Anomalous Magnetic Moment of the Electron. Atoms* **7** (2019).
15. Fan, X., Myers, T. G., Sukra, B. A. D. & Gabrielse, G. *Measurement of the Electron Magnetic Moment. Phys. Rev. Lett.* **130,** 071801 (2023).
16. Breit, G. *The Magnetic Moment of the Electron. Nature* **122,** 649–649 (1928).
17. Sturm, S. *et al. g-factor measurement of hydrogenlike* $^{28}Si^{13+}$ *as a challenge to QED calculations. Phys. Rev. A* **87,** 030501 (2013).

18. Heiße, F. *et al. High-Precision Determination of g Factors and Masses of* $^{20}Ne^{9+}$ *and* $^{22}Ne^{9+}$. *Phys. Rev. Lett.* **131,** 253002 (2023).
19. Sailer, T. *Direct Bound-Electron g-Factor Difference Measurement of Coupled Ions at Alphatrap.* PhD thesis (Universität Heidelberg, 2022).
20. Zatorski, J. *et al. Extraction of the electron mass from g-factor measurements on light hydrogenlike ions. Phys. Rev. A* **96,** 012502 (2017).
21. Mohr, P. J. & Taylor, B. N. *CODATA recommended values of the fundamental physical constants: 1998. Rev. Mod. Phys.* **72,** 351–495 (2000).
22. Tiesinga, E., Mohr, P., Newell, D. & Taylor, B. *CODATA Recommended Values of the Fundamental Physical Constants: 2018.* en (2021).
23. Sturm, S. *et al. High-precision measurement of the atomic mass of the electron. Nature* **506,** 467–470 (2014).
24. Heiße, F. *et al. High-precision mass spectrometer for light ions. Phys. Rev. A* **100,** 022518 (2019).
25. Sturm, S. *et al. The ALPHATRAP experiment. The European Physical Journal Special Topics* **227,** 1425–1491 (2019).
26. Köhler, F. *et al. Isotope dependence of the Zeeman effect in lithium-like calcium. Nature Communications* **7,** 10246 (2016).
27. Salg, M. *et al. Proton and neutron electromagnetic radii and magnetic moments from lattice QCD.* 2023.
28. Schneider, G. *et al. Double-trap measurement of the proton magnetic moment at 0.3 parts per billion precision. Science* **358,** 1081–1084 (2017).
29. Fermi, E. *Über die magnetischen Momente der Atomkerne. Zeitschrift für Physik* **60,** 320–333 (1930).
30. Gentile, T. R., Nacher, P. J., Saam, B. & Walker, T. G. *Optically polarized* ^{3}He. *Rev. Mod. Phys.* **89,** 045004 (2017).
31. Farooq, M. *et al. Absolute Magnetometry with* ^{3}He. *Phys. Rev. Lett.* **124,** 223001 (2020).
32. Ramsey, N. F. *Magnetic Shielding of Nuclei in Molecules. Phys. Rev.* **78,** 699–703 (1950).
33. Stone, N. *Table of recommended nuclear magnetic dipole moments.* Tech. rep. (International Atomic Energy Agency, 2019).
34. Stone, N. J. *Table of Nuclear Magnetic Dipole and Electric Quadrupole Moments.* Tech. rep. NUCLEAR PHYSICS AND RADIATION PHYSICS (International Atomic Energy Agency (IAEA), 2014), 171.
35. Crespo López-Urrutia, J. R., Beiersdorfer, P., Savin, D. W. & Widmann, K. *Direct Observation of the Spontaneous Emission of the Hyperfine Transition* $F = 4$ *to* $F = 3$ *in Ground State Hydrogenlike* $^{165}Ho^{66+}$ *in an Electron Beam Ion Trap. Phys. Rev. Lett.* **77,** 826–829 (1996).
36. Fella, V. *et al. Magnetic moment of* ^{207}Pb *and the hyperfine splitting of* $^{207}Pb^{81+}$. *Phys. Rev. Res.* **2,** 013368 (2020).

37. Ullmann, J. *et al. High precision hyperfine measurements in Bismuth challenge bound-state strong-field QED. Nature Communications* **8,** 15484 (2017).

38. Skripnikov, L. V. *et al. New Nuclear Magnetic Moment of* ^{209}Bi*: Resolving the Bismuth Hyperfine Puzzle. Phys. Rev. Lett.* **120,** 093001 (2018).

39. Wehrli, D., Puchalski, M. & Pachucki, K. *QED theory of the nuclear magnetic shielding in H and* ^{3}He. *Phys. Rev. A* **105,** 032808 (2022).

40. Pachucki, K. *Nuclear mass and size corrections to the magnetic shielding. Phys. Rev. A* **108,** 062806 (2023).

41. Zemach, A. C. *Proton Structure and the Hyperfine Shift in Hydrogen. Phys. Rev.* **104,** 1771–1781 (1956).

42. Grotch, H. & Yennie, D. R. *Effective Potential Model for Calculating Nuclear Corrections to the Energy Levels of Hydrogen. Rev. Mod. Phys.* **41,** 350–374 (1969).

43. Pohl, R. *et al. The size of the proton. Nature* **466,** 213–216 (2010).

44. Glazov, D. & Shabaev, V. *Finite nuclear size correction to the bound-electron g factor in a hydrogenlike atom. Physics Letters A* **297,** 408–411 (2002).

45. Karshenboim, S. G. *Precision physics of simple atoms: QED tests, nuclear structure and fundamental constants. Physics Reports* **422,** 1–63 (2005).

46. Karr, J.-P., Marchand, D. & Voutier, E. *The proton size. Nature Reviews Physics* **2,** 601–614 (2020).

47. Shabaev, V. M., Artemyev, A. N., Yerokhin, V. A., Zherebtsov, O. M. & Soff, G. *Towards a Test of QED in Investigations of the Hyperfine Splitting in Heavy Ions. Phys. Rev. Lett.* **86,** 3959–3962 (2001).

48. Mathur, B. S., Crampton, S. B., Kleppner, D. & Ramsey, N. F. *Hyperfine Separation of Tritium. Phys. Rev.* **158,** 14–17 (1967).

49. Wineland, D. J. & Ramsey, N. F. *Atomic Deuterium Maser. Phys. Rev. A* **5,** 821–837 (1972).

50. Hellwig, H. *et al. Measurement of the Unperturbed Hydrogen Hyperfine Transition Frequency. IEEE Transactions on Instrumentation and Measurement* **19,** 200–209 (1970).

51. Schuessler, H. A., Fortson, E. N. & Dehmelt, H. G. *Hyperfine Structure of the Ground State of* ^{3}He^{+} *by the Ion-Storage Exchange-Collision Technique. Phys. Rev.* **187,** 5–38 (1969).

52. Sun, W. *et al. Measurement of Hyperfine Structure and the Zemach Radius in* ^{6}Li^{+} *Using Optical Ramsey Technique. Phys. Rev. Lett.* **131,** 103002 (2023).

53. Guan, H. *et al. Probing atomic and nuclear properties with precision spectroscopy of fine and hyperfine structures in the* ^{7}Li^{+} *ion. Phys. Rev. A* **102,** 030801 (2020).

54. Pachucki, K., Patkó š, V. ě. & Yerokhin, V. A. *Hyperfine splitting in* ^{6,7}Li^{+}. *Phys. Rev. A* **108,** 052802 (2023).

55. Guan, H. *et al. Precision Spectroscopy and Nuclear Structure Parameters in* ^{7}*Li*$^{+}$ *ion.* 2024.

56. Wineland, D. J. & Dehmelt, H. G. *Principles of the stored ion calorimeter. Journal of Applied Physics* **46,** 919–930 (1975).

57. Scholl, T. J. *et al. Precision measurement of relativistic and QED effects in heliumlike beryllium. Phys. Rev. Lett.* **71,** 2188–2191 (1993).
58. Qi, X.-Q. *et al. Theoretical hyperfine splittings of* $^{7,9}Be^{2+}$ *ions for future studies of nuclear properties. Phys. Rev. A* **107,** L010802 (2023).
59. Patkó š, V. ě., Yerokhin, V. A. & Pachucki, K. *Higher-Order QED Corrections to the Hyperfine Splitting in* ^{3}He. *Phys. Rev. Lett.* **131,** 183001 (2023).
60. Wineland, D., Ekstrom, P. & Dehmelt, H. *Monoelectron Oscillator. Phys. Rev. Lett.* **31,** 1279–1282 (1973).
61. Brown, L. S. & Gabrielse, G. *Precision spectroscopy of a charged particle in an imperfect Penning trap. Phys. Rev. A* **25,** 2423–2425 (1982).
62. Brown, L. S. & Gabrielse, G. *Geonium theory: Physics of a single electron or ion in a Penning trap. Rev. Mod. Phys.* **58,** 233–311 (1986).
63. Myers, E. G., Wagner, A., Kracke, H. & Wesson, B. A. *Atomic Masses of Tritium and Helium-3. Phys. Rev. Lett.* **114,** 013003 (2015).
64. Gabrielse, G., Haarsma, L. & Rolston, S. *Open-endcap Penning traps for high precision experiments. International Journal of Mass Spectrometry and Ion Processes* **88,** 319–332 (1989).
65. Ketter, J., Eronen, T., Höcker, M., Streubel, S. & Blaum, K. *First-order perturbative calculation of the frequency-shifts caused by static cylindrically-symmetric electric and magnetic imperfections of a Penning trap. International Journal of Mass Spectrometry* **358,** 1–16 (2014).
66. Koehler, F. *Bound-Electron g-Factor Measurements for the Determination of the Electron Mass and Isotope Shifts in Highly Charged Ions.* PhD thesis (Universität Heidelberg, 2015).
67. Ketter, J. *Theoretical treatment of miscellaneous frequency-shifts in Penning traps with classical perturbation theory.* PhD thesis (Universität Heidelberg, 2015).
68. Häffner, H. *et al. High-Accuracy Measurement of the Magnetic Moment Anomaly of the Electron Bound in Hydrogenlike Carbon. Phys. Rev. Lett.* **85,** 5308–5311 (2000).
69. Schuh, M. *et al. Image charge shift in high-precision Penning traps. Phys. Rev. A* **100,** 023411 (2019).
70. Ulmer, S. *First Observation of Spin Flips with a Single Proton Stored in a Cryogenic Penning Trap.* PhD thesis (Universität Heidelberg, 2011).
71. Nyquist, H. *Thermal Agitation of Electric Charge in Conductors. Phys. Rev.* **32,** 110–113 (1928).
72. Higuchi, T. *Development for an improved comparison of proton-to-antiproton charge-to-mass ratio.* PhD thesis (2018).
73. Wolfram Research Inc. *Mathematica, Version 13.3.* Champaign, IL, 2023.
74. Cornell, E. A., Weisskoff, R. M., Boyce, K. R. & Pritchard, D. E. *Mode coupling in a Penning trap: π pulses and a classical avoided crossing. Phys. Rev. A* **41,** 312–315 (1990).

75. Cohen-Tannoudji, C., Diu, B. & Laloe, F. *Quantum Mechanics, Volume 1* (1986).
76. Sturm, S., Wagner, A., Schabinger, B. & Blaum, K. *Phase-Sensitive Cyclotron Frequency Measurements at Ultralow Energies. Phys. Rev. Lett.* **107,** 143003 (2011).
77. Rau, S. *High-precision measurement of the deuteron's atomic mass.* PhD thesis (Ruprecht-Karls-Universität Heidelberg, 2020).
78. Feynman, R., Leighton, R. & Sands, M. in *The Feynman Lectures on Physics, Vol. III: The New Millennium Edition: Quantum Mechanics* chap. 6 (Basic Books, 2011). ISBN: 978-0-465-02501-5.
79. Feynman, R., Leighton, R. & Sands, M. in *The Feynman Lectures on Physics, Vol. III: The New Millennium Edition: Quantum Mechanics* chap. 12 (Basic Books, 2011). ISBN: 978-0-465-02501-5.
80. Woodgate, G. *Elementary Atomic Structure.* 187–193 (1980).
81. Breit, G. & Rabi, I. I. *Measurement of Nuclear Spin. Phys. Rev.* **38,** 2082–2083 (1931).
82. Hentschel, K. in *Compendium of Quantum Physics* (eds Greenberger, D., Hentschel, K. & Weinert, F.) 468–470 (Springer Berlin Heidelberg, Berlin, Heidelberg, 2009). ISBN: 978-3-540-70626-7.
83. Schrödinger, E. *An Undulatory Theory of the Mechanics of Atoms and Molecules. Physical Review* **28,** 1049–1070 (1926).
84. Cohen-Tannoudji, C., Diu, B. & Laloe, F. *Quantum Mechanics, Volume 1* Second, 458–460 (2019).
85. Whiting, E. *An empirical approximation to the Voigt profile. Journal of Quantitative Spectroscopy and Radiative Transfer* **8,** 1379–1384 (1968).
86. Bloch, F. *Nuclear Induction. Phys. Rev.* **70,** 460–474 (1946).
87. Brown, L. S. *Geonium lineshape. Annals of Physics* **159,** 62–98 (1985).
88. Thomas, L. H. *I. The kinematics of an electron with an axis. The London, Edinburgh, and Dublin Philosophical Magazine and Journal of Science* **3,** 1–22 (1927).
89. Jackson, J. D. *Classical electrodynamics* second, 543 (Wiley, 1975).
90. Lambiase, G. & Papini, G. *Spin-rotation coupling and Thomas precession of ions in a storage ring. Journal of Physics: Conference Series* **442,** 012073 (2013).
91. Sturm, S. *The g-factor of the electron bound in* $^{28}Si^{13+}$*: The most stringent test of bound-state quantum electrodynamics.* PhD thesis (Johannes-Gutenberg Universität Mainz, 2012).
92. Dehmelt, H. *Continuous Stern-Gerlach effect: Principle and idealized apparatus. Proc Natl Acad Sci U S A* **83,** 2291–2294 (1986).
93. Mooser, A. *Der g-Faktor des Protons.* PhD thesis (Universität Mainz, 2014).
94. Schneider, A. *Design of the Analysis Trap and He Ion Source for the 3He2+ magnetic moment measurement* (Universität Heidelberg, 2019).
95. Schneider, A. *et al. A Novel Penning-Trap Design for the High-Precision Measurement of the* $^{3}He^{2+}$ *Nuclear Magnetic Moment. Annalen der Physik* **531,** 1800485 (2019).

96. Dickopf, S. *Design, installation and characterisation of a microwave transmission line for driving the transitions of the $^3He^+$ hyperfine structure in a Penning trap* (Universität Heidelberg, 2020).
97. Schneider, A. *Measurement of the g-factors and zero-field hyperfine splitting of 3He+ in a Penning trap*. PhD thesis (Universität Heidelberg, 2022).
98. Van Dyck R. S., J., Farnham, D. L., Zafonte, S. L. & Schwinberg, P. B. *Ultrastable superconducting magnet system for a penning trap mass spectrometer. Review of Scientific Instruments* **70,** 1665–1671 (1999).
99. Zafonte, S. L. & Dyck, R. S. V. *Ultra-precise single-ion atomic mass measurements on deuterium and helium-3. Metrologia* **52,** 280 (2015).
100. Diel, C. *First mass measurements with the MPIK/UW-PTMS*. PhD thesis (Universität Heidelberg, 2011).
101. Streubel, S. *Kontrolle der Umwelteinflüsse auf THe-Trap am Beispiel der Bestimmung des Massenverhältnisses von Kohlenstoff-12 zu Sauerstoff-16*. PhD thesis (Universität Heidelberg, 2014).
102. Höcker, M. *Precision Mass Measurements at THe-Trap and the FSU trap.* PhD thesis (Universität Heidelberg, 2016).
103. Segal, T. *Mass Measurements of Neon Isotopes at THe-Trap.* PhD thesis (Universität Heidelberg, 2019).
104. Wikipedia. *Helium — Wikipedia, The Free Encyclopedia.* http://en.wikipedia.org/w/index.php?title=Helium&oldid=1192483184. [Online; accessed 05-January-2024]. 2024.
105. Redshaw, M. *et al. Fabrication and characterization of field emission points for ion production in Penning trap applications. International Journal of Mass Spectrometry* **379,** 187–193 (2015).
106. Rodegheri, C. D. C. *Neuartige kryogene Penning-Falle für den Nachweis von Spin-Übergängen eines Protons und Bestimmung seines g-Faktors.* PhD thesis (Universität Mainz, 2014).
107. Walter, H. *Analyse von NMR-Daten aus dem Magneten von THe-Trap* (Universität Heidelberg, 2017).
108. Heinzen, D. J. & Wineland, D. J. *Quantum-limited cooling and detection of radio-frequency oscillations by laser-cooled ions. Phys. Rev. A* **42,** 2977–2994 (1990).
109. Bohman, M. *et al. Sympathetic cooling of protons and antiprotons with a common endcap Penning trap. Journal of Modern Optics* **65,** 568–576 (2018).
110. Bohman, M. *Sympathetic Cooling of a Proton with Resonant Image Current Coupling*. PhD thesis (Universität Heidelberg, 2021).
111. Dubin, D. H. E. & O'Neil, T. M. *Trapped nonneutral plasmas, liquids, and crystals (the thermal equilibrium states). Rev. Mod. Phys.* **71,** 87–172 (1999).
112. Wiesinger, M. *Sympathetic Cooling of a Single Individually-Trapped Proton in a Cryogenic Penning Trap.* PhD thesis (Universität Heidelberg, 2023).

113. Norton, F. J. *Permeation of Gases through Solids. Journal of Applied Physics* **28,** 34–39 (1957).

114. Kim, Y.-K. *et al. Electron-Impact Cross Sections for Ionization and Excitation Database.* 2004.

115. Chichkov, B. N., Momma, C., Nolte, S., von Alvensleben, F. & Tünnermann, A. *Femtosecond, picosecond and nanosecond laser ablation of solids. Applied Physics A* **63,** 109–115 (1996).

116. Kaiser, A. *Characterization of an ultra-stable voltage supply and implementation of sympathetic laser cooling for the $^3He^{2+}$ g-factor measurement* (Universität Heidelberg, 2022).

117. Wineland, D. J., Bollinger, J. J. & Itano, W. M. *Laser-Fluorescence Mass Spectroscopy. Phys. Rev. Lett.* **50,** 628–631 (1983).

118. Green, E. I. *The story of Q. American Scientist* **43,** 584–594 (1955).

119. Müller, M. *Design and implementation of a non-destructive ion detection system for the ^3He g-factor experiment.* 2020.

120. Ramo, S., Whinnery, J. R. & Van Duzer, T. *Fields and waves in communication electronics* (John Wiley & Sons, 1994).

121. Mattis, D. C. & Bardeen, J. *Theory of the Anomalous Skin Effect in Normal and Superconducting Metals. Phys. Rev.* **111,** 412–417 (1958).

122. Beasley, M. R., Labusch, R. & Webb, W. W. *Flux Creep in Type-II Superconductors. Phys. Rev.* **181,** 682–700 (1969).

123. Weigel, A. *Detection Electronics Design and First Observation of Bound-Electron Spin Transitions at the ALPHATRAP g-Factor Experiment*. PhD thesis (Universität Heidelberg, 2019).

124. Bock, N. V. *Theoretische Modellierung einer Penning-Falle zur Nutzung sympathetischer Laserkühlung und Charakterisierung einer dafür vorgesehenen Präzisionsspannungsquelle* (Universität Heidelberg, 2022).

125. Welch, P. *The use of fast Fourier transform for the estimation of power spectra: A method based on time averaging over short, modified periodograms. IEEE Transactions on Audio and Electroacoustics* **15,** 70–73 (1967).

126. Alonso, J. *et al. A miniature electron-beam ion source for in-trap creation of highly charged ions. Review of Scientific Instruments* **77,** 03A901 (2006).

127. Kwiatkowski, A., Bollen, G., Redshaw, M., Ringle, R. & Schwarz, S. *Isobaric beam purification for high precision Penning trap mass spectrometry of radioactive isotope beams with SWIFT. International Journal of Mass Spectrometry* **379,** 9–15 (2015).

128. Bayes, T. *LII. An essay towards solving a problem in the doctrine of chances. By the late Rev. Mr. Bayes, FRS communicated by Mr. Price, in a letter to John Canton, AMFR S. Philosophical transactions of the Royal Society of London,* 370–418 (1763).

129. James, F. *et al. Minuit. CERN Program Library Long Writeup D* **506,** 1993 (1994).

130. Markus Köhli, K. R. *Statistical Methods in Experimental Physics.* 2023.

131. Hastings, W. K. *Monte Carlo sampling methods using Markov chains and their applications. Biometrika* **57,** 97–109 (1970).

132. Ge, H., Xu, K. & Ghahramani, Z. *Turing: a language for flexible probabilistic inference.* in *International Conference on Artificial Intelligence and Statistics, AISTATS 2018, 9-11 April 2018, Playa Blanca, Lanzarote, Canary Islands, Spain* (2018), 1682–1690.

133. Köhler, F. *Bound-electron g-factor measurements for the determination of the electron mass and isotope shifts in highly charged ions.* PhD thesis (Ruprecht-Karls-Universität Heidelberg, 2015).

134. Schüßler, R. X. *First High-Precision Mass Measurements at PENTATRAP on highly charged Xe and Re ions.* PhD thesis (Ruprecht-Karls-Universität Heidelberg, 2019).

135. Häffner, H. *Präzisionsmessung des magnetischen Moments des Elektrons in wasserstoffähnlichem Kohlenstoff.* PhD thesis (Universität Mainz, 2000).

136. Will, C. *Sympathetic Cooling of Trapped Ions Coupled via Image Currents: Simulation and Measurement.* PhD thesis (Universität Heidelberg, 2023).

137. Dehmelt, H., Nagourney, W. & Sandberg, J. *Self-excited mono-ion oscillator. Proceedings of the National Academy of Sciences* **83,** 5761–5763 (1986).

138. D'Urso, B., Odom, B. & Gabrielse, G. *Feedback Cooling of a One-Electron Oscillator. Phys. Rev. Lett.* **90,** 043001 (2003).

139. Herkenhoff, J. *et al. A digital feedback system for advanced ion manipulation techniques in Penning traps. Review of Scientific Instruments* **92,** 103201 (2021).

140. Wineland, D. J., Itano, W., Bergquist, J. & Bollinger, J. *Trapped ions and laser cooling* (1985).

141. Shiga, N., Itano, W. M. & Bollinger, J. J. *Diamagnetic correction to the $^9Be^+$ ground-state hyperfine constant. Phys. Rev. A* **84,** 012510 (2011).

142. Dickopf, S. *et al. Precision spectroscopy on ^{9}Be challenges limitations of nuclear structure.* Submitted to Nature (2024).

143. Boucard, S. & Indelicato, P. *Relativistic many-body and QED effects on the hyperfine structure of lithium-like ions. The European Physical Journal D* **8,** 59–73 (2000).

144. *PRS10 — Rubidium frequency standard with low phase noise.* 2023.

145. Mooser, A. *Der g-Faktor des Protons.* PhD thesis (Johannes Gutenberg-Universität Mainz, 2013).

146. Borchert, M. J. *et al. Measurement of Ultralow Heating Rates of a Single Antiproton in a Cryogenic Penning Trap. Phys. Rev. Lett.* **122,** 043201 (2019).

147. Allan, D. W. *Statistics of atomic frequency standards. Proceedings of the IEEE* **54,** 221–230 (1966).

148. Powles, J. G. *The Adiabatic Fast Passage Experiment in Magnetic Resonance. Proceedings of the Physical Society* **71,** 497 (1958).

149. Hardy, C., Edelstein, W. & Vatis, D. *Efficient adiabatic fast passage for NMR population inversion in the presence of radiofrequency field inhomogeneity and frequency offsets. Journal of Magnetic Resonance (1969)* **66,** 470–482 (1986).

150. Arapoglou, I. *First measurement of the ground-state g-factor of boronlike argon $^{40}Ar^{13+}$ in Alphatrap*. PhD thesis (Universität Heidelberg, 2019).

151. Tellinghuisen, J. *Statistical Error Propagation. The Journal of Physical Chemistry A* **105,** 3917–3921 (2001).

152. Kielkopf, J. F. *New approximation to the Voigt function with applications to spectral-line profile analysis. J. Opt. Soc. Am.* **63,** 987–995 (1973).

153. Foreman-Mackey, D., Hogg, D. W., Lang, D. & Goodman, J. *emcee: The MCMC Hammer. Publications of the Astronomical Society of the Pacific* **125,** 306–312 (2013).

154. Hoffman, M. D. & Gelman, A. *The No-U-Turn Sampler: Adaptively Setting Path Lengths in Hamiltonian Monte Carlo.* 2011.

155. Revels, J., Lubin, M. & Papamarkou, T. *Forward-Mode Automatic Differentiation in Julia. arXiv:1607.07892 [cs.MS]* (2016).

156. Rau, S. *et al. Penning trap mass measurements of the deuteron and the HD^+ molecular ion. Nature* **585,** 43–47 (2020).

157. Schiff, L. I. & Snyder, H. *Theory of the Quadratic Zeeman Effect. Phys. Rev.* **55,** 59–63 (1939).

158. Fletcher, G. D., Lipson, S. J. & Larson, D. J. *Observation of a magnetic-field–dependent g-factor ratio. Phys. Rev. Lett.* **58,** 2535–2538 (1987).

159. Moskovkin, D. L. & Shabaev, V. M. *Zeeman effect of the hyperfine-structure levels in hydrogenlike ions. Phys. Rev. A* **73,** 052506 (2006).

160. Stone, N. J. *Table of Nuclear Electric Quadrupole Moments.* Tech. rep. ATOMIC AND MOLECULAR PHYSICS (International Atomic Energy Agency (IAEA), 2021), 68.

161. Pachucki, K. & Puchalski, M. *Accurate determination of Be magnetic moment. Optics Communications* **283.** Quo vadis Quantum Optics?, 641–643 (2010).

162. Shabaev, V. M., Glazov, D. A., Malyshev, A. V. & Tupitsyn, I. I. *Recoil Effect on the g Factor of Li-Like Ions. Phys. Rev. Lett.* **119,** 263001 (2017).

163. Karshenboim, S. G. & Ivanov, V. G. *The g factor of the proton. Physics Letters B* **566,** 27–34 (2003).

164. Pachucki, K., Patkóš, V. & Yerokhin, V. A. *Accurate determination of $^{6,7}Li$ nuclear magnetic moments. Physics Letters B* **846,** 138189 (2023).

165. Rudziński, A., Puchalski, M. & Pachucki, K. *Relativistic, QED, and nuclear mass effects in the magnetic shielding of H3e. The Journal of Chemical Physics* **130,** 244102 (2009).

166. Wehrli, D., Spyszkiewicz-Kaczmarek, A., Puchalski, M. & Pachucki, K. *QED Effect on the Nuclear Magnetic Shielding of ^{3}He. Phys. Rev. Lett.* **127,** 263001 (2021).

167. Bohr, A. & Weisskopf, V. F. *The Influence of Nuclear Structure on the Hyperfine Structure of Heavy Elements. Phys. Rev.* **77,** 94–98 (1950).

168. Djukanovic, D. *et al. Zemach radius of the proton from lattice QCD.* 2023.

169. Distler, M. O., Bernauer, J. C. & Walcher, T. *The RMS charge radius of the proton and Zemach moments. Physics Letters B* **696,** 343–347 (2011).

170. Tomalak, O. *Two-photon exchange on the neutron and the hyperfine splitting. Phys. Rev. D* **99,** 056018 (2019).

171. Patkó š, V. ě., Yerokhin, V. A. & Pachucki, K. *Nuclear polarizability effects in* ^{3}He$^+$ *hyperfine splitting. Phys. Rev. A* **107,** 052802 (2023).

172. Puchalski, M. & Pachucki, K. *Ground-state hyperfine splitting in the* Be^+ *ion. Phys. Rev. A* **89,** 032510 (2014).

173. Kramida, A. E. *Critical Compilation of Wavelengths and Energy Levels of Singly Ionized Beryllium (Be II). Physica Scripta* **72,** 309 (2005).

174. Drake, G. *Theoretical energies for the n= 1 and 2 states of the helium isoelectronic sequence up to Z= 100. Canadian Journal of Physics* **66,** 586–611 (1988).

175. Beigang, R., Schmidt, D. & West, P. *LASER SPECTROSCOPY OF HIGH RYDBERG STATES OF LIGHT ALKALINE-EARTH ELEMENTS : Be AND Mg. Journal de Physique Colloques* **44,** C7-229-C7–237 (1983).

176. Wang, M., Huang, W., Kondev, F., Audi, G. & Naimi, S. *The AME 2020 atomic mass evaluation (II). Tables, graphs and references*. Chinese Physics C* **45,** 030003 (2021).

177. Fan, X. *An Improved Measurement of the Electron Magnetic Moment.* PhD thesis (Harvard University, 2022).

178. Kromer, K. *Environmentally-induced systematic effects at the high-precision mass spectrometer PENTATRAP* (Universität Heidelberg, 2019).

179. Köhler, F. *et al. The electron mass from g-factor measurements on hydrogen-like carbon* $^{12}C^{5+}$*. Journal of Physics B: Atomic, Molecular and Optical Physics* **48,** 144032 (2015).

180. Repp, J. *et al. PENTATRAP: a novel cryogenic multi-Penning-trap experiment for high-precision mass measurements on highly charged ions. Applied Physics B* **107,** 983–996 (2012).

181. Kromer, K. *et al. Observation of a Low-Lying Metastable Electronic State in Highly Charged Lead by Penning-Trap Mass Spectrometry. Phys. Rev. Lett.* **131,** 223002 (2023).

182. PENTATRAP. $^9Be^{3+}$ *mass.* Private Communication. 2023.

183. Sikora, B. $^9Be^{3+}$ *bound-electron g-factor.* Private Communication. 2023.

184. Mooser, A. *et al. A New Experiment for the Measurement of the g-Factors of* $^3He^+$ *and* $^3He^{2+}$*. Journal of Physics: Conference Series* **1138,** 012004 (2018).

185. Yerokhin, V. A., Pachucki, K., Harman, Z. & Keitel, C. H. *Nuclear magnetic shielding in heliumlike ions. Phys. Rev. A* **109,** 032808 (2024).

186. Tu, B. *et al. Tank-Circuit Assisted Coupling Method for Sympathetic Laser Cooling. Advanced Quantum Technologies* **4,** 2100029 (2021).

187. Schmidt, P. O. *et al. Spectroscopy Using Quantum Logic. Science* **309,** 749–752 (2005).

188. Myatt, C. J., Burt, E. A., Ghrist, R. W., Cornell, E. A. & Wieman, C. E. *Production of Two Overlapping Bose-Einstein Condensates by Sympathetic Cooling*. *Phys. Rev. Lett.* **78,** 586–589 (1997).

189. Bohman, M. *et al. Sympathetic cooling of a trapped proton mediated by an LC circuit*. *Nature* **596,** 514–518 (2021).

190. Will, C. *et al. Sympathetic cooling schemes for separately trapped ions coupled via image currents*. *New Journal of Physics* **24,** 033021 (2022).

191. Door, M. in preperation. PhD thesis (Universität Heidelberg).

192. Dhillon, S. S. *et al. The 2017 terahertz science and technology roadmap*. *Journal of Physics D: Applied Physics* **50,** 043001 (2017).

193. *Signal Generator Extension Modules*. [Online; accessed 29-March-2024].

194. Kaiser, A. *et al. Josephson voltage standards as ultra-stable low-noise voltage source for precision Penning-trap experiments*. Submitted to APL (2024).

195. Beutel, U. to be published (2024).

196. Sasidharan, S. *et al. Penning-Trap Mass Measurement of Helium-4*. *Phys. Rev. Lett.* **131,** 093201 (2023).

197. Uhlenbeck, G. E. & Ornstein, L. S. *On the Theory of the Brownian Motion*. *Phys. Rev.* **36,** 823–841 (1930).

198. Lemons, D. S. & Gythiel, A. *Paul Langevin's 1908 paper "On the Theory of Brownian Motion" ["Sur la théorie du mouvement brownien," C. R. Acad. Sci. (Paris) 146, 530-533 (1908)]*. *American Journal of Physics* **65,** 1079–1081 (1997).

199. Fokker, A. D. *Die mittlere Energie rotierender elektrischer Dipole im Strahlungsfeld*. *Annalen der Physik* **348,** 810–820 (1914).

200. Planck, M. *Über einen Satz der statistischen Dynamik und seine Erweiterung in der Quantentheorie* (Reimer, 1917).

201. Meucci, A. *Review of statistical arbitrage, cointegration, and multivariate Ornstein-Uhlenbeck* (2009).

202. Vatiwutipong, P. & Phewchean, N. *Alternative way to derive the distribution of the multivariate Ornstein–Uhlenbeck process*. *Advances in Difference Equations* **2019,** 276 (2019).

203. Gentle, J. E. *Computational statistics,* 315–317 (Springer, 2010).

204. Gardiner, C. W. *et al. Handbook of stochastic methods* (springer Berlin, 1985).

205. Wiener, N. *Generalized harmonic analysis*. *Acta Mathematica* **55,** 117–258 (1930).

206. Khintchine, A. *Korrelationstheorie der stationären stochastischen Prozesse*. *Mathematische Annalen* **109,** 604–615 (1934).

207. Wikipedia. *Rayleigh distribution — Wikipedia, The Free Encyclopedia*. http://en.wikipedia.org/w/index.php?title=Rayleigh%20distribution&oldid=1182004951. [Online; accessed 15-November-2023]. 2023.

208. Rackauckas, C. & Nie, Q. *Differentialequations.jl–a performant and feature-rich ecosystem for solving differential equations in julia. Journal of Open Research Software* **5,** 15 (2017).

List of figures

List of tables

Appendix A.

Thermal motion

In Section 2.5, the detection and thermalization of the axial motion via the resonant RLC circuit was described. The statistic nature of the added noise term in Eq. (2.47) makes a full deterministic solution of the differential equation impossible.

In this chapter, I will outline a statistical solution of the particles motion inside the Penning trap. Initially, the main goal was the prediction of the achievable cooling capabilities of the new coupling trap design, but the general framework developed here showed to have further applications. This includes sampling of time series detection data, sampling of cycles of the phase-sensitive detection method and the numerical integration of the asymmetric spin-flip probability lineshape.

A.1. Statistical solutions of the Langevin equation

The system of particle and noise driven resonator, Eq. (2.47), is a particular case of a general white noise driven linear state-space system. It may be written as

$$\frac{\mathrm{d}}{\mathrm{d}t}\vec{x} = A\vec{x} + \delta\vec{F}(t), \tag{A.1}$$

where $\vec{x}$ are the phase space coordinates, A is the matrix describing the drift components and $\delta\vec{F}(t)$ is a white noise force that leads to diffusion. Such systems are called Ornstein-Uhlenbeck processes and their statistical solutions have been thoroughly investigated [197]. The above equation is called the Langevin equation of the process [198]. Alternatively, the process may be expressed by the Fokker-Planck equation which describes the evolution of the probability in phase space [199, 200].

It can be checked that the formal solution

$$\vec{x}(t) = e^{At}\vec{x}_0 + \int_0^t \mathrm{d}t' e^{A(t-t')}\delta\vec{F}(t'), \tag{A.2}$$

where e^{At} is a matrix exponential, solves the Langevin equation. As prior knowledge of the noise term $\delta\vec{F}(t')$ is not given this can not be computed analytically.

The statistical quantities that can be solved for in this type of equation are the mean $\vec{M}(t)$ and covariance matrix $\Sigma(t)$ of the phase space coordinates. The only knowledge available of the white noise $\delta\vec{F}(t)$ is that its mean is zero

$$\left\langle \delta\vec{F}(t) \right\rangle = 0 \tag{A.3}$$

and it is fully uncorrelated between times t and t'

$$\left\langle \delta F_i(t)\delta F_j(t') \right\rangle = 2B_{ij}\delta(t-t'). \tag{A.4}$$

Here $\delta(t-t')$ is the Dirac delta function and the matrix B_{ij} the correlation matrix. This allows to compute the mean value of Eq. (A.2)

$$\begin{aligned}\vec{M}(t) = \left\langle \vec{x}(t) \right\rangle &= \left\langle e^{At}\vec{x}_0 \right\rangle + \left\langle \int_0^t \mathrm{d}t' e^{A(t-t')}\delta\vec{F}(t') \right\rangle = e^{At}\vec{x}_0 + \int_0^t \mathrm{d}t' e^{A(t-t')}\left\langle \delta\vec{F}(t') \right\rangle \\ &= e^{At}\vec{x}_0,\end{aligned} \tag{A.5}$$

where $\left\langle \cdots \right\rangle$ is an average over the all the possible implementations of the statistical variables. Similarly the covariance matrix can be computed, again utilizing the vanishing of the mean of the noise:

$$\begin{aligned}\Sigma_{ij}(t) &= \left\langle x_i(t)x_j(t) - M_i(t)M_j(t) \right\rangle \\ &= \left\langle \int_0^t \mathrm{d}t' \int_0^t \mathrm{d}t'' (e^{A(t-t')})_{ik}\delta F_k(t')(e^{A(t-t'')})_{jl}\delta F_l(t'') \right\rangle \\ &= \int_0^t \mathrm{d}t' \int_0^t \mathrm{d}t'' (e^{A(t-t')})_{ik}(e^{A(t-t'')})_{jl}\left\langle \delta F_k(t')\delta F_l(t'') \right\rangle \\ &= \int_0^t \mathrm{d}t' \int_0^t \mathrm{d}t'' (e^{A(t-t')})_{ik}(e^{A(t-t'')})_{jl}2B_{kl}\delta(t'-t'') \\ &= \int_0^t \mathrm{d}t' (e^{A(t-t')})_{ik}(e^{A(t-t')})_{jl}2B_{kl} \\ &= \left(\int_0^t \mathrm{d}t' e^{A(t-t')}2Be^{A^T(t-t')} \right)_{ij},\end{aligned} \tag{A.6}$$

where in the second to last step the Dirac delta of the noise covariance Eq. (A.4) was evaluated[1] and the Einstein summing convention is used throughout. It's now advantageous to express the matrix exponential in the eigenbasis of A, where it is diagonal. Let Q be the matrix which diagonalizes A to

$$\Lambda = Q^{-1}AQ = \mathrm{diag}(\lambda_i), \tag{A.7}$$

where λ_i are the eigenvalues of A corresponding to the eigenvectors in Q. This simplifies the matrix exponential to

$$e^{At} = Qe^{\Lambda t}Q^{-1} = Q\,\mathrm{diag}(e^{\lambda_i t})Q^{-1}. \tag{A.8}$$

[1] Typically, the evaluation would require an integral over the whole real axis. As the surface of integration always contains the line $t' = t''$, where the covariance of the noise is non-zero this is not a problem.

This allows to further evaluate Eq. (A.6) to

$$\begin{aligned}\Sigma_{ij}(t) &= \left(\int_0^t \mathrm{d}t' Q e^{\Lambda(t-t')} Q^{-1} 2B (Q^{-1})^T e^{\Lambda(t-t')} Q^T\right)_{ij} \\ &= Q_{ik}\left(\int_0^t \mathrm{d}t' e^{\Lambda(t-t')} 2B' e^{\Lambda(t-t')}\right)_{kl} Q^T_{lj} = Q_{ik}\Sigma'_{kl}Q^T_{lj}.\end{aligned} \tag{A.9}$$

For the transformed Σ'_{kl} the integral may be evaluated to give

$$\Sigma'_{kl}(t) = \int_0^t \mathrm{d}t' e^{(\Lambda_{km}+\Lambda_{nl})(t-t')} 2B'_{mn} = \begin{cases} 2B'_{kl}t, & \text{if } \lambda_k + \lambda_l = 0, \\ 2\frac{B'_{kl}}{\lambda_k+\lambda_l}\left(e^{(\lambda_k+\lambda_l)t} - 1\right), & \text{otherwise,}\end{cases} \tag{A.10}$$

For a wide range of problems, including the damped axial motion, all modes are coupled to the dissipative component and their eigenvalues thus have negative real part. Then the exponential goes to zero in the above equation and also in the equation for the mean value M. Therefore,

$$\Sigma'^{\infty}_{kl} = \Sigma'_{kl}(t \to \infty) = -2\frac{B'_{kl}}{\lambda_k + \lambda_l}, \tag{A.11}$$

and the backtransformed value

$$\Sigma^{\infty}_{kl} = \left\langle x_k(t \to \infty) x_l(t \to \infty)\right\rangle = (Q\Sigma'^{\infty}Q^T)_{kl} \tag{A.12}$$

in the original phase space coordinates converges to a value independent of the initial phase space point. This signifies a reached thermal equilibrium of the phase space. Furthermore, the diagonal entries of this equilibrium phase space covariance matrix are equal to the square of the thermal amplitudes or equivalently proportional to the thermal energy of the modes. The problem of calculating the mean drift of the phase space vector and the covariance matrix $\Sigma(t)$ is now translated to a problem of linear algebra. Only the eigendecomposition of the matrix A expressed through Q and Λ is needed, then all other quantities may be calculated via simple sums and matrix multiplications.

While this derivation is somewhat straight forward to follow and does not need a very big background knowledge, there is a significantly easier to use result for $\Sigma(t)$ given in ref. [201]:

$$\begin{aligned}\mathrm{vec}(\Sigma(t)) &= 2\left(\int_0^t e^{(A\otimes\mathbb{1}_N + \mathbb{1}_N\otimes A)(t-t')}\right)\mathrm{vec}(B) \\ &= 2(A\otimes\mathbb{1}_N + \mathbb{1}_N\otimes A)^{-1}\left(e^{(A\otimes\mathbb{1}_N+\mathbb{1}_N\otimes A)t} - \mathbb{1}_{2N}\right)\mathrm{vec}(B),\end{aligned} \tag{A.13}$$

where $\otimes$ is the Kronecker Product, $\mathbb{1}_k$ is the unity matrix of dimension $k\times k$, $N\times N$ is the dimension of the square matrix A and $\mathrm{vec}(\cdots)$ is called the stack operator and transforms the matrix to a column vector by stacking its columns. The last step is only possible if the matrix in the exponential is invertable. For the case of Σ^{∞} the exponential again goes to zero and what is left is

$$\mathrm{vec}(\Sigma^{\infty}) = -2(A\otimes\mathbb{1}_N + \mathbb{1}_N\otimes A)^{-1}\mathrm{vec}(B). \tag{A.14}$$

A.2. Solution of the Fokker-Planck equation

The Fokker-Planck equation is a differential equation for the probability density function $p(\vec{x}, t)$ of the state-space vector $\vec{x}$. Having solved the Langevin equation of the Ornstein-Uhlenbeck for the mean $\vec{M}(t)$ and covariance matrix $\Sigma(t)$ enables directly to write down the solution of the Fokker-Planck equation [202]

$$p(\vec{x}, t) = \frac{1}{\sqrt{|2\pi\Sigma(t)|}} \exp\left(-\frac{1}{2}(\vec{x} - \vec{M}(t))^T \Sigma^{-1}(t)(\vec{x} - \vec{M}(t))\right), \tag{A.15}$$

where $|2\pi\Sigma(t)|$ is the determinant of the matrix $2\pi\Sigma(t)$. The state-space vector $\vec{x}$ is distributed according to a multivariate normal distribution with mean $\vec{M}(t)$ and covariance $\Sigma(t)$. This distribution has a maximum for values $\vec{x} = \vec{M}(t)$ that follow the deterministic trajectory without noise.

For the steady-state or thermal distribution the mean $\vec{M}(t)$ goes to zero and the covariance will be replaced by Σ^{∞}.

$$p(\vec{x}) = \frac{1}{\sqrt{|2\pi\Sigma^{\infty}|}} \exp\left(-\frac{1}{2}\vec{x}^T (\Sigma^{\infty})^{-1}\vec{x}\right). \tag{A.16}$$

This is the probability to observe a point $\vec{x}$ at time t at equilibrium without having prior knowledge about the previous phase space history.

The probability Eq. (A.15) is implicitly the probability to observe $\vec{x}$ given the initial point $\vec{x}_0$ at time $t = 0$, as given in $\vec{M}(t)$. The transition probability density to observe the point $(\vec{x}, t)$ after having observed $(\vec{x}', t')$ is thus

$$p(\vec{x}, t \mid \vec{x}', t') = \frac{1}{\sqrt{|2\pi\Sigma(t - t')|}} \exp\left(-\frac{1}{2}(\vec{x} - e^{A(t-t')}\vec{x}')^T \Sigma^{-1}(t - t')(\vec{x} - e^{A(t-t')}\vec{x}')\right). \tag{A.17}$$

Even at thermal equilibrium, observing two points consecutively is most likely if the second point lies on the deterministic path given by $e^{A(t-t')}$. This can be expressed also as the probability distribution around the mean path taken with timesteps τ. The probability to transition from $\vec{x}_t$ to $\vec{x}_{t+\tau} = e^{A\tau}\vec{x}_t + \delta\vec{x}$ is

$$p(\delta\vec{x}, \tau) = \frac{1}{\sqrt{|2\pi\Sigma(\tau)|}} \exp\left(-\frac{1}{2}\delta\vec{x}^T \Sigma^{-1}(\tau)\delta\vec{x}\right), \tag{A.18}$$

which depends only on the step size τ [201]. The probability $p(\delta\vec{x}, \tau)$ is the probability density of the multivariate normal distribution $N(0, \Sigma(\tau))$ with zero mean and covariance $\Sigma(\tau)$.

A.2.1. Generation of time domain data

Particular solutions of the trajectory $\vec{x}(t)$ of Eq. (A.1) can be sampled similar to probability distribution, the difference being that successively sampled points are correlated to the previous point. Given an initial point $\vec{x}_n$ the next point after a timestep τ can be taken as

$$\vec{x}_{n+1} = e^{A\tau}\vec{x}_n + \delta\vec{x}, \quad \delta\vec{x} \sim N(0, \Sigma(\tau)) \tag{A.19}$$

where $\delta\vec{x} \sim N(0, \Sigma(\tau))$ means that $\delta\vec{x}$ is sampled from the multivariate normal distribution with density given in Eq. (A.18).

This kind of sampling is very easy to implement, as it requires only to calculate the matrix exponential $e^{A\tau}$ and covariance matrix $\Sigma(\tau)$. Sampling of the multivariate distribution $N(0, \Sigma(\tau))$ is also straightforward and can be translated to sampling from one dimensional normal distributions [203].

A.3. Power spectral density

In practice, the power spectral density may reveal more readily observable information as the directly detected noise signal in the time domain. This is especially true for detected thermal noise, as is the case for the dip detection employed in Penning trap experiments. The power spectral density matrix of the solution Eq. (A.2) is defined as

$$\Sigma_{i,j}(\omega)_T = \left\langle x_i^*(\omega) x_j(\omega) \right\rangle_T = \frac{1}{T} \Big\langle \int_0^T \mathrm{d}t_1 e^{i\omega t_1} x_i(t_1) \int_0^T \mathrm{d}t_2 e^{-i\omega t_2} x_j(t_2) \Big\rangle, \tag{A.20}$$

compare ref. [204] Section 1.4.2. On the diagonal, $i = j$, this formula is the continuous time version, $f_s \to \infty$, of the average computed Welch periodogram without overlapping and Fourier window of $T_{\mathrm{FFT}} = T$ seconds, compare Section 5.1. The detection time T is typically taken to infinity for the theoretical derivation, but practically it is off course finite. The finiteness of the experimental detection signal leads to what is called spectral leakage which may lead to undesired consequences. For the evaluation, the stationary case is assumed, such that the deterministic term in Eq. (A.2) can be dropped. Similar to the derivation in Eq. (A.10), the averaging is pulled into the integral to simplify them via the Dirac delta. With a similar definition of the primed values in the eigenbasis of A, the autocovariance

$$\Sigma'_{k,l}(t_1, t_2) = 2\frac{B'_{k,l}}{\lambda_k + \lambda_l} \left[e^{\lambda_k t_1 + \lambda_l t_2} - e^{\lambda_l |t_2 - t_1|} \right] \tag{A.21}$$

can be used to calculate[2]

$$\Sigma'_{k,l}(\omega)_T = \int_0^T \mathrm{d}t_1 e^{i\omega t_1} \int_0^T \mathrm{d}t_2 e^{-i\omega t_2} \Sigma'(t_1, t_2). \tag{A.22}$$

Evaluating this intermediate result involves only integration of exponentials but turns out rather lengthy to yield

$$\begin{aligned} \Sigma'_{k,l}(\omega)_T = \frac{1}{T} \frac{2B'_{k,l}}{\lambda_k + \lambda_l} \Bigg[& \frac{1}{\lambda_k + i\omega} \frac{1}{\lambda_l - i\omega} \left(e^{(\lambda_k + i\omega)T} - 1 \right) \left(e^{(\lambda_l - i\omega)T} - 1 \right) \\ & + \frac{1}{(\lambda_l - i\omega)^2} \left(e^{(\lambda_l - i\omega)T} - 1 \right) - \frac{T}{\lambda_l - i\omega} \\ & + \frac{1}{(\lambda_l + i\omega)^2} \left(e^{(\lambda_l + i\omega)T} - 1 \right) - \frac{T}{\lambda_l + i\omega} \Bigg]. \end{aligned} \tag{A.23}$$

[2] This result can also be found in ref. [204] Eq.(4.4.47). The result of the autocovariance reduces to the covariance Eq. (A.10) for $t_1 = t_2 = t$.

The power spectral density matrix in the unprimed basis is (the subscript T is the time and the superscript is for transposing)

$$\Sigma(\omega)_T = Q\Sigma'(\omega)_T Q^T. \tag{A.24}$$

For the limiting case, a simpler result can be derived, see ref. [204] Eq. (4.4.58)

$$\Sigma(\omega)_\infty = \frac{1}{2\pi}(A - i\omega\mathbb{1}_N)^{-1}B(A^T + i\omega\mathbb{1}_N)^{-1}. \tag{A.25}$$

Later, the calculations of this section will be used for the axial frequency detection to calculate the dip lineshape directly from the matrices A and B. Similarly, they can be applied also to interacting systems, such as the coupling trap, Eq. (8.8) and other sympathetic cooling schemes, to calculate the theoretical detection lineshapes in the frequency domain.

A.4. Thermal amplitudes

The thermal amplitudes can by calculated via the equilibrium value of the covariance matrix $\Sigma^\infty = \left\langle \vec{x}(\infty)^T \vec{x}(\infty) \right\rangle$ derived above.

A.4.1. Resonator

As a first example, this framework is applied to the thermally driven resonator. The eom, in analogy to Eq. (2.47), may be written as

$$\frac{\mathrm{d}}{\mathrm{d}t}\begin{pmatrix}\zeta\\ \tilde{\zeta}\end{pmatrix} = \underbrace{\begin{pmatrix}0 & \omega_R\\ -\omega_R & -\Gamma_R\end{pmatrix}}_{A}\underbrace{\begin{pmatrix}\zeta\\ \tilde{\zeta}\end{pmatrix}}_{\vec{\zeta}} + \underbrace{\begin{pmatrix}0\\ \Gamma_R\tilde{\zeta}_{th}(t)\end{pmatrix}}_{\delta\vec{F}(t)}. \tag{A.26}$$

The matrix B, defined through Eq. (A.4), has only a single component at $B_{22} = b$. In this example, the longer path of utilizing the eigendecomposition of A is still feasible. The eigenvalues and diagonalization matrix are

$$\lambda_{1,2} = -\frac{\Gamma_R}{2} \pm i\omega_R^{'}, \quad Q = \begin{pmatrix}\lambda_2/\omega_R & \lambda_1/\omega_R\\ 1 & 1\end{pmatrix}, \quad Q^{-1} = i\frac{\omega_R}{2\omega_R^{'}}\begin{pmatrix}1 & -\lambda_1/\omega_R\\ -1 & \lambda_2/\omega_R\end{pmatrix} \tag{A.27}$$

where $\omega_R^{'} = \sqrt{\omega_R^2 - \Gamma_R^2/4}$. Calculating

$$B^{'} = Q^{-1}B(Q^{-1})^T = -\frac{b}{4\omega_R^{'2}}\begin{pmatrix}\lambda_1^2 & -\omega_R^2\\ -\omega_R^2 & \lambda_2^2\end{pmatrix}, \tag{A.28}$$

gives

$$\Sigma^{'\infty} = \frac{b}{2\omega_R^{'2}}\begin{pmatrix}2\lambda_1 & -\omega_R^2/\Gamma_R\\ -\omega_R^2/\Gamma_R & 2\lambda_2\end{pmatrix} \tag{A.29}$$

which finally yields the simple result

$$\Sigma^{\infty} = \left\langle \vec{\zeta}^{T}(\infty)\vec{\zeta}(\infty)\right\rangle = Q\Sigma^{'\infty}Q^{T} = \frac{b}{\Gamma_R}\begin{pmatrix}1 & 0\\ 0 & 1\end{pmatrix} \equiv \frac{1}{2}\rho^2_{\zeta,th}\begin{pmatrix}1 & 0\\ 0 & 1\end{pmatrix}, \tag{A.30}$$

where $\rho_{\zeta,th}$ is the thermal amplitude of the resonator phase space coordinates. The off-diagonal entries being zero is a interpreted as fully uncorrelated position and velocity at thermal equilibrium.

The value of $b = \frac{1}{2}\rho^2_{\zeta,th}\Gamma_R$ can be reproduced via the definition of $\tilde{\zeta}_{th} = \frac{d_{\text{eff}}}{e\omega_R}I_{th}$. The autocorrelation function of the thermal Johnson-Nyquist noise I_{th} is related to the one-sided power spectral density $i^2_{th} = 4k_BT_z/R$ via the Wiener–Khinchin theorem to yield [71, 205, 206]

$$\left\langle I_{th}(t)I_{th}(t')\right\rangle = 2\frac{k_BT_z}{R}\delta(t-t'). \tag{A.31}$$

Therefore

$$\rho^2_{\zeta,th} = 2\frac{b}{\Gamma_R} = 2\frac{k_BT_z}{R}\frac{d^2_{\text{eff}}\Gamma_R}{e^2\omega_R^2} = 2\frac{k_BT_z}{e^2\frac{R^2}{L}}d^2_{\text{eff}} = \frac{q^2}{e^2}\frac{\Gamma_R}{\gamma_z}\frac{\omega_z^2}{\omega_R^2}\rho^2_{z,th}, \tag{A.32}$$

where the definition of the thermal radius Eq. (2.48) was used to express $\rho^2_{\zeta,th}$ via measurable quantities only.

A.4.2. Axial motion

The axial motion coupled to the resonator is given by Eq. (2.47) and is quoted here

$$\frac{\mathrm{d}}{\mathrm{d}t}\begin{pmatrix}z\\ \tilde{z}\\ \zeta\\ \tilde{\zeta}\end{pmatrix} = \underbrace{\begin{pmatrix}0 & \omega_z & 0 & 0\\ -\omega_z & 0 & 0 & \frac{e\omega_R}{q\omega_z}\gamma_z\\ 0 & 0 & 0 & \omega_R\\ 0 & -\frac{q\omega_z}{e\omega_R}\Gamma_R & -\omega_R & -\Gamma_R\end{pmatrix}}_{A}\underbrace{\begin{pmatrix}z\\ \tilde{z}\\ \zeta\\ \tilde{\zeta}\end{pmatrix}}_{\vec{x}} + \underbrace{\begin{pmatrix}0\\ 0\\ 0\\ \Gamma_R\tilde{\zeta}_{th}(t)\end{pmatrix}}_{\delta\vec{F}(t)}. \tag{A.33}$$

The single entry of the matrix $B_{44} = b = \frac{1}{2}\rho^2_{\zeta,th}\Gamma_R$ was derived in the previous example. Here, using the eigendecomposition of A to arrive at a symbolic result is not feasible. Solving Eq. (A.14) via symbolic calculations performed with Mathematica [73] gives the diagonal matrix

$$\Sigma^{\infty} = \begin{pmatrix}\frac{1}{2}\rho^2_{z,th} & 0 & 0 & 0\\ 0 & \frac{1}{2}\rho^2_{z,th} & 0 & 0\\ 0 & 0 & \frac{1}{2}\rho^2_{\zeta,th} & 0\\ 0 & 0 & 0 & \frac{1}{2}\rho^2_{\zeta,th}\end{pmatrix}. \tag{A.34}$$

To arrive at this result, the various definitions $\omega_R^2 = 1/(LC)$, $\Gamma_R = 1/(RC)$, $\gamma_z = \frac{q^2R}{d^2_{\text{eff}}m}$ and the definition of the thermal radius $\frac{1}{2}m\omega_z^2\rho^2_{z,th} = k_BT_z$ where used. This is in fact a derivation of the thermal radius of the axial motion.

Because Σ^∞ is diagonal, the steady state probability density Eq. (A.16) factorizes for the four components of the state-space vector. Because the z and $\tilde{z}$-coordinate are normally distributed, the amplitude ρ_z is Maxwell distributed

$$p(\rho_z) = \frac{\rho_z}{\frac{1}{2}\rho_{z,th}^2} \exp\left(-\frac{\rho_z^2}{\rho_{z,th}^2}\right), \tag{A.35}$$

and the phase φ_z is uniform distributed [207]

$$p(\varphi_z) = \frac{1}{2\pi}. \tag{A.36}$$

A.4.3. Cyclotron mode via quadrupolar coupling

To investigate the thermal amplitudes via the lower sideband quadrupole coupling of the cyclotron mode Eq. (2.63) a few simplification will be made. The resonator coordinates will be omitted and rather the axial mode will be treated as directly coupled to the heat bath. As the coupling in the eom is given in terms of amplitudes, a damping Γ_Z and random force on both Z and $\tilde{Z}$ has to be introduced. For $\Phi = \pi/2$ the eom with noise is

$$\frac{\mathrm{d}}{\mathrm{d}t}\begin{pmatrix} Z \\ \tilde{Z} \\ X^+ \\ Y^+ \end{pmatrix} = \underbrace{\frac{1}{4}\begin{pmatrix} -\Gamma_Z & 0 & -\frac{|C|}{\omega_z} & 0 \\ 0 & -\Gamma_Z & 0 & -\frac{|C|}{\omega_z} \\ \frac{|C|}{\omega_+} & 0 & 0 & 0 \\ 0 & \frac{|C|}{\omega_+} & 0 & 0 \end{pmatrix}}_{A} \underbrace{\begin{pmatrix} Z \\ \tilde{Z} \\ X^+ \\ Y^+ \end{pmatrix}}_{\vec{x}} + \begin{pmatrix} \delta F_Z(t) \\ \delta F_{\tilde{Z}}(t) \\ 0 \\ 0 \end{pmatrix}. \tag{A.37}$$

The matrix B for the uncorrelated noise terms $\delta F_Z(t)$ and $\delta F_{\tilde{Z}}(t)$ has entries $B_{11} = B_{22} = b$ and the rest is zero. Using Eq. (A.14) gives

$$\Sigma^\infty = \frac{4b}{\Gamma_Z}\begin{pmatrix} 1 & 0 & 0 & 0 \\ 0 & 1 & 0 & 0 \\ 0 & 0 & \frac{\omega_z}{\omega_p} & 0 \\ 0 & 0 & 0 & \frac{\omega_z}{\omega_p} \end{pmatrix}. \tag{A.38}$$

The prefactor can now be identified with the thermal axial radius squared $\frac{4b}{\Gamma_Z} = \frac{1}{2}\rho_{z,th}^2$. This result is a derivation of the ratio between the axial and cyclotron squared radii quoted in Eq. (2.66).

Here Σ^∞ is diagonal, so the distributions of the axial and cyclotron thermal distributions factorize. After a sufficient coupling time $T_{\text{couple}} > 1/\gamma_z$, the radius ρ_+ is thus also Maxwell distributed

$$p(\rho_+) = \frac{\rho_+}{\frac{1}{2}\rho_{+,th}^2} \exp\left(-\frac{\rho_+^2}{\rho_{+,th}^2}\right), \tag{A.39}$$

and the phase φ_+ uniformly distributed

$$p(\varphi_+) = \frac{1}{2\pi}. \tag{A.40}$$

A.5. Sampling of the detection signal

As explained in Section A.2.1, time domain data can be generated straight forward. There are several advantages compared to generating time domain data by differential equation solvers. For one, the solution of the deterministic path through the exponential $e^{A\tau}$ is valid for any τ, while for a differential equation the update rule must have step sizes typically much smaller than the fastest oscillation frequency. Secondly, in differential equation solvers divergences can occur after long integration time. These divergences may occur here as well, but can be identified much more easily, as they would occur in the eigenvalues of A.

Due to the first reason, using this method, time domain data can be sampled with arbitrary time steps, while still reflecting all the necessary physics.

A.5.1. Sampling downmixed time signal and generating spectra

As an example, time signal data can be generated directly at the sampling frequency of the detection system. This time domain data can then be downmixed by multiplication with a sinusoidal signal at frequency ω_{DM} reflecting the downmixer used in the experiment. Taking the matrix and noise terms from Eq. (A.33) and the update rule from Eq. (A.19), the detection signal y_n is generated via

$$y_n = \kappa(\zeta_n + c_n)\cos(\omega_{\mathrm{DM}} n\tau), \quad c_n \sim N(0, \Sigma_c), \tag{A.41}$$

where $\tau = 1/f_s$ is the reciprocal of the sampling rate f_s, κ accounts for amplification and unit conversion of the signal and c_n is an additional white noise. This white noise term experimentally stems from the input noise of the cryogenic amplifier, compare ref. [76]. The initial point $\vec{x}_0$ can be sampled from the thermal distribution $N(0, \Sigma^\infty)$ for a full thermal spectrum, or from any initial non-thermal point, e.g. a point with axial coordinates after a PnA/PnP cycle.

The generated data can then be transformed into a spectrum via the same method as the experimentally recorded spectrum, i.e. Welch's method. Figure A.1 shows an experimentally taken spectrum using $^9\mathrm{Be}^{3+}$ at $\nu_z \approx 484$ kHz with the parameters of the detection system $f_s = 102400$ Hz, $T_{\mathrm{FFT}} = 6$ s, an averaging time of 60 s, downmix frequency $\omega_{\mathrm{DM}} = 2\pi \cdot 460$ kHz and a generated spectrum with the same parameters. For the generated spectrum, the resonator and ion parameters for the matrix A are taken from a fit of the theoretical lineshape, Eq. (2.51). The value of the amplification κ and white noise variance Σ_c are adjusted to match the observed amplitude and noise background. The generated spectrum is virtually indistinguishable from the real experimental data. This shows that the detection signal is well understood and that our experimental detection signal has no additional unexplained components. Additionally, generating the 60 s of time signal takes only a couple of seconds with this method (implemented in Julia), which is orders of magnitude faster than generating the data using differential equations solvers.

A.5.2. Sampling cycles of the phase-sensitive detection

Cycles of the phase-sensitive detection techniques can be simulated by sampling of the thermal phase space, the application of Eq. (2.78), and subsequent generation of the detection signal using Eq. (A.41). The required steps are outlined in more detail below:

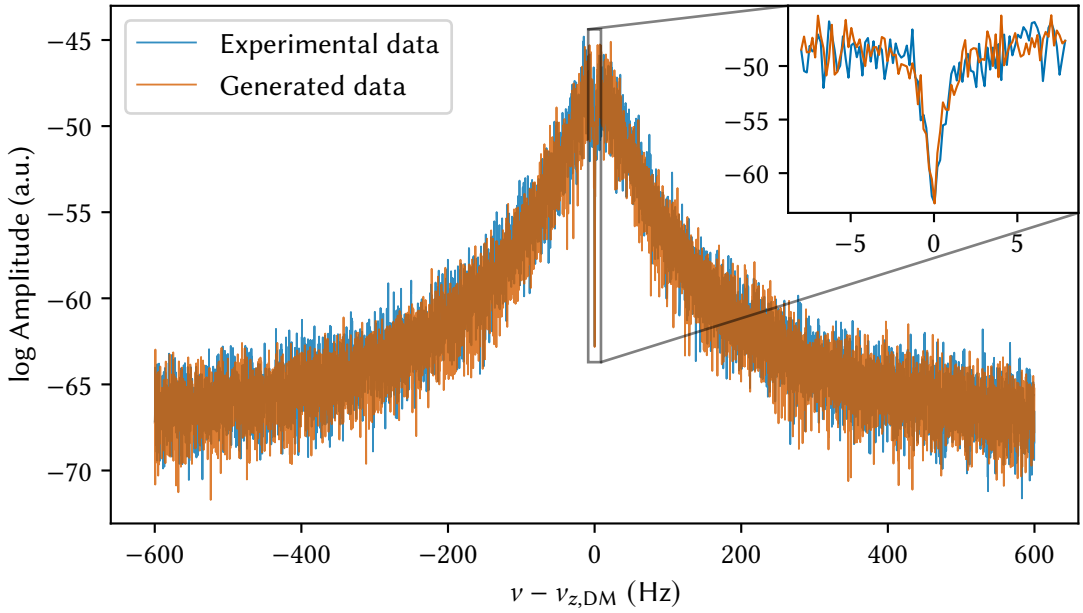

Figure A.1: Generated dip signal compared to real experimental data. The x-axis shows the frequency relative to the downmixed axial frequency. For details see text.

1. Following cyclotron cooling, the modified cyclotron motion is normally distributed with the thermal amplitude $\rho_{+,\mathrm{th}}$. Thus, initially, N two-dimensional samples

   $$(x_+, y_+)_i \sim \mathrm{Normal}(0, \mathrm{diag}(\rho_{+,\mathrm{th}}, \rho_{+,\mathrm{th}}))$$

   are drawn.

2. The dipole excitation displaces the coordinates in phase space by

   $$(x_+, y_+)_i \to (x_+ + B_+, y_+)_i,$$

   assuming a specific phase of the excitation.

3. During the free evolution, the modified cyclotron motion evolves according to the matrix E_+, Eq. (2.14),

   $$(x_+, y_+)_i \to E_{+,i}(x_+, y_+)_i.$$

   To include systematic shifts effects to the finite amplitude, $E_{+,i}$ must be calculated with the shifted cyclotron frequency $\omega_+(\rho^2_{+,i})$, where $\rho^2_{+,i} = (x_{+,i} + B_+)^2 + y^2_{+,i}$.

4. For the coupling into the thermal axial motion, first N samples

   $$(z, \tilde{z})_i \sim \mathrm{Normal}(0, \mathrm{diag}(z_{\mathrm{th}}, z_{\mathrm{th}}))$$

   are drawn. Then the coupling is performed by

   $$(z, \tilde{z}, x_+, y_+) \to C_{\mathrm{PnP/PnA}}(z, \tilde{z}, x_+, y_+),$$

compare Eq. (2.73) and Eq. (2.74). At this point, the standard deviation of the phases

$$\varphi_i = \arctan(z_i, \tilde{z}_i)$$

can be calculated. However, this neglects the readout jitter of the detection.

5. To simulate the detection signal, the thermal resonator coordinate samples

$$(\zeta, \tilde{\zeta})_i \sim \text{Normal}(0, \text{diag}(\zeta_{\text{th}}, \zeta_{\text{th}}))$$

are drawn. Using $\vec{x}_{0,i} = (z, \tilde{z}, \zeta, \tilde{\zeta})_i$ as a starting point, the detection signal for each sample i is generated via the update rule Eq. (A.19) and converted to the detected down-mixed signal with Eq. (A.41). Here, the detected phases are calculated from the FFT of the signal.

The last step is rather computationally expensive, as it requires generating the full several thousand samples long detection signal for each sample of $(z, \tilde{z}, \zeta, \tilde{\zeta})_i$. However, compared to generating the detection signal by use of numerical differential equation integrators, the computation time is vastly reduced.

A.6. Asymmetric transition lineshape

In Section 3.3, several additions to the simple Rabi flopping transition probability were discussed. The most troublesome, is the potential asymmetric lineshape due to B_2 derived by Brown, ref. [62], as it shifts the effective center of the resonance, see Figure 3.5. The derivation relies on the assumption Eq. (3.29). For the electron-spin resonance fits with this lineshape, the assumptions can be verified, see Section 7.4.5. The weakest condition is given by $\gamma_z/2\pi = 2.52$ Hz compared to the fit Rabi frequency which is up to $\Omega/2\pi \approx 0.5$ Hz and it is not clear, to which level the above assumptions need to be fulfilled and if this would lead to changes of the probability lineshape.

Here, an attempt is made to numerically integrate the transition probability directly from the Bloch equations and the ion's thermal motion. To this end, the Bloch equations, Eq. (3.22), without explicit decoherence,

$$\frac{\mathrm{d}}{\mathrm{d}t}\begin{pmatrix} M_x \\ M_y \\ M_z \end{pmatrix} = \begin{pmatrix} 0 & \Delta - 2\frac{\Delta\omega}{\rho_{z,th}^2}z^2 & 0 \\ -\Delta + 2\frac{\Delta\omega}{\rho_{z,th}^2}z^2 & 0 & \Omega \\ 0 & -\Omega & 0 \end{pmatrix}\begin{pmatrix} M_x \\ M_y \\ M_z \end{pmatrix}, \tag{A.42}$$

is used. The change of the transition frequency due to B_2 and the thermal motion is included by the additional term $2\Delta\omega z^2/\rho_{z,th}^2$. The dynamics of the Bloch equations, e.g. the rotation of the spin vector in the rotating frame, for small detunings and Rabi frequencies, is much slower than the axial oscillation z. The full integration of this formula for a single detuning would require time stepping slower than a period of the axial oscillation $T_{\nu_z} \approx 2$ µs and up to the typical excitation times of tens of seconds, making this very computationally expensive. However, as the axial motion is independent of the spin motion, it can be integrated simply by the update rule from above Eq. (A.19) for arbitrary time steps. Assuming that the fast oscillation

of z with v_z do not influence the Bloch vector, and rather the thermal correlations of z at the much slower timescales of γ_z are relevant, the Bloch equations can be integrated with much slower time stepping[3].

The integration of the Bloch equation is performed with a 7th-order Runge-Kutta method using the DifferentialEquations.jl Julia package [208]. Figure A.2 shows the lineshape Eq. (3.27) and the simulated transition probability for the $^9Be^{3+}$ parameters in this experiment ($\delta\omega/2\pi$ = 18 Hz, other parameters from Table 5.2). The simulation of the transition probability replicates

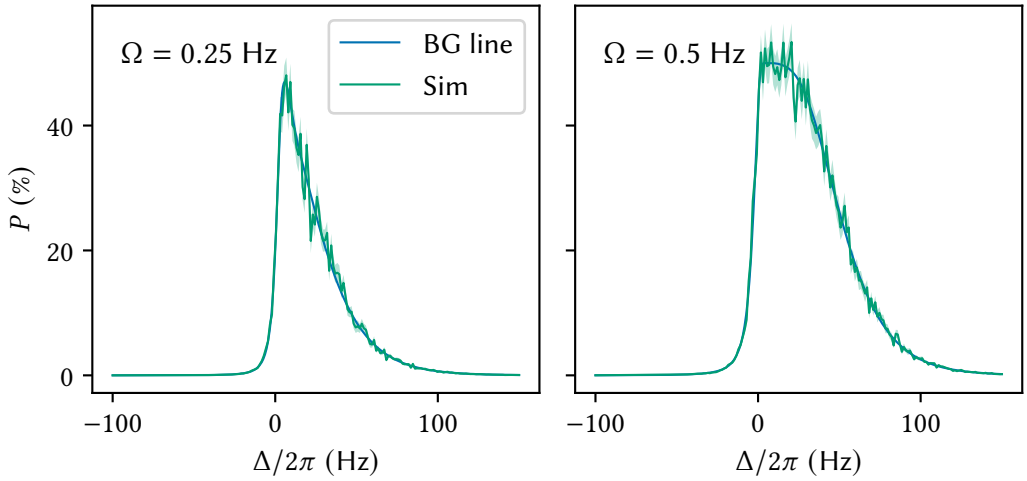

Figure A.2: Simulation of the asymmetric lineshape. The simulated lineshape fits the Brown-Gabrielse solution Eq. (3.27) very well. The small error bar is due to the finite number of simulation samples at each detuning.

the Brown-Gabrielse lineshape perfectly, solidifying its use for the measurements performed here.

The case of a reduced linewidth parameter $\delta\omega/2\pi = 1$ and increased Rabi frequency $\Omega/2\pi$ = 15 is shown in Figure A.3[4]. These values do not align with the assumptions, Eq. (3.29) and indeed, the simulation and Brown-Gabrielse line do not fit in this case.

[3]The same assumption is made in ref. [62]

[4]The current linewidth parameter (via B_2) already limits the resonance width and thus the statistical precision. A reduction of B_2 is thus intended.

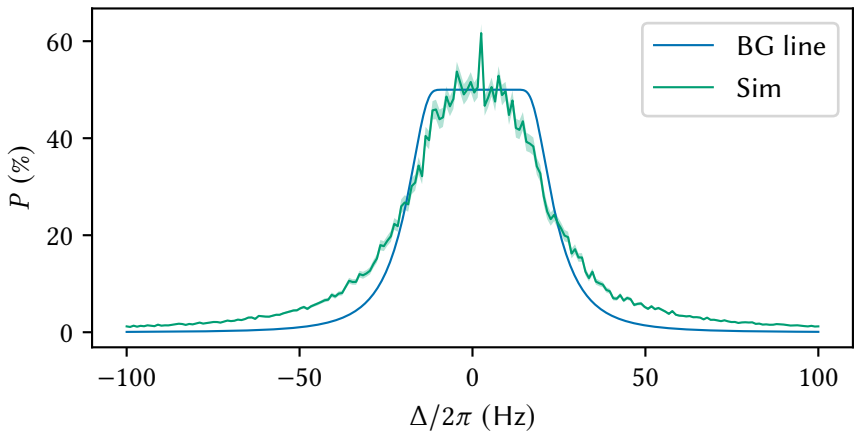

Figure A.3: Simulation of the asymmetric lineshape with a smaller linewidth parameter $\delta\omega/2\pi = 1$ Hz and larger Rabi frequency $\Omega/2\pi = 15$ Hz.

Appendix B.

Dip lineshape

Here, a discussion of the dip lineshape and the error estimates associated with it are given. The discussion here is data driven and uses dip and double-dip spectra from the nuclear-spin transition measurements.

B.1. Dip axial frequency determination

Generally, the dip fits are performed as described in Section 5.4. This involves the definitions of a transfer function, a resonator lineshape and a dip lineshape.

Following, three dip lineshape models will be introduced.

Simple model

In this model, the ideal resonator lineshape, Eq. (2.53), and dip lineshape, Eq. (2.51), are used:

$$f_{\mathrm{res}}(\omega \mid \omega_R, \Gamma_R) = \frac{1}{1 + \left(\frac{\omega_R^2 - \omega^2}{\omega \Gamma_R}\right)^2}, \quad f_{\mathrm{dip}}(\omega \mid \omega_z, \gamma_z) = \frac{1}{1 + \left(\frac{\omega_R^2 - \omega^2}{\omega \Gamma_R} - \frac{\omega \gamma_z}{\omega_z^2 - \omega^2}\right)^2}. \tag{B.1}$$

With FFT time

In Section A.3, the power spectral density given a fixed Fourier transform time windows was derived. With the result, Eq. (A.24), and the matrices A and B defined for the resonator, Section A.4.1, and the axial motion, Section A.4.2, respectively, the lineshapes

$$f_{\mathrm{res}}(\omega \mid \omega_R, \Gamma_R) = \Sigma(\omega \mid \omega_R, \Gamma_R)_{T,22}, \quad f_{\mathrm{dip}}(\omega \mid \omega_z, \gamma_z) = \Sigma(\omega \mid \omega_R, \Gamma_R)_{T,44} \tag{B.2}$$

can be computed[1].

[1] For both cases, the matrix B has only a single component. The resulting power spectral density will be proportional to this value, and it can thus be absorbed in a_1 by setting $B_{22} = 1$ and $B_{44} = 1$, for the thermal resonator and axial motion, respectively.

With Gaussian ν_z

Here, white noise fluctuations of the axial frequency ν_z are incorporated into the dip lineshape by weighting ν_z with a Gaussian:

$$f_{\mathrm{dip}}(\omega \mid \omega_z, \gamma_z, \sigma_{\omega_z}) = \frac{1}{\sqrt{2\pi\sigma_{\omega_z}^2}} \int \mathrm{d}\delta\omega_z \frac{e^{-\frac{1}{2}\delta\omega_z^2/\sigma_{\omega_z}^2}}{1 + \left(\frac{\omega_R^2-\omega^2}{\omega\Gamma_R} - \frac{\omega\gamma_z}{(\omega_z+\delta\omega_z)^2-\omega^2}\right)^2}. \tag{B.3}$$

This integration is done numerically by quadrature and the resonator lineshape defined in the simple model is used.

Depth of the dip

For this discussion, the transfer function is taken to be

$$f_{\mathrm{tf}}(y(\omega), \omega \mid a_0, a_1) = 10 \log_{10}(a_0 + a_1 y(\omega)), \tag{B.4}$$

i.e. without a first-order frequency dependence of the detection system (i.e. $a_2 = 0$ in Eq. (5.7)). The three models are fit to a sample spectrum with the fit procedure outlined in Section 5.4, compare Figure 5.5, and see Figure B.1 for the results.

In the simple model, the dip fit shorts the resonator all the way to its noise floor, which is expected, as the ideal dip function is zero at $\omega = \omega_z$. However, in the data this is obviously not the case. The calculation of the power spectral density takes into account spectral bleeding due to the finite FFT acquisition time, here $T = T_{\mathrm{FFT}} = 6$ s. This model fits the data much better, explaining the non-ideal shortening of the dip. Similarly, the integration over Gaussian noise of ν_z fits the data well. Though in the latter, the fitted $\sigma_{\omega_z} \approx 2\pi \cdot 160$ mHz seems rather large when compared to the shot-to-shot jitter of the axial frequency $\sigma(\omega_z) \approx 2\pi \cdot 30$ mHz.

A problem of using the simple model is that the data points close to ω_z will disproportionally contribute to the fit value of ω_z since they give rise to large variations in the chi-square sum, effectively increasing the fit uncertainty. Additionally, if the dip is not centered on the resonator, because the minimum will ‘pull‘ the fit. However, this leads only to significant shifts far off center, where the dip is highly asymmetric.

Slope of the transfer function

A linear frequency response (slope), $a_2 \neq 0$, of the detection system is now included in the transfer function. Directly, the slope leads to a shift of the fitted resonator frequency by $\sim$ 1.5 Hz. A comparison of the determined axial frequency of the models and the influence of the additional slope is shown in Figure B.2. While the models with FFT time and with Gaussian ν_z agree and shift in similarly by including the slope, this is not the case for the simple model. However, with the slope parameter all three models agree. In the evaluation of all statistical results, the model with Gaussian ν_z and a slope is used. This model is chosen over the one derived via the power spectral density because the latter can not be used for double dips, see the next section.

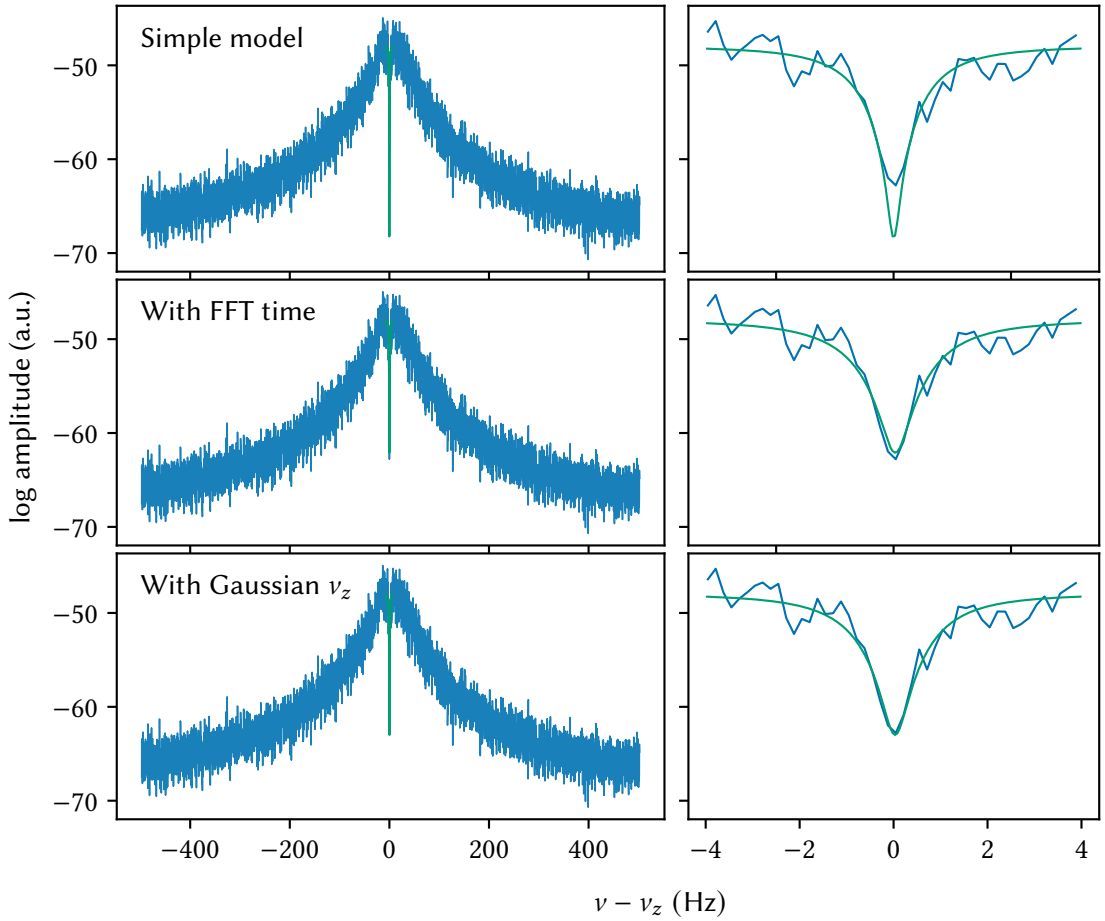

Figure B.1: Dip lineshape comparison. The data is plotted in blue and the fits in green. For details see text.

Axial frequency shifts due to resonator systematic

Here, the dip fits with the Gauss model are performed with a shifted input resonator frequency, see Figure B.3. Also shown is the expected shift when the problem is turned around, i.e. the resonator frequency is actually shifted, but the input value for the fit is fixed.

The determined dependency

$$\delta\nu_z/\delta\nu_R \approx -7.6\ \text{mHz/Hz} \tag{B.5}$$

agrees well with the previous plot, where a 1.5 Hz resonator shift due to the slope resulted in around 10 mHz shifts.

While the resonator is determined from the fits with a shot-to-shot stability of around 0.5 Hz, a systematic shift in the measurements might occur. As shown above, a neglected slope parameter can lead to such a shift. Concluding, the shift due to the slope parameter is taken as

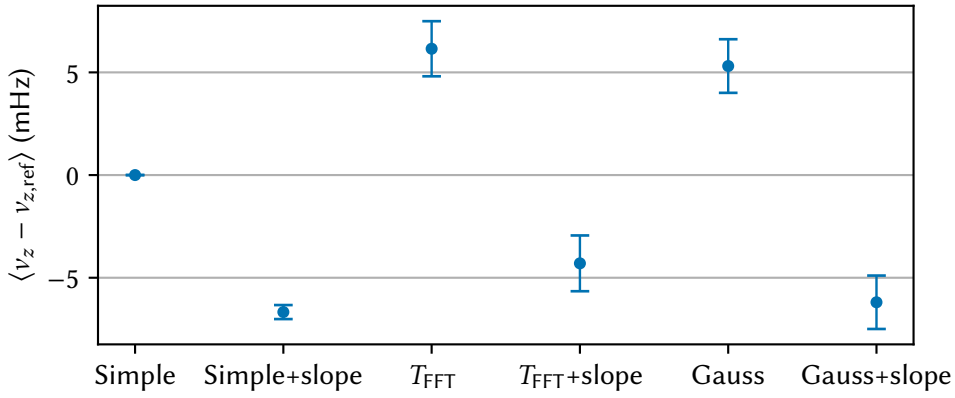

Figure B.2: Comparison of fitted axial frequencies of the three models, with and without a frequency slope of the detection system. A total of 140 axial dips are used for this comparison.

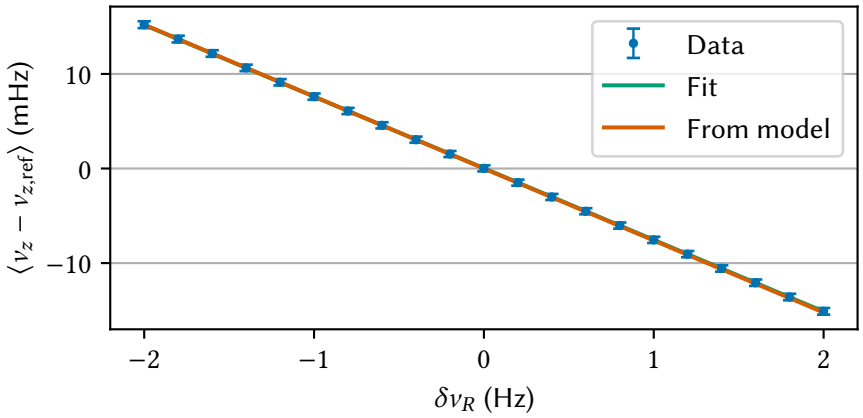

Figure B.3: The fitted axial frequency when the resonator frequency is shifted by $\delta\nu_R$. The green and orange curve overlap. For details see text.

an estimate for systematic uncertainties of the ν_R determination and a conservative value of twice this shift, $\delta\nu_R = 3.0$ Hz, corresponding to about 4% of the 3dB width $\Gamma_R/2\pi$, see Table 5.2, is chosen. This is comparable to uncertainties assigned at other experiments, see e.g. refs. [19, 77]. Using the above scaling, the final dip axial frequency uncertainty

$$\sigma(\nu_z)_{\text{dip}} = 23 \text{ mHz} \tag{B.6}$$

is calculated. This uncertainty could likely be reduced by more systematic studies.

B.2. Double-dip cyclotron frequency determination

In the calculation, Eq. (2.68), of the modified cyclotron frequency using the double-dip technique, the three detected dip frequencies $\omega_{z,1}$, $\omega_{z,2}$ and ω_z are required. Additional to the single

axial dip, ω_z, for which the above discussion applies, the two frequencies $\omega_{z,1}$ and $\omega_{z,2}$ are fit with a double-dip lineshape. The method to include spectral bleeding via the power spectral density calculation from Section A.3 can, however, not be applied to the double-dip[2], because the differential equation including the sinusoidal excitation is non-linear. As the shortcomings of the simple model also apply here, e.g. the finite dip depth increases the fit uncertainty, the model with Gaussian distributed ν_z and a slope in the transfer function is used for all double-dip fits. The double-dip lineshape is given by

$$f_{\mathrm{dip}}(\omega \mid \omega_{z,1}, \gamma_{z,1}, \omega_{z,2}, \gamma_{z,2}, \sigma_{\omega_z}) = \frac{1}{\sqrt{2\pi\sigma_{\omega_z}^2}} \int \mathrm{d}\delta\omega_z \frac{e^{-\frac{1}{2}\delta\omega_z^2/\sigma_{\omega_z}^2}}{1 + \left(\frac{\omega_R^2-\omega^2}{\omega\Gamma_R} - \frac{\omega\gamma_{z,1}}{\omega_{z,1}^2-\omega^2} - \frac{\omega\gamma_{z,2}}{\omega_{z,2}^2-\omega^2}\right)^2}. \tag{B.7}$$

Similar to before, from a dataset of 140 dips and double-dips, the dependence on the resonator is estimated by varying the resonator frequency in the fit of double-dips and axial dips to recalculate the modified cyclotron frequency, see Figure B.4. The determined dependency

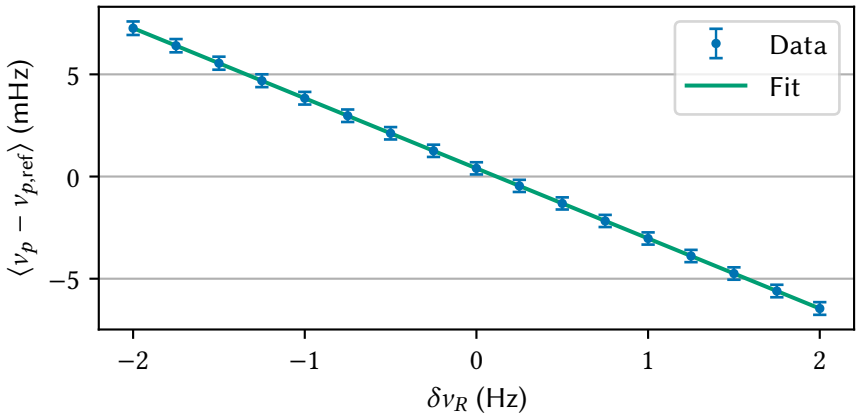

Figure B.4: During the fits of the axial and double-dip to determine the modified cyclotron frequency, the resonator frequency is shifted by $\delta\nu_R$. For details see text.

$$\delta\nu_+/\delta\nu_R \approx -3.4\ \mathrm{mHz/Hz} \tag{B.8}$$

is slightly smaller than the one for the axial dip only, owing to a partial cancellation of the shifts in Eq. (2.68). Using the same estimate as before, $\delta\nu_R < 3$ Hz, a systematic uncertainty on $\sigma(\nu_+)_{\mathrm{dip}} = 10$ mHz is calculated. The propagation to ν_c is one-to-one, as the axial frequency is suppressed greatly in the invariance theorem, thus,

$$\sigma(\nu_c)_{\mathrm{dip}} = 10\ \mathrm{mHz}. \tag{B.9}$$

[2] At least not trivially.

B.3. Double-dip lineshape derivation

The derivation of the lineshape of the double dip, Eq. (2.70), is based on a simple model of the two axial eigenmodes, which form during the quadrupolar sideband drive, interacting with the resonator as two independent particles would. At the time of writing this thesis, I could not find a direct derivation of the double dip lineshape starting from the quadrupolar drive and interaction with the resonator.

In the following, starting from the quadrupolar coupling, compare Eq. (2.60), and the coupling to the resonator, Eq. (2.47), the lineshape of the double dip is derived. The coupled eom of the axial z, resonator ξ and radial modified cyclotron r_+ coordindate are

$$\begin{aligned}
\frac{\mathrm{d}}{\mathrm{d}t}\tilde{z} &= -\omega_z z + C\cos(\omega_{\mathrm{RF}}t)\frac{r_+}{\omega_z} + \frac{e\omega_R}{q\omega_z}\gamma_z\tilde{\xi} \\
\frac{\mathrm{d}}{\mathrm{d}t}\tilde{r}_+ &= -\omega_+ r_+ + C\cos(\omega_{\mathrm{RF}}t)\frac{z}{\omega_+} \\
\frac{\mathrm{d}}{\mathrm{d}t}\tilde{\xi} &= -\frac{q\omega_z}{e\omega_R}\Gamma_R\tilde{z} - \omega_R\xi - \Gamma_R\tilde{\xi} + \Gamma_R\tilde{\xi}_{th},
\end{aligned} \tag{B.10}$$

where coupling C was taken as real. Similar to the derivation done for the single dip, Eq. (2.49), the Fourier transform of the eom is taken. Using that $\cos(at)f(t)$ transforms as $\frac{1}{2}(f(\omega+a) + f(\omega-a))$ and the definition of the conjugate variables, the FT of the eom are

$$\begin{aligned}
-\frac{\omega^2}{\omega_z}z(\omega) &= -\omega_z z(\omega) + \frac{C}{2\omega_z}\left[r_+(\omega-\omega_{\mathrm{RF}}) + r_+(\omega+\omega_{\mathrm{RF}})\right] + i\omega\frac{e\omega_R}{q\omega_z}\gamma_z\xi \\
-\frac{\omega^2}{\omega_z}r_+(\omega) &= -\omega_+ r_+(\omega) + \frac{C}{2\omega_+}\left[z(\omega-\omega_{\mathrm{RF}}) + z(\omega+\omega_{\mathrm{RF}})\right] \\
-\frac{\omega^2}{\omega_R}\xi(\omega) &= -i\frac{\omega}{\omega_z}\frac{q\omega_z}{e\omega_R}\Gamma_R z(\omega) - \omega_R\xi(\omega) - i\frac{\omega}{\omega_R}\Gamma_R\xi(\omega) + \Gamma_R\tilde{\xi}_{th}(\omega)
\end{aligned} \tag{B.11}$$

Solving the second row for r_+ and inserting into the first row gives terms

$$r_+(\omega\pm\omega_{\mathrm{RF}}) = \frac{C}{2(\omega_+^2 - (\omega\pm\omega_{\mathrm{RF}})^2)}\left[z(\omega) + z(\omega\pm 2\omega_{\mathrm{RF}})\right]. \tag{B.12}$$

Here, the assumption, that the eigenmodes are only slightly perturbed is made. From this follows that $z(\omega\pm 2\omega_{\mathrm{RF}}) \ll z(\omega)$ for frequencies ω not to far away from ω_z, i.e. the frequency components at the natural oscillation frequency are much larger than the far off-resonant second term. Neglecting the second term allows to solve for

$$z(\omega) = i\omega\frac{\omega_z}{\omega_R}\frac{e\omega_R}{q\omega_z}\gamma_z K(\omega)\xi(\omega), \tag{B.13}$$

where $K(\omega)$ is defined as

$$K(\omega) = \left(\omega_z^2 - \omega^2 - \frac{C^2}{4}\left[\frac{1}{\omega_+^2 - (\omega-\omega_{\mathrm{RF}})^2} + \frac{1}{\omega_+^2 - (\omega+\omega_{\mathrm{RF}})^2}\right]\right)^{-1}. \tag{B.14}$$

The detection signal $U(\omega) \propto \tilde{\xi}(\omega) = i\omega\xi(\omega)$, which can now be solved similar to the derivation of the single dip

$$U(\omega) = U_{th}(\omega)\frac{1}{1 + i\left(\frac{\omega^2-\omega_R^2}{\omega\Gamma_R} + \omega\gamma_z K(\omega)\right)}. \tag{B.15}$$

Taking the complex norm gives

$$|U(\omega)|^2 = |U_{th}(\omega)|^2\frac{1}{1 + \left(\frac{\omega_R^2-\omega^2}{\omega\Gamma_R} - \omega\gamma_z K(\omega)\right)^2}. \tag{B.16}$$

Quite obviously, for no coupling, $C = 0$, the single dip, Eq. (2.51), is reproduced.

In the case of the magnetron double dip, the derivation is identical and only the function $K(\omega)$ needs to be adjusted. Summarizing both cases and also inserting the Rabi frequency Ω, compare Eq. (2.65), $C = 4\Omega\sqrt{\omega_\pm\omega_z}$ gives

$$\begin{aligned} K_\pm(\omega) &= \left(\omega_z^2 - \omega^2 \mp 4\Omega\omega_\pm\omega_z\left[\frac{1}{\omega_\pm^2 - (\omega - \omega_{\mathrm{RF}})^2} + \frac{1}{\omega_\pm^2 - (\omega + \omega_{\mathrm{RF}})^2}\right]\right)^{-1} \\ &\approx \frac{1}{\omega_z^2 - \omega^2 \mp \frac{4\Omega\omega_\pm\omega_z}{\omega_\pm^2 - (\omega \pm \omega_{\mathrm{RF}})^2}}, \end{aligned} \tag{B.17}$$

where in the last line the formula is approximated around the axial frequency $\omega \approx \omega_z$ and close to the sideband resonance $\omega_{\mathrm{RF}} \approx \mp\omega_z + \omega_\pm$.

In contrast to the double dip lineshape in Eq. (2.70), the axial eigenfrequencies of the coupled axial plus radial system do not directly occur in the lineshape, but rather the radial frequencies directly. Additionally, this lineshape implicitly includes the widths of the two dips due to non-ideal, detuned, sideband coupling. At this point, further application of math might lead to a solution more closely resembling the heuristically derived lineshape Eq. (2.70)[3]. In any case, for the $^9Be^{3+}$ double dips in this work, using the above lineshape leads to insignificant changes $|\delta\nu_+| < 0.1$ mHz of the determined modified cyclotron frequency compared to using Eq. (2.70).

[3] At this point I did try some more approximations, but the path was not obvious to me. Probably a partial fraction decomposition of $K(\omega)$ will reveal $\omega_{z,1,2}$ as the poles. The difficulty here lies therein that the solution needs further approximations as the zeroes of the denominator are found by polynomials of quartic order and not second order as opposed to the eigenfrequencies $\omega_{z,1,2}$, compare Eq. (2.67).

Acknowledgments

Von fast 10 Jahren Studium an der Uni Heidelberg war ich 7 Jahre Mitglied der Gruppe Blaum am MPIK. Dieser maßgebliche und lange Teil meines Studiums wurde durch die tolle Arbeitsatmosphäre und Zusammenarbeit mit vielen Personen am Institut wesentlich geprägt. Hier möchte ich einige dieser Personen hervorheben und mich für deren Unterstützung bedanken.

Lieber Klaus,
dir möchte ich ganz besonders danken, denn deine tolle Leitung der Abteilung hat mir die schöne Zeit am Institut, sei es während des Bachelors, des Masters und der Promotion, erst ermöglicht. Deine große Unterstützung in allen Belangen hat mir in den stressigen Situationen während meiner Promotion die nötige Ruhe zurückgegeben, vielen Dank auch dafür! Für die Promotion hätte ich mir keinen besseren Chef vorstellen können!

Lieber Andi,
in der knappen Zeit von etwa 3 Jahren ist aus dem quasi leeren Tritiumlabor ein funktionierendes Penningfallen Experiment entstanden, mit dem auch direkt erfolgreiche Messungen durchgeführt werden konnten. Dieser Erfolg, welcher maßgeblich von deiner Rolle als Gruppenleiter des Experiments abhängig war, hebt zusätzlich deine großartigen Kentnisse im Bereich der Penningfallen hervor. Für die große Menge an technischen und methodischen Erkentnisse die du mir vermittelt hast und deine Hilfe beim Aufbau und der Durchführung der Experimente bin ich dir sehr dankbar.

Ein großer Dank gebührt allen aktuellen und ehemaligen Mitgliedern des 3He-Trap/µTEx Teams. Von den ehemaligen Mitgliedern möchte ich mich speziell bei Antonia und Alex bedanken. Alex, die Zeit mit dir im Labor war immer spaßig und lehrreich zugleich - eine perfekte Kombination. Antonia, die Zusammenarbeit mit dir war straightforward und deine Geduld bei der Ionenarbeit bewundernswert. Bei Marius und Annabelle möchte ich mich für die tolle Zeit im Labor und abseits bedanken. Mit euch hat sich die Zeit am Institut oft gar nicht nach Arbeit angefühlt! Ich wünsche euch für die nächste Zeit bei µTEx alles Gute und hoffe auch in Zukunft von euch zu hören. Das gleiche gilt für die jüngeren/neuen Mitglieder, Ute, Anton, Philipp und Ankush!

Ein ganz großes Dankeschön gilt auch den Mitglieder der anderen Penningfallenexperimente am Institut. Die Zeit mit euch, Kathrin, Charlotte, Jonathan, Menno, Jost und Christoph (natürlich auch Annabelle und Marius), am Institut, bei Konferenzen, bei den MATS-Tagen oder bei sonstigen geselligen Aktivitäten war mir ein großes Vergnügen. Danke Sergey, dass du die

Messung der Beryllium-9 Masse an PENTATRAP möglich gemacht hast. Ein dickes Danke geht an Sven für die vielen wichtigen Erklärungen und Diskussionen rund um Penningfallenmethoden und ebenso an Fabian für seine Fülle an weitergebenem Literaturwissen. Euch beiden wünsche ich ganz viel Erfolg bei euren zukünftigen Projekten an LSym und ALPHATRAP!

Bei der Theoretikergruppe von Christoph Keitel, insbesondere bei Bastian, Vladimir und Zoltan bedanke ich mich für die produktive Kooperation die in einer (hoffentlich) erfolgreichen Publikation endet.

Lieber Herr Jochim, vielen Dank, dass Sie das Zweitgutachten meiner Arbeit übernommen haben. Ihre AMO Vorlesungen waren ein Highlight meines Studiums - Ihre Faszination der Physik hat eine prägenden Einfluss bei mir hinterlassen.

Abseits von den Forschern am Institut möchte ich mich auch ganz herzlich bei Gabi, für ihre Organisations und Problemlösungskünste, und bei den Kollegen in der Feinwerkmechanik, die ganz maßgeblich beteiligt sind beim Design und der Herstellung vieler Teile unseres Experiments, bedanken.

Zuletzt möchte ich mich bei meinen Eltern bedanken. Ihr habt mich auf meinem langen Weg zur Promotion immer unterstützt und mir zu jedem Zeitpunkt das nötige Vertrauen gegeben.